UNIVERSIDADE FEDERAL DO AMAZONAS
PRÓ-REITORIA DE PESQUISA E PÓS-GRADUAÇÃO
INSTITUTO DE CIÊNCIAS EXATAS
PROGRAMA DE PÓS-GRADUAÇÃO EM QUÍMICA

Theoretical Study of the Pt/TiO_2 Interface in Photocatalytic Systems

Ericson Hamissés Nunes Souza Thaines

Manaus - AM
April - 2024

Ericson Hamissés Nunes Souza Thaines

Theoretical Study of the Pt/TiO_2 Interface in Photocatalytic Systems

Tese de doutorado submetida ao Programa de Pós-Graduação em Química da Universidade Federal do Amazonas exigida para o título de doutorado em Química.

Orientador
Prof. Dr. Leandro Aparecido Pocrifka
Coorientador
Prof. Dr. Renato Garcia de Freitas Sobrinho

Universidade Federal do Amazonas
Pró-Reitoria de Pesquisa e Pós-Graduação
Instituto de Ciências Exatas

Manaus - AM
April - 2024

Ficha Catalográfica

Ficha catalográfica elaborada automaticamente de acordo com os dados fornecidos pelo(a) autor(a).

T364e

Thaines, Ericon Hamissés Nunes Souza
Estudo teórico da interface Pt/TiO2 em sistemas fotocatalíticos / Ericon Hamissés Nunes Souza Thaines . 2024
166 f.: il. color; 31 cm.

Orientador: Leandro Aparecido Pocrifka
Coorientador: Renato Garcia de Freitas Sobrinho
Tese (Doutorado em Química) - Universidade Federal do Amazonas.

1. Refinamento de Rietveld. 2. Dft. 3. Neb. 4. Interface Pt(111)/TiO2(hkl). 5. Modelagem de materiais. I. Pocrifka, Leandro Aparecido. II. Universidade Federal do Amazonas III. Título

I dedicate this work to my parents and my wife for all the support and understanding they gave me.

ACKNOWLEDGEMENTS

First, I would like to thank my parents (Diva and Erickson) and my brothers (Pablo and Djuliano) for their love, encouragement, and help throughout my life. I want to thank my wife (Karine) for her love, being a companion, and her support and strength in difficult times. To everyone in my family, especially my aunt Rute and my uncle Enildo, for all her support and love, Rutiane and Mattheus are my brothers-cousins. To my in-laws (Rodolfo and Clara) and sisters-in-law (Joany and Meire) for all the support provided.

I want to express my deep gratitude to Professor Dr. Leandro Aparecido Pocrifka, who accepted this mentoring adventure without him the PhD could not have happened. Also, I want to express my deep gratitude to Professor Dr. Renato Garcia de Freitas Sobrinho for his advisor, friendship, concern for learning, good coffee and conversations, and for accepting and trusting me as his advisor since 2015.

To all GEMaTA-LEEN colleagues and professors, especially Professor Dr. Raimundo Ribeiro Passos, who was present at my qualification presentation, João, Marinaldo, Magno, Brenner, Cezar, Ananias, Gabriel, Fagnaldo, Leonan, João Pedro, and Rebeca.

To all LCM/LMM group Gabriel, Iuri, Vanessa, Marcos, Matheus, José Luiz, Caio, Simone, Junieli, Isabella, thanks for the coffee moments, papers discussion, jokes, and Carolina candy. To all #Quarantine group, Bakinha, Leo gap, Leozão, Shawan, Vitor, Carmine, Elton, Kaká, Bonato, and Rodrigo for the jokes, fun and dark humor.

To all EDJA family for their support and for making the teaching class lighter and more exciting.

To the financial support for the PPGQ/UFAM through CAPES, CNPQ and FAPEAM.

“Do your best in the conditions you have, while you don’t have better conditions, to do even better!”(Mario Sergio Cortella)

Resumo

O presente trabalho apresenta um estudo das propriedades estruturais e eletrônicas do TiO_2, Fe - doped TiO_2, $Pt(1\,1\,1)/TiO_2(hkl)$ interface, e $Pt_3(1\,1\,1)/TiO_2(hkl)$ interface, sondando as propriedades fotocatlíticas a partir de uma abordagem teórica. O estudo dos materiais tem como partida a caracterização por difração de raio-X, onde foi indexado picos relacionados as fases TiO_2 - anatase, TiO_2 - rutilo, e Pt. As fases anatase e rutilo TiO_2 dopadas com Fe, $Pt(1\,1\,1)/TiO_2(hkl)$ interface, e $Pt_3(1\,1\,1)/TiO_2(hkl)$ interface, foram investigadas usando uma abordagem experimental e teórica, e as fases caracterizadas por difração de raios-X com refinamento Rietveld. As propriedades eletrônicas foram caracterizadas usando cálculos DFT/ondas planas. A reação de divisão da água nas superfícies anatase (*0 1 0*) TiO_2 e TiO_2-Fe foi investigada. As energias de ativação de 0,29 eV e 0,08 eV foram estimadas para estruturas de anatase pura TiO_2 e anatase TiO_2-Fe. A partir do refinamento de Rietveld, foram analisados as deformações na rede cristalina das fases utilizando a análise do μstrain, onde observa-se que a fase TiO_2 - anatase sofre maior deformação em relação a fase Pt, como pode ser observado nos valores calculados de bulk modulus (B_0), visto que $B_{0-Pt} > B_{0-TiO_2}$. A simulação do material ocorreu utilizando os parâmetros cristalográficos obtidos previamente com o refinamento de Rietveld. O estudo da interface $Pt(1\ 1\ 1)/TiO_2(h\ k\ l)$ foi realizado considerando dois planos da fase TiO_2, (*1 0 1*) e (*0 0 1*), os quais foram observados no refinamento de Rietveld. A partir da análise de *PDOS* da interface, foi observado um novo estado eletrônico entre as bandas de valência e banda de condução da fase TiO_2, atribuído à fase Pt. A modelagem teórica da interface $Pt_3(1\ 1\ 1)/TiO_2(h\ k\ l)$ considerando a fração de aproximadamente 60% da fase TiO_2 e 40% da fase $FasePt$ determinada no refinamento Rietveld. A interface $Pt_3(1\ 1\ 1)/TiO_2(1\ 0\ 1)$ apresentou a menor energia de ativação para divisão da molécula de hidrogênio de 0,19 eV com caráter exotérmico. Para a divisão da água, ambas as interfaces $Pt_3(1\,1\,1)/TiO_2(h\,k\,l)$ apresentaram a mesma energia de ativação $\sim$ 1,4 eV com caráter endotérmico.

Palavras-chave: Refinamento de Rietveld, DFT, NEB, Interface $Pt(1\ 1\ 1)/TiO_2(h\ k\ l)$, Modelagem de Materiais.

Abstract

The present work presents a study of the structural and electronic properties of TiO_2, Fe - doped TiO_2, $Pt(1\,1\,1)/TiO_2(hkl)$ interface, and $Pt_3(1\,1\,1)/TiO_2(hkl)$ interface, probing the photocatalytic properties from a theoretical approach. The study of the materials starts with characterization by X-ray diffraction, where peaks related to the phases TiO_2 - anatase, TiO_2 - rutile, and Pt were indexed. Anatase and rutile phases of TiO_2 doped with Fe, $Pt(1\,1\,1)/TiO_2(hkl)$ interface, and $Pt_3(1\,1\,1)/TiO_2(hkl)$ interface were investigated using both experimental and theoretical approaches, and the phases were characterized by X-ray diffraction with Rietveld refinement. Electronic properties were characterized using DFT/plane-wave calculations. Water splitting reaction on anatase surfaces (*0 1 0*) TiO_2 and TiO_2-Fe was investigated. Activation energies of 0.29 eV and 0.08 eV were estimated for pure anatase TiO_2 and anatase TiO_2-Fe structures. From Rietveld refinement, deformations in the crystal lattice of the phases were analyzed using μstrain analysis, where it is observed that the anatase TiO_2 phase undergoes greater deformation compared to the Pt phase, as can be seen in the calculated values of bulk modulus (B_0), since B_{0-Pt} > B_{0-TiO_2}. Material simulation was carried out using the crystallographic parameters obtained previously with Rietveld refinement. The study of the $Pt(1\,1\,1)/TiO_2(h\,k\,l)$ interface was conducted considering two planes of the TiO_2 phase, (*1 0 1*) and (*0 0 1*), which were observed in the Rietveld refinement. From the analysis of interface *PDOS*, a new electronic state between the valence band and conduction band of the TiO_2 phase, attributed to the Pt phase, was observed. Theoretical modeling of the $Pt_3(1\,1\,1)/TiO_2(h\,k\,l)$ interface considering approximately 60% of the TiO_2 phase and 40% of the Pt phase determined in the Rietveld refinement. The $Pt_3(1\,1\,1)/TiO_2(1\,0\,1)$ interface showed the lowest activation energy for hydrogen molecule splitting of 0.19 eV with exothermic character. For water splitting, both interfaces $Pt_3(1\,1\,1)/TiO_2(h\,k\,l)$ presented the same activation energy $\sim$ 1.4 eV with endothermic character.

Keywords: Rietveld Refinement, DFT, NEB, TiO_2, $Pt(1\,1\,1)/TiO_2(h\,k\,l)$ interface, Material Modeling.

LIST OF FIGURES

LIST OF TABLES

LIST OF SYMBOLS AND ABBREVIATIONS

- TiO_2 - Titanium Dioxide
- Pt - Platinum
- DFT - Density Function Theory
- $cutoff$ - Cutoff Energy
- ELF - Electron Localization Functional
- $PDOS$ - Density of Projected States
- $\Delta(n)$ - Electronic Charge Density
- NEB - Nudged Elastic Band
- e^- - Electron
- h^+ - Hole
- EOS - Equation of State
- Ry - Rydberg
- XRD - X-Ray Diffraction
- CIF - Crystallography Information File
- $ICSD$ - Inorganic Crystal Structure Database
- $\mu strain$ - Microstrain
- B_0 - Bulk modulus

CONTENTS

1

INTRODUCTION

The global worry for sustainable energy solutions has been a long discussion due to the environmental impacts of fossil fuel consumption and Human impacts. Renewable energy resources have emerged as a transition priority towards a more sustainable energy future [1, 2]. Solar energy, green fuel, and wind energy hold immense promise as alternatives for the energy matrix. However, the nature of each resource necessitates innovative approaches to energy conversion, storage, and utilization for global use [3–5]. One of the renewable energy research is the development of efficient and cost-effective materials for converting solar energy into electricity or storable fuels [6, 7]. Water splitting is a direct conversion of solar energy into clean fuels such as hydrogen and oxygen [8, 9]. Oxygen and hydrogen gas can be obtained from water splitting. Basset *et al.* [10] studied photocatalytic O_2 and H_2 reactions on the TiO_2 surface. The authors [10] performed first-principles computations based on the density functional theory (DFT) and determined that the reaction depends on hole/electron effective masses, the (*1 1 0*) TiO_2 anatase plane presented hole mobility to the O_2/H_2O potential, and the (*0 0 1*) plane showed electron mobility to the H^+/H_2O potential. Due to the 3.2 eV and 3.0 eV band gap values for the anatase and rutile phases, respectively, TiO_2 cannot use the solar spectrum efficiently. An alternative approach to band gap engineering is doping with metallic or non-metallic atoms [11–14]. Through an experimental study and DFT calculations, Cen *et al.* [15] investigated CO_2 conversion to CO using Mn-doped TiO_2 anatase. According to the authors [15], DFT calculations demonstrated that doping could promote surface vacancy formation and change the material's light response range. Sui *et al.* [16] studied photocatalytic H_2 evolution on anatase TiO_2 through transmission electron microscopy (TEM) and DFT calculations. The authors [16] reported a self-hydrogenated shell generated around TiO_2 nanoparticles when applying UV irradiation.

Titanium dioxide (TiO_2), a widely studied semiconductor, offers unique advantages such as high stability, low cost, and environmental compatibility, making it an attractive material for renewable energy applications [17–19]. The first work on the electrochemical photolysis of water in the presence of platinum and TiO_2 electrodes under ultraviolet light was described by Fujishima and Honda [20]. Yang *et al.* [21] studied water splitting on TiO_2 anatase using temperature-programmed-desorption (TPD) and time-of-flight (TOF) methods. According to the authors [21], water splitting occurs on the surface of TiO_2 anatase under irradiation of 266 nm; the first product is $OH^{\cdot}$, and then the H species is formed by the presence of $OH^{\cdot}$ on the surface. Yamazaki *et al.* [22] reported the morphological change of the TiO_2 rutile from nanorods to nanoparticles on the photocatalytic activity for the oxygen evolution reaction from water oxidation. Through time-resolved microwave conductivity measurements, the authors [22] observed that the recombination of the photogenerated carriers occurs more easily on the TiO_2 nanorod surface. However, the practical use of pure TiO_2 in energy conversion processes is limited by its band gap value, which restricts its absorption of solar radiation. Thus, TiO_2-based materials exhibit small efficiency in the use of solar energy [23]. Therefore, research has explored various strategies to enhance the optical, structural, and electronic properties of TiO_2, with a particular focus on band gap engineering through doping with metallic atoms [24–26] or metal/TiO_2 interfaces [27, 28].

The process of introducing impurities into the crystal lattice of a pure (intrinsic) semiconductor at a low level is known as doping. The added impurity atom is called a dopant atom, and its presence in the crystal can alter the electrical and optical properties of the material. A doped semiconductor is referred to as an extrinsic semiconductor [29–31]. Doping of TiO_2 with metallic or non-metallic atoms offers a strategy to modify its electronic properties as a band gap and enhance its photocatalytic performance for water splitting and other catalytic reactions [32–34]. Among dopants, the iron

(Fe) atom can tune the electronic and structural properties of TiO_2, enhancing its utility in renewable energy applications. Fe doping has emerged in interest due to its abundance, low cost, and ability to tune the electronic properties of materials, promoting surface vacancy formation and introducing new electronic states into the TiO_2 band gap [26, 35, 36]. A photocatalyst with a suitable band gap can be modified according to interest, and the overall efficiency of photoconversion can be improved. Band gap can be modified according to the lattice constant, composition, and morphology. Pereira *et al.* [37] studied the effect of TiO_2 nanotube morphology with deposit ZnS nanoparticles through a theoretical and experimental approach. The Rietveld refinement showed that it is possible to deposit ZnS along the TiO_2 nanotube, and band structure calculations showed a decrease in the band gap values. Many methods, such as the sol-gel method [38], hydrothermal method [39], solvothermal method [40], and Pechini method [41], have been reported for the synthesis of Fe-doped TiO_2. The mentioned methods have advantages and disadvantages, but it is possible to observe difficulties in obtaining Fe-doped TiO_2. The Fe-doped TiO_2 materials are well-known and have been previously studied to enhance the TiO_2 photocatalytic properties [42–45]. However, to enhance understanding of Fe-doped TiO_2 material behavior, it needs to provide a detailed description and comprehensive discussion on the influence of Fe doping on TiO_2 structure and photocatalytic performance. The description can also explore the effects of the iron atom state with oxygen vacancy and TiO_2 structure behavior with Fe doping.

The metal/oxide materials, such as the Pt/TiO_2 interface, exhibit important properties in catalytic or photocatalytic reactions within sustainable energy systems, such as energy storage and photoelectrocatalysis. However, synthesizing these two distinct phases is a complex experimental procedure. Many experimental techniques have been reported in the literature for obtained metal/oxide interfaces, including the Pechini method, solvothermal processes, electrochemical deposition, microwave-assisted methods, and others. Thus, synthesizing metal/oxide interfaces demands access to appropriate infrastructure and reagents [46–50]. At the metal/oxide interfaces, distinct properties are observed from the isolated bulk materials. These interfacial properties can arise from various factors, including altering lattice parameters or strain, significantly influencing electronic and structural properties. The extent of lattice parameter or strain changing at the metal/oxide interface is contingent upon the materials' hardness. For example, the metallic phase may strain the oxide phase or vice versa [51, 52]. This kind of interface forms a Schottky junction, enhancing the catalytic activity of the TiO_2 and minimizing the use of Pt, which is a noble metal expensive [53–55]. The Pt/TiO_2 interface is utilized as a photocatalyst for hydrogen production via water splitting, presenting high hydrogen production rate (HGR) values. The hydrogen evolution reaction (HER) can produce sustainable hydrogen fuel using renewable energy sources [56, 57]. Several materials have been studied and developed for HER catalysts. Platinum (Pt) metal-based catalysts are well-known as the most effective HER catalysts [58, 59]. Lamoureux *et al* [60], described the hydrogen evolution (HER) and oxidation (HOR) on the $Pt(1\,1\,1)$ from a First-principle study. The authors [60] proposed better $Pt(1\,1\,1)$ activity for HER and water reorganization energy from a microkinetic model based on DFT, suggesting that at low pH, HER proceeds:

$$H_3O^+ +^* +e^- \rightarrow H^* + H_2O \qquad \text{(reaction-1)}$$

and the mechanism:

$$H_3O^+ + H^* + e^- \rightarrow H_2 + H_2O +^* . \qquad \text{(reaction-2)}$$

The microkinetic model and the results showed good agreement with the experimental. However, its practical application is limited due to platinum's high cost and limited availability [61]. Many studies have been conducted on alternative catalysts, such as Pt/oxide-based materials, as potential replacements for Pt [62–64]. Pt supported on TiO_2 (Pt/TiO_2) is widely studied for its catalytic and photocatalytic properties as a cost-effective alternative catalyst [65–67]. Pt/TiO_2 forms a Schottky junction, resulting from the interface between a n-type semiconductor (TiO_2) and a metal (Pt). This interface material plays a pivotal role in enhancing the catalytic or photocatalytic activity of the semiconductor, particularly in the presence of noble metals. Pt/TiO_2 interfaces are well-known for their ability to modify the electronic properties of materials and improve their performance in various applications [68, 69]. In photocatalysis, electrons (e^-) and holes (h^+) charge carriers are separated through excitation and play distinct roles in reactions such as oxidation and reduction. However, driven reactions by electrons or holes often occur at reaction sites in very close proximity, which can limit the reaction due to the recombination of e^-/h^+ carriers.Therefore, a Pt/TiO_2 interface can inhibit or prolong the recombination of electrons and holes due to the distinct electronic structures of TiO_2 and Pt [46, 70]. However, other interfaces presented higher HGR values than the Pt/TiO_2, which can be related to a competition of phenomena on the Pt/TiO_2 interface surface, as hydrogen spillover and water splitting [71, 72].

With the catalytic production of hydrogen gas, primarily on noble metals [73], the phenomenon of hydrogen spillover (Figure 1) can be observed [74].

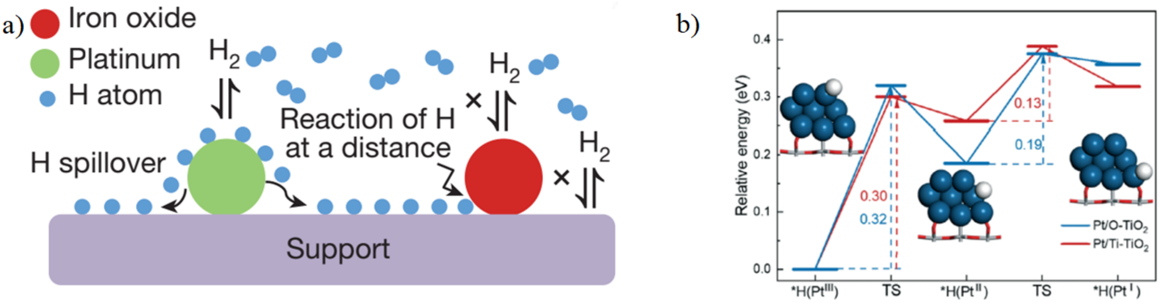

Figure 1 – a) General representation of the H_2 molecule spillover mechanism scheme and b) Energy barrier for the migration of the $-H$ atom using DFT.
[73, 75] - adapted.

The spillover is the migration or transport of a dissociated molecule adsorbed on the surface of a metal onto a support. Typically, the metallic surface is a noble metal, and the support is an oxide. Therefore, understanding spillover at the atomic level plays an important role in comprehending methods for hydrogen storage as fuel for alternative energy sources. The graphical representation of the spillover mechanism can be seen in Figure 1-a, where the phenomenon occurs on the platinum surface. The migration of the hydrogen atom ($-H$) on the metal occurs with a low energy barrier, about 0.35 eV, as shown in Figure 1-b, as observed by Zheng *et al.* [75], who studied the migration of the $-H$ atom on the rutile $Pt/TiO2$(*1 1 0*) interface using density functional theory (DFT). According to the authors, the low energetic barrier of the $-H$ atom migration can be achieved at room temperature, leading to possible practical applications for common use. Nørskov *et al.* [76] studied Cyclic Voltammograms for hydrogen on Pt(*1 1 1*) and Pt(*1 0 0*) from DFT/PW/PBE-GGA and observed that the differential binding energy for H in 0.25 ML is -0.45 eV and -0.60 eV for $Pt(1\ 1\ 1)$ and $Pt(1\ 0\ 0)$ surfaces, respectively. Thus, the authors [76] showed that hydrogen's interaction with Pt is strongly depends on the adsorption plane. Marković *et al.* [77] performed experimental studies on the kinetics of the HER. The authors [77] determined that the HER follows the Tafel reaction on the $Pt(1\ 1\ 0)$ surface and the Heyrovsky reaction on the $Pt(1\ 0\ 0)$ surface but did not determine the main mechanism on the $Pt(1\ 1\ 1)$ surface. In this sense, Nørskov *et al.* obtained DFT calculations for the HER in an electrochemical double layer on the $Pt(1\ 1\ 1)$ electrode. The authors investigated the Tafel reaction $2H_ads \rightarrow H_2$, where the energy barrier was 0.55 eV, and the Heyrovsky reaction $H_{ads} + H^+ + e^- \rightarrow H_2$, where the energy barrier was 0.35 eV, the Heyrovsky reaction is probably the main mechanism, and as the Tafel reaction is close in activation energy, both mechanisms can work in parallel. Several studies have investigated the importance of the $Pt(1\ 1\ 1)$ surface by the adsorption of Hydrogen on $Pt(1\ 1\ 1)$ [78–80]. Sugino *et al.* [81] reported the precision required to describe H adsorption, using DFT at the dRPA, PBE, and vdW-DFT levels of theory to determine the adsorption energy (E_{ads}) of H on $Pt(1\ 1\ 1)$. It was found that the E_{ads} obtained using dRPA and PBE were in good agreement, specifically when the experimental lattice constant was used, suggesting that PBE can predict the relative stability of Hfcc and Htop reported the precision required to describe H adsorption, using DFT at the dRPA and PBE.

1.1 Main Goal

The present work proposes the theoretical study of the TiO_2, Fe - doped TiO_2, $Pt(111)/TiO_2(hkl)$ interface, and $Pt_3(111)/TiO_2(hkl)$ aiming to investigate the structural and electronic properties while monitoring their application in photocatalytic systems.

BIBLIOGRAPHY

1 SINGH, S. Energy crisis and climate change: Global concerns and their solutions. *Energy: Crises, Challenges and Solutions*, Wiley Online Library, p. 1–17, 2021. 18

2 ALBERT, J. S. et al. Human impacts outpace natural processes in the amazon. *Science*, American Association for the Advancement of Science, v. 379, n. 6630, p. eabo5003, 2023. 18

3 NADALETI, W. C.; LOURENÇO, V. A.; AMERICO, G. Green hydrogen-based pathways and alternatives: towards the renewable energy transition in south america's regions–part a. *International Journal of Hydrogen Energy*, Elsevier, v. 46, n. 43, p. 22247–22255, 2021. 18

4 CHERP, A. et al. National growth dynamics of wind and solar power compared to the growth required for global climate targets. *Nature Energy*, Nature Publishing Group UK London, v. 6, n. 7, p. 742–754, 2021. 18

5 MECKLING, J. et al. Why nations lead or lag in energy transitions. *Science*, American Association for the Advancement of Science, v. 378, n. 6615, p. 31–33, 2022. 18

6 BAXTER, J. et al. Nanoscale design to enable the revolution in renewable energy. *Energy & Environmental Science*, Royal Society of Chemistry, v. 2, n. 6, p. 559–588, 2009. 18

7 WANG, Q. et al. Strategies to improve light utilization in solar fuel synthesis. *Nature Energy*, Nature Publishing Group UK London, v. 7, n. 1, p. 13–24, 2022. 18

8 LI, X. et al. Water splitting: from electrode to green energy system. *Nano-Micro Letters*, Springer, v. 12, p. 1–29, 2020. 18

9 YU, Z.-Y. et al. Clean and affordable hydrogen fuel from alkaline water splitting: past, recent progress, and future prospects. *Advanced Materials*, Wiley Online Library, v. 33, n. 31, p. 2007100, 2021. 18

10 HARB, M.; JEANTELOT, G.; BASSET, J.-M. Insights into the most suitable tio2 surfaces for photocatalytic o2 and h2 evolution reactions from dft calculations. *The Journal of Physical Chemistry C*, ACS Publications, v. 123, n. 46, p. 28210–28218, 2019. 18

11 CHEN, D. et al. Carbon and nitrogen co-doped tio2 with enhanced visible-light photocatalytic activity. *Industrial & engineering chemistry research*, ACS Publications, v. 46, n. 9, p. 2741–2746, 2007. 18

12 SOBANA, N.; MURUGANADHAM, M.; SWAMINATHAN, M. Nano-ag particles doped tio2 for efficient photodegradation of direct azo dyes. *Journal of Molecular Catalysis A: Chemical*, Elsevier, v. 258, n. 1-2, p. 124–132, 2006. 18

13 OHNO, T.; MITSUI, T.; MATSUMURA, M. Photocatalytic activity of s-doped tio2 photocatalyst under visible light. *Chemistry letters*, Oxford University Press, v. 32, n. 4, p. 364–365, 2003. 18

14 VALENTIN, C. D. et al. Characterization of paramagnetic species in n-doped tio2 powders by epr spectroscopy and dft calculations. *The Journal of Physical Chemistry B*, ACS Publications, v. 109, n. 23, p. 11414–11419, 2005. 18

15 DENG, B. et al. Enhanced solar conversion of co2 to co using mn-doped tio2 based on photo-thermochemical cycle. *ChemistrySelect*, Wiley Online Library, v. 4, n. 1, p. 236–244, 2019. 18

16 LU, Y. et al. Self-hydrogenated shell promoting photocatalytic h2 evolution on anatase tio2. *Nature communications*, Nature Publishing Group UK London, v. 9, n. 1, p. 2752, 2018. 19

17 JAKSIK, J. et al. Nanostructured functional materials for advanced three-dimensional (3d) solar cells. *Solar Energy Materials and Solar Cells*, Elsevier, v. 167, p. 121–132, 2017. 19

18 KAPILASHRAMI, M. et al. Probing the optical property and electronic structure of tio2 nanomaterials for renewable energy applications. *Chemical reviews*, ACS Publications, v. 114, n. 19, p. 9662–9707, 2014. 19

19 LI, Z. et al. Recent progress in defective tio2 photocatalysts for energy and environmental applications. *Renewable and Sustainable Energy Reviews*, Elsevier, v. 156, p. 111980, 2022. 19

20 FUJISHIMA, A.; HONDA, K. Electrochemical photolysis of water at a semiconductor electrode. *nature*, Nature Publishing Group UK London, v. 238, n. 5358, p. 37–38, 1972. 19

21 GENG, Z. et al. Highly efficient water dissociation on anatase tio2 (101). *The Journal of Physical Chemistry C*, ACS Publications, v. 120, n. 47, p. 26807–26813, 2016. 19

22 YAMAZAKI, Y. et al. Developing active tio2 nanorods by examining the influence of morphological changes from nanorods to nanoparticles on photocatalytic activity. *ACS Applied Nano Materials*, ACS Publications, v. 1, n. 10, p. 5927–5935, 2018. 19

23 DIEBOLD, U. The surface science of titanium dioxide. *Surface science reports*, Elsevier, v. 48, n. 5-8, p. 53–229, 2003. 19

24 SOBANA, N.; MURUGANADHAM, M.; SWAMINATHAN, M. Nano-ag particles doped tio2 for efficient photodegradation of direct azo dyes. *Journal of Molecular Catalysis A: Chemical*, Elsevier, v. 258, n. 1-2, p. 124–132, 2006. 19

25 OHNO, T.; MITSUI, T.; MATSUMURA, M. Photocatalytic activity of s-doped tio2 photocatalyst under visible light. *Chemistry letters*, Oxford University Press, v. 32, n. 4, p. 364–365, 2003. 19

26 THAINES, E. H. et al. Influence of fe-doping on the structural and electronic properties of the tio2 anatase: Rutile. *The Journal of Physical Chemistry C*, ACS Publications, v. 127, n. 46, p. 22518–22529, 2023. 19, 20

27 NANDI, D. et al. Metal/metal oxide decorated graphene synthesis and application as supercapacitor: a review. *Journal of Materials Science*, Springer, v. 55, n. 15, p. 6375–6400, 2020. 19

28 JIANG, J. et al. Recent advances in metal oxide-based electrode architecture design for electrochemical energy storage. *Advanced materials*, Wiley Online Library, v. 24, n. 38, p. 5166–5180, 2012. 19

29 JR, W. D. C. *Materials science and engineering an introduction*. [S.l.: s.n.], 2007. 19

30 KITTEL, C. *Introduction to solid state physics*. [S.l.]: John Wiley & sons, inc, 2005. 19

31 ASHCROFT, N. W.; MERMIN, N. D. *Física do estado sólido*. [S.l.]: Cengage Learning, 2011. 19

32 ISMAEL, M. Enhanced photocatalytic hydrogen production and degradation of organic pollutants from fe (iii) doped tio2 nanoparticles. *Journal of Environmental Chemical Engineering*, Elsevier, v. 8, n. 2, p. 103676, 2020. 19

33 QIN, Y. et al. Nitrogen-doped hydrogenated tio2 modified with cds nanorods with enhanced optical absorption, charge separation and photocatalytic hydrogen evolution. *Chemical Engineering Journal*, Elsevier, v. 384, p. 123275, 2020. 19

34 ALOTAIBI, A. M. et al. Enhanced photocatalytic and antibacterial ability of cu-doped anatase tio2 thin films: theory and experiment. *ACS applied materials & interfaces*, ACS Publications, v. 12, n. 13, p. 15348–15361, 2020. 19

35 MISHRA, A. et al. Waste ilmenite sludge-derived low-cost mesoporous fe-doped tio2: A versatile photocatalyst for enhanced visible light photocatalysis without a cocatalyst. *Journal of Environmental Chemical Engineering*, Elsevier, p. 110319, 2023. 20

36 MAHADADALKAR, M. A. et al. Electrospun fe doped tio2 fiber photocatalyst for efficient wastewater treatment. *Chemosphere*, Elsevier, v. 330, p. 138599, 2023. 20

37 SANTANNA, M. et al. The effect of tio2 nanotube morphological engineering and zns quantum dots on the water splitting reaction: A theoretical and experimental study. *international journal of hydrogen energy*, Elsevier, v. 43, n. 14, p. 6838–6850, 2018. 20

38 ISARI, A. A. et al. Photocatalytic degradation of rhodamine b and real textile wastewater using fe-doped tio2 anchored on reduced graphene oxide (fe-tio2/rgo): Characterization and feasibility, mechanism and pathway studies. *Applied Surface Science*, Elsevier, v. 462, p. 549–564, 2018. 20

39 SHI, J. et al. Hydrothermal synthesis of graphene wrapped fe-doped tio2 nanospheres with high photocatalysis performance. *Ceramics International*, Elsevier, v. 44, n. 7, p. 7473–7480, 2018. 20

40 WANG, Q. et al. Solvothermal preparation of fe-doped tio2 nanotube arrays for enhancement in visible light induced photoelectrochemical performance. *Journal of Alloys and Compounds*, Elsevier, v. 690, p. 139–144, 2017. 20

41 VASQUEZ, G. C. et al. Laser-induced anatase-to-rutile transition in tio2 nanoparticles: promotion and inhibition effects by fe and al doping and achievement of micropatterning. *The Journal of Physical Chemistry C*, ACS Publications, v. 119, n. 21, p. 11965–11974, 2015. 20

42 LIU, Y. et al. Enhanced visible light photocatalytic properties of fe-doped tio2 nanorod clusters and monodispersed nanoparticles. *Applied surface science*, Elsevier, v. 257, n. 18, p. 8121–8126, 2011. 20

43 HAN, G. et al. Controlling surface oxygen vacancies in fe-doped tio2 anatase nanoparticles for superior photocatalytic activities. *Applied Surface Science*, Elsevier, v. 507, p. 144916, 2020. 20

44 PISKUNOV, S. et al. C-, n-, s-, and fe-doped tio2 and srtio3 nanotubes for visible-light-driven photocatalytic water splitting: Prediction from first principles. *The Journal of Physical Chemistry C*, ACS Publications, v. 119, n. 32, p. 18686–18696, 2015. 20

45 GEORGE, S. et al. Role of fe doping in tuning the band gap of tio2 for the photo-oxidation-induced cytotoxicity paradigm. *Journal of the American Chemical Society*, ACS Publications, v. 133, n. 29, p. 11270–11278, 2011. 20

46 LINSEBIGLER, A. L.; LU, G.; JR, J. T. Y. Photocatalysis on tio2 surfaces: principles, mechanisms, and selected results. *Chemical reviews*, ACS Publications, v. 95, n. 3, p. 735–758, 1995. 20, 22

47 CORNELIUS, T. W. et al. Piezoelectric response and electrical properties of pb (zr1-xtix) o3 thin films: The role of imprint and composition. *Journal of Applied Physics*, AIP Publishing, v. 122, n. 16, 2017. 20

48 LI, H. et al. A self-assembled 3d pt/tio2 architecture for high-performance photocatalytic hydrogen production. *Nanoscale*, The Royal Society of Chemistry, v. 7, n. 5, p. 1610–1615, 2015. 20

49 GEPPERT, T. N. et al. Hor activity of pt-tio2-y at unconventionally high potentials explained: the influence of smsi on the electrochemical behavior of pt. *Journal of The Electrochemical Society*, IOP Publishing, v. 167, n. 8, p. 084517, 2020. 20

50 FUKU, K. et al. Highly dispersed platinum nanoparticles on tio2 prepared by using the microwave-assisted deposition method: An efficient photocatalyst for the formation of h2 and n2 from aqueous nh3. *Chemistry–An Asian Journal*, Wiley Online Library, v. 7, n. 6, p. 1366–1371, 2012. 20

51 JIANG, J. et al. Recent advances in metal oxide-based electrode architecture design for electrochemical energy storage. *Advanced materials*, Wiley Online Library, v. 24, n. 38, p. 5166–5180, 2012. 21

52 MURALIDHARAN, N. et al. Strain engineering to modify the electrochemistry of energy storage electrodes. *Scientific reports*, Nature Publishing Group, v. 6, n. 1, p. 1–9, 2016. 21

53 YOSHIMURA, N. et al. Enhancement of photocatalytic activity for hydrogen production by surface modification of pt-tio2 nanoparticles with a double layer of photosensitizers. *Chemistry–A European Journal*, Wiley Online Library, v. 26, n. 70, p. 16939–16946, 2020. 21

54 CAN, E.; URALCAN, B.; YILDIRIM, R. Enhancing charge transfer in photocatalytic hydrogen production over dye-sensitized pt/tio2 by ionic liquid coating. *ACS Applied Energy Materials*, ACS Publications, v. 4, n. 10, p. 10931–10939, 2021. 21

55 KIM, S. B. et al. Promoting metal–support interaction on pt/tio2 catalyst by antimony for enhanced carbon monoxide oxidation activity at room temperature. *Industrial & Engineering Chemistry Research*, ACS Publications, v. 61, n. 40, p. 14793–14803, 2022. 21

56 LIU, J. et al. Recent progress in non-precious metal single atomic catalysts for solar and non-solar driven hydrogen evolution reaction. *Advanced Sustainable Systems*, Wiley Online Library, v. 4, n. 11, p. 2000151, 2020. 21

57 GUAN, J.; BAI, X.; TANG, T. Recent progress and prospect of carbon-free single-site catalysts for the hydrogen and oxygen evolution reactions. *Nano Research*, Springer, v. 15, n. 2, p. 818–837, 2022. 21

58 HONG, Y.-R. et al. Crystal facet-manipulated 2d pt nanodendrites to achieve an intimate heterointerface for hydrogen evolution reactions. *Journal of the American Chemical Society*, ACS Publications, v. 144, n. 20, p. 9033–9043, 2022. 21

59 DU, L. et al. Low-pgm and pgm-free catalysts for proton exchange membrane fuel cells: stability challenges and material solutions. *Advanced Materials*, Wiley Online Library, v. 33, n. 6, p. 1908232, 2021. 21

60 LAMOUREUX, P. S.; SINGH, A. R.; CHAN, K. ph effects on hydrogen evolution and oxidation over pt (111): insights from first-principles. *Acs Catalysis*, ACS Publications, v. 9, n. 7, p. 6194–6201, 2019. 21

61 SEH, Z. W. et al. Combining theory and experiment in electrocatalysis: Insights into materials design. *Science*, American Association for the Advancement of Science, v. 355, n. 6321, p. eaad4998, 2017. 21

62 FU, Q. et al. Interface-confined ferrous centers for catalytic oxidation. *science*, American Association for the Advancement of Science, v. 328, n. 5982, p. 1141–1144, 2010. 21

63 MASUDA, T. et al. Role of cerium oxide in the enhancement of activity for the oxygen reduction reaction at pt–ceo x nanocomposite electrocatalyst-an in situ electrochemical x-ray absorption fine structure study. *The Journal of Physical Chemistry C*, ACS Publications, v. 116, n. 18, p. 10098–10102, 2012. 21

64 MACINO, M. et al. Tuning of catalytic sites in pt/tio2 catalysts for the chemoselective hydrogenation of 3-nitrostyrene. *Nature Catalysis*, Nature Publishing Group UK London, v. 2, n. 10, p. 873–881, 2019. 21

65 VIKRANT, K. et al. Platinized titanium dioxide (pt/tio2) as a multi-functional catalyst for thermocatalysis, photocatalysis, and photothermal catalysis for removing air pollutants. *Applied Materials Today*, Elsevier, v. 23, p. 100993, 2021. 21

66 ANTOLINI, E. Photo-assisted methanol oxidation on pt-tio2 catalysts for direct methanol fuel cells: A short review. *Applied Catalysis B: Environmental*, Elsevier, v. 237, p. 491–503, 2018. 21

67 QI, L. et al. High-surface area mesoporous pt/tio2 hollow chains for efficient formaldehyde decomposition at ambient temperature. *Journal of hazardous materials*, Elsevier, v. 301, p. 522–530, 2016. 21

68 SCHOTTKY, W. Zur halbleitertheorie der sperrschicht-und spitzengleichrichter. *Zeitschrift für Physik*, Springer, v. 113, p. 367–414, 1939. 21

69 TUNG, R. T. Applied physics reviews. *The physics and chemistry of the Schottky barrier height*, v. 1, n. 1, p. 011304, 2014. 21

70 WU, X. et al. Solar energy-driven lignin-first approach to full utilization of lignocellulosic biomass under mild conditions. *Nature catalysis*, Nature Publishing Group UK London, v. 1, n. 10, p. 772–780, 2018. 22

71 YU, J.; QI, L.; JARONIEC, M. Hydrogen production by photocatalytic water splitting over pt/tio2 nanosheets with exposed (001) facets. *The Journal of Physical Chemistry C*, ACS Publications, v. 114, n. 30, p. 13118–13125, 2010. 22

72 GAO, F.; XU, Z.; ZHAO, H. Flame spray pyrolysis made pt/tio2 photocatalysts with ultralow platinum loading and high hydrogen production activity. *Proceedings of the Combustion Institute*, Elsevier, v. 38, n. 4, p. 6503–6511, 2021. 22

73 KARIM, W. et al. Catalyst support effects on hydrogen spillover. *Nature*, Nature Publishing Group, v. 541, n. 7635, p. 68–71, 2017. 22

74 KHOOBIAR, S. Particle to particle migration of hydrogen atoms on platinum—alumina catalysts from particle to neighboring particles. *The Journal of Physical Chemistry*, ACS Publications, v. 68, n. 2, p. 411–412, 1964. 22

75 ZHENG, X. et al. Understanding the effect of interfacial interaction on metal/metal oxide electrocatalysts for hydrogen evolution and hydrogen oxidation reactions on the basis of first-principles calculations. *Catalysis Science & Technology*, Royal Society of Chemistry, v. 10, n. 14, p. 4743–4751, 2020. 22

76 KARLBERG, G. et al. Cyclic voltammograms for h on pt (111) and pt (100) from first principles. *Physical review letters*, APS, v. 99, n. 12, p. 126101, 2007. 22, 23

77 MARKOVIĆ, N.; GRGUR, B.; ROSS, P. N. Temperature-dependent hydrogen electrochemistry on platinum low-index single-crystal surfaces in acid solutions. *The Journal of Physical Chemistry B*, ACS Publications, v. 101, n. 27, p. 5405–5413, 1997. 23

78 SHIH, A. J.; ARULMOZHI, N.; KOPER, M. T. Electrocatalysis under cover: enhanced hydrogen evolution via defective graphene-covered pt (111). *ACS Catalysis*, ACS Publications, v. 11, n. 17, p. 10892–10901, 2021. 23

79 LIU, L.; LIU, Y.; LIU, C. Enhancing the understanding of hydrogen evolution and oxidation reactions on pt (111) through ab initio simulation of electrode/electrolyte kinetics. *Journal of the American Chemical Society*, ACS Publications, v. 142, n. 11, p. 4985–4989, 2020. 23

80 LAMOUREUX, P. S.; SINGH, A. R.; CHAN, K. ph effects on hydrogen evolution and oxidation over pt (111): insights from first-principles. *Acs Catalysis*, ACS Publications, v. 9, n. 7, p. 6194–6201, 2019. 23

81 YAN, L. et al. Hydrogen adsorption on pt (111) revisited from random phase approximation. *The Journal of chemical physics*, AIP Publishing, v. 149, n. 16, 2018. 23

2

THEORETICAL FRAMEWORK

The theoretical description of materials or solids is known as *materials modeling*, which is carried out through mathematical models resulting in quantitative or qualitative properties of interest at the atomic level. Choosing theoretical models plays a fundamental role in developing materials or solids studies. Materials modeling is grounded in quantum mechanics to describe the behavior of materials or solids at the atomic level, and it can be used to study electronic and structural properties. The mathematical models employed are complex, and transformations and/or approximations are used to solve the equations [1, 2].

2.1 Schrödinger equation

The equation presented by Erwin Schrödinger in 1926 [3] describes the mechanics of atoms and molecules; that is, it describes the wave function of a particle through the time-dependent equation (t):

$$\left[-\frac{\hbar^2}{2m}\nabla^2 + V(\vec{r})\right]\Psi(\vec{r},t) = i\hbar\frac{\partial\Psi}{\partial t}(\vec{r},t), \tag{2.1}$$

where Ψ is the wave function, $\hbar$ is the reduced Planck constant, m is the mass of the particle, V is the potential in which the particle is moving, and ∇^2 is the Laplacian operator acting on the coordinates of the system, written as,

$$\nabla^2 = \frac{\partial^2}{\partial x^2} + \frac{\partial^2}{\partial y^2} + \frac{\partial^2}{\partial z^2}. \tag{2.2}$$

The time independent Schrödinger equation, equation (2.3), can be expressed in simplified form as,

$$\hat{H}\psi = E\psi, \tag{2.3}$$

where $\hat{H}$ is the Hamiltonian mathematical operator and E is the energy of the system. The operator $\hat{H}$, equation (2.3), includes terms of kinetic energy and potential energy:

$$\hat{H} = \hat{T} + \hat{V}, \tag{2.4}$$

where $\hat{T}$ is the operator of kinetic energy, expressed as the sum of ∇^2, equation (2.2), over all particles in the system:

$$\hat{T} = -\frac{\hbar^2}{2}\sum_k \frac{\nabla^2}{m_k}, \tag{2.5}$$

and $\hat{V}$ is the operator of potential energy, considering the Coulombic repulsion and attraction between electrons and nuclei as follows:

$$\hat{V} = \frac{1}{4\pi\epsilon_0}\sum_i \sum_{i<j} \frac{e_i e_j}{\Delta r_{ij}}, \tag{2.6}$$

where Δr_{ij} is the distance between particles, e_i and e_j represent the charges of the particles. Considering an electron, the charge will be $-e$, and for the nucleus, it will be Ze, where Z is the atomic number. From equation (2.6), $\hat{V}$ can be written as follows:

$$\hat{V} = \frac{1}{4\pi\epsilon_0}\left[\underbrace{-\sum_i \sum_I \left(\frac{Z_I e^2}{\Delta r_{iI}}\right)}_{\text{nucleus-electron attraction}} + \underbrace{\sum_i \sum_{j<i} \left(\frac{e^2}{\Delta r_{ij}}\right)}_{\text{electron-electron repulsion}} + \underbrace{\sum_I \sum_{J<I} \left(\frac{Z_I Z_J e^2}{\Delta R_{IJ}}\right)}_{\text{nucleus-nucleus repulsion}}\right]. \tag{2.7}$$

Although the Schrödinger equation describes an atomic system, its analytical solution is not trivial. Various mathematical methods are involved in its resolution and possible acquisition of the system's wave function. Equation (2.1) has an analytical solution for hydrogen atoms and for so-called hydrogen-like systems, such as H_2^+, He^+, Li^{2+}, etc. In other words, approximations are necessary for any system containing many electrons to solve the equation. This includes calculations to obtain electronic states and energies of periodic systems, for example [4, 5].

2.2 Born-Oppenheimer approximation

M. Born and J. R. Oppenheimer [6] introduced the first of several approximations used to simplify the solution of the Schrödinger equation. The Born-Oppenheimer approximation takes into account the fact that nuclei have a much larger mass compared to electrons. Consequently, the velocity of electrons is much greater than that of the nuclei, causing electrons to react almost instantaneously to the movement of the nuclei. Thus, the Born-Oppenheimer approximation decouples nuclear motion from electronic motion, meaning that electronic motion occurs in a fixed nuclear field. The complete Hamiltonian for a system can be written as:

$$\hat{H} = \hat{T}_n(\vec{R}) + \hat{T}_e(\vec{r}) + \hat{V}_{ne}(\vec{R},\vec{r}) + \hat{V}_{ee}(\vec{r}) + \hat{V}_{nn}(\vec{R}). \tag{2.8}$$

The Born-Oppenheimer approximation allows for decoupling the nuclear and electronic parts, meaning that the two parts can be solved independently. Thus, the electronic Hamiltonian is represented as follows:

$$\hat{H}_{ele} = -\frac{1}{2}\sum_i \nabla^2 - \frac{1}{2}\sum_i\sum_I \left(\frac{Z_I}{|\vec{R}_I - \vec{r}_i|}\right) + \sum_i\sum_{j<i}\left(\frac{1}{|\vec{r}_i - \vec{r}_j|}\right) + \sum_I\sum_{J<I}\left(\frac{Z_I Z_J}{|\vec{R}_I - \vec{R}_J|}\right). \tag{2.9}$$

It is noticeable in the equation above (2.9) that the nuclear kinetic term is not represented. Thus, $\hat{H}_{ele}$ (2.9) is used in the Schrödinger equation (2.3) to describe the motion of electrons in a fixed nuclear field.

$$\hat{H}_{ele}\psi_{ele}(\vec{R},\vec{r}) = E_{eff}(\vec{R})\psi_{ele}(\vec{R}), \tag{2.10}$$

where E_{eff} is the effective nuclear potential function and depends on the nuclear coordinates. Thus, the nuclear Hamiltonian is described as:

$$H_{nuclear} = \hat{T}_n(\vec{R}) + E_{eff}(\vec{R}). \tag{2.11}$$

Equation (2.11) describes vibrational, rotational, and translational states of the nucleus, and solving this approximation provides vibrational spectra, free energy, enthalpy, or other physical observables of interest [7].

2.3 Density Functional Theory (DFT)

Density Functional Theory (DFT) [8, 9] has proven to be an efficient method for calculating energy, band structure in solids, or other properties of various systems. DFT describes the properties of a given system through charge density functionals in space ($n(r)$) instead of using the wave function (ψ) as in early *ab-initio* calculation methods, enabling the description of a multi-electronic system. The use of $n(r)$ as a variable for describing an electronic system was initially introduced by Drude, who represented the thermal and electrical conduction of a metal by applying kinetic gas theory [10]. However, it was the work of Pierre Hohenberg and Walter Kohn in 1964 that defined, for a non-homogeneous electron gas system, the number of electrons related to the electronic density according to the equation [8]:

$$N[n] \equiv \int n(r)dr = N, \tag{2.12}$$

where N is the number of electrons in the system.

The development of DFT began in the 1920s with the independent works of Llewellyn H. Thomas and Enrico Fermi. In these works, $n(r)$ is obtained by considering a gas of non-interacting uniform electrons, with the system's total energy as a functional of this density separated into its kinetic and potential contributions. In the same decade, Dirac contributed to the description of the works by including the exchange term for an electron gas, and the model became known as Thomas-Fermi-Dirac [11–13].

2.3.1 The Hohenberg-Kohn theorems

The modern foundation of DFT originates in the Hohenberg-Kohn (HK) theorems in 1964 [8], which demonstrated the existence of a functional that determines the energy and density of the ground state. In HK's work, a system in a large box was considered, moving under the influence of a given external potential $v(r)$ and an arbitrary number of electrons N

subjected to Coulomb interaction. Thus, the Hamiltonian of the system can be represented as follows,

$$H = \hat{T} + \hat{V} + \hat{U}, \tag{2.13}$$

where $\hat{T}$ is the operator for kinetic energy,

$$\hat{T} \equiv \frac{1}{2} \int \nabla \psi^*(r) \nabla \psi(r) dr, \tag{2.14}$$

$\hat{V}$ is the operator for Coulombic repulsion,

$$\hat{V} \equiv \int v(r) \psi^*(r) \psi(r) dr, \tag{2.15}$$

$\hat{U}$ is the external potential,

$$\hat{U} = \frac{1}{2} \int \frac{1}{|r - r'|} \psi^*(r) \psi^*(r') \psi(r') \psi(r) dr dr', \tag{2.16}$$

where $\hat{U}$ is a functional of the density $n(r)$ and an additive constant in the Hamiltonian to describe the electronic system.

The electronic density in the non-degenerate ground state (Ψ) is defined by the following equation:

$$n(r) \equiv (\Psi, \psi^*(r) \psi(r) \Psi), \tag{2.17}$$

or in terms of the integral:

$$n(r) = \int \psi^*(r) \psi(r). \tag{2.18}$$

Hohenberg and Kohn employed the variational principle to prove their theorem, which states that, for a given $\hat{H}$, the ground state wave function Ψ generates the minimum energy. Thus, assuming a second potential with the ground state Ψ', which produces the same density $n(r)$, it is possible to denote the Hamiltonian and ground state energies associated with Ψ and Ψ' by $\hat{H}$, $\hat{H}$, E, and E', respectively. This is obtained through the minimization property of the ground state,

$$E' = (\Psi', H' \Psi') < (\Psi, H' \Psi) = (\Psi, (H + V' - V) \Psi), \tag{2.19}$$

so that,

$$E' < E + \int [v'(r) - v(r)] n(r) dr. \tag{2.20}$$

Exchanging the quantities, one finds the same as,

$$E < E' + \int [v'(r) - v(r)]n(r)dr. \tag{2.21}$$

The addition of equations (2.20) and (2.21) leads to inconsistency,

$$E + E' < E + E'. \tag{2.22}$$

When considering the difference between the Hamiltonians and assuming that both wave functions produce the same electron density, a proof is described by the *"reductio ad absurdum"* of the equation (2.22). Thus, $v(r)$ is a unique function of $n(r)$.

The ground state Ψ is a functional of $n(r)$, as are the kinetic and interaction energies. Therefore, a functional is defined as:

$$F[n(r)] \equiv (\Psi, (\hat{T} + \hat{U})\Psi), \tag{2.23}$$

where $F[n]$ is the universal functional of Hohenberg-Kohn and for a given potential $v(r)$ the energy functional is defined as,

$$E_v[n] \equiv \int v(r)n(r)dr + F[n]. \tag{2.24}$$

Hohenberg and Kohn established that for a given approximate electronic density $n'(r)$ describing a system, it will yield an energy equal to or greater than the exact energy of the system as follows:

$$E[n'] \geq E[n] = E_0, \tag{2.25}$$

where n' is an arbitrary density satisfying the condition of equation (2.12).

2.3.2 Kohn-Sham equations

In 1965, W. Kohn and L. J. Sham developed self-consistent equations based on the work of Hohenberg-Kohn that include exchange and correlation effects [9]. Kohn-Sham introduced the concept of non-interacting electrons with antisymmetric orbitals (single-particle orbitals), considering an arbitrary system of non-interacting particles such that the electron density is equivalent to that of the real system composed of interacting particles. The energy functional of the ground state of a non-homogeneous electron gas in a static potential $v(r)$, with electron-electron Coulomb repulsion, can be written as follows:

$$E_v[n] = \int v(r)n(r)dr + \frac{1}{2}\int\int \frac{n(r)n'(r)}{|r-r'|}drdr' + G[n], \tag{2.26}$$

where $n(r)$ is the density and $G[n]$ is a universal density functional and can be written in the form:

$$G[n] \equiv T_s[n] + E_{xc}[n], \tag{2.27}$$

where $T_s[n]$ is the kinetic energy functional of a system of non-interacting electrons with density $n(r)$ and E_{xc} is the non-classical electron-electron interaction term of exchange and correlation.

From a stationary property, can obtain the condition:

$$\int \delta n(r)dr = o, \tag{2.28}$$

one can write the equation

$$\int \delta n(r)\left\{v_{eff} + \frac{\delta T_s[n]}{\delta n(r)}\right\}dr = 0, \tag{2.29}$$

where,

$$v_{eff} = v(r) + \int \frac{n(r')}{|r-r'|}dr' + \mu_{xc}(n(r)), \tag{2.30}$$

where,

$$\mu_{xc} = \frac{n\delta E_{xc}(n)}{\delta n}, \tag{2.31}$$

where μ_{xc} is the exchange and correlation contribution term for a chemical potential of a uniform gas with density n.

Therefore, for a given v_{eff} and μ, one obtains $n(r)$ which satisfies equations (2.28) and (2.29) by solving the Schrödinger equation for a particle

$$\left\{-\frac{1}{2}\nabla^2 + v_{eff}\right\}\psi_i(r) = \epsilon_i\psi_i, \tag{2.32}$$

where the density $n(r)$ can be expressed as:

$$n(r) = \sum_{i=1}^{N}|\psi_i(r)|^2, \tag{2.33}$$

where N is the number of electrons. To obtain the ground state (Ψ_{KS}), the wave function can be written as N_{KS} Kohn-Sham orbitals ($\psi_i(r)$) by the Slater determinant:

$$\Psi_{KS} = \frac{1}{\sqrt{N!}} \begin{vmatrix} \psi_1(r_1) & \psi_2(r_2) & \cdots & \psi_N(r_1) \\ \psi_1(r_2) & \psi_2(r_2) & \cdots & \psi_N(r_2) \\ \vdots & \vdots & \ddots & \vdots \\ \psi_1(r_N) & \psi_2(r_N) & \cdots & \psi_N(r_N) \end{vmatrix} . \tag{2.34}$$

The orbitals are eigenfunctions of the Kohn-Sham Hamiltonian:

$$H_{KS} = -\frac{1}{2}\nabla^2 + v_{eff}(r). \tag{2.35}$$

The equations (2.30), (2.31), (2.32), and (2.33) represent the self-consistent field (SCF) cycle of Kohn-Sham, as shown in Figure 2. In the Kohn-Sham SCF, the exact density of the ground state of a real system with interacting electrons is described by a density of non-interacting electron system that provides an approximation to the real ground state density. The self-consistent field cycle proposed by Kohn-Sham is similar to the self-consistent field cycle proposed by Hartree-Fock.

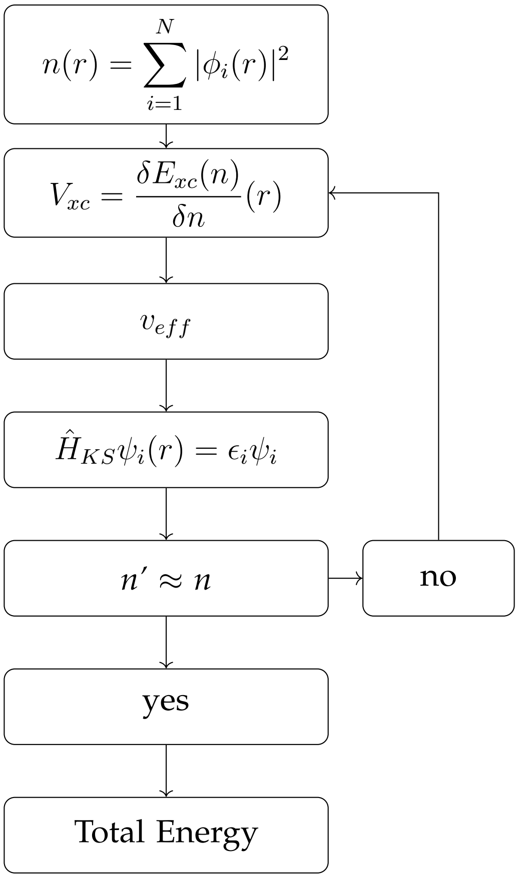

Figure 2 – Self-consistent cycle for the determination of energy and properties of an electronic system.

Therefore, the self-consistent cycle of Kohn-Sham allows for the calculation of the ground state energy as follows:

$$E_0[n(r)] = \sum_i^N \epsilon_i - \frac{1}{2}\int \frac{n'(r)n(r)}{|r-r'|}drdr' + E_{xc}[n(r)] - \int n(r)\mu_{xc}(r)dr. \tag{2.36}$$

The potential μ_{xc} is not known, and the functionals used to construct this exchange-correlation potential are derived from approximations, known as exchange-correlation functionals. Many works have developed different functionals, the most commonly used being the Local Density Approximation (LDA) and the Generalized Gradient Approximations (GGA) [14].

2.4 Periodic Structures

With the formulation of quantum mechanics, the treatment of a solid material attempts to explain its structural and electronic properties based on its primary constituents, the atoms, and their arrangements in space. The atomic-level description of a solid is grounded in the principles of quantum mechanics, as illustrated by advances in the understanding of electronic and structural properties of new materials, including complex materials whose spatial arrangement is formed by many atoms in disordered configurations [15, 16].

A periodic structure, such as a crystal, is a system of infinite points with regular arrangements throughout space, constituting the so-called Bravais lattice. These lattice points can be defined by three translation vectors $\vec{a}$, $\vec{b}$, and $\vec{c}$, such that the arrangement of atoms in the system appears the same when viewed from a point $\mathbf{r}$ and from a point $\mathbf{r'}$ translated relative to the vectors by an integer multiple:

$$r' = r + u_1\vec{a} + u_2\vec{b} + u_3\vec{c}, \tag{2.37}$$

where u_n are integers, the periodic structure is defined concerning the set of points r' for all integer values of u_n. The structure is formed when a basis is attached to each point of the lattice as follows:

1. A Bravais lattice is an arrangement of infinite points with the *same* arrangement and orientation, such that the arrangement appears identical when viewed from any of its points

2. A three-dimensional (3D) Bravais lattice consists of all points with position vectors **R** of the form,

$$\mathbf{R} = u_1\vec{a} + u_2\vec{b} + u_3\vec{c}, \tag{2.38}$$

where $\vec{a}$, $\vec{b}$ e $\vec{c}$ are linearly independent vectors forming a basis.

So, a Bravais lattice possesses translational symmetry, meaning a point geometrically equivalent to another by a translation operation on the points of this lattice. For this reason, the potential energy of the system exhibits periodicity with the periodicity of the lattice in question in the form:

$$U(r + \mathbf{R}_n) = U(r), \tag{2.39}$$

where ***R*** is a translation vector that takes one lattice point to another; *n* indicates the site. With the unit cell defined in the Bravais lattice, three primitive translation vectors $\vec{a}$, $\vec{b}$, and $\vec{c}$ are obtained

2.4.1 Bloch's Theorem

Swiss physicist Felix Bloch demonstrated that the solutions to the Schrödinger equation for a periodic potential, defined by equation (2.39), must be in the form of plane waves ($e^{iK.r}$) times a function with the periodicity of the Bravais lattice [16, 17]:

$$\psi(r + R) = \psi_{n\mathbf{K}}(r) = e^{i\mathbf{K}.r}u_{n\mathbf{K}}(r), \tag{2.40}$$

where u_{nk} takes the form of the equation (2.39):

$$u_{n\mathbf{K}}(r + R) = u_{n\mathbf{K}}(r), \tag{2.41}$$

where ***K*** are vectors in reciprocal space and $u_{n\mathbf{K}}(r)$ are the Bloch orbitals. The term *n* is known as the band index.

For the periodic system, with $u_{n\mathbf{K}}(r)$ expanded in terms of plane wave basis:

$$u_{n\mathbf{K}}(r) = \sum_{G} C_{iG}e^{iG.r}, \tag{2.42}$$

where *G* is the reciprocal lattice vector. Thus, the wave function defined in equation (2.40) can be written as follows:

$$\psi_{n,\mathbf{K}}(r) = \sum_{G} C_{iG} e^{iG.r}. \tag{2.43}$$

Thus, the equation proposed by Kohn-Sham (2.32) can be written as:

$$\left\{-\frac{1}{2}\nabla^2 + v_{eff}\right\} \sum_{G} C_{i,K+G} e^{i(K+G).r} = \epsilon_i \sum_{G} C_{i,K+G} e^{i(K+G).r}, \tag{2.44}$$

and multiplying the above equation by $e^{-i(K+G').r}$ and integrating over the space of a unit cell, obtain:

$$\sum_{G'} [H_{GG'} + V_{G-G'}] = \epsilon_i C_{i,K+G}, \tag{2.45}$$

where

$$H_{GG'} = \frac{1}{2} |K+G|^2 \delta_{GG'}, \tag{2.46}$$

which represents the kinetic energy, and:

$$V_{G-G'} = V_{ion}(G-G') + V_H(G-G') + V_{xc}(G-G'), \tag{2.47}$$

where $V_{ion}(G-G')$ is the electron-nucleus interaction, $V_H(G-G')$ is the Coulombic repulsion, and $V_{xc}(G-G')$ is the exchange-correlation term, the potentials defined by $V_{G-G'}$ being the Fourier component.

$$V_{G-G'} = \int_{vc} \hat{V}(r) e^{i(G-G').r} dr. \tag{2.48}$$

Bloch's theorem is interpreted as a boundary condition for the solution of the Schrödinger equation for a periodic potential. The eigenvalues and eigenfunctions of the single-electron states are then classified through the wave vectors ***K***.

2.4.2 Pseudopotentials

The electronic description of a solid primarily considers the valence electrons of the atoms. Conyers Herring in 1940 [18] proposed a method to calculate wave functions in a crystal, that is, a method that describes electronic states and orbitals in a periodic material. The state functions of a periodic material are expanded in plane waves, and the boundary conditions at the unit cell boundary are met using a large number of plane waves. This results in a good description of the periodic system. Thus, reducing the number of plane waves used while maintaining the descriptive method facilitates the electronic description of a periodic system. Herring proposed using orthogonalized plane waves (OPWs), a linear combination expansion of states near the nucleus, to reduce the number of plane waves [19]. An OPW is described by superimposing plane waves and core states. Therefore, a core orbital can be described as follows:

$$\phi_c(\mathbf{k},\mathbf{r}) = N^{-\frac{1}{2}} \sum_{\mathbf{R}} e^{ik.\mathbf{R}} \phi_c(\mathbf{r} - \mathbf{R}), \tag{2.49}$$

and the OPW in the form:

$$\phi^{OPW}(\mathbf{k},\mathbf{r}) = (N\Omega)^{-\frac{1}{2}} e^{i\mathbf{k}.r} - \sum_{c} \lambda_{c,\mathbf{k}} \phi_c(\mathbf{k}.\mathbf{r}), \tag{2.50}$$

where $\langle \phi_c | \phi^{OPW} \rangle$ = 0, N is the number of unit cells, Ω is the volume of the unit cell, and the sum is over the core states.

Considering that there is no overlap between core states:

$$\int \phi_c^*(\mathbf{r} - \mathbf{R}) \phi_c'(\mathbf{r} - \mathbf{R'}) dr = \delta_{cc'} \delta_{\mathbf{RR'}}, \tag{2.51}$$

and the $\lambda_{c,\mathbf{k}}$ coefficient is defined as:

$$\lambda_{c,\mathbf{k}} = \Omega^{-\frac{1}{2}} \int e^{i\mathbf{k}.\mathbf{r}} \phi_c^*(\mathbf{r}) dr, \tag{2.52}$$

it is worth noting that core orbital functions are Bloch states and can be written as follows:

$$\phi_c(\mathbf{k},\mathbf{r} + \mathbf{R'}) = e^{i\mathbf{k}.\mathbf{R'}} \phi_c(\mathbf{k},\mathbf{r}). \tag{2.53}$$

The OPW functions behave like plane waves for distances far from the atoms, i.e., the valence electrons, and exhibit atomic-like characteristics near them, i.e., the core electrons.

The method proposed by Herring presents convergence issues due to its basic procedure, which involves orthogonalizing each plane wave with core state functions, assuming complicated forms. In 1959, Phillips and Kleinman [20], Antonik [21], and later Austin et al. [22] proposed, starting from the plane wave, that it is possible to obtain the same eigenvalues as the secular equation of the Herring's OPW method in a simpler way, known as the *Pseudopotential Method*, as depicted in Figure 3.

One can define a projection operator for the core orbitals $|\phi_c\rangle$ as:

$$\hat{P} = \sum_{c} |\phi_c\rangle \langle \phi_c|, \tag{2.54}$$

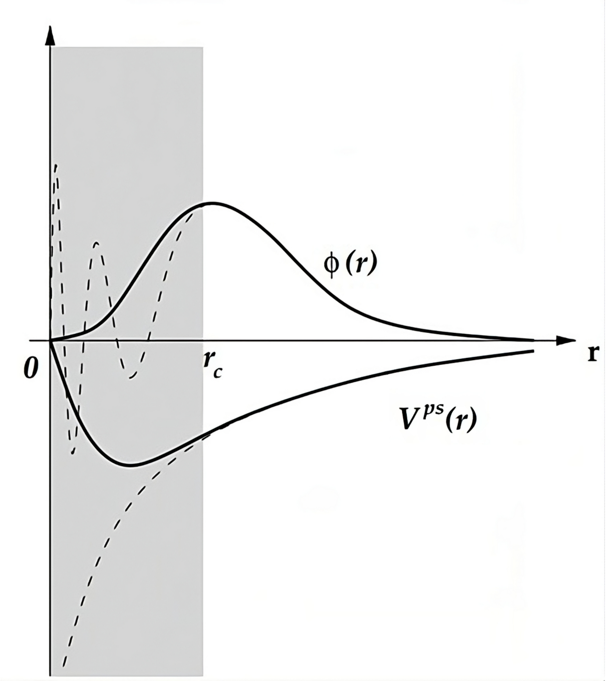

Figure 3 – Construction of the wave function $\phi(r)$ using the pseudopotential method. Adapted from [23].

and an OPW can be expressed as follows:

$$|\mathbf{k}+\mathbf{G}\rangle_{OPW} = (1-\hat{P})\,|\mathbf{k}+\mathbf{G}\rangle = |\mathbf{k}+\mathbf{G}\rangle - \sum_{c} |\phi_c\rangle \langle\phi_c|\mathbf{k}+\mathbf{G}\rangle\,, \tag{2.55}$$

where $|\mathbf{k}+\mathbf{G}\rangle$ represents a plane wave with wavevector **k**+**G**. The orbital for a given electronic state will be a combination of OPWs as follows:

$$|\phi_{\mathbf{k}i}\rangle \equiv |\mathbf{k}i\rangle = (1-\hat{P})\sum_{\mathbf{G}} C_{\mathbf{k}\mathbf{G}}\,|\mathbf{k}+\mathbf{G}\rangle\,. \tag{2.56}$$

The Schrödinger equation can be written in terms of the combination of plane waves as follows:

$$\hat{H}\,|\phi_{\mathbf{k}i}\rangle = \epsilon_{\mathbf{k}i}\,|\phi_{\mathbf{k}i}\rangle\,. \tag{2.57}$$

Expanding the above equation (2.57) in terms of equations (2.54), (2.55), and (2.56), the Schrödinger equation can be written in the form:

$$\left(\hat{H} + \sum_{c}(\epsilon_{\mathbf{k}i}-\epsilon_c)\,|\phi_c\rangle\langle\phi_c|\right)|\mathbf{k}+\mathbf{G}\rangle = \epsilon_{\mathbf{k}i}\,|\mathbf{k}+\mathbf{G}\rangle\,. \tag{2.58}$$

The sum over all core states represents an operator acting on a plane wave. Thus, the repulsive potential V_R can be written as:

$$\hat{V}_R = \sum_c (\epsilon_{\mathbf{k}i} - \epsilon_c) \left|\phi_c\right\rangle \left\langle\phi_c\right| . \tag{2.59}$$

This way, the equation (2.57) can be written as:

$$(\hat{H} + \hat{V}_R) \left|\phi_{\mathbf{k}i}\right\rangle = \epsilon_{\mathbf{k}i} \left|\phi_{\mathbf{k}i}\right\rangle . \tag{2.60}$$

The equation above possesses the same eigenvalue as equation (2.57). Thus, one can write $\left|\phi_{\mathbf{k}i}\right\rangle$ = (1 - $\hat{P}$) $\left|\phi^{PS}_{\mathbf{k}i}\right\rangle$, where $\left|\phi^{PS}_{\mathbf{k}i}\right\rangle$ is the smooth part of $\left|\phi_{\mathbf{k}i}\right\rangle$,so one can write equation (2.60) in the form:

$$(\hat{H} + \hat{V}_R) \left|\phi^{PS}_{\mathbf{k}i}\right\rangle = \epsilon_{\mathbf{k}i} \left|\phi^{PS}_{\mathbf{k}i}\right\rangle , \tag{2.61}$$

where $\left|\phi^{PS}_{\mathbf{k}i}\right\rangle$ is called the *pseudofunction*. If the Hamiltonian can be written as:

$$\hat{H} = -\frac{\hbar^2}{2m}\nabla^2 + \hat{V},$$

where $\hat{V}$ is the potential of the periodic system, the Schrödinger equation (2.61) can be written as:

$$\left(-\frac{\hbar^2}{2m}\nabla^2 + \hat{V}_{PS}\right) \left|\phi^{PS}_{\mathbf{k}i}\right\rangle = \epsilon_{\mathbf{k}i} \left|\phi^{PS}_{\mathbf{k}i}\right\rangle , \tag{2.62}$$

where $\hat{V}_{PS} = \hat{V}(\mathbf{r}) + \hat{V}_R$ is the pseudopotential.

2.5 Rietveld Method

The Rietveld method [24], created by Hugo Rietveld in the 1960s, was initially used to refine the intensities measured through neutron scattering for single crystals. The method involves fitting the experimentally obtained diffractogram to a theoretical diffractogram, thus providing information such as lattice parameters, percentages of crystalline phases in the sample, average crystallite size, and quantitatively determining lattice strains, among other structural properties.

One can perform an intensity simulation involving the diffraction pattern through an equation deduced by Rietveld:

$$y_{ic} = s \sum_{k=1}^{k_2} m_k L_k |F^2| G_{ik}, \tag{2.63}$$

where s is a scale factor, m_k is the multiplicity factor for the k-th reflection, L_k is the Lorentz polarization factor, F_k is the structure factor, and G_{ik} is the peak profile function;

During refinement, adjusting the parameters influences the quality of the process, so appropriate functions should be used to achieve satisfactory results regarding the shape, width, and even the height of the reflection. The profile function fits the shape of peaks in a diffraction pattern. Among the possible functions, two stand out: Gaussian (2.64) and Lorentzian (2.65):

$$G = \frac{\sqrt{C_0}}{H_k\sqrt{\pi}} e^{\left[\frac{C_0(2\theta_i - \theta_k)^2}{K_k^2}\right]}, \tag{2.64}$$

and

$$L = \frac{\sqrt{C_1}}{H_k\sqrt{\pi}} \frac{1}{\left[1 + \frac{C_1(2\theta_i - \theta_k)^2}{K_k^2}\right]}, \tag{2.65}$$

where $C_0 = 4\ln 2$, $C_1 = 4$, and H_k represent the total full width at half maximum of the Bragg reflection (k), which can be defined as:

$$H_k = U tang^2\theta + V tang\theta + W. \tag{2.66}$$

Both can be used independently; however, for the fitting to resemble X-ray diffraction similarity adequately, they should be combined, yielding a third function, the pseudo-Voigt:

$$pV = \eta L + (1 - \eta)G, \tag{2.67}$$

where η is the mixing parameter of the pseudo-Voigt function and can be written as:

$$\eta = 1.36603q - 0.47719q^2 + 0.1116q^3, \tag{2.68}$$

where:

$$q = \frac{H_L}{H}. \tag{2.69}$$

Additionally, it is considered:

$$H = (H_G^5 + AH_G^4 H_L + BH_G^3 B_L^2 + CH_G^2 H_L^3 + DH_G H_L^4 + H_L^5)^{\frac{1}{5}}, \tag{2.70}$$

where A, B, C, and D are normalization constants.

The Lorentzian fraction can be written as:

$$\eta = N_A + N_B(2\theta),$$

where N_A and N_B are refinement parameters. The pseudo-Voigt equation (2.67) can be rewritten as:

$$pV - TCHZ = \eta L + (1 - \eta)G, \tag{2.71}$$

where $pV - TCHZ$ was proposed by Thompson-Cox-Hastings [25] and in this case, G represents the full width at half maximum (H_G), and $pV - TCHZ$ is used as a function of H_G and H_L

2.6 Elastic Strains in solids

The analysis of deformation in solids considers a crystal as a continuous and non-periodic medium. Hooke's law and Newton's 2nd law is used for deformation analysis. According to Hooke's law, deformation is directly proportional to stress in an elastic solid, valid only for small deformations. When high deformations are observed, Hooke's law is not satisfied, thus resulting in a *non-linear region* [17].

A solid undergoing uniform deformation has its coordinate axes changing orientation, as shown in Figure 4.

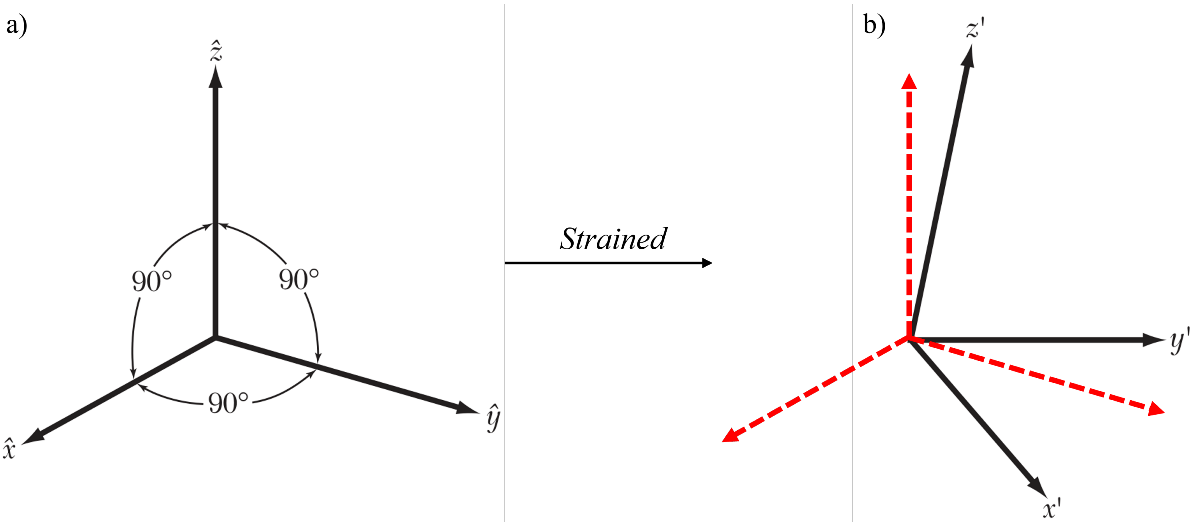

Figure 4 – Coordinate system to describe a state of strain. a) absence of deformation and b) after deformation. $\hat{x}$, $\hat{y}$, and $\hat{z}$ are orthogonal vectors. Adapted from [17].

The vectors $\hat{x}$, $\hat{y}$, and $\hat{z}$ are orthogonal vectors of unit length, and the relationship between the new axes x', y', and z' can be expressed as follows [17]:

$$\mathbf{x'} = (1+\epsilon_{xx})\hat{\mathbf{x}} + \epsilon_{xy}\hat{\mathbf{y}} + \epsilon_{xz}\hat{\mathbf{z}}; \tag{2.72}$$

$$\mathbf{y'} = \epsilon_{yx}\hat{\mathbf{x}} + (1+\epsilon_{yy})\hat{\mathbf{y}} + \epsilon_{yz}\hat{\mathbf{z}}; \tag{2.73}$$

$$\mathbf{z'} = \epsilon_{zx}\hat{\mathbf{x}} + \epsilon_{zy}\hat{\mathbf{y}} + (1+\epsilon_{zz})\hat{\mathbf{z}}, \tag{2.74}$$

where $\epsilon_{\alpha\beta}$ are the strain coefficients. After elongation, the particle will be at position:

$$\mathbf{r}' = x\mathbf{x}' + y\mathbf{y}' + z\mathbf{z}'.$$

Thus, the displacement **R** caused by elongation is given by:

$$\mathbf{R} \equiv \mathbf{r}' - \mathbf{r} = x(\mathbf{x}' - \hat{\mathbf{x}}) + y(\mathbf{y}' - \hat{\mathbf{y}}) + z(\mathbf{z}' - \hat{\mathbf{z}}). \tag{2.75}$$

Considering the equations 2.72, 2.73, and 2.74, **R** is written as:

$$\mathbf{R} \equiv (x\epsilon_{xx} + y\epsilon_{yx} + z\epsilon_{zx})\hat{\mathbf{x}} + (x\epsilon_{xy} + y\epsilon_{yy} + z\epsilon_{zy})\hat{\mathbf{y}} + (x\epsilon_{xz} + y\epsilon_{yz} + z\epsilon_{zz})\hat{\mathbf{z}}. \tag{2.76}$$

The equation 2.76 can be written more generally by defining functions u, v, and w such that the displacement is given by:

$$\mathbf{R}(\mathbf{r}) = u(\mathbf{r})\hat{\mathbf{x}} + v(\mathbf{r})\hat{\mathbf{y}} + w(\mathbf{r})\hat{\mathbf{z}}. \tag{2.77}$$

If the elongation is not uniform, u, v, and w are local strains. Considering the origin of **r** in the region of interest and comparing equations 2.76 and 2.77, one obtains, by expanding **R** in a Taylor series and setting **R**(0)=0,

$$x\epsilon_{xx} \cong x\frac{\partial u}{\partial x}; \qquad y\epsilon_{yx} \cong y\frac{\partial v}{\partial y}; \qquad etc. \tag{2.78}$$

The coefficients $\epsilon_{\alpha\beta}$ can be related to the coefficients $e_{\alpha\beta}$, which are related to the deformation of the solid, as follows:

$$e_{xx} \equiv \epsilon_{xx} = \frac{\partial u}{\partial x}; \qquad e_{yy} \equiv \epsilon_{yy} = \frac{\partial y}{\partial y}; \qquad e_{zz} \equiv \epsilon_{zz} = \frac{\partial w}{\partial z}, \tag{2.79}$$

The other components of strain, e_{xy}, e_{yz}, and e_{zx}, are defined in terms of changes in the angles between the axes, according to equations 5, 2.73, and 2.74:

$$e_{xy} \equiv \mathbf{x}' \cdot \mathbf{y}' \cong \epsilon_{yx} + \epsilon_{xy} = \tfrac{\partial u}{\partial y} + \tfrac{\partial v}{\partial x}; \tag{2.80}$$

$$e_{yz} \equiv \mathbf{y}' \cdot \mathbf{z}' \cong \epsilon_{zy} + \epsilon_{yz} = \tfrac{\partial v}{\partial z} + \tfrac{\partial w}{\partial y}; \tag{2.81}$$

$$e_{zx} \equiv \mathbf{z}' \cdot \mathbf{x}' \cong \epsilon_{zx} + \epsilon_{xz} = \tfrac{\partial u}{\partial z} + \tfrac{\partial w}{\partial x}. \tag{2.82}$$

For small deformations, the strain is directly proportional to the stress, meaning the strain components are linear functions of the stress components [17]:

$$e_{xx} = S_{11}X_x + S_{12}Y_y + S_{13}Z_z + S_{14}Y_z + S_{15}Z_x + S_{16}X_y; \tag{2.83}$$

$$e_{yy} = S_{21}X_x + S_{22}Y_y + S_{23}Z_z + S_{24}Y_z + S_{25}Z_x + S_{26}X_y; \tag{2.84}$$

$$e_{zz} = S_{31}X_x + S_{32}Y_y + S_{33}Z_z + S_{34}Y_z + S_{35}Z_x + S_{36}X_y; \tag{2.85}$$

$$e_{yz} = S_{41}X_x + S_{42}Y_y + S_{43}Z_z + S_{44}Y_z + S_{45}Z_x + S_{46}X_y; \tag{2.86}$$

$$e_{zx} = S_{51}X_x + S_{52}Y_y + S_{53}Z_z + S_{54}Y_z + S_{55}Z_x + S_{56}X_y; \tag{2.87}$$

$$e_{xy} = S_{61}X_x + S_{62}Y_y + S_{63}Z_z + S_{64}Y_z + S_{65}Z_x + S_{66}X_y, \tag{2.88}$$

and,

$$X_x = C_{11}e_{xx} + C_{12}e_{yy} + C_{13}e_{zz} + C_{14}e_{yz} + C_{15}e_{zx} + C_{16}e_{xy}; \tag{2.89}$$

$$Y_y = C_{21}e_{xx} + C_{22}e_{yy} + C_{23}e_{zz} + C_{24}e_{yz} + C_{25}e_{zx} + C_{26}e_{xy}; \tag{2.90}$$

$$Z_z = C_{31}e_{xx} + C_{32}e_{yy} + C_{33}e_{zz} + C_{34}e_{yz} + C_{35}e_{zx} + C_{36}e_{xy}; \tag{2.91}$$

$$Y_z = C_{41}e_{xx} + C_{42}e_{yy} + C_{43}e_{zz} + C_{44}e_{yz} + C_{45}e_{zx} + C_{46}e_{xy}; \tag{2.92}$$

$$Z_x = C_{51}e_{xx} + C_{52}e_{yy} + C_{53}e_{zz} + C_{54}e_{yz} + C_{55}e_{zx} + C_{56}e_{xy}; \tag{2.93}$$

$$X_y = C_{61}e_{xx} + C_{62}e_{yy} + C_{63}e_{zz} + C_{64}e_{yz} + C_{65}e_{zx} + C_{66}e_{xy}, \tag{2.94}$$

$$\tag{2.95}$$

where S_{ij} are strain constants, X, Y, and Z are the stress components, and C_{ij} are the elastic stiffness constants in Voigt notation.

2.7 Anisotropic Microstrain

The microstrain broadening (μstrain) is observed due to local variations in spacings d within the crystallites of a diffraction sample. The model to describe this phenomenon was proposed by Stephens [26], which considers that the spacing d between the lattice planes for any reflection can be defined by the Miller indices hkl as:

$$\frac{1}{d^2} = M_{hkl} = Ah^2 + Bk^2 + Cl^2 + Dkl + Ehl + Fhk, \tag{2.96}$$

where $A...F$ are parameters of the reciprocal lattice and can be generically represented as α_i, with $i = 1, ..., 6$. The parameters α_i have a Gaussian distribution characterized by a covariance matrix in the form [26]:

$$C_{ij} = \langle (\alpha_i - < a_i >) \cdot (\alpha_j - < \alpha_j >) \rangle \, . \tag{2.97}$$

$C_{ii} = \sigma^2(\alpha_i)$ is the variance of α_i and not the elastic stiffness constant. The parameter M_{hkl} varies linearly with α_i, so the variance of M_{hkl} is given by:

$$\sigma^2(M_{hkl}) = \sum_{i,j} C_{ij} \frac{\partial M}{\partial \alpha_i} \frac{\partial M}{\partial \alpha_j}. \tag{2.98}$$

Relating the partial derivatives to equation 2.96, obtain:

$$\frac{\partial M}{\partial \alpha_1} = h^2; \quad \frac{\partial M}{\partial \alpha_2} = k^2; \quad \frac{\partial M}{\partial \alpha_3} = l^2; \quad \frac{\partial M}{\partial \alpha_4} = kl; \quad \frac{\partial M}{\partial \alpha_5} = hl; \quad \frac{\partial M}{\partial \alpha_6} = hk. \tag{2.99}$$

With the definition from equation 2.99, we can construct a variance-covariance matrix as follows:

$$\frac{\partial M}{\partial \alpha_i} \frac{\partial M}{\partial \alpha_j} = \begin{bmatrix} h^4 & h^2k^2 & h^2l^2 & h^2kl & h^3l & h^3k \\ h^2k^2 & k^4 & k^2l^2 & k^3l & hk^2l & hk^3 \\ h^2l^2 & k^2l^2 & l^4 & kl^3 & hl^3 & hkl^2 \\ h^2kl & k^3l & kl^3 & k^2l^2 & hkl^2 & hk^2l \\ h^3l & hk^2l & hl^3 & hkl^2 & h^2l^2 & h^2kl \\ h^3k & hk^3 & hkl^2 & hk^2l & h^2kl & h^2k^2 \end{bmatrix}. \tag{2.100}$$

So equation 2.98 can be rewritten as:

$$\sigma^2(M_{HKL}) = \sum_{HKL} S_{HKL} h^H k^k l^L, \tag{2.101}$$

where the term S_{HKL} is defined by $H + K + L = 4$. In the most general case, the triclinic system has 15 independent parameters S_{HKL}. For the description of anisotropic broadening, there are restrictions, as shown in two examples in Table 1.

Using the Bragg equation, $\sin\theta = \lambda/(2d) = \lambda M^{\frac{1}{2}}/2)$, the contribution of anisotropic broadening to the full width at half maximum ($FWHM$) of the diffraction line is given by [26]:

$$\Gamma_A^2 = \sigma^2(M_{hkl}). \tag{2.102}$$

From the constraints presented in Table 1 and relating equations 2.100 and 2.102, we obtain the expression for Γ_A^2 for the cubic system with $m - 3$ and $m - 3m$ symmetries as follows:

$$\Gamma_A^2 = S_{400}(h^4 + k^4 + l^4) + 3S_{220}(h^2k^2 + h^2l^2 + k^2l^2), \tag{2.103}$$

Table 1 – Restrictions on the anisotropic broadening parameters (S_{hkl}). Adapted [26].

Crystal system	Restrictions on parameters	Parameters S_{hkl}
Cubic	A = B = C, D = E = F = 0	$S_{400} = S_{040} = S_{004}$, $S_{220} = S_{202} = S_{022}$
Tetragonal	A = B, D = E = F = 0	$S_{400} = S_{040}$, $S_{202} = S_{022}$, S_{004}, S_{022}

and for the tetragonal system with $4/mmm$ symmetry:

$$\Gamma_A^2 = S_{400}(h^4 + k^4) + S_{004}(l^4) + 3S_{220}(h^2k^2) + 3S_{202}(h^2l^2 + k^2l^2). \tag{2.104}$$

Stephens' model, implemented in the $GSAS-II$ program, the Gaussian variance (σ^2) varies with the 2θ angle as follows:

$$\sigma^2 = (U + \sigma_s^2 d^4) tang^2\theta + V tang\theta + W, \tag{2.105}$$

where U, V, and W are terms related to X-ray diffraction analysis in terms of the angular divergence from the radiation entrance to the monochromator and were described by Caglioti *et al.* [27]. An additional type of broadening is introduced for the profile coefficient γ, where two classes of reflections can be defined. The first class is related to the sublattice (defined by three vectors and includes the origin) and has the following expression for the coefficient γ:

$$\gamma = \frac{X + X_e cos\phi}{cos\theta} + (Y + Y_e cos\phi + \gamma_S d^2) tang\theta, \tag{2.106}$$

and the second part is related to the remaining reflections as follows:

$$\gamma = \frac{X + X_S cos\phi}{cos\theta} + (Y + Y_e cos\phi + \gamma_S d^2) tang\theta. \tag{2.107}$$

The relationship between equations 2.106 and 2.107 demonstrates that the reflections exhibit different particle size anisotropy compared to the other set. The microstrain broadening has two contributions, one Gaussian (σ_s^2) and one Lorentzian (γ_s), and they are determined as follows:

$$\sigma_s = (1 - \eta)\Gamma_s, \tag{2.108}$$

and

$$\Gamma_s = \eta\Gamma_s. \tag{2.109}$$

For the function used in *GSAS-II*, microstrain is best described by a surface in reciprocal space where the radial distance from the origin is given by:

$$S_{s(hkl)} = \frac{\pi d^2}{1800}\sqrt{\sum_{HKL} S_{HKL} h^H k^K l^L} 100\%, \tag{2.110}$$

where the function is appropriate for Laue symmetry.

2.7.1 Microstrain Analysis

Microstrain in the $GSAS-II$ program can be represented in three ways: isotropic, uniaxial, and generalized. The generalized representation uses a second-order expansion model through an analysis using generalized spherical harmonics [28]. The functions to be expanded into spherical harmonics are the elements of the microstrain correlation matrix ($\Delta_{ij}(g)$):

$$\Delta_{ij}(g) = \frac{1}{N_g}\sum_{k=1}^{N_g}\Delta\varepsilon_i(\mathbf{R}_k,g)\Delta\varepsilon_j(\mathbf{R}_k,g) + \frac{1}{N_g}\sum_{k=1}^{N_g}\frac{1}{V_k}\int d\mathbf{r}\Delta\varepsilon_i(\mathbf{R}_k+\mathbf{r},g)\Delta\varepsilon_j(\mathbf{R}_k+\mathbf{r},g), \quad (2.111)$$

where the first term is related to functions depending on the crystal orientation g and the position vector ($\mathbf{R}_k$), the second term is related to elastic strain with ($\mathbf{R}_k$+$\mathbf{r}$,g), and ε denotes the strain tensor. The variance of the strains can be written as follows:

$$\sigma_{\mathbf{h}}(\mathbf{y})P_{\mathbf{h}}(\mathbf{y}) = \sum_{l=0}^{\infty}\left[\frac{2}{(2l+1)}\right]I_l^m(\mathbf{h},\mathbf{y}) \qquad (l = par), \quad (2.112)$$

where $\mathbf{h}$ represents a unit vector, $P_{\mathbf{h}}$ is the reduced pole distribution written as $P_{\mathbf{h}} = (1/2)[p_{\mathbf{h}}(\mathbf{y})+ p_{-\mathbf{h}}(\mathbf{y})]$, and I_l^m is the variance of the microstrain distribution defined as follows:

$$I_l^m(\mathbf{h},\mathbf{y}) = \sum_{i=1}^{6}\sum_{j=1}^{6}E_iE_j\rho_i\rho_jt_{ijl}(\mathbf{h},\mathbf{y}), \quad (2.113)$$

where E represents the combination of lattice parameters, ρ represents the indices of the elastic constant tensors, and t is the stress tensor written as:

$$t_{ijl}(\mathbf{h},\mathbf{y}) = A_{ijl}^0(\mathbf{y})P_l^0(\Phi) + \sum_{m=1}^{l}[A_{ijl}^m(\mathbf{y})cos\ m\beta + B_{ijl}^m(\mathbf{y})sen\ m\beta]P_l^m(\Phi), \quad (2.114)$$

where Φ is the polar angle, β is the azimuthal angle, and:

$$A_{ijl}^m = \alpha_{ijl}^{m0}P_l^0(\Psi) + \sum_{n=1}^{l}(\alpha_{ijl}^{mn}cos\ n\gamma + \beta_{ijl}^{mn}sen\ n\gamma)P_l^n(\Psi) \qquad (m = 0, ..., l), \quad (2.115)$$

and

$$B_{ijl}(\mathbf{y}) = \gamma_{ijl}^{m0}P_l^0(\Psi) + \sum_{n=1}^{l}(\gamma_{ijl}^{mn}cos\ n\gamma + \delta_{ijl}^{mn}sen\ n\gamma)P_l^n(\Psi) \qquad (m = 1, ..., l), \quad (2.116)$$

where the coefficients α_{ijl}^{mn}, $\beta^{mn}ijl$, γijl^{mn}, and δ_{ijl}^{mn} are obtained from the coefficients C_{ijl}^{mn}.

The variance of the microstrain distribution can be succinctly represented as follows [28]:

$$I_l^m(\mathbf{h},\mathbf{y}) = \sum_{\nu=1}^{15}t_{vl}(\mathbf{h},\mathbf{y})j_{v_4}(a_1,a_2,a_3), \quad (2.117)$$

and

$$t_{ijl}(\mathbf{h}, \mathbf{y}) = \sum_{\mu=1}^{\mu_l} C^{\mu}_{ijl}(\mathbf{y}) j_{\mu}(a_1, a_2, a_3). \tag{2.118}$$

The functions $t_{vl}(\mathbf{h}, \mathbf{y})$ are linear combinations of $t_{ijl}(\mathbf{h}, \mathbf{y})$, and $C^{\mu}ijl(\mathbf{h}, \mathbf{y})$ are linear combinations of $Aijl^m$ and B^m_{ijl}. Relating equations 2.118 and 2.117, obtain:

$$I^m_l(\mathbf{h}, \mathbf{y}) = \sum_{\mu=1}^{\mu_{l+4}} E_{\mu l}(\mathbf{y}) j_{\mu,l+4}(a_1, a_2, a_3). \tag{2.119}$$

In the $GSAS$ program, to simultaneously process several diffraction patterns recorded in different sample directions, the same number of independent sets of parameters from the Popa/Stephens model [26, 28, 29] is required.

2.8 Equations of State

The equations of state (EOS) are usually derived from parameters such as pressure (P), volume (V), temperature (T), and the number of particles (n) in the form:

$$P = f(V, T, n), \tag{2.120}$$

or

$$V = f(P, T, n). \tag{2.121}$$

The EOS in solids and the electronic and structural properties are related to the various conditions to which materials can be subjected [30].

Determining the EOS for a solid is not trivial due to the anisotropic nature of stress/compression phenomena, which can be a peculiarity of the particular solid in question. When a deformation (variation in pressure, temperature, composition, electric or magnetic fields) is applied to any solid, points **r** undergo displacement (e.g., stress), which is a function of position and can be expressed by a stress function $u(\mathbf{r})$. Thus, an infinitesimal variation (dr) is observed between two points (which in a crystal can be connected to the interplanar distance) that change, and the value (dr') in the solid under stress can, assuming that the deformation function is continuous and in the limit of small deformations, be expressed as

$$dr' = dr + e(\mathbf{r})dr, \tag{2.122}$$

where *e*(**r**) is the tensor derived from the strain function:

$$e_{ij} = \frac{\partial u_j}{\partial r_i}. \tag{2.123}$$

Strain is a dimensionless tensor field, and the stress tensor ($\sum$) can be defined as,

$$\sum = \frac{1}{2}(e + e'), \tag{2.124}$$

where e' indicates the modification, the diagonal elements $\sum_{ii}$ of the tensor represent the elongation fraction of an element aligned along the i axis. In contrast, the off-diagonal elements ($\sum_{ij}$) are connected to the angular deformation of two vectors aligned along the i and j axes in tensioned solids [30].

The deformation field acting on the material must be associated with an external or internal force (**F**) acting on each volume element. Thus, an external force per unit volume $F(\mathbf{r})$ is defined, and a stress tensor (τ) is defined with elements given by:

$$F(r_i) = \sum_j \frac{\partial \tau_{ij}}{\partial r_{ij}}, \tag{2.125}$$

where τ_{ij} is the force acting on a face perpendicular to the i and j directions.

The bulk modulus (B_0) of a given material can be described as:

$$B_0 = -V\left(\frac{\partial P}{\partial V}\right)_T, \tag{2.126}$$

where B_0 represents the material's resistance to isotropic compression [30].

2.8.1 EOS Parameters

An empirical equation of state can be used to produce or adjust pressure-volume data or be rationalized as a connection for intramolecular interpretations of a material under study. These equations of state allow determining the bulk modulus (B_0) and the first derivative of pressure B_0'. If these parameters are independently known, they can be used to validate the fit of the equation of state to different experiments [30].

All empirical equations of state are based on the definition of pressure, in terms of the Helmholtz free energy F, expressed as a function of volume at constant temperature.

$$P = \left(-\frac{\partial F}{\partial V}\right)_T. \tag{2.127}$$

The isothermal equation of state, assuming that the free energy simply coincides with the strain energy [30].

Determining an expression for the free energy in terms of volume, the equation of state is obtained as:

$$P(V) = -\left(\frac{\partial F}{\partial f}\right)_T \left(\frac{\partial f}{\partial F}\right), \tag{2.128}$$

or,

$$P(f) = -\left(\frac{\partial F}{\partial f}\right)_T. \tag{2.129}$$

From equation (2.127), one can obtain B_0':

$$B_0' = \left(\frac{\partial B_0}{\partial P}\right). \tag{2.130}$$

Assuming that the bulk modulus (B_0) varies linearly with pressure, one can write the relationship:

$$-V\frac{\partial P}{\partial V} = B_0 + B_0' P. \tag{2.131}$$

Integrating the above equation (2.131), we obtain the equation of state proposed by Murnaghan [31] as follows:

$$P = \frac{B_0}{B_0'}\left[\left(\frac{V_0}{V}\right)^{B_0'} - 1\right], \tag{2.132}$$

where V_0 is the equilibrium volume, or its inverse form:

$$\left(1 + \frac{B_0'}{B_0}P\right)^{-\frac{1}{B_0'}} = \frac{V}{V_0}. \tag{2.133}$$

Francis Birch [32] proposed expanding the Murnaghan equation (2.132) in the Eulerian strain to obtain the Birch-Murnaghan equation. Considering a Lagrangian approach, A. Keane [33] assumed that the pressure can be expressed with a power series in the material strain following the expression:

$$\frac{P}{B_0} = \frac{B_0'}{(B_\infty')^2}\left[\left(\frac{V_0}{V}^{B_\infty'}\right) - 1\right] - \left(\frac{B_0'}{B_\infty'} - 1\right) ln\frac{V_0}{V}, \tag{2.134}$$

where, $B_0' - 1 > B_\infty' > B_0'/2$, and when $B_0' = B_\infty'$ the equation above (2.134) reduces to the Murnaghan equation (2.132).

BIBLIOGRAPHY

1 GIUSTINO, F. *Materials modelling using density functional theory: properties and predictions*. [S.l.]: Oxford University Press, 2014. 34

2 LEE, J. G. *Computational materials science: an introduction*. [S.l.]: CRC press, 2016. 34

3 SCHRÖDINGER, E. An undulatory theory of the mechanics of atoms and molecules. *Physical review*, APS, v. 28, n. 6, p. 1049, 1926. 34

4 LEVINE, R. D. *Quantum mechanics of molecular rate processes*. [S.l.]: Courier Corporation, 2011. 36

5 SHOLL, D. S.; STECKEL, J. A. *Density functional theory: a practical introduction*. [S.l.]: John Wiley & Sons, 2011. 36

6 BORN, M.; OPPENHEIMER, R. On the quantum theory of molecules. In: *Quantum Chemistry: Classic Scientific Papers*. [S.l.]: World Scientific, 2000. p. 1–24. 36

7 MCQUARRIE, D. A. *Quantum chemistry*. [S.l.]: University Science Books, 2008. 37

8 HOHENBERG, P.; KOHN, W. Inhomogeneous electron gas. *Physical review*, APS, v. 136, n. 3B, p. B864, 1964. 37

9 KOHN, W.; SHAM, L. J. Self-consistent equations including exchange and correlation effects. *Physical review*, APS, v. 140, n. 4A, p. A1133, 1965. 37, 39

10 DRUDE, P. Zur elektronentheorie der metalle; ii. teil. galvanomagnetische und thermomagnetische effecte. *Annalen der physik*, Wiley Online Library, v. 308, n. 11, p. 369–402, 1900. 37

11 THOMAS, L. H. The calculation of atomic fields. In: CAMBRIDGE UNIVERSITY PRESS. *Mathematical proceedings of the Cambridge philosophical society*. [S.l.], 1927. v. 23, n. 5, p. 542–548. 37

12 FERMI, E. Application of statistical gas methods to electronic systems. *Rendiconti dell'Accademia Nazionale dei Lincei*, v. 6, p. 602, 1927. 37

13 DIRAC, P. A. Note on exchange phenomena in the thomas atom. In: CAMBRIDGE UNIVERSITY PRESS. *Mathematical proceedings of the Cambridge philosophical society*. [S.l.], 1930. v. 26, n. 3, p. 376–385. 37

14 ZIESCHE, P.; KURTH, S.; PERDEW, J. P. Density functionals from lda to gga. *Computational materials science*, Elsevier, v. 11, n. 2, p. 122–127, 1998. 42

15 VIANNA, J. D. M. *Teoria Quântica de Moléculas e Sólidos: simulaçao computacional*. [S.l.]: Livraria da Física, 2004. 42

16 ASHCROFT, N. W.; MERMIN, N. D. *Física do estado sólido*. [S.l.]: Cengage Learning, 2011. 42, 43

17 KITTEL, C.; MCEUEN, P. *Introduction to solid state physics*. [S.l.]: John Wiley & Sons, 2018. 43, 49, 50, 51

18 HERRING, C. A new method for calculating wave functions in crystals. *Physical Review*, APS, v. 57, n. 12, p. 1169, 1940. 44

19 FAZZIO, A.; CANUTO, S.; VIANNA, J. D. M. *Teoria quântica de moléculas e sólidos: Simulaçao computacional*. [S.l.]: Editora Livraria da Física, 2018. 45

20 PHILLIPS, J. C.; KLEINMAN, L. New method for calculating wave functions in crystals and molecules. *Physical Review*, APS, v. 116, n. 2, p. 287, 1959. 45

21 ANTONČÍK, E. Approximate formulation of the orthogonalized plane-wave method. *Journal of Physics and Chemistry of solids*, Elsevier, v. 10, n. 4, p. 314–320, 1959. 45

22 AUSTIN, B. J.; HEINE, V.; SHAM, L. General theory of pseudopotentials. *Physical Review*, APS, v. 127, n. 1, p. 276, 1962. 45

23 KAXIRAS, E. *Atomic and electronic structure of solids*. [S.l.: s.n.], 2003. 46

24 RIETVELD, H. M. A profile refinement method for nuclear and magnetic structures. *Journal of applied Crystallography*, International Union of Crystallography, v. 2, n. 2, p. 65–71, 1969. 47

25 THOMPSON, P.; COX, D.; HASTINGS, J. Rietveld refinement of debye–scherrer synchrotron x-ray data from al2o3. *Journal of Applied Crystallography*, International Union of Crystallography, v. 20, n. 2, p. 79–83, 1987. 49

26 STEPHENS, P. W. Phenomenological model of anisotropic peak broadening in powder diffraction. *Journal of Applied Crystallography*, International Union of Crystallography, v. 32, n. 2, p. 281–289, 1999. 51, 52, 53, 55

27 CAGLIOTI, G.; PAOLETTI, A. t.; RICCI, F. Choice of collimators for a crystal spectrometer for neutron diffraction. *Nuclear Instruments*, Elsevier, v. 3, n. 4, p. 223–228, 1958. 53

28 POPA, N. C. Stress and strain. Wiley Online Library, 2019. 54, 55

29 POPA, N. The (hkl) dependence of diffraction-line broadening caused by strain and size for all laue groups in rietveld refinement. *Journal of Applied Crystallography*, International Union of Crystallography, v. 31, n. 2, p. 176–180, 1998. 55

30 SCHETTINO, V.; BINI, R. *Materials under extreme conditions: molecular crystals at high pressure*. [S.l.]: World Scientific, 2013. 55, 56

31 MURNAGHAN, F. D. The compressibility of media under extreme pressures. *Proceedings of the National Academy of Sciences*, National Acad Sciences, v. 30, n. 9, p. 244–247, 1944. 57

32 BIRCH, F. Elasticity and constitution of the earth's interior. *Journal of Geophysical Research*, Wiley Online Library, v. 57, n. 2, p. 227–286, 1952. 57

33 KEANE, A. An investigation of finite strain in an isotropic material subjected to hydrostatic pressure and its seismological applications. *Australian Journal of Physics*, CSIRO Publishing, v. 7, n. 2, p. 322–333, 1954. 57

3

$Influence\ of\ Fe - Doping\ on\ the\ Structural\ and\ Electronic\ Properties\ of\ the\ TiO_2\ Anatase : Rutile$

3.1 Abstract

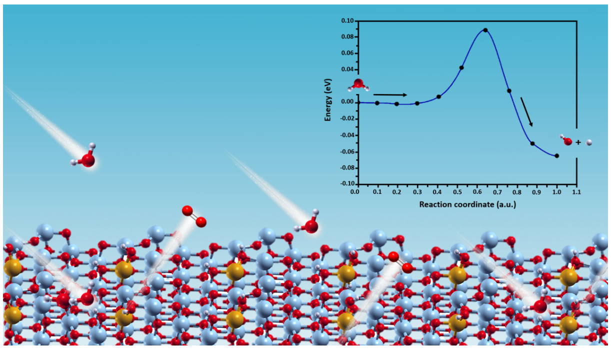

The Fe-doped anatase and rutile TiO_2 phases were investigated using a combined experimental and theoretical approach. The Fe-doped phases were characterized by X-ray diffraction with Rietveld refinement. The band structure and projected density of state (PDOS) were fully characterized using DFT/Plane waves calculations on a supercell model with 48 atoms. The band gap of 3.17 eV and 2.95 eV was estimated for the pure anatase and rutile TiO_2 phases. The band gap values decreased to 3.00 and 2.13 eV with the Fe doping for anatase and rutile TiO_2-Fe phases, respectively. The water-splitting reaction on the anatase (*0 1 0*) TiO_2 and TiO_2-Fe surfaces was investigated. The quantum efficiency assessed by the transfer rate of electrons and holes is increased with the presence of Fe in the TiO_2 structure. The initial steps of the reaction mechanism and the transition states were determined using the NEB (Nudged Elastic band) method considering the species involved H_2O, $OH^{\cdot}$, and H^+ on the (*0 1 0*) TiO_2 surface. The activation energies of 0.29 eV and 0.08 eV were estimated for pure anatase TiO_2 and anatase TiO_2-Fe structures. The DFT/Plane Waves calculations on the

synthesized Fe-doped material are predicted to improve its photocatalytic properties toward water-splitting.

Keywords: TiO_2, water splitting, Rietveld refinement, Materials Modelling, NEB

3.2 Experimental and Computational Details

3.2.1 Materials Preparation

Titanium dioxide (TiO_2) and Fe-doped TiO_2 were obtained from a polymeric resin prepared by the Pechini method [1]. The reagents used were citric acid (AC–Synth®), ethylene glycol (EG – Synth®), titanium isopropoxide ($C_{12}H_{28}O_4Ti$ - Sigma-Aldrich®–97%), and ferric chloride hexahydrate (5.0 wt% $FeCl_2 \cdot 4H_2O$ - Sigma- Aldrich®).

Samples preparation. Titanium dioxide (TiO_2) material was prepared as follows: initially, the polymeric resin was prepared with the molar ratio 1:8:32 ($AC : EG : C_{12}H_{28}O_4Ti$). In a breaker with vigorous stirring, approximately 8.97 g of the citric acid (AC) was dissolved in 6.27 mL of the ethylene glycol (EG), under constant maintenance and heating, at around 80°C. In this aqueous solution, 1.047 mL of the $C_{12}H_{28}O_4Ti$ was slowly dissolved, and the temperature was raised to 80°C after 1.0 hours of obtaining the polymeric resin. Then there was the thermal treatment, where the resin was taken to the muffle to evaporate the organic materials, with a heating rate of 5 °C/min, and the thermal treatment was 600 °C for two hours. The TiO_2 material was obtained in powder form. The Fe–doped TiO_2 (TiO_2–Fe 5%) material was prepared as follows: initially, the polymeric resin precursor was the same for the TiO_2 material, but the molar ratio was 1:8:32:5 ($AC : EG : C_{12}H_{28}O_4Ti : FeCl_2 \cdot 4H_2O$). After to obtained the TiO_2 polymer resin, approximately 32.6 mg of the $FeCl_2 \cdot 4H_2O$ was slowly dissolved, under constant maintenance and heating, at around 80°C for 1.0 hours. The thermal treatment was 600°C for two hours with a heating rate of 5 °C/min. The Fe–doped TiO_2 material was obtained in powder form. The experimental set – up and the powder form materials can be seen in the annex A1-supplementary information Figure 26.

3.2.2 Materials Characterization

The X-ray diffraction (XRD) pattern was obtained using a Bruker-D8 Advance model, which provides Cu K α radiation (λ=0.154 nm) and uses the 2θ range from 20° up to 120°, with an increment and time for a step of 0.01 degrees and 0.1s, respectively. For the crystal phase identification, a Rietveld refinement [2] was performed using the General Structure Analysis System (GSAS) program [3] suite with the EXPGUI interface [4]. The first mathematical expression of the Rietveld refinement and other formulations [5], defined diffraction peak width as a function of the d-spacing of the diffraction angle. Therefore, peaks of interest close to the diffraction angle present different widths. Then, to model the experimental data, the present study uses the peak profile function developed by Stephens [6]. The author [6] considers that the diffraction peak widths are not a function of d-spacing, which can arise from anisotropic effects of the sample size broadening or a point pattern of defects. Thus, an anisotropic effect is observed in the half-width of the reflections, and a model developed by Larson & von Dreele [3] was used to explain these effects.

The International Center for Diffraction Data (ICDD) catalog identified the crystalline phase. Besides this, to correct the line broadening for the instrumental effects, we have used the described as:

$$\beta = \sqrt{\beta^2_{Exp} - \beta^2_{Standard}}, \tag{3.1}$$

where β is the full-width at half-maximum (FWHM) of the peak, $\beta_{Standard}$ was obtained from standard LaB_6 powder (SRM660-National Institute of Standard Technology) using the Caglioti [7] equation:

$$\beta_{Standard} = \sqrt{utan\theta^2 + vtan\theta + w}. \tag{3.2}$$

To investigate the electron density maps, we used the model described in the literature [8]. The point (x, y, z) of the crystallite cell with volume (V) is calculated by the Fourier series using the structural factors F(h, k, l):

$$\rho(x,y,z) = \frac{1}{2} \sum_{h=-Nx/2}^{Nx/2} \sum_{k=-Ny/2}^{Ny/2} \sum_{l=-Nz/2}^{Nz/2} F(h)exp[-2\pi i(hx + ky + kz)], \tag{3.3}$$

where (x, y, z) represents a vector (**r**) of real space, with one vector space (a, b, c) and another vector (***h*, *k*, *l***), which represent the coordinates of one vector from the reciprocal space with base (a^*, b^*, c^*), which then coordinates from the diffraction plane given by Bragg's Law. The resolution for the Fourier transforms obtained was used only for a range of $sin(\theta)/\lambda < 0.6\text{Å}^{-1}$ along with the *(0 0 1)*-*hkl* reflections for TiO_2 crystal structures.

The crystallographic parameters estimated by Rietveld refinement were used to calculate the electronic band structures and projected density of states (PDOS) for the TiO_2-anatase, TiO_2-rutile, and Fe-doped TiO_2 unit cells.

3.2.3 Computational Details

All calculations have been performed based on the density functional theory (DFT) [9, 10] plane-wave calculation as implemented in the Quantum-ESPRESSO package [11]. Electronic interactions were described by Perdew and Wang [12] (PW91) exchange-correlation functional and ultrasoft pseudopotentials proposed by Vanderbilt [13] , with electrons from O ($2s$, $2p$), Ti ($3s$, $3p$, $4s$, $3d$), and Fe ($3s$, $3p$, $4s$, $3d$) shells explicitly included. We performed the optimization convergence test of the system, and the plane-wave basis set the cutoff for the smooth wave functions was 60 Ry (anatase) and 50 Ry (rutile). For the Brillouin zone, integrations were performed 8x8x6 k-points (anatase), and 8x8x10 k-points (rutile) mesh sampling based on the Monkhorst-Pack scheme [14] , which are sufficient to provide satisfactory accuracy of the DFT calculations. The (*a, b, c*) lattice parameters and the (*x, y, z*) internal coordinates were fully optimized. Any significant difference compared to atomic positions was obtained from Rietveld refinement.

The electronic structure calculations were carried out using a DFT/GGA+U approach with the Hubbard correction [15, 16] . In the present calculations, the strong on-site Coulomb repulsion term U and the screened exchange interaction parameter J are used to describe the localized Ti-$3d$ electrons of TiO_2 and Fe-$3d$ electrons of the iron atom following formalism [17, 18]:

$$E_{GGA+U} = E_{GGA} + \frac{U-J}{2}\sum_{\sigma}\left[\left(\sum_{i}\rho_{ii}^{\sigma}\right) - \left(\sum_{i,j}\rho_{ij}^{\sigma}\rho_{ji}^{\sigma}\right)\right], \tag{3.4}$$

where ρ_{ij}^{σ} is the density matrix of d electrons. The spherically averaged Hubbard term U describes the increase in energy caused by the placement of an additional electron on the d orbitals, and the term J ($\sim$ 1.0 eV) represents the screened exchange energy. The matrix for the one-electron potential is given by the derivate of equation(3.4) for ρ_{ij}^{σ}

$$V_{ij} \equiv \frac{\delta E_{GGA+U}}{\delta \rho_{ij}^{\sigma}} = \frac{\delta E_{GGA}}{\delta \rho_{ij}^{\sigma}} + (U - J)\left[\frac{1}{2}\delta_{ij} + \rho_{ij}^{\sigma}\right]. \tag{3.5}$$

The effective Hubbard term $U_{eff} = U - J$, which accounts for the on-site Coulomb repulsion for each affected orbital, is the only external parameter used for this approach. We use the value of $U_{eff} = 5.0\ eV$ (anatase), $5.5\ eV$ (rutile) ($U_d < 5.00\ eV$ were considered, please see in annex A1-supplementary information), and 3.0 eV (Fe-atom) (which is consistent with previously reported DFT/GGA+U calculations) [16, 18–21].

In order to calculate Fe-doped, a spin-polarized calculation was considered. Starting magnetization of 0.25 Bohr (μ_B) was applied on the Fe atom during calculations. The Fe-doped TiO_2 was simulated from a 2 x 2 x 1 supercell constructed with 16 Ti and 32 O atoms for anatase and rutile TiO_2, and k-point grid sampling was set as 4 x 4 x 2 (anatase) and 4 x 4 x 6 (rutile) in the supercells. The energy cutoff was set to 50 Ry, and the kinetic energy cutoff of 500 Ry for both phases. The TiO_2 -anatase and TiO_2 -rutile unit cells used for the supercell construction were obtained from the Rietveld refinement. The calculations with Fe-doped have been carried out with the removal of an oxygen atom (see Figure 27) to perform the charge balance between the titanium atom and the iron atom. The electronic structure calculations were described through band structures (BS), which were calculated using the k-points path suggested by Curtarolo *et al.* [22], the projected density of states (PDOS), and the local density of electronic entropy (LDEE). For investigating the (*0 1 0*) surface reactivity of the anatase and rutile, we constructed a supercell model with four atomic layers keeping the last two fixed and 20 Å of vacuum. The energy cutoff was set to 60 Ry, and the k-point grid was set as Γ point. The adsorption energy of the water molecule (E_{ads}) was according to equation:

$$E_{ads} = E_{sys+H_2O}^{relax} - E_{sys}^{relax} - E_{H_2O}^{relax}, \tag{3.6}$$

where E_{sys} is the energy of the relaxed system; E_{H_2O} is the energy of the isolated water molecule calculated using the same protocol and E_{sys+H_2O} is the energy of the relaxed system with adsorbed one water molecule. The transition state of water-splitting on TiO_2-anatase, TiO_2-rutile, and Fe-doped TiO_2 surfaces was obtained using Nudged Elastic Band (NEB) method.

The annex A1-supplementary information shows all the coordinates (*x y z*) obtained from Rietveld refinement and used in the computation simulations.

3.3 Results and Discussion

3.3.1 Structural Characterization

The Rietveld refinement is a powerful tool to obtain lattice strain and qualitative and quantitative characterization of crystalline structures. Figure 5 shows that the X-ray diffraction pattern from Fe-doped TiO_2 peaks corresponds to two different polymorphic crystalline phases of TiO_2.

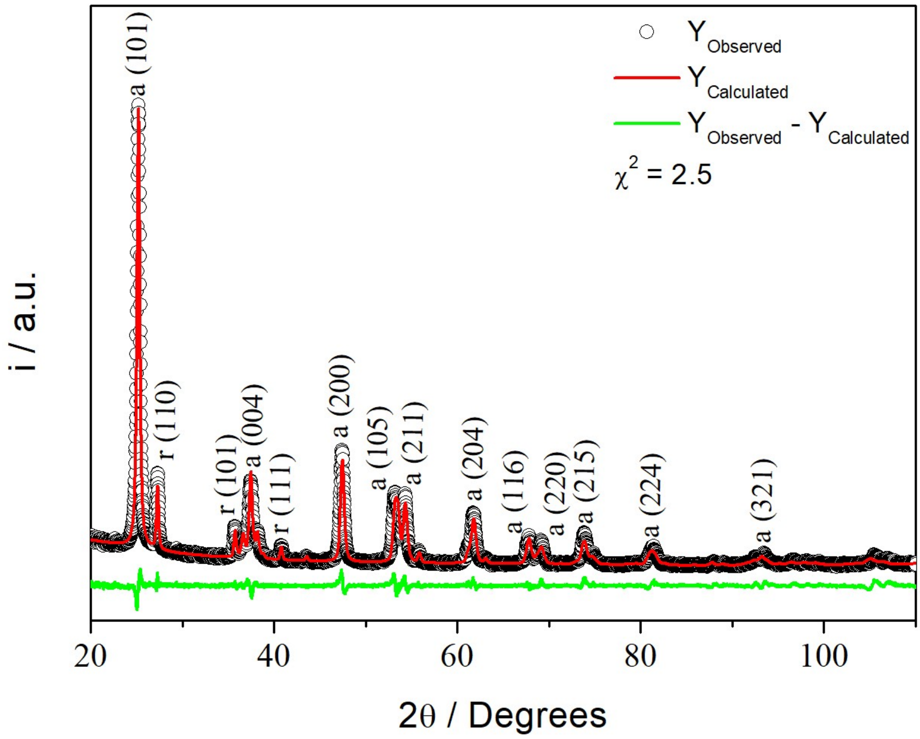

Figure 5 – Rietveld refinement pattern for TiO_2–$Fe_5\%$.

It can be observed in Figure 1 that XRD patterns show reflections at 2θ = 25.0783 (*1 0 1*)-*hkl* plane, 2θ = 37.5485 (*0 0 4*)-*hkl* plane, 2θ = 47.3291 (*2 0 0*)-*hkl* plane, 2θ = 53.1974 (*1 0 5*)-*hkl* plane, 2θ = 54.1755 (*2 1 1*)-*hkl* plane, and those of lesser intensity at 2θ = 61.7554 (*2 0 4*)-*hkl* plane, 2θ = 67.8683 (*1 1 6*)-*hkl* plane, 2θ = 69.0909 (*2 2 0*)-*hkl* plane, 2θ = 73.9811 (*2 1 5*)-*hkl* plane, 2θ = 81.3166 (*2 2 4*)-*hkl* plane, and 2θ = 93.2978 (*3 2 1*)-*hkl* plane, which was related to TiO_2–anatase tetragonal crystalline phase (CIF-202242-ICSD). Furthermore, reflections at 2θ = 27.2789 (*1 1 0*)-*hkl* plane, 2θ = 35.5924 (*1 0 1*)-*hkl* plane, and 2θ = 40.7272 (*1 1 1*)-*hkl* plane, which was related to TiO_2–rutile tetragonal crystalline phase (CIF-7802-ICSD). Reflections assigned to the iron atom were not observed in XRD patterns, suggesting that doping is substitutional and occurs in the TiO_2 structure. Abdulla-Al-Mamun *et al.* [23] studied the photocatalytic cytotoxic activity of $Ag@Fe$-doped TiO_2 nanocomposites. The Fe-doped TiO_2 atomic ratios (in %) of the iron atom to TiO_2 were 1, 3, 5, 7, and 10%, and were prepared through the sol-gel method. The authors observed through XRD measurements only anatase and rutile phases of TiO_2. Moradi *et al.* [24] observed the same behavior in Fe-doped TiO_2 samples obtained through the sol-gel method. The XRD patterns showed TiO_2 phase-related only characteristic diffraction peaks. Therefore, the same experimental conditions described herein suggest that Fe atoms are inserted into the TiO_2 structure.

According to TiO_2-anatase CIF-202242-ICSD, TiO_2-anatase is a tetragonal crystalline structure of space group number 141(I41/amdZ) and lattice parameter a = b = 3.78479(3)Å, and c = 9.51237(12) Å. The lattice parameter obtained from Rietveld refinement was a = b =3.84368(23) Å and c = 9.6558(7) Å. Also, according to TiO_2-rutile CIF-7802-ICSD, TiO_2-rutile is a tetragonal crystalline of space group 136 (P42/mnm), and lattice parameter a = b =4.5941 Å, and c = 2.9589 Å. The lattice parameter obtained from Rietveld refinement was a = b = 4.6620(4) Å and c = 3.0082(4) Å. Thus, both TiO_2-anatase and TiO_2-rutile phases agree with the reference ICSD structures. The Rietveld refinement exhibited good statistical agreement for theoretical and ICSD data (χ^2 = 2.5). It has been noted that there is no difference between TiO_2 pure (P25-degussa) and Fe-doped TiO_2 in the XRD pattern (see Figure 28). The Fe-doped in the TiO_2 structure can be verified from the lattice parameters reported in Table SI2. As the Fe^{2+} ionic radius (0.61 Å) is smaller than the Ti^{4+} ionic radius (0.74 Å) [25] , Fe-doped leads to a smaller unit cell volume (see Table SI2). According to Hume-Rothery prediction [26], the iron atom satisfies some conductions for doped in the titanium dioxide, presenting a close valency and electronegativity (1.54 for the titanium atom and 1.83 for the iron atom at the Pauling scale) [27].

3.4 Electronic Properties

The electronic properties were studied, analyzing the band structures and projected density of states (PDOS) for the structures obtained from Rietveld refinement TiO_2 -anatase:rutile and Fe–doped TiO_2 . As discussed previously, the XDR patterns and Rietveld refinement suggested that the doping with iron atoms is substitutional and occurs in the TiO_2 crystalline structure. Thus, Rietveld refinement provides the pure TiO_2 anatase:rutile and Fe – doped TiO_2 anatase:rutile structures without explicitly considering the impurity states introduced by doping with iron atoms, which occurs due it is not observed a second phase in the XDR patterns.

The electronic band structures and projected density of states (PDOS) calculated for TiO_2-anatase (a-TiO_2) and Fe-doped TiO_2-anatase (a-TiO_2-Fe) indicate the semiconductor behavior in both systems, Figure 6, where it is possible to observe in the PDOS the p orbitals of oxygen atoms are in the valence band (VB). In contrast, the conduction band (CB) has located the d orbitals of titanium atoms.

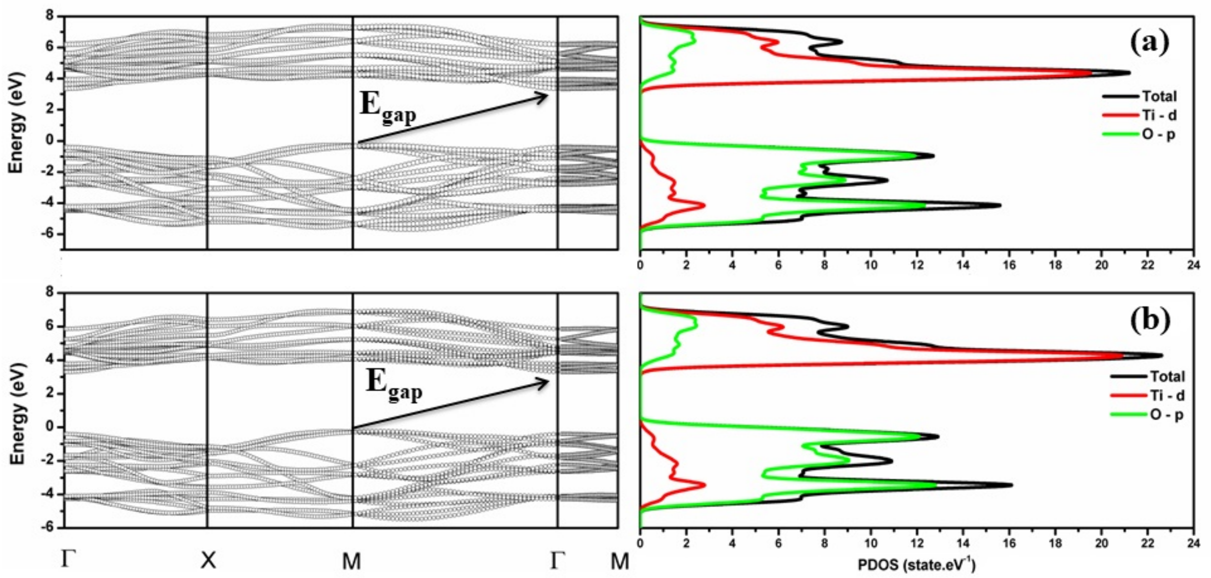

Figure 6 – Band structure and projected density of states (PDOS) for anatase (a) TiO_2 and (b) TiO_2–$Fe_{5\%}$ from Rietveld refinement structure.

Huang *et al.* [28] studied the nitrogen concentration effects on the TiO_2 anatase. The authors observed that the major component of the valence band of a-TiO_2 is the O-2p state, while the conduction band is the Ti-3d state. Through first-principles calculations of the mono and co-doped anatase TiO_2 , Ibrahim *et al.* [29] observed the same electronic properties. For the anatase TiO_2 phase, the k-points are the tetragonal path system, the BS shows that both systems (a-TiO_2 and a-TiO_2–$Fe_{5\%}$) are semiconductors with an indirect band gap, and the band gap values calculated are E_g(a-TiO_2) = 3.17 eV ($M \to \Gamma$) and E_g(a-TiO_2–$Fe_{5\%}$) = 3.00 eV ($M \to \Gamma$). In the literature, the anatase TiO_2 is considered a semiconductor with an experimental band gap of 3.20 eV [30]. The observed band gap value decreased from 3.17 eV to 3.00 eV with the Fe doping on the a-TiO_2 , where it is possible to find an experimental band gap for TiO_2 containing 1.0% Fe of 2.6 eV [31]. The shift of the conduction band accompanies the decrease in the band gap values, as observed in calculating the effective mass, m^*, according to the equation:

$$m^* = \frac{\hbar^2}{\left(\frac{d^2E}{d\kappa^2}\right)} \tag{3.7}$$

The effective mass is inversely proportional to the second derivate of energy about the k-vector; therefore, the hole in the valence band has a greater effective mass than the electron in the conduction band.

It is observed in Figure 7, that the electronic band structures and PDOS for TiO_2-rutile (r-TiO_2) and Fe-doped TiO_2-rutile (r-TiO_2-Fe), which also indicates the semiconductor behavior in both systems. One can observe, in PDOS, that both systems show similar features between the valence and conduction bands, wherein d orbitals titanium atoms have the largest contribution in the conduction band. The p orbitals oxygen atoms are responsible for most of the valence band of both systems.

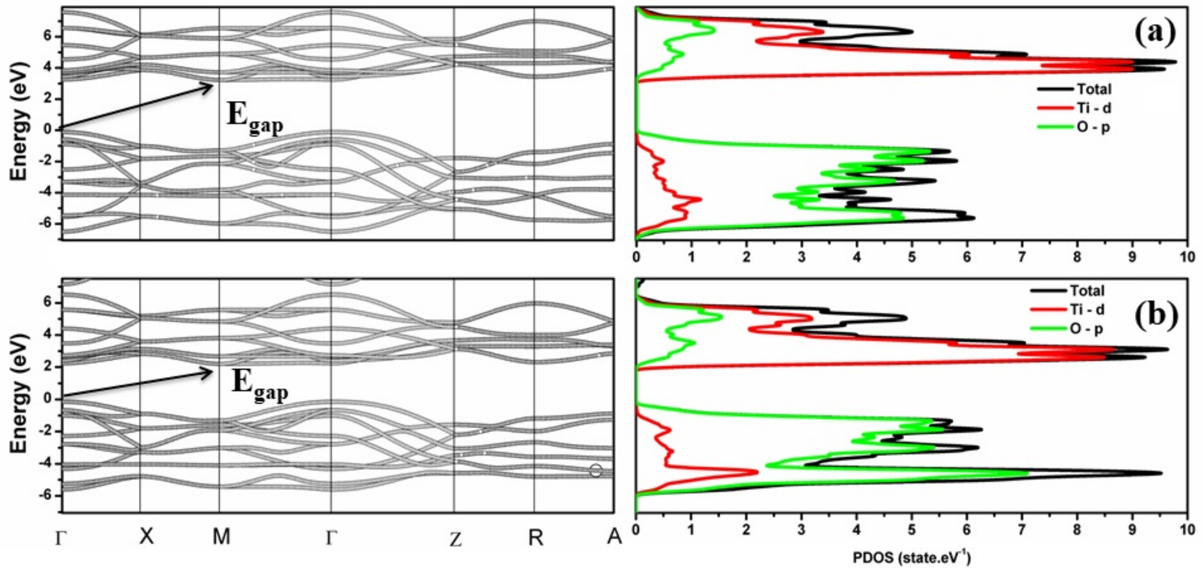

Figure 7 – Band structure and projected density of states (PDOS) for rutile (a) TiO_2 and (b) TiO_2–$Fe_{5\%}$ from Rietveld refinement structure.

Schmidt *et al.* [32] studied the electronic and optical properties of the polymorph TiO_2. The authors reported for TiO_2 rutile predominantly 2p-O states in the valence band and 3d-Ti states in the conduction band. The electronic band structures were calculated for the rutile TiO_2 phase, where the k-points are the tetragonal path system [22]. The BS shows that both systems (r-TiO_2 and r-TiO_2 - $Fe_{5\%}$) have the behavior of a semiconductor with an indirect band gap, and the gap values calculated are E_g(r-TiO_2) = 2.95 eV ($\Gamma \rightarrow M$) and E_g(r-TiO_2 – $Fe_{5\%}$) = 2.13 eV ($\Gamma \rightarrow M$). The rutile TiO_2 is considered a semiconductor with an experimental band gap of 3.00 eV [30, 33]. The band gap value decreases from 2.95 eV to 2.13 eV with the Fe doping on the r-TiO_2, where it is possible to find an experimental band gap for TiO_2 containing 1.0% iron of 2.6 eV [31]. The shift of the conduction band accompanies the decrease in the band gap value, which can be observed considering the effective mass (Eq. 3.7) of the electron and hole.

The decrease in the band gap values observed in the anatase and rutile phases with the doping of the iron atom indicates the substitution of the Ti^{4+} by Fe^{2+} ion, which presents an ionic radius of 0.605 Å and 0.63 Å [34], respectively. Then it is possible to note a mild tensile strain due to the difference between the ionic radius, also observed in the Rietveld refinement with the increase in the unit cell volume. The effects of tensile strain on the electronic band structures caused a decrease in the band gap value.

We performed the band gap energy using diffuse reflectance spectroscopy with Wood-Tauc plots for pure TiO_2 and Fe-doped TiO_2 , as shown in the Figure 30, and the optical properties were calculated for pure TiO_2 and Fe-doped TiO_2 . The band gap energy for pure TiO_2 is 3.22 eV and Fe-doped TiO_2 is 2.81 eV, where the Fe doping led to a decrease in the band gap energy. The band gap energy was determined theoretically with anatase TiO_2 (a-TiO_2) presented E g = 3.17 eV and Fe-doped a-TiO_2 with E_g = 3.00 eV (Figure 6), and rutile TiO_2 (r-TiO_2) presented E_g = 2.95 eV and Fe-doped r-TiO_2 presented Eg = 2.13 eV (Figure 7). Therefore, in both structures obtained by Rietveld refinement, a decrease in the band gap energy was observed in the band gap energy using diffuse reflectance spectroscopy with the close values.

To simulate the substitutional doping of iron atoms in the TiO_2, we have started from the commonly employed 2 x 2 x 1 supercell (48 atoms). Eight possible doping sites for the iron atom in the (010) plane was considered four titanium atoms on the surface and four on the first layer. All 8-sites for Fe doping and its BS and PDOS are described in the annex A1-supplementary information. Reyes *et al.* [31] studied the doping of iron atoms in TiO_2 using the sol-gel method to prepare materials. The materials of TiO_2 were doped with Fe using as a precursor $FeCl_2$ and calcined at 600 ºC. Through Mössbauer characterization of TiO_2 with Fe (1.0% wt), samples presented about 66.81% of Fe^{2+} species. The same experimental conditions described by the authors [31] were used in the present work. Therefore, the calculations considered the substitutional doping of Ti^{4+} by Fe^{2+}.

The PDOS of the supercell TiO_2 -anatase and TiO_2-rutile can be observed along the supercell, Figure 8 a-c. The contribution of the Ti atoms to the largest part of the conduction band and the O atoms to the largest part of the valence band. The PDOS of the supercell Fe-doped

TiO_2 -anatase and TiO_2 -rutile that present the lowest energy (see in annex A1-supplementary information) is shown in Figure 8 b-d.

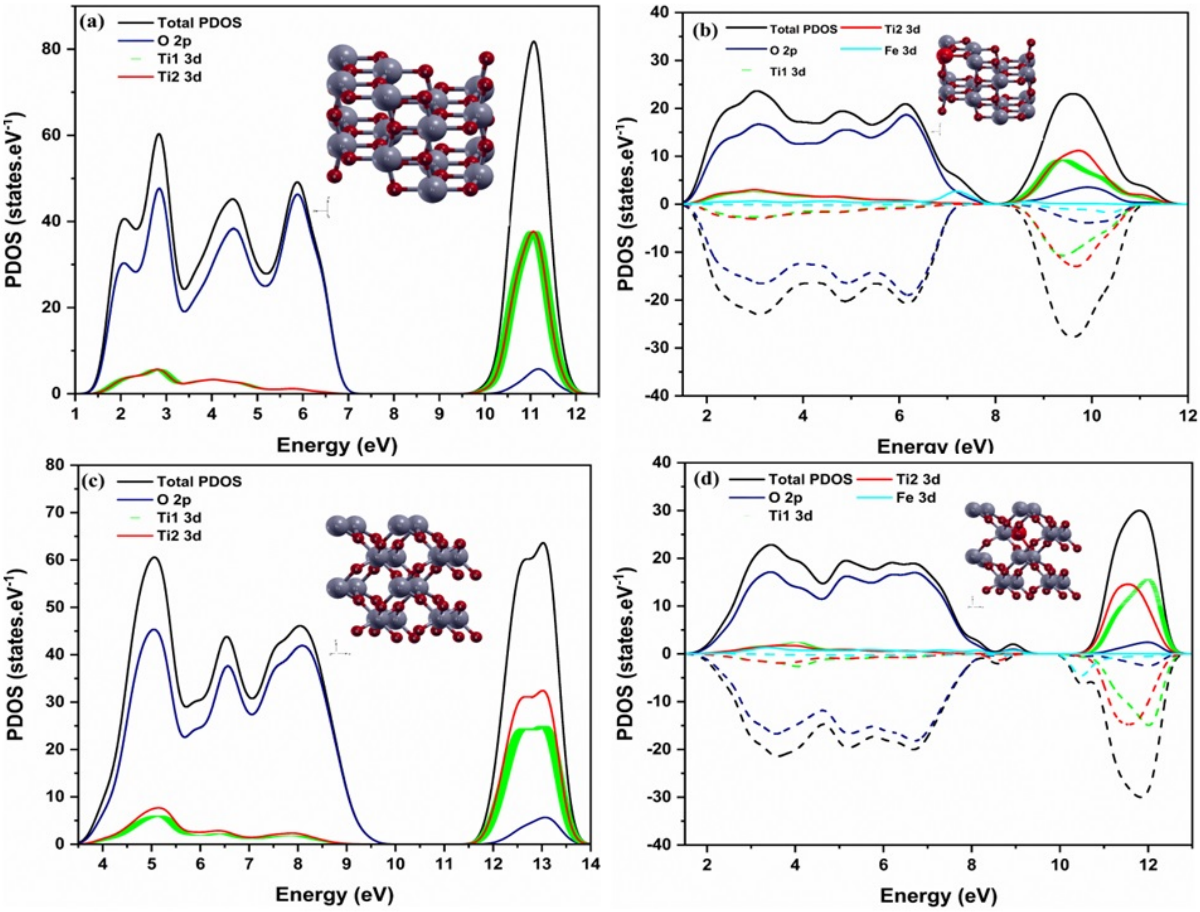

Figure 8 – Total density states and PDOS on the p and d orbitals of (a) anatase TiO_2, (b) anatase TiO_2-Fe, (c) rutile TiO_2, and (d) rutile TiO_2–Fe. The solid line is set to spin up, and the dashed line to spin down.

New states emerge in both the doping cases and the positions are mainly located between the valance and conduction bands, Figure 8 b-d. It can be seen that the new states for both systems consist mainly of $3d$ orbitals of the Fe atoms, $2p$ orbitals of O atoms mainly contribute to the valence band, and $3d$ orbitals of Ti atoms contribute to the conduction band. The most striking difference from Figure 8 a-c is that the Fe^{2+} $3d$ states appear in the PDOS within the band gap. The Fe^{2+} $3d$ states are spread from approximately 0 eV to about 0.5 eV, Figure 8b, with a predominance of spin up near the valence band and 0.5 eV to about 1 eV, Figure 8d, with predominance to spin down near the valence band; an overlap of the $3d$ states of Ti can be seen in the PDOS for both systems. Fe^{2+} states in the band gap should also be reflected in the photocatalytic property compared to pure TiO_2.The electronic band structures were determined for the two systems doping with Fe atoms, Figure 9 a-b.

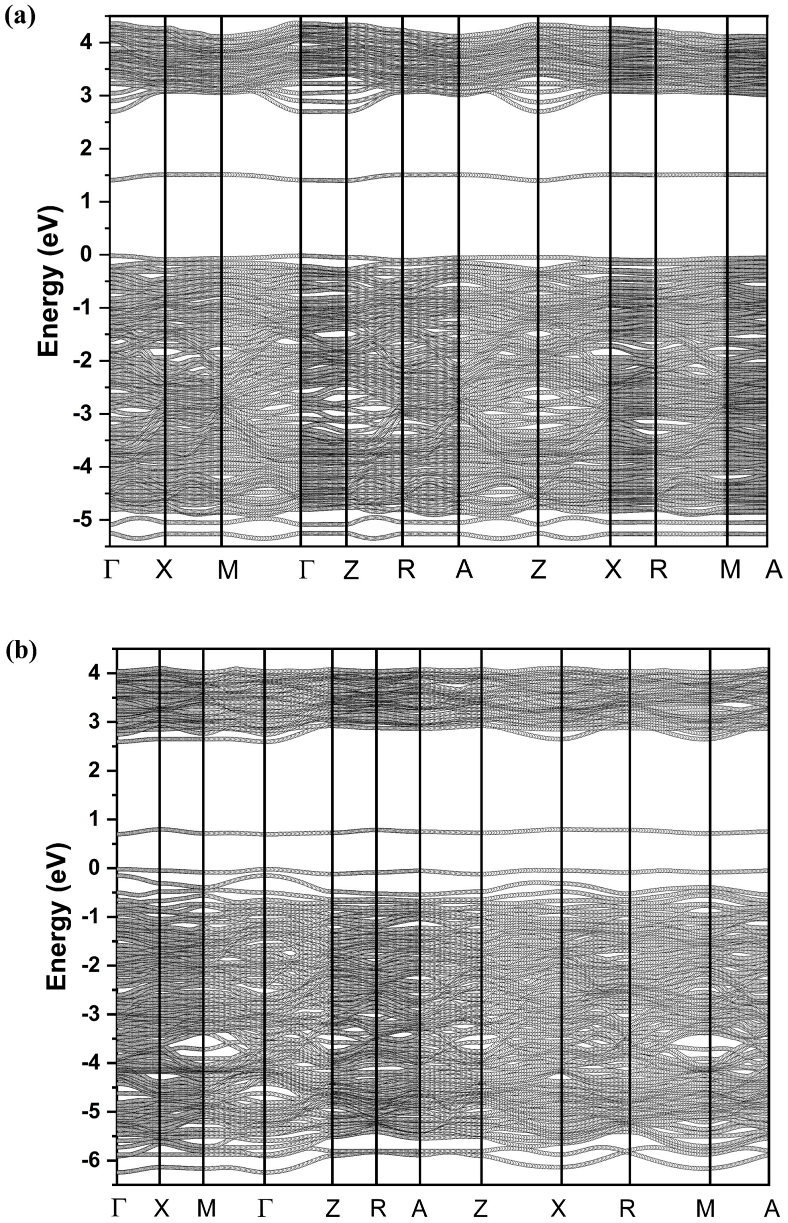

Figure 9 – Band structure for (a) a-TiO_2-Fe and (b) r-TiO_2–Fe.

It can be observed that there is a general trend of the existence of a defect in the band structure between the valence band and conduction band for both systems attributed to the iron atom. For a-TiO_2-Fe, Figure 9-a, the band gap with the biggest energy is 2.41 eV with the defect near the conduction band, and for r-TiO_2 -Fe, Figure 9-b, the band gap with the lowest energy is 2.37 eV with the defect near the valence band.

The quantum efficiency of a photocatalyst is affected by the transfer rate of electrons and holes generated by an excitation. The charge rate of charge carriers can be indirectly assessed by the effective mass of electrons and holes, which can be related to the following equation [35]:

$$\nu = \frac{\hbar\kappa}{m^*}, \tag{3.8}$$

where m^* is the effective mass of charge carriers, κ is the wave vector, $\hbar$ is the reduced Planck's constant, and ν is the transfer rate of electrons and holes. The is inversely proportional to their; namely, the greater the effective mass of the carriers, the slower the transfer rate of the carriers, as shown in eq 3.7. Therefore, the small effective mass can promote the migration of charge carriers and inhibit the recombination of charge carriers. To explain the difference in photocatalytic efficiency between phases anatase and rutile, as well as pure and doped, the effective mass of the electron ($m^*_{e^-}$) and hole ($m^*_{h^+}$) was calculated along the directions designated for the band gap, Table 8, solving the eq 3.7 in the bands of valence and conduction of the systems.

Table 2 – Effective mass of electron and hole for a-TiO_2 , a-TiO_2–Fe, r-TiO_2, and r-TiO_2–Fe.

System		$m^*_{e^-}$	$m^*_{h^+}$
Anatase	calculation	0.1609	0.3203
	[31]	0.1412	0.2028
a-TiO_2–$Fe_{5\%}$	calculation	0.2401	0.2854
Rutile	calculation	0.2570	0.8613
	[31]	0.1284	1.0018
a-TiO_2–$Fe_{5\%}$	Calculation	0.5333	0.6427

From Table 8, it is observed that the and the anatase phase is smaller than the rutile phase, indicating that the transfer rate of the holes and electrons in the anatase phase is possibly faster. When doped with the iron atom, a decrease in the effective masses of the holes is noted, in which the a-TiO_2-Fe has a less effective mass. This indicates that the photoexcited charge carriers of a-TiO_2 and a-TiO_2-Fe migrate more easily and transfer to their interior surface to participate in photocatalytic reactions due to their lighter effective masses. However, when the ratio analyzed, a value of 0.5 and 0.3 is observed for anatase and rutile, respectively, and approximately 0.8 for both phases doped with the iron atom. With doping, the rate of mobility of charge carriers increases with respect to pure phases. Through DFT calculations of the difference in the photocatalytic activity of the TiO_2 polymorphs, Zang *et al.* [36] also observed that the effective masses of charge carriers of the anatase phase are less than of charge carriers in the rutile phase.

In order to study the behavior with Fe-doped phases stability, the local density electronic entropy was calculated, Figure 10 a-b.

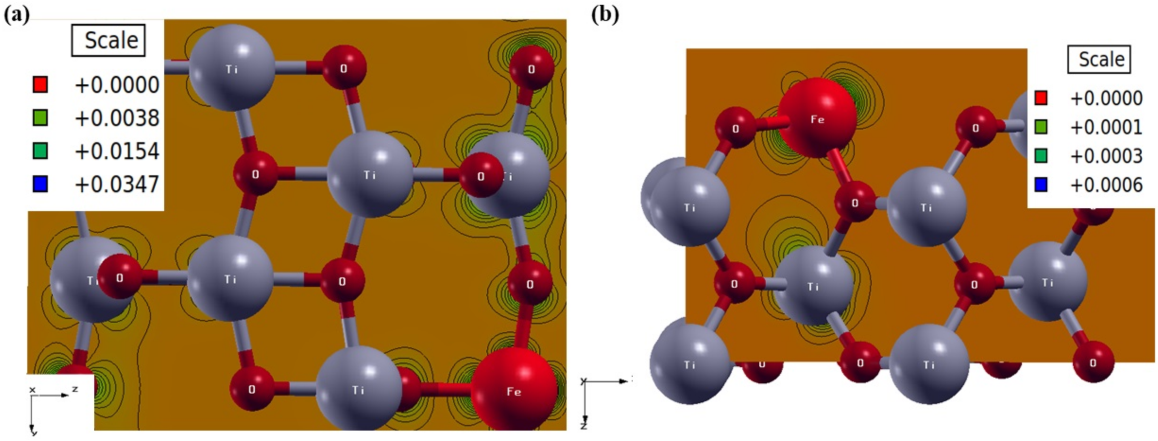

Figure 10 – Local density of electronic entropy for (a) a-TiO_2-Fe and (b) r-TiO_2–Fe.

Electronic entropy is usually thought of as a small quantitative correction and can be calculated from the band structure following equation [37]:

$$S_{elec}^{band} = -k_B \int \rho[f - lnf + (1-f)ln(1-f)]dE, \tag{3.9}$$

where ρ is the density of states, f is the Fermi distribution function, and k_B is Boltzmann constant. A local density of states can be defined following equation:

$$\rho(E, r) = \sum_i |\psi_i(r)^2|\delta(E_F - e_i), \tag{3.10}$$

the factor $|\psi_i(r)^2|$ means that each state contributes more to the high-density regions. It is observed in Figure 10 a-b that the contours of the isolines of the local density electronic entropy represent the effect of the iron atom on the neighboring oxygen and titanium atoms, in which the electronic entropy is located on the iron atom for both systems.

Also, a covalent character is observed between the iron atom and the oxygen atoms due to the overlapping of the isolines. The a-TiO_2-Fe system has a maximum value of 0.0348 k_B/atom, and the r-TiO_2-Fe system has a maximum value of 0.0006 k_B/atom; that is, the a-TiO_2 phase has greater doping effects. When the Fe atom is inserted into the crystalline structure of anatase and rutile TiO_2 phases, the electronic structure is modified. This was observed by Sauvage *et al.* [38] that studied the effects of Fe doping on anatase TiO_2 for application in Lithium-Ion Batteries and Photocatalysis experimentally. A band gap decrease was observed, and an improvement by Fe doping in charge/discharge. Through DFT/PBE+U calculations of the Rh, Nb-codoped rutile TiO_2. Ghuman and Singh [39] observed that the electronic density is located in the doping atoms and has a covalent character between the doping and neighboring oxygen atom.

Table 3 shows the water adsorption energies and bond distances for a water molecule on the Ti (or Fe) adsorption sites at the (*0 1 0*) surface.

Table 3 – Estimated water adsorption energies (E_{ads}) and bond distances for a water molecule on the surface for the a-TiO_2 , a-$TiO2$–Fe, r-TiO_2, and r-TiO_2–Fe.

System	E_{ads} (eV)	$Ti_{surface}$–O_w (Å)	$Fe_{surface}$–O_w (Å)
Anatase	-0.6149	2.2390	
a-TiO_2–Fe	-0.9360		2.1842
Rutile	-1.2422	2.1296	
r-TiO_2–Fe	-0.4608	2.0529	

The adsorption energy (E_{ads}) on a-TiO_2 is predicted to be about 0.6 eV larger than r-TiO_2 , and distance on a-TiO_2 is about 0.1 Å longer than the distance on r-TiO_2, in good agreement with values reported by Selloni *et al.* [40]. The authors [40] observed a similar length of the $Ti_{surface}$–O_w presented a range about from 2.1 Å to 2.3 Å, and E_{ads} presented a range about from -0.6 eV to -1.0 eV depending on the adorption site at the a-TiO_2 surface. The $Ti_{surface}$–O_w bond decrease and the E_{ads} increase were observed in the Fe-doped TiO_2 anatase and rutile, where the anatase phase $Ti_{surface}$–O_w bond length is bigger than the rutile phase, and the anatase phase E_{ads} is the smallest, which presented -0.9360 eV. The metal-doped TiO_2 presents adsorption energy that is smaller than pure TiO_2 . Yang *et al.* [41] studied the super hydrophilic Fe^{3+}-doped TiO_2 by experimental and DFT approach. Through the hydroxyl adsorption on the TiO_2 and $Fe@TiO_2$, adsorption energy was obtained the -1.59 eV and -1.66 eV, respectively, a short variation between the pure and doped systems. The same behavior was observed by Shao *et al.* [42] that studied the nickel-doped TiO_2 in electrochemical activities. According to authors [42], the adsorption energy of a water molecule on TiO_2 (*0 0 1*) presented -0.936 eV, and Ni-doped TiO_2 (*0 0 1*) presented -1.165 eV. This behavior observed in the doped TiO_2 , with the smallest adsorption energy, evidences that the water molecule binds to the anatase surface weaklier than Fe-doped. In contrast, the water molecule binds to the surface rutile more strongly than the Fe-doped. Therefore, the TiO_2-anatase points more toward a behavior where binding with a water molecule is neither too strong nor too weak and is more sensitive to iron doping than the TiO_2-rutile about the local density electronic entropy. Thus, for the application as a catalyst, as used for water splitting reaction, the anatase phase can present an improved performance than the rutile. In this sense, the TiO_2-anatase was chosen to simulate the initial water-splitting reaction.

3.5 Reaction path of the water splitting

Water splitting was studied on the pure a-TiO_2 and a-TiO_2-Fe systems from the structural and electronic properties. The geometries of the surface in the plane (*0 1 0*) with species of the initial states (IS), transition state (TS), and final state (FS) are involved in the mechanism for the water splitting between the pure a-TiO_2, and a-TiO_2-Fe systems are shown in Figure 11 a,b, respectively.

In order to obtain a molecular scale understanding of the fundamental reaction path and estimate the activation energy barrier for water splitting, CI-NEB calculations were performed with ten images, where the initial and final states were proposed from the mechanism [43]:

$$H_2O_{ads} + h^+_{BV} \rightleftharpoons OH^{\cdot}_{ads} + H^+_{ads}, \tag{3.11}$$

where $H_2O_{ads} + h^+_{BV}$, $OH^{\cdot}_{ads}$, and H^+_{ads} are adsorbed on pure a-TiO_2 and a-TiO_2-Fe systems surface. The activation energy barrier (E_a) was calculated following equation:

$$E_a = E_{TS} - E_{IS}, \tag{3.12}$$

where E_{TS} is the energy of the transition state and E_{IS} is the energy of the initial state. The reaction energy (ΔE) is calculated as:

$$\Delta E = E_{FS} - E_{IS}, \tag{3.13}$$

where E_{FS} is the energy of the final state.

The IS corresponds to the (*0 1 0*) surface with a chemically adsorbed H_2O molecule, and the FS corresponds to surfaces that have dissociated water molecules such as OH and H species adsorbed on the surface, in which the OH and H groups attached to the Ti and O atoms of the surface, respectively. For the reaction path, different TS was found for the pure a-TiO_2 and a-TiO_2-Fe surfaces, as observed in Figures 11-a and 11-b, respectively. It is observed that the H_2O molecule is distorted, resulting in HO–H with a bond length of approximately 1.00 Å for the pure a-TiO_2 surface, Figures 11-a. However, for the a-TiO_2-Fe surface, the TS consists of dissociation of the H_2O molecule, with OH attached to the Fe atom and the H at a distance of 1.23 Å from the surface oxygen atom, Figure 11-b.

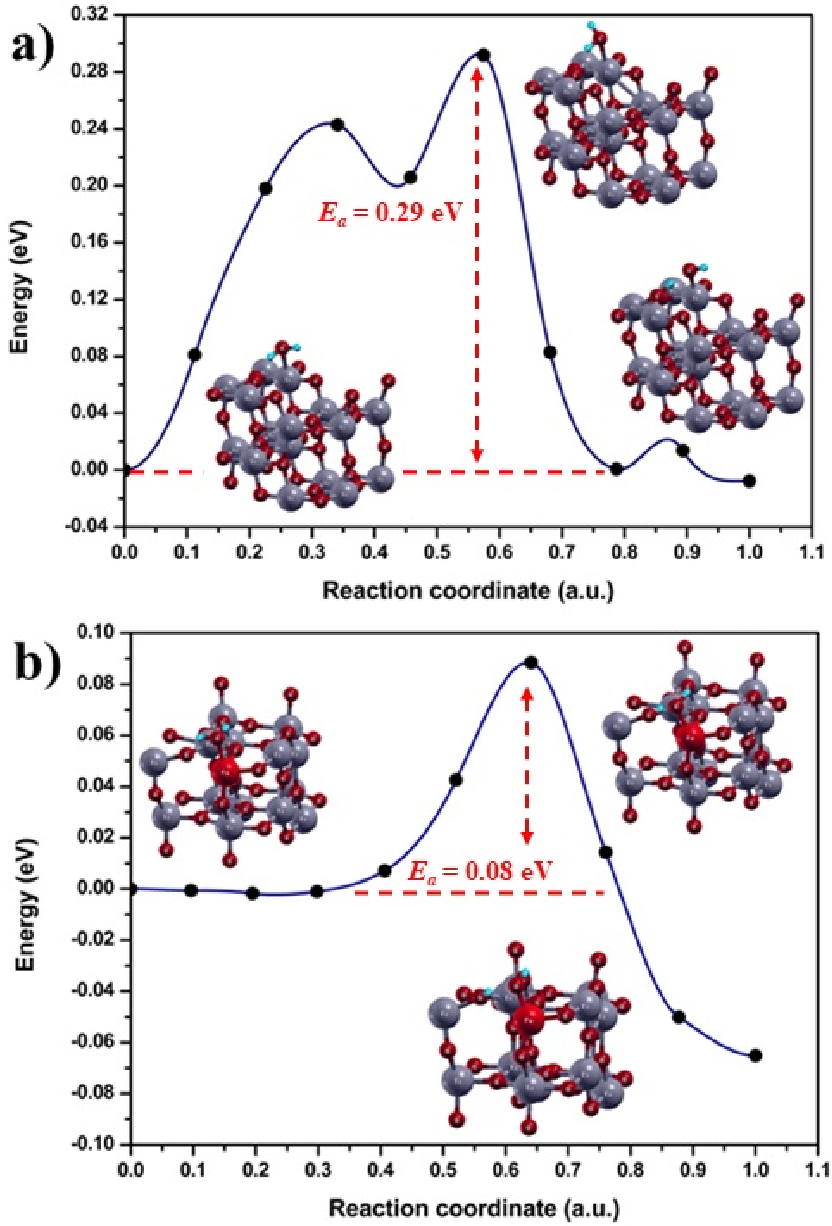

Figure 11 – Reaction pathway and reaction barrier of single water molecule dissociation on (a) a-TiO_2 and (b) a-TiO_2–Fe.

The reaction energy (ΔE) calculations indicate that the cleavage of the water molecule has a small exothermic character, both pure a-TiO_2 (ΔE = -0.007 eV) and a-TiO_2-Fe (ΔE = - 0.06 eV). Although the differences in the values of ΔE were insignificant for both systems, the activation energy barriers (E_a) predicted for the cleavage of water on pure a-TiO_2, and a-TiO_2-Fe surfaces are 0.29 eV and 0.08 eV, respectively. Xu *et al.* [44] simulated the water splitting in different oxides using the NEB method. One of them was the rutile TiO_2 in the plane (*1 1 0*), which obtained an activation energy barrier for the water splitting of approximately 0.38 eV. Ghuman *et al.* [45] studied the mechanism of adsorption and dissociation of water on the surface of pure r-TiO_2 and doped with Fe (II) atoms through the NEB method. For r-TiO_2, the activation energy barrier for water dissociation in the study was approximately 0.9 eV; for rutile TiO_2 doped with Fe (II) atom, it was approximately 0.2 eV. Therefore, the values found in the present work compared with the literature indicate that the surface a-TiO_2 -Fe is energetically more favorable for the cleavage of the water in relation to the pure a-TiO_2 surface.

The $E_{a(a-TiO_2-Fe)} < E_{a(a-TiO_2)}$ can be related to the structural and electronic properties of the Fe-doped TiO_2 . Thus, It is possible to notice that the $Ti-O$ bond length in the pure TiO_2 present 1.93 Å while the $Fe-O$ bond length in the Fe-doped TiO_2 present 1.86 Å. Analyzing the electronic charge density ($\Delta n(r)$), the pure TiO_2 present the $\Delta n(r)_{total}$ = 1.3148 $e^-/\text{Å}^3$, and Fe-doped TiO_2 present $\Delta n(r)_{total}$ =6.2353 $e^-/\text{Å}^3$, which can be seen in Figure 33 in the annex A1-supplementary information. In this sense, the Fe-doped TiO_2 enhanced structural and electronic properties, which can be attributed to the smallest activation energy for water-splitting. We performed a photoelectrochemistry study of water splitting on the pure TiO_2 and Fe-doped TiO_2 to provide experimental support about why Fe-doped TiO_2 provides less activation energy for water-splitting, see experimental set – up in Figure 34 . When we evaluate the photocurrent as a function of the wavelength (λ), we observe a different behavior between pure TiO_2 and Fe-doped TiO_2 , see in Figure 34a. We have observed that both pure TiO_2 and Fe-doped TiO_2 show photocurrent close to λ = 320 nm. However, Fe-doped TiO_2 demonstrates a higher photocurrent than pure TiO_2 , and increased photocurrent in the wavelength between 500 nm and 600 nm contrasts with pure TiO_2, which only responds at λ = 320 nm. As a result, Fe-doped TiO_2 exhibits a significant increase in the photocurrent as a function of the wavelength curve, indicating better charge separation, particularly in the visible region. In addition, we then measured the time-dependent photocurrent response in the ON and OFF states, see in Figure 34b. The photocurrent response is enhanced by Fe doping when compared with pure TiO_2. Therefore, the photocatalytic properties of the Fe-doped TiO_2 are better than the pure TiO_2 , indicating the smaller activation energy for the water-splitting reaction, previously shown in the theoretical calculation. In this sense, the photoelectrochemical (PEC) water-splitting performance was analyzed for pure TiO_2 and Fe-doped TiO_2 , see in Figure S9. The PEC performance was best for the Fe-doped TiO_2 under AM 1.5G. The photocurrent of the pure TiO_2, Fe-doped TiO_2 dark and illuminated are 425, 0, and 1200 μA.cm^{-2}, respectively, at 0.8 V versus reversible hydrogen electrode (RHE), suggesting much more efficient charge separation and collection of the Fe-doped TiO_2 than pure TiO_2.

Furthermore, a photoelectrochemistry study of water splitting on the pure TiO_2 photoanode and Fe-doped TiO_2 photoanodes was performed in a photoelectrochemical cell as presented in Figure 34a in order to provide experimental support. When evaluated the photocurrent as a function of the wavelength (λ), it is possible to observe an increasing of 300 % at 320 nm in photocurrent values for TiO_2-Fe compared to TiO_2 materials, as presented in Figure 34b. It is possible to observed that both pure TiO_2 and Fe-doped TiO_2 photoanodes presented photocurrent close to $\lambda \approx 320$ nm. However, it is important to stress out that Fe-doped TiO_2 photoanodes demonstrated photocurrent in the wavelength between 450 nm and 650 nm contrasts with pure TiO_2 photoanode , which presented band only at $\lambda \approx 320$ nm. As a result, Fe-doped TiO_2 photoanodes exhibits a significant increase in the photocurrent as a function of the wavelength curve, indicating better charge separation, particularly in the visible region. In addition, it was measured photocurrent transients generated during photoirradiation (E = 0.5 V) time-dependent for Fe-doped TiO_2 and TiO_2 photoanodes, as presented in Figure 34c. It is possible to notice that the photocurrent response is enhanced by 350 % for Fe-doping TiO_2 photoanodes when compared with pure TiO_2 photoanode. Therefore, the photocatalytic properties of the Fe-doped TiO_2 are better than the pure TiO_2, indicating the smaller activation energy for the water-splitting reaction, previously shown in the theoretical calculation.

The photoelectrochemical water splitting measurements were performed under radiated TiO_2 photoanode and Fe-doped TiO_2 radiated and non-radiated (dark) photoanodes using linear scan voltammetry, as presented in Figure 34d. As evinced in Figure 32d, Fe-doped TiO_2 photoanodes under AM 1.5G presented improvement along photoelectrochemical water splitting reaction. It is possible to observe an enhancement of 135% along the photocurrent at 1.2 V for Fe-doped photoanode compared to pure TiO_2 photoanode.

Finally, the present study focused primarily on theoretical investigations of the initial water splitting reaction mechanism. However, it is important to observe that a photoelectrochemistry study of water splitting was conducted as part of this study to provide experimental support. Thus, the theoretical simulations aimed to provide insights into the reaction mechanisms of water-splitting, offering a molecular-scale understanding of the initial reaction mechanism and estimating activation energy barriers.

3.6 Conclusions

The metal-doping strategy to enhance the TiO_2 photocatalytic properties toward water splitting is adequate but lacks a better understanding of the mechanism. The effect of the Fe atoms in the structural and electronic properties of the doped anatase and rutile phases as well as water-splitting on their (*0 1 0*) surfaces, was investigated in the present study.

The Fe-doped anatase and rutile TiO_2 have been successfully synthesized up to 10% of atomic ratio. The Rietveld refinement is in good agreement with the previously reported experiments. The lattice parameters are decreased, leading to smaller unit cell volume. Furthermore, replacing a Ti^{4+} with a spin-polarized Fe^{2+} atom in the unit cell must lead to oxygen vacancy. The effect of this modification has been assessed through DFT/PW calculations. A defect in the band structure between the valence and conduction bands with large $3d$ states of Fe^{2+} contribution has been shown. The predicted band gaps for anatase and rutile are 3.17 eV and 2.95 eV, respectively, close to the experimental values. However, we have shown that the Fe-doped TiO_2 lead to smaller band gaps. The anatase phase presents greater sensitivity to Fe-doping with respect to the rutile phase. The effective mass of the carriers was calculated, indicating that the transfer rate of holes and electrons in the anatase is faster than in rutile.

The water adsorption on the Ti and Fe sites was estimated to assess the surface reactivity towards water-splitting. The adsorption energy is estimated to be larger (in absolute values) for rutile compared to anatase. Water tends to adsorb on the Fe sites than on the Ti sites, with adsorption energies -0.9360 eV more stable.

The mechanism of water splitting leading to adsorbed $OH^{\cdot}$ and H^+ species has been investigated. The transition states of the anatase TiO_2 mechanism showed an activation energy barrier of 0.29 eV, and Fe-doped anatase TiO_2 presented an activation energy barrier of 0.08 eV. This is an indication that the Fe-doped anatase TiO_2 favors that water splitting. Experimental measurements evidence the improvement of water splitting reaction for Fe-doped TiO_2 compared to TiO_2 photoanodes.

3.7 Acknowledgments

The authors would like to thank the Brazilian research-funding institutions FAPEAM, FAPEMAT, FAPEMIG and CNPq by financial resources. The authors also would like to thank Dr. Walber Goncalves Guimaraes Jr. (presently at UFSCAR) due to help with the optical dielectric calculations. We also thank CENAPAD/SP, UFMT-STI/Server and ACQUA-INCT (http://www.acqua-inct.org) for providing computational time.

BIBLIOGRAPHY

1 PECHINI, M. P. *Method of preparing lead and alkaline earth titanates and niobates and coating method using the same to form a capacitor*. [S.l.]: Google Patents, 1967. US Patent 3,330,697. 62

2 RIETVELD, H. M. A profile refinement method for nuclear and magnetic structures. *Journal of applied Crystallography*, International Union of Crystallography, v. 2, n. 2, p. 65–71, 1969. 63

3 LARSON, A. C.; DREELE, R. B. V. Gsas. *Report lAUR*, p. 86–748, 1994. 63

4 TOBY, B. H. Expgui, a graphical user interface for gsas. *Journal of applied crystallography*, International Union of Crystallography, v. 34, n. 2, p. 210–213, 2001. 63

5 THOMPSON, P.; COX, D.; HASTINGS, J. Rietveld refinement of debye–scherrer synchrotron x-ray data from al2o3. *Journal of Applied Crystallography*, International Union of Crystallography, v. 20, n. 2, p. 79–83, 1987. 63

6 STEPHENS, P. W. Phenomenological model of anisotropic peak broadening in powder diffraction. *Journal of Applied Crystallography*, International Union of Crystallography, v. 32, n. 2, p. 281–289, 1999. 63

7 CAGLIOTI, G.; PAOLETTI, A. t.; RICCI, F. Choice of collimators for a crystal spectrometer for neutron diffraction. *Nuclear Instruments*, Elsevier, v. 3, n. 4, p. 223–228, 1958. 63

8 MARCH, N. H. Electron density theory of atoms and molecules. *The Journal of Physical Chemistry*, ACS Publications, v. 86, n. 12, p. 2262–2267, 1982. 63

9 HOHENBERG, P.; KOHN, W. Inhomogeneous electron gas. *Physical review*, APS, v. 136, n. 3B, p. B864, 1964. 64

10 KOHN, W.; SHAM, L. J. Self-consistent equations including exchange and correlation effects. *Physical review*, APS, v. 140, n. 4A, p. A1133, 1965. 64

11 GIANNOZZI, P. et al. Quantum espresso: a modular and open-source software project for quantum simulations of materials. *Journal of physics: Condensed matter*, IOP Publishing, v. 21, n. 39, p. 395502, 2009. 64

12 PERDEW, J. P.; WANG, Y. Accurate and simple analytic representation of the electron-gas correlation energy. *Physical review B*, APS, v. 45, n. 23, p. 13244, 1992. 64

13 VANDERBILT, D. Soft self-consistent pseudopotentials in a generalized eigenvalue formalism. *Physical review B*, APS, v. 41, n. 11, p. 7892, 1990. 64

14 MONKHORST, H. J.; PACK, J. D. Special points for brillouin-zone integrations. *Physical review B*, APS, v. 13, n. 12, p. 5188, 1976. 64

15 ANISIMOV, V. I.; ZAANEN, J.; ANDERSEN, O. K. Band theory and mott insulators: Hubbard u instead of stoner i. *Physical Review B*, APS, v. 44, n. 3, p. 943, 1991. 64

16 PATRICK, C. E.; GIUSTINO, F. Gw quasiparticle bandgaps of anatase tio2 starting from dft+ u. *Journal of Physics: Condensed Matter*, IOP Publishing, v. 24, n. 20, p. 202201, 2012. 64, 65

17 DUDAREV, S. L. et al. Electron-energy-loss spectra and the structural stability of nickel oxide: An lsda+ u study. *Physical Review B*, APS, v. 57, n. 3, p. 1505, 1998. 64

18 SHAO, G. Red shift in manganese-and iron-doped tio2: a dft+ u analysis. *The Journal of Physical Chemistry C*, ACS Publications, v. 113, n. 16, p. 6800–6808, 2009. 64, 65

19 VU, N. H. et al. Anatase–rutile phase transformation of titanium dioxide bulk material: a dft+ u approach. *Journal of Physics: Condensed Matter*, IOP Publishing, v. 24, n. 40, p. 405501, 2012. 65

20 CHENG, G. et al. Visible-light-driven deep oxidation of no over fe doped tio2 catalyst: Synergic effect of fe and oxygen vacancies. *Applied Catalysis B: Environmental*, Elsevier, v. 277, p. 119196, 2020. 65

21 LIU, B.; ZHAO, X. The synergetic effect of v and fe-co-doping in tio2 studied from the dft+ u first-principle calculation. *Applied Surface Science*, Elsevier, v. 399, p. 654–662, 2017. 65

22 SETYAWAN, W.; CURTAROLO, S. High-throughput electronic band structure calculations: Challenges and tools. *Computational materials science*, Elsevier, v. 49, n. 2, p. 299–312, 2010. 65, 69

23 ABDULLA-AL-MAMUN, M.; KUSUMOTO, Y.; ISLAM, M. S. Enhanced photocatalytic cytotoxic activity of ag@ fe-doped tio2 nanocomposites against human epithelial carcinoma cells. *Journal of Materials Chemistry*, Royal Society of Chemistry, v. 22, n. 12, p. 5460–5469, 2012. 67

24 MORADI, H. et al. Fabrication of fe-doped tio2 nanoparticles and investigation of photocatalytic decolorization of reactive red 198 under visible light irradiation. *Ultrasonics sonochemistry*, Elsevier, v. 32, p. 314–319, 2016. 67

25 SHANNON, R. D. Revised effective ionic radii and systematic studies of interatomic distances in halides and chalcogenides. *Acta crystallographica section A: crystal physics, diffraction, theoretical and general crystallography*, International Union of Crystallography, v. 32, n. 5, p. 751–767, 1976. 67

26 W, S. R. E. H.-R.; W, H. C. *The structure of metals and alloys*. [S.l.]: Institute of Metals and the Institution of Metallurgists, 1969. 67

27 MIRACLE, D. B.; SENKOV, O. N. A critical review of high entropy alloys and related concepts. *Acta Materialia*, Elsevier, v. 122, p. 448–511, 2017. 67

28 YANG, K.; DAI, Y.; HUANG, B. Study of the nitrogen concentration influence on n-doped tio2 anatase from first-principles calculations. *The journal of physical chemistry C*, ACS Publications, v. 111, n. 32, p. 12086–12090, 2007. 68

29 IBRAHIM, H. H.; MOHAMED, A. A.; IBRAHIM, I. A. Electronic and optical properties of mono and co-doped anatase tio2: First principles calculations. *Materials Chemistry and Physics*, Elsevier, v. 252, p. 123285, 2020. 68

30 KAPILASHRAMI, M. et al. Probing the optical property and electronic structure of tio2 nanomaterials for renewable energy applications. *Chemical reviews*, ACS Publications, v. 114, n. 19, p. 9662–9707, 2014. 68, 69

31 LOPEZ, T. et al. Characterization of iron-doped titania sol–gel materials. *Journal of Materials Chemistry*, Royal Society of Chemistry, v. 12, n. 3, p. 714–718, 2002. 68, 70, 73

32 LANDMANN, M.; RAULS, E.; SCHMIDT, W. The electronic structure and optical response of rutile, anatase and brookite tio2. *Journal of physics: condensed matter*, IOP Publishing, v. 24, n. 19, p. 195503, 2012. 69

33 BURDETT, J. K. et al. Structural-electronic relationships in inorganic solids: powder neutron diffraction studies of the rutile and anatase polymorphs of titanium dioxide at 15 and 295 k. *Journal of the American Chemical Society*, ACS Publications, v. 109, n. 12, p. 3639–3646, 1987. 69

34 AHRENS, L. H. The use of ionization potentials part 1. ionic radii of the elements. *Geochimica et cosmochimica Acta*, Elsevier, v. 2, n. 3, p. 155–169, 1952. 70

35 YU, W.; ZHANG, J.; PENG, T. New insight into the enhanced photocatalytic activity of n-, c-and s-doped zno photocatalysts. *Applied Catalysis B: Environmental*, Elsevier, v. 181, p. 220–227, 2016. 72

36 ZHANG, J. et al. New understanding of the difference of photocatalytic activity among anatase, rutile and brookite tio2. *Physical Chemistry Chemical Physics*, The Royal Society of Chemistry, v. 16, n. 38, p. 20382–20386, 2014. 73

37 ZHOU, F.; MAXISCH, T.; CEDER, G. Configurational electronic entropy and the phase diagram of mixed-valence oxides: the case of li x fepo 4. *Physical review letters*, APS, v. 97, n. 15, p. 155704, 2006. 74

38 ANDRIAMIADAMANANA, C. et al. Room-temperature synthesis of iron-doped anatase tio2 for lithium-ion batteries and photocatalysis. *Inorganic Chemistry*, ACS Publications, v. 53, n. 19, p. 10129–10139, 2014. 74

39 GHUMAN, K. K.; SINGH, C. V. A dft+ u study of (rh, nb)-codoped rutile tio2. *Journal of Physics: Condensed Matter*, IOP Publishing, v. 25, n. 8, p. 085501, 2013. 74

40 ASCHAUER, U. et al. Influence of subsurface defects on the surface reactivity of tio2: water on anatase (101). *The Journal of Physical Chemistry C*, ACS Publications, v. 114, n. 2, p. 1278–1284, 2010. 75

41 YANG, Y. et al. Superhydrophilic fe3+ doped tio2 films with long-lasting antifogging performance. *ACS Applied Materials & Interfaces*, ACS Publications, v. 13, n. 2, p. 3377–3386, 2021. 75

42 SHAO, C. et al. Nickel-enhanced electrochemical activities of shape-tailored tio2 {001} nanocrystals for water treatment: A combined experimental and dft studies. *Electrochimica Acta*, Elsevier, v. 376, p. 138066, 2021. 75

43 PHAM, T. A.; PING, Y.; GALLI, G. Modelling heterogeneous interfaces for solar water splitting. *Nature materials*, Nature Publishing Group UK London, v. 16, n. 4, p. 401–408, 2017. 76

44 XU, H. et al. Splitting water on metal oxide surfaces. *The Journal of Physical Chemistry C*, ACS Publications, v. 115, n. 40, p. 19710–19715, 2011. 77

45 GHUMAN, K. K. Mechanistic insights into water adsorption and dissociation on amorphous tio2-based catalysts. *Science and Technology of Advanced Materials*, Taylor & Francis, v. 19, n. 1, p. 44–52, 2018. 77

4

$Influence\ of\ Strain\ Effect\ and\ TiO_2(h\ k\ l)$ $on\ the\ Structural\ and\ Electronic$ $Properties\ of\ Pt(1\ 1\ 1)/TiO_2\ (h\ k\ l)$ $Interfaces$

4.1 Abstract

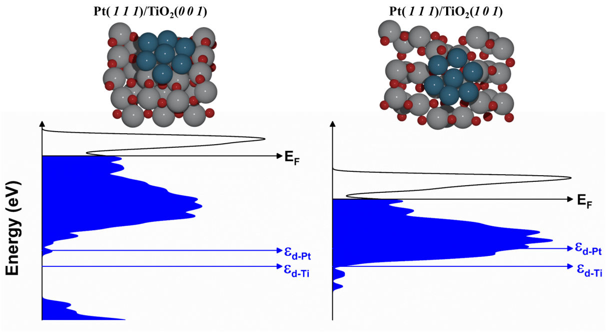

The $Pt(1\ 1\ 1)/TiO_2(h\ k\ l)$ interface has photocatalytic potential for hydrogen evolution reactions (HER), which has been extensively explored. However, the influence of the strain effects a $TiO_2(h\ k\ l)$ phase within this interface remains a considerable subject for comprehension. In this context, we studied $Pt(1\ 1\ 1)/TiO_2(h\ k\ l)$ interfaces through a combination of experimental and theoretical methods. The $Pt(1\ 1\ 1)/TiO_2(h\ k\ l)$ interfaces were characterized through X-ray diffraction (XRD) using Rietveld refinement, where different planes were observed for the phases, such as $TiO_2(1\ 0\ 1)$, $TiO_2(0\ 0\ 1)$ and $Pt(1\ 1\ 1)$. From the refinement, the deformation in the phase was analyzed through the $\mu strain$, where the TiO_2 phase is prone to suffer greater deformation than the Pt phase. This can be evidenced by $\mu strain_{TiO_2} > \mu strain_{Pt}$ and the bulk modulus (B_0), where $B_{0-Pt} > B_{0-TiO_2}$. Therefore, the strain along the

$Pt(1\ 1\ 1)/TiO_2(h\ k\ l)$ interface can be induced by the Pt phase. The electronic properties of the $Pt(1\ 1\ 1)/TiO_2(h\ k\ l)$ interface were carried out using DFT/Plane waves calculations. The PDOS behavior of the $Pt(1\ 1\ 1)/TiO_2(h\ k\ l)$ showed a new state between valence and conduction bands, with the largest contribution of the $Pt-5d$ state. The behavior of the d-band demonstrated that the $Pt(1\ 1\ 1)/TiO_2(0\ 0\ 1)$ interface has antibonding states below the Fermi energy, while the $Pt(1\ 1\ 1)/TiO_2(1\ 0\ 1)$ interface has antibonding states above the Fermi energy. We propose that the $Pt(1\ 1\ 1)/TiO_2(1\ 0\ 1)$ interface exhibits better photocatalytic activity compared to the $Pt(1\ 1\ 1)/TiO_2(0\ 0\ 1)$ interface due to the improved electronic properties induced by the strain along the $Pt(1\ 1\ 1)/TiO_2(h\ k\ l)$ interface, and the behavior of the d-band.

Keywords: Rietveld refinement, DFT, $Pt(1\ 1\ 1)/TiO_2(h\ k\ l)$ interface, materials modeling.

4.2 Experimental and Theoretical

4.2.1 Materials Preparation

The $Pt(1\ 1\ 1)/TiO_2(h\ k\ l)$ interface was synthesized using the Pechini method [1] The precursors used were citric acid (Synth PA), ethylene glycol (Mallinckrodt), and titanium (IV) isopropoxide ($Ti[OCH(CH_3)_2]_4$/Sigma - Aldrich) for the TiO_2 phase precursor and hexahydrate chloroplatinic acid ($H_2PtCl_6 \cdot H_2O$/Sigma - Aldrich) for Pt precursor. All reagents used presented analytical purity.

The primary solution was obtained by dissolving the metal precursor in the ethylene glycol under stirring at 70 ºC. Then, citric acid was then added. After complete dissolution and obtaining a homogeneous solution, the solution was heated at 110 ºC for an hour to undergo polyesterification, resulting in a gel-like solution calcined at 500 ºC for two hours. Thus, the obtained material was in the form of powder, and it could be characterized.

4.2.2 Materials Characterization

The $Pt(1\ 1\ 1)/TiO_2(h\ k\ l)$ interface was characterized through X-ray diffraction analysis using a Rigaku Demax/2500 PC diffractometer, where the used source is Cu - Kα radiation (λ = 0.154 nm). The analysis covered 2θ degree range of 10° to 130°, employing a step increment and time of 0.01° and 0.1 s, respectively. The crystallographic phases were determined through

Rietveld refinement [2] implemented in the General Structure Analysis System II (GSAS-II) software [3]. The initial mathematical representation of Rietveld refinement and subsequent formulations, as described in previous studies [4], formulated that the diffraction peak width is a function of the d-spacing and diffraction angle. Hence, for peaks characterized near the diffraction angle, distinct variations in their widths become apparent. The variations in the experimental data are characterized using the peak profile function introduced by Stephens [5]. Therefore, variations in half-widths of reflections indicating anisotropic effects were noted, and to elucidate these effects, a model proposed by Larson and von Dreele [6] was employed.

The International Center for Diffraction Data (ICDD) database was used to characterize the crystalline phases. Additionally, to compensate for the line broadening due to instrumental effects, employed the following method:

$$\beta^2 = (\beta^2_{Exp} - \beta^2_{Standard}), \tag{4.1}$$

where β_{Exp} is the full-width at half-maximum (FWHM) of the peak, $\beta Standard$ was obtained from standard LaB_6 powder (SRM660-National Institute of Standard Technology) using the Caglioti equation [7]:

$$\beta_{Standard} = (Utan\theta^2 + Vtan\theta + W)^{\frac{1}{2}}. \tag{4.2}$$

The lattice parameters determined through Rietveld refinement were used to calculate the electronic properties for the TiO_2-anatase and platinum unit cells, which also used to proposed the theoretical model for $Pt(1\ 1\ 1)/TiO_2(h\ k\ l)$ interface.

4.2.3 Computational details

All theoretical calculations were conducted using density functional theory [8, 9] plane-wave (DFT/PW) calculation implemented on the Quantum-ESPRESSO package [10]. The exchange-correlation interactions were described by Perdew and Wang [11] (P W91) functional to calculate the energies used in calculating the bulk modulus. The electronic properties were calculated using the exchange-correlation interactions described by the functional developed by Perdew-Burke-Ernzerhof [12] (PBE) and ultrasoft pseudopotentials proposed by Vanderbilt [13], with electrons from O ($2s$, $2p$), Ti ($3s$, $3p$, $4s$, $3d$), and Pt ($4f$, $5d$, $6s$) shells explicitly included. We performed the optimization convergence test of the system, and the plane-wave basis set the cutoff for the smooth wave functions was 55 Ry. The electronic structure calculations were carried out using a DFT/PBE+U approach with the Hubbard correction. We use the value of U_{eff} = 3.5 eV for d-Ti and p-O [14], considering DFT/PBE+U_d+U_p. For the Brillouin zone, integrations were performed 4 x 4 x 2 k-points (Pt(*1 1 1*)/TiO_2(*0 0 1*) interface), and 6 x 4 x 2 k-points (Pt(*1 1 1*)/TiO_2(*1 0 1*) interface) mesh sampling based on the Monkhorst-Pack scheme [15]. The Pt(*1 1 1*)/TiO_2(*h k l*) interface was simulated from a 3 x 2 slab constructed for the (*1 0 1*) and (*0 0 1*) planes with 78 atoms of the anatase TiO_2 phase and 7 atoms of the platinum phase in the plane (*1 1 1*) considering a maximum fraction of approximately 60% of the TiO_2 phase and 40% of the Pt phase determined in the Rietveld refinement.

The d-band structure analysis, was calculated from Projected Density of States (PDOS) for Ti and Pt d-band center, where d-band center (ϵ_d) can be calculated from:

$$\epsilon_d = \frac{\int_{-\infty}^{E_F} E_{(n_d)}(E)dE}{\int_{-\infty}^{E_F} n_d(E)dE}, \tag{4.3}$$

where $n_d(E)$ is e density of states of Ti and Pt d-orbitals, obtained from PDOS.

The charge density difference (Δn_d) was calculated according to equation:

$$\Delta n_d = \Delta n_{d(AB)} - \Delta n_{d(A)} - \Delta n_{d(B)}, \tag{4.4}$$

where $\Delta n_{d(AB)}$ is charge density of the Pt(*1 1 1*)/TiO_2(*h k l*) interface, $\Delta n_{d(A)}$ is charge density of the isolated Pt(*1 1 1*), and $\Delta n_{d(B)}$ charge density of the isolated TiO_2(*h k l*). The adsorption energy (E_{ads}) of the Pt(*1 1 1*) onto TiO_2(*h k l*) was according to equation:

$$E_{ads} = E_{sys} - E_A - E_B, \tag{4.5}$$

where E_{sys} is the energy of the Pt(*1 1 1*)/TiO_2(*h k l*) interface; E_A is the energy of the isolatedPt(*1 1 1*) calculated using the same protocol and E_B is the energy of the isolated TiO_2(*h k l*).

4.3 Results and discussion

4.3.1 Characterization and properties structural

The crystalline characterization phases and structural properties of the Pt(*1 1 1*)/TiO_2(*h k l*) interface were studied by XRD and Rietveld refinement, Figure 12.

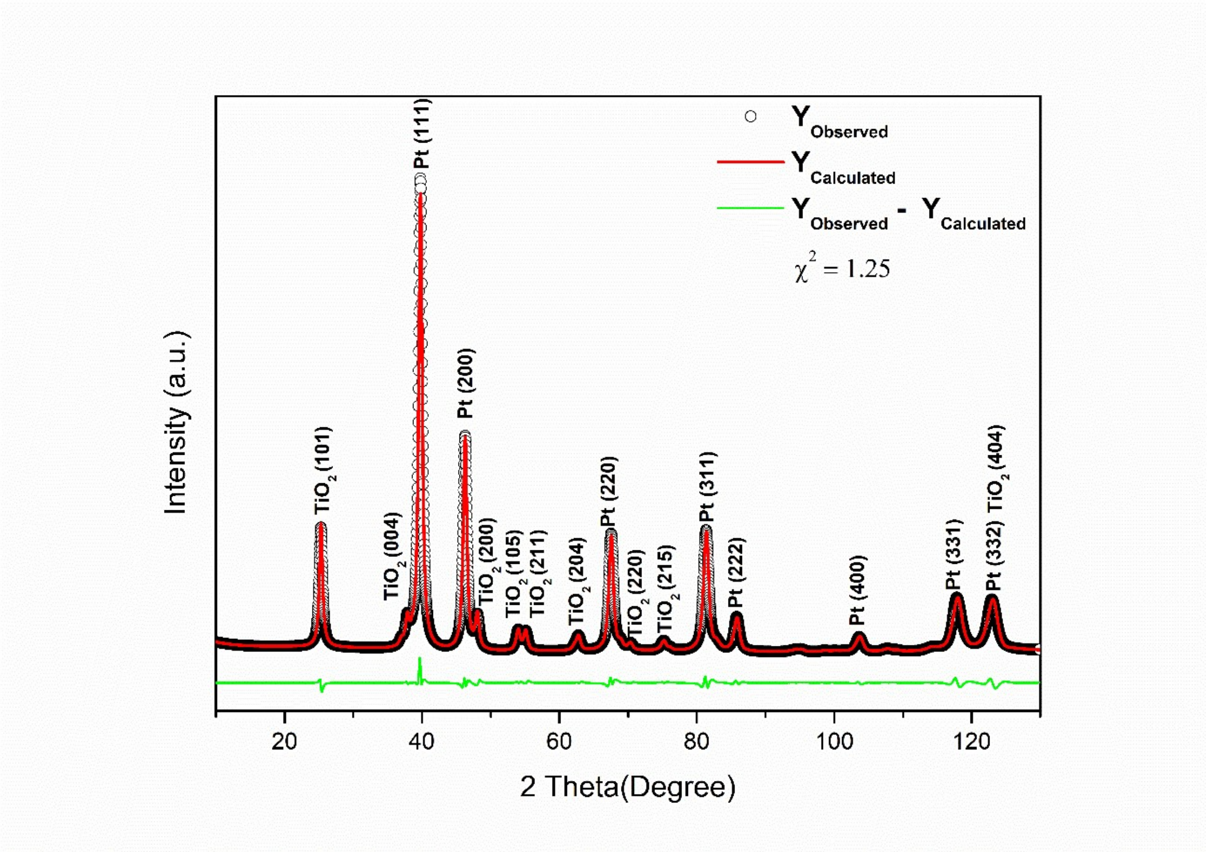

Figure 12 – XRD and Rietveld refinement pattern for Pt/TiO_2 crystalline phases.

Also, cartesian coordinates of TiO_2 and Pt crystalline phases obtained from Rietveld refinement were presented in annex B1-supplementary information Table 10 and Table 11. As observed, the reflections set correspond to two different crystalline phases of TiO_2 and Pt, whereas XRD patterns showed the TiO_2 reflections at 25.2978 *(1 0 1)-hkl* plane, 37.6865 *(0 0 4)-hkl* plane, 48.0438 *(2 0 0)-hkl* plane, 53.9373 *(1 0 5)-hkl* plane, 55.2413 *(2 1 1)-hkl* plane, 62.7398 *(2 0 4)-hkl* plane, 70.2382 *(2 2 0)-hkl* plane, 75.1285 *(2 1 5)-hkl* plane, and 123.0532 *(4 0 4)-hkl* plane related to TiO_2 – anatase crystalline phase (TiO_2 – CIF ICSD 93098). Furthermore, reflections at 39.7178 *(1 1 1)-hkl* plane, 46.2382 *(2 0 0)-hkl* plane, 67.4796 *(2 2 0)-hkl* plane, 81.4984 *(3 1 1)-hkl* plane, 85.7366 *(2 2 2)-hkl* plane, 103.3416 *(4 0 0)-hkl* plane, 117.6865 *(3 3 1)-hkl* plane, and 123.0532 *(3 3 2)-hkl* plane related to Pt crystalline phase (Pt - CIF ICSD 243678). The structural and statistical parameters related to the Rietveld refinement, shown in Figure 12, are presented in Table 4. The acceptance of refinement data depends on whether the weighted index (R_{wp}) is lower than 10% [16] and the variance between the observed values and the values expected under the model in question (χ^2) is lower than two [16]. Therefore, the Rietveld refinement for the Pt/TiO_2 interface agreed with Rietveld proceedings.

As shown in Table 13, lattice parameters (a, b, c,α, β, and γ) were in agreement with

Table 4 – Structural and statistical parameters using Rietveld refinement for Pt/TiO_2 materials.

Parameters/phase	Tetragonal/Anatase - TiO_2	Cubic/Pt
a/Å	3.77891(11)	3.91492(3)
b/Å	3.77891 (0)	3.91492 (0)
c/Å	9.4799(5)	3.91492 (0)
$\alpha = \beta = \gamma$ /degrees	90.0	90.0
V/Å^3	135.374(9)	60.0026(15)
Particle size/nm	12.81	12.43
Wt. Fraction	0.59919	0.40081
χ^2	1.25	
R(F2)	0.0211	
wRp	0.0451	
GOF	1.16	

those values obtained for file card CIF - ICSD 93098 for anatase TiO_2 - tetragonal crystalline phase (space group I41/amdZ, $a = b = 3.7840(7)$ Å, $c = 9.500(2)$ Å, and $\alpha = \beta = \gamma = 90.0°$) and file card CIF - ICSD 243678 for Pt - cubic crystalline phase (space group Fm-3m, $a = b = c = 3.92316(2)$ Å, and $\alpha = \beta = \gamma = 90.0°$). Furthermore, particle size and $\mu strain$ were evaluated as described below.

The constant wavelength (CW) profile implemented into the $GSAS - II$ routine uses a pseudo-Voigt convolution and asymmetry function and the microstrain broadening description of Stephens *et al.* [5]. The Gaussian broadening of the peak (σ^2) modifies with 2θ as:

$$\sigma^2 = Utan^2\theta + Vtan\theta + W, \tag{4.6}$$

where U, V, and W are the coefficients described by Caglioti *et al.* [7], and the Lorentzian broadening will follow,

$$\gamma = \frac{X}{cos\theta} + Ytan\theta, \tag{4.7}$$

where for which the two terms accommodate potential sample crystallite size and microstrain broadening, respectively. Therefore, the particle size broadening can be calculated from:

$$\frac{\Delta d}{d^2} = \frac{\Delta 2\theta cot\theta}{d} = constant, \tag{4.8}$$

from Bragg's law, then:

$$\frac{\Delta d}{d^2} = \frac{2\Delta 2\theta cot\theta sin\theta}{\lambda}, \tag{4.9}$$

thus, the broadening is:

$$\frac{\lambda \Delta d}{2d^2 cos\theta} = \Delta 2\theta, \tag{4.10}$$

where the term $\Delta d/d^2$ is related to the Lorentzian broadening (X).

It is possible to notice in Table 13 that the particle size is 12.81 nm and 12.43 nm for TiO_2 and Pt crystalline phases, respectively. Kibis *et al.* [17] studied Pt/TiO_2 activity in low-temperature ammonia oxidation. Moreover, the authors also performed Rietveld refinement for Pt/TiO_2 samples. According to the authors [17], Pt/TiO_2 samples were obtained from two methods, which presented 4.7 nm and 18.8 nm. Particle sizes vary from 4 nm up to 20 nm, also shown in the literature [18–20]. Therefore, the lattice parameters and particle size presented herein agree with the literature.

The structural behavior of the $Pt(1\ 1\ 1)/TiO_2(h\ k\ l)$ interface was also studied through the microstrain ($\mu strain$) behavior of the Pt and TiO_2 phases and the bulk modulus behavior fitted from an equation of states (EOS), as shown in Figure 13a-d.

The $\mu strain$ is observed through non-uniform lattice distortions, which create deviations in the d-spacing on a plane, resulting in peak broadening in the diffraction pattern [21, 22]. The 3D graphical representation of $\mu strain$ is obtained through the S_{hkl} values from the Rietveld refinement. The $\mu strain$ along the [$h\ k\ l$]–direction be calculated from [5]:

$$S_s(hkl) = \frac{\pi d^2}{18000}\Gamma_s^2, \tag{4.11}$$

where Γ_s^2 for a cubic symmetry (Pt – phase) is:

$$\Gamma_c^2 = S_{400}(h^4 + k^4 + l^4) + 3S_{220}(h^2k^2 + h^2l^2 + k^2l^2), \tag{4.12}$$

and for a tetragonal symmetry (TiO_2 – phase) is:

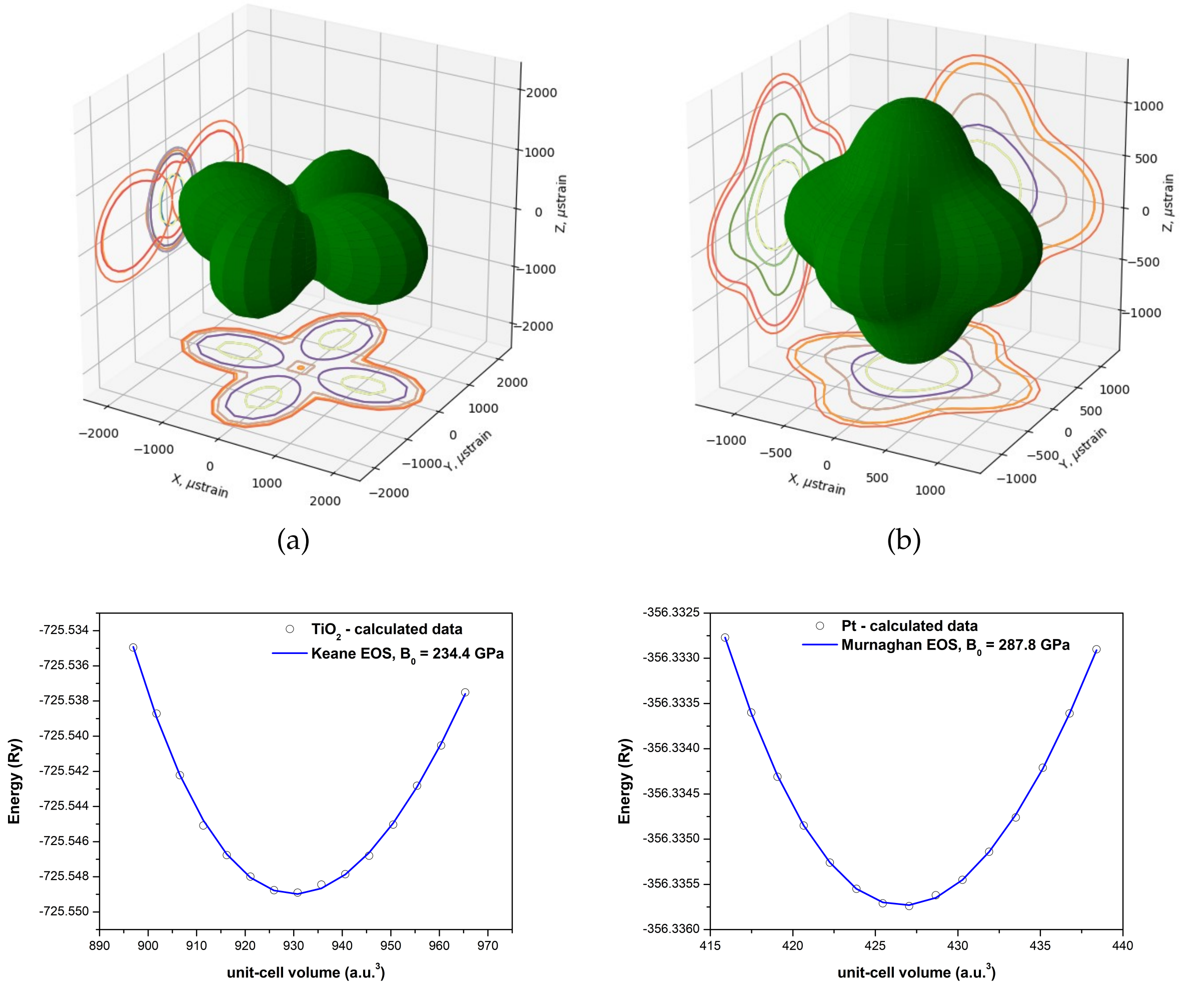

(a) (b)

(c) (d)

Figure 13 – $\mu strain$ contour plots obtained using Stephen's anisotropic strain model in GSAS-II package. The size of each volume represents the overall $\mu strain$ from (a) TiO_2 with projection for [1 0 1] direction and (b) Pt with projection for [1 1 1] direction. Equation of state (EOS) from DFT - data Murnaghan and Keane fitting for (c) TiO_2 and (d) Pt.

$$\Gamma_T^2 = S_{400}(h^4 + k^4) + S_{004}(l^4) + 3S_{220}(h^2l^2) + 3S_{202}(h^2l^2 + k^2l^2), \tag{4.13}$$

where S_{HKL} are parameters adjustable from Rietveld refinement and restricted by phase's symmetry.

In Figure 13a, it is possible to observe the $\mu strain$ for the TiO_2 phase with projection in the [*1 0 1*] direction, which presents a tetragonal system with anisotropic strain parameters S_{400}, S_{004}, S_{220}, and S_{202}. The maximum values found for the TiO_2 phase $\mu strain$ in Figure 13a were on the order of $2x10^3$ in the x and y axes. Muregesan *et al.* [23] studied the anatase TiO_2 phase at different temperatures synthesized via sol-gel route and analyzed the $\mu strain$ using the Rietveld refinement. A ccording to the authors [23], at 773 K observed, a maximum value of the $\mu strain$ of $5x10^3$ in the x and y axes, and 873 K of $10x10^3$ in the x, y, and z axes. The current study agrees with the experimental results observed at 773.15 K (500 ºC) of the $\mu strain$ values as described by the authors [23]. It is possible to notice the absence of $\mu strain_{(TiO_2)}$ z-axis projections, which can be analyzed by parameters S_{400} > > S_{004}, suggesting that the TiO_2 crystallite is anisotropic. In Figure 13b shows the 3D $\mu strain$ for the Pt phase with projection in the [*1 1 1*], which presents a cubic system with parameters S_{400} and S_{220}. T he maximum values found for the Pt phase $\mu strain$ in Figure 13b were on the order of $1x10^3$ in the x and y axes. As observed in Figures 13a-b, the magnitude of $\mu strain$ is different in the TiO_2 and Pt phases ($\mu strain_{(TiO_2)}$ > $\mu strain_{Pt}$), indicating bigger deformation and defects in the TiO_2 phase caused by the Pt phase.

As exposed above, the TiO_2 and Pt phases exhibited deformation, with $\mu strain_{(TiO_2)}$ > $\mu strain_{Pt}$. However, materials can exhibit two stress types: tensile and compressive strain. Thus, modifying the lattice parameters of materials is possible from the fully relaxed geometry to the tensile and compressive deformation. In this sense, obtaining a graph of energy vs. lattice volume from the modification is possible, which generates a quasi-parabolic graph that can be adjusted using an equation of state (EOS). The chosen EOS must have parameters for a specific material, such as properties obtained under the same synthesis experimental condition or proximity. Therefore, the EOS is defined as the relationship between energy and lattice volume that describes the behavior of materials under tension and compression. The simplest approach for an isothermal EOS is in terms of the bulk modulus (B_0), defined as the ability to resist volume variation with uniform stress and compression deformation.

The anisotropic microstrain ($\mu strain$) behavior observed for the TiO_2 and Pt phases can be discussed in light of the B_0 values [24, 25] shown in Figures 13c-d. It is possible to notice in Figure 13c that the B_0 value for the TiO_2 phase is 234.4 GPa, adjusted by the equation developed by Keane [26], and in Figure 13d, the B_0 value for the Pt phase is 287.8 GPa, adjusted by the equation developed by Murnaghan [27]. The bulk modulus (B_0) of a given material can be described as:

$$B_0 = -V \left(\frac{\partial P}{\partial V} \right)_T , \tag{4.14}$$

where B_0 represents the resistance of the material to isotropic compression [28]. Murnaghan proposed the following equation:

$$P = \frac{B_0}{B_0^{'}}\left[\left(\frac{V_0}{V}\right)^{B_0^{'}} - 1\right], \tag{4.15}$$

where V_0 is the equilibrium volume. Keane assumptions that pressure can be expressed with a power series on the deformation of the material following the expression:

$$\frac{P}{B_0} = \frac{B_0^{'}}{(B_\infty^{'})^2}\left[\left(\frac{V_0}{V}\right)^{B_0^{'}} - 1\right] - \left(\frac{B_0^{'}}{B_\infty^{'}} - 1\right) ln\frac{V_0}{V} \tag{4.16}$$

where $B_0^{'} - 1 > B_\infty^{'} > B_o^{'}/2$ and $B_0^{'}= B_\infty^{'}$ the above equation reduces to the Murnaghan equation. TiO_2 and Pt are distinct materials with different crystal structures, bonding characteristics, and responses to compression and tesion. Thus, the use of different EOS reflects the distinct characteristics of each phase.

Dong *et al.* [29] studied the structural transformation of the anatase TiO_2 phase using synchrotron X-ray diffraction and Raman spectroscopy under different pressures. The authors [29] used the Birch-Murnaghan equation of state to fit the experimental values and obtained a B_0 value of 243 GPa for anatase TiO_2 nanoparticles. Similarly, Pischedda *et al.* [30] used X-ray diffraction and Raman spectroscopy under different pressures to study the structural stability of the anatase TiO_2 phase. The authors [30] also used the Birch-Murnaghan equation state to fit the experimental data and obtained a B_0 value of 237 GPa. Çagin *et al.* [31] studied the mechanical and thermal properties of the transition metals with a face-centered cubic structure. According to the authors [31], by varying the temperature from 300 K to 1500 K and monitoring the B_0 values, a decrease in values was observed, and a value of 256.24 GPa was reported for Pt at 300 K. However, an experimental value of B_0 for Pt of the 278.3 GPa can be found [32]. The choice of EOS should provide parameters for a specific material, such as properties obtained under the same synthesis conditions or proximity. It is important to note that the B_0 obtained for TiO_2 and Pt phases are close experimental values reported in the literature. In order to study the pressure as a function of the volume, the TiO_2 and Pt phases was analyzed a pressure vs. unit-cell volume as shown in Figure 14.

It is possible to notice in Figure 14a-b that the increase of the pressure leads to a decrease in the values of unit-cell volume for both TiO_2 and Pt phases. The smaller unit-cell volume is related to the shorter bond length, leading to a compressed structure and volume with increased pressure [33, 34]. The rate of volume changing can be observed by first-order exponential decay fitting in Figure 14a-b, where the decay constant for TiO_2 and Pt were $t_{(1-TiO_2)}$ = 64.891 (R^2 = 0.9999) and Pt $t_{(1-Pt)}$ = 35.029 (R^2=0.9999). Thus, the TiO_2 phase presented a

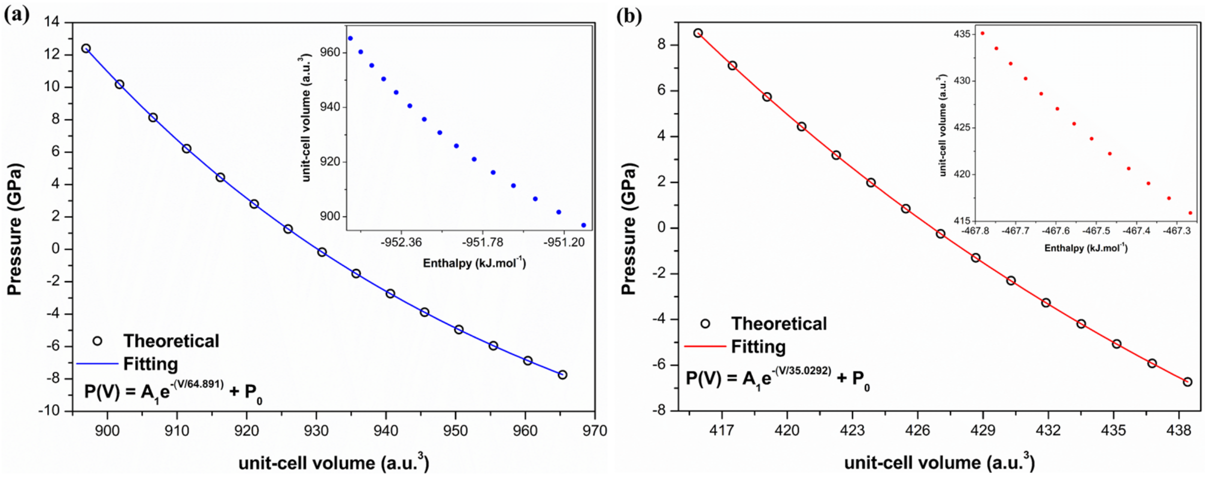

Figure 14 – Pressure as a function of unit-cell volume with first-order exponential decay of materials a) TiO_2 and b) Pt.

bigger volume change rate than the Pt phase. The analysis enthalpy (H) plays a pivotal role in determining structural and electronic properties in materials. It is possible to observe that at minimum energy volume, the TiO_2 phase presented $H_{(V_0 TiO_2)}$ = -952.2 $kJ.mol^-1$, and the Pt phase presented $H_{(V_0 Pt)}$ = -467.6 $kJ.mol^-1$. The TiO_2 phase presented in the literature an $\Delta_f H^0_{(solid-anatase/TiO_2)}$= -938.72 $kJ.mol^-1$ [35], and the Pt phase is well defined that $\Delta_f H^0_{(Pt-c)}$ = 0 $kJ.mol^{-1}$ [36]. However, it is possible to find the binding energies of the one Pt atom in the metal cluster of the 420-480 $kJ.mol^{-1}$ [37]. Therefore, the TiO_2 phase provides a bigger enthalpy variation (ΔH) than the Pt phase, in which $\Delta H_{(TiO_2)}$ = -1.66 $kJ.mol^{-1}$ and ΔH_{Pt} = -0.58 $kJ.mol^{-1}$.

In summary, the TiO_2 phase displays a higher susceptibility to deformation its crystalline structure when compared to the Pt phase. This observation is consistent with the results obtained from $\mu strain$ ($\mu strain_{(TiO_2)} > \mu strain_{Pt}$) and bulk modulus ($B_{(0-TiO_2)}$<$B_{(0-Pt)}$). Consequently, at the $Pt(1\ 1\ 1)/TiO_2(h\ k\ l)$ interface, the TiO_2 phase undergoes stress induced by the Pt phase, in which the TiO_2 phase has a bigger volume change rate with $t_{(TiO_2)} > t_{Pt}$ and produces more energy with the volume change ($\Delta H_{(TiO_2)} > \Delta H_{Pt}$). Thus, the stress along the $Pt(1\ 1\ 1)/TiO_2(h\ k\ l)$ interface induced by the Pt phase has the potential to enhance the material's catalytic performance by tuning its electronic and structural properties.

4.3.2 Theoretical model for $Pt(1\ 1\ 1)/TiO_2(h\ k\ l)$ interface

As discussed previously, XDR and Rietveld refinement evidence the formation of the $Pt(1\ 1\ 1)/TiO_2(h\ k\ l)$, where the Pt phase presented reflections at 39.7178 *(1 1 1)-hkl* plane with the biggest intensity and the TiO_2 phase presented reflections at 25.2978 *(1 0 1)-hkl* plane and 37.6865 *(0 0 4)-hkl* plane with the biggest intensity, where wt. fraction of the TiO_2 phase is 60%, and the Pt phase is 40%, approximately. In this sense, DFT analysis was carried out in order to model possible Pt(*1 1 1*)$/TiO_2$(*0 0 1*) and Pt(*1 1 1*)$/TiO_2$(*1 0 1*) interfaces with wt. fraction close to the determined by Rietveld refinement, shown in Figures 15a-b.

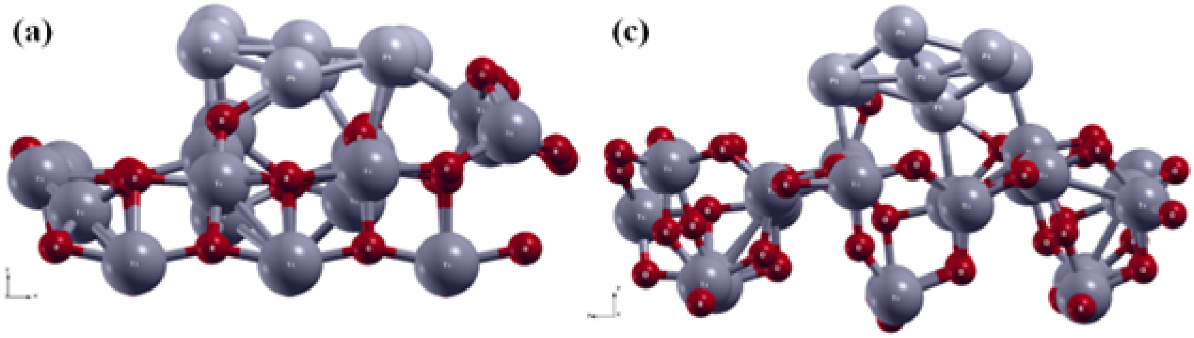

Figure 15 – The optimized structures of (a) Pt(*1 1 1*)$/TiO_2$(*0 0 1*) interface and (b) Pt(*1 1 1*)$/TiO_2$(*1 0 1*) interface.

The Pt - Pt, Pt - O, and Pt - Ti bond lengths play a fundamental role in the structural and electronic properties of the Pt(*1 1 1*)$/TiO_2$(*h k l*) interface. Thus, analyzing bond length variation between atoms at the interface is pivotal to probing the interface behavior. All the bond lengths of the optimized structures of the Pt(*1 1 1*)$/TiO_2$(*h k l*) interface can be seen in Table 12 in the annex B1-supplementary information. It is possible to observe that the Pt - Pt bond length on the Pt_7 phase varies from 2.5186 Å up to 2.8105 Å for Pt(*1 1 1*)$/TiO_2$(*0 0 1*) and Pt(*1 1 1*)$/TiO_2$(*1 0 1*) interface. A similar Pt - Pt bond length was reported in the literature, such as varied between 2.50 Å to 2.80 Å [38–41]. The Pt(*1 1 1*)$/TiO_2$(*0 0 1*) interface presented only one Pt - O bond with 2.0811 Å length, and the Pt(*1 1 1*)$/TiO_2$(*1 0 1*) interface presented two Pt - O bond with 2.0094 and 2.1374 length. However, the Pt(*1 1 1*)$/TiO_2$(*0 0 1*) interface presented an 8-fold Pt - Ti bond that varies from 2.3723 up to 2.7775 , which the bond lengths of the Pt atom presented with four-coordinated Ti atom ($Ti - 4c$), five-coordinated Ti atom ($Ti - 5c$), and six-coordinated Ti atom ($Ti - 6c$). The Pt(*1 1 1*)$/TiO_2$(*1 0 1*) interface presented a 3-fold Pt - Ti bond that varies from 2.4752 Å up to 2.7628 Å, which the bond lengths of the Pt atom presented only with six-coordinated Ti atom ($Ti - 6c$). Through DFT calculation of the bonding and electron energy-level alignment at Metal(*0 0 1*)$/TiO_2$(*0 0 1*) interfaces, Chen *et al.* [42] observed a similar length of the Pt - O and Pt - Ti bond presented 2.04 Å and 2.73 Å, respectively. All the bond length observed for Pt(*1 1 1*)$/TiO_2$(*0 0 1*) and Pt(*1 1 1*)$/TiO_2$(*1 0 1*) interface agreed with literature data [38–42].

4.3.3 Electronic properties for $Pt(1\ 1\ 1)/TiO_2(h\ k\ l)$ interface

Platinum (Pt) and titanium dioxide (TiO_2) are well-known and have been previously studied for their electronic properties, mainly in photoelectrochemistry reactions [43]. From structures determined by Rietveld refinement, the TiO_2 presents a semiconductor behavior, with an energy band gap of 3.00 eV, where the experimental energy band gap is 3.20 eV [44], and Pt presents metallic behavior with conduction and valence bands overlapping, see in annex B1-supplementary information Figure 36. The Projected Density of States (PDOS) was performed for the $Pt(1\ 1\ 1)/TiO_2(h\ k\ l)$ interface, as shown in Figure 16.

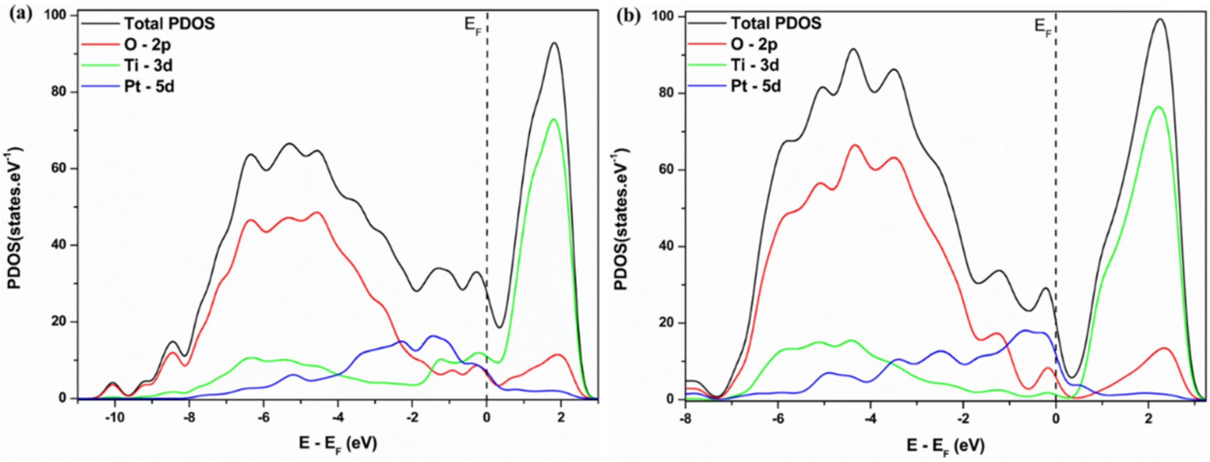

Figure 16 – Projected Density of States (PDOS) (a) $Pt(1\ 1\ 1)/TiO_2(0\ 0\ 1)$ interface and (b) $Pt(1\ 1\ 1)/TiO_2(1\ 0\ 1$ interface.

It is possible to notice in Figure 16a-b that the PDOS behavior is different when compared with the isolate TiO_2 and Pt phases, see in annex B1-supplementary information Figure 36. The TiO_2 phase PDOS is similar to both PDOS in Figure 16a-b, but there is no energy band gap between valence and conduction bands, presenting a metallic behavior. Both PDOS of the phases presented the O - $2p$ state with the largest contribution in the valence band (VB) and the Ti - $3d$ state with the largest contribution in the conduction band (CB). Further, a new state between VB and CB is observed with the largest contribution of the Pt - $5d$ state, which is close to the Fermi energy (E_F). The Pt - $5d$ state in the $Pt(1\ 1\ 1)/TiO_2(0\ 0\ 1)$ interface, Figure 16a, is localized to the smallest energy below E_F close -2.0 eV, while the Pt - $5d$ state in the $Pt(1\ 1\ 1)/TiO_2(1\ 0\ 1)$ interface, Figure 16b, is localized to biggest energy close to 0 eV. Wang *et al.* [45] studied the size effect of the platinum particles on TiO_2 support through DFT. The authors [45] performed PDOS for different $Pt_x/TiO_2(1\ 0\ 1)$, where the $Pt_8/TiO_2(1\ 0\ 1)$ system was observed in Pt - d states below Fermi energy, which suggested a strong interaction between the first layer of the Pt and the TiO_2 support. Tamura *et al.* [46] used the First-principles study to investigate the electronic and structural properties of the Pt/TiO_2 interface. The authors [46] built a unit cell considering the Pt(0 0 1)/TiO_2(0 0 1) interface and calculated the PDOS, where Pt - d states close to the Fermi energy and between VB and CB were observed. Still analyzing the PDOS of the Pt(1 1 1)/TiO_2($h\ k\ l$) interface, Figure 16a-b, the contribution of the O - 2p and Ti - 3d states can be observed close or overlapping the Pt - 5d states within the range of -2 to 0 eV, indicating the formation of the Pt - O, and Pt - Ti bonds, which was discussed previously, the Pt(1 1 1)/TiO_2(0 0 1) interface presented only one Pt - O bond and eight Pt - Ti bonds and the Pt(1 1 1)/TiO_2(1 0 1) interface showed two Pt - O bonds and three Pt - Ti bonds.

The bonds between the atmos of the optimized structure can also be observed in the charge density distribution (Δn) and electron localization function (ELF) of the Pt(1 1 1)/TiO_2($h\ k\ l$) interface, as shown in Figure 17.

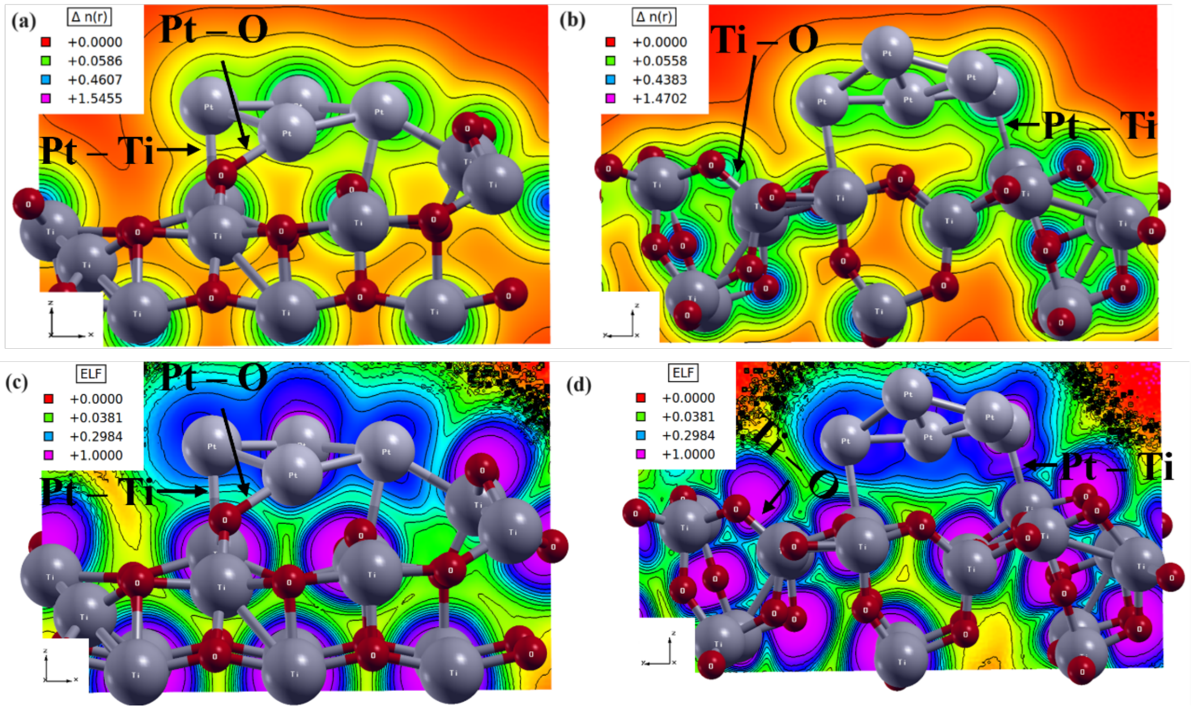

Figure 17 – 2D Charge density distribution (Δn) and electron localization function (ELF) of the (a) - (c) Pt(1 1 1)/TiO_2(0 0 1) interface and (b) – (d) Pt(1 1 1)/TiO_2(1 0 1) interface.

It is possible to observe in Figure 17a-d that the 2D charge density distribution (Δn) and electron localization function (ELF) are located on the oxygen atoms in the TiO_2 phase and located on the Pt atoms in the Pt phase for both systems. The Pt(1 1 1)/TiO_2(0 0 1) interface, Figure 17a, presented a Ti - O bond with a more ionic character than the Pt(1 1 1)/TiO_2(1 0 1) interface, where the value ELF 0.03, Figure 17c. The Pt(1 1 1)/TiO_2(0 0 1) interface, Figure 17b, shows that the Ti - O bond has more covalent character due to the overlapping of the isolines and the value ELF 0.2, Figure 17-d. Further, the o verlapping of the isolines and value ELF is observed between the TiO_2 and Pt phases, evidenced by the Pt - O and Pt - Ti bonds observed in the $Pt(1\ 1\ 1)/TiO_2(h\ k\ l)$ interface in the optimized structures, Figure 15a-b, and PDOS, Figure 16a-b. Still analyzing the charge density distribution (Δn), the $Pt(1\ 1\ 1)/TiO_2(0\ 0\ 1)$ interface, Figure 17a, presented the Δn maximum values (Δn_{max}) about 1.54 and the $Pt(1\ 1\ 1)/TiO_2(0\ 0\ 1)$ interface about 1.47. The difference in the Δn_{max} shows that the electronic behavior of the $Pt(1\ 1\ 1)/TiO_2(h\ k\ l)$ interface changes with the TiO_2 plane.

The charge density distribution (Δn) of the TiO_2 phase is well described in the literature, demonstrating that Δn is accumulated in the oxygen atoms due to the electronegativity values of oxygen and titanium atoms [47](O = 3.5, Ti = 1.32, and Pt = 1.44 on the Pauling scale) [48]. However, the Δn of the $Pt(1\ 1\ 1)/TiO_2(h\ k\ l)$ interface is not well described in the literature, which depends on the kind of the interface studied, like size clusters of the Pt phase, crystalline arrangement of Pt phase or only one Pt atom, and the TiO_2 phase planes. Zhang *et al.* [49] studied the Pt/TiO_2 interface for SO_2 gas sensing through experimental and density functional theory investigation. The authors [49] described the metal/semiconductor interface considering Pt single atom on the TiO_2 ($1\ 0\ 1$) surface and calculated the electronic properties. The charge density of the Pt/TiO_2 interface showed that it accumulated in the oxygen atoms, and the overlapping of the Δn-basins between oxygen and titanium atoms led to a structure of the covalent character. Furthermore, the Pt single atom presented a smooth accumulated of the charge, but this behavior can be associated with the SO_2 molecule adsorbed on the TiO_2 surface. On the other hand, Wu *et al.* [50], investigated Pt cluster on the TiO_2 surface with oxygen vacancies for electrocatalyst hydrogen evolution. The authors [50] studied the $Pt_4/TiO_2(1\ 0\ 1)$ and $Pt_4/TiO_2(1\ 0\ 1)$-O_V interfaces using the DFT and calculated the electronic properties. The Pt_4 cluster used was pyramid-like, and the charge density distribution of the Pt_4/TiO_2(1 0 1)-O_V interface showed a structure with charge density accumulated strength in the oxygen atoms and platinum atoms close to the TiO_2 surface, where the platinum atom further away from TiO_2 surface presented charge density distribution close of the zero. Moreover, the charge density distribution shown in the interface was localized, indicating an ionic character and Δn maximum values of about 0.7. Another kind of Pt/TiO_2 interface was described by Chen *et al.* [42] using density functional theory. The authors [42] built a unit-cell model with $Pt(0\ 0\ 1)$-$fcc/TiO_2(0\ 0\ 1)$ considering two kinds of interface, one with Pt - O bonds interface and with another Pt - Ti bonds interface. The density charge of the interfaces showed the accumulation of the charge in the oxygen atoms and platinum atoms close to the TiO_2 surface for the interface with Pt - O bonds and an increase accumulated of the charge in the titanium atoms and platinum atoms for the interface with Pt - Ti bonds. Therefore, the type of Pt/TiO_2 interface that is studied impacts how the interface can be used in practical applications.

Metal/oxide interfaces, such as Pt/TiO_2, have practical applications in many important catalytic or photocatalytic reactions [51–53]. Therefore, it is essential to analyze the behavior of the d-band, as it plays a fundamental role in the reactivity of metal or alloy surfaces. Table 5 shows the d-band center (ϵ_d) and d-band width (w_d) of the $Pt(1\ 1\ 1)/TiO_2(h\ k\ l)$ interface.

Table 5 – Electronic structure of the d-band projected: d-band center (ϵ_d), d-band width (w_d) and Fermi energy (E_F) of the TiO_2, Pt isolate phase and $Pt(1\ 1\ 1)/TiO_2(h\ k\ l)$ interface.

d-band shape	TiO_2	Pt	$Pt(1\ 1\ 1)/TiO_2(0\ 0\ 1)$		$Pt(1\ 1\ 1)/TiO_2(1\ 0\ 1)$	
	Ti d-band	Pt d-band	Ti d-band	Pt d-band	Ti d-band	Pt d-band
ϵ_d	-7.03	-3.73	-4.40	-2.72	-4.43	-2.48
w_d	4.34	2.27	3.26	1.76	1.46	1.91
E_F	8.64	16.96	7.33		2.78	

The d-band center (ϵ_d) and d-band width (w_d) provide important characteristics of the catalytic process of the system, such as correlating the ϵ_d shifts up of the material with antibonding states above Fermi energy. Analyzing the isolated phases of Pt and TiO_2, it was observed that the ϵ_{d-TiO_2} and ϵ_{d-Pt} were -7.03 eV and -3.73 eV, respectively. However, by coupling the phases and forming the $Pt(1\ 1\ 1)/TiO_2(h\ k\ l)$ interface, there was a shift in the ϵ_d value towards more positive values. At the $Pt(1\ 1\ 1)/TiO_2(0\ 0\ 1)$ interface, the energy levels of $\epsilon_{(d-TiO_2)}$and $\epsilon_{(d-Pt)}$ were found to be -4.40 eV and -2.72 eV, respectively. The ϵ_d values were below the Fermi energy level, which indicates that the antibonding states are also below the Fermi energy. In contrast, at the $Pt(1\ 1\ 1)/TiO_2(1\ 0\ 1)$ interface, the $\epsilon_{(d-TiO_2)}$ and $\epsilon_{(d-Pt)}$ values were -4.43 eV and -2.48 eV, respectively, with the ϵ_d values closer the Fermi energy level, which indicates the possibility that the antibonding states are above the Fermi energy. Therefore, the $Pt(1\ 1\ 1)/TiO_2(1\ 0\ 1)$ interface can present the most significant trend in the activity of some catalytic processes than the $Pt(1\ 1\ 1)/TiO_2(0\ 0\ 1)$ interface, once that d-band center upshift lead to a stronger interaction adsorbate-surface. Zhou *et al.* [54] investigated the Pt/TiO_2 interface for CO molecule oxidation, monitoring the crystal facets of TiO_2. The authors [54] using the operando XAS/DRIFT and DFT studies, related the CO oxidation activity in the order$Pt(1\ 1\ 1)/TiO_2(1\ 0\ 1)$ > $Pt(1\ 1\ 1)/TiO_2(1\ 0\ 0)$ > $Pt(1\ 1\ 1)/TiO_2(0\ 0\ 1)$. Zhang *et al.* [55], studied the morphology and facets dependent on the TiO_2 phase in the Pt/TiO_2 interface. According to the authors [55], the activity CO conversion with water gas shift following the order $Pt(1\ 1\ 1)/TiO_2(1\ 0\ 0) \approx Pt(1\ 1\ 1)/TiO_2(1\ 0\ 1)$ > $Pt(1\ 1\ 1)/TiO_2(0\ 0\ 1)$. On the other hand, Wu *et al.* [56], studied the Pt/TiO_2 interactions with different facets of the TiO_2 for hydrodeoxygenation (HDO) of *m*-cresol. The authors [56] used experimental and theoretical approaches and proposed that the *CO* chemisorption and adsorption, which is correlated with the HDO reactions, follow the order $Pt(1\ 1\ 1)/TiO_2(1\ 0\ 0)$ > $Pt(1\ 1\ 1)/TiO_2(0\ 0\ 1)$ > $Pt(1\ 1\ 1)/TiO_2(1\ 0\ 1)$ of the encapsulation degree. Chen *et al.* [57], investigated the facet-engineered TiO_2 drives photocatalytic activity and Pt/TiO_2 interface stability. According to the author [57], the $Pt/TiO_2(0\ 0\ 1)$ and $Pt/TiO_2(1\ 0\ 1)$ interfaces are very much alike for use as catalysts for hydrogen evolution reaction, with proton adsorption energy small for both interfaces. However, the $Pt/TiO_2(1\ 0\ 1)$ interface is superior to the $Pt/TiO_2(0\ 0\ 1)$ interface for catalysts for oxygen evolution reaction.

The catalytic or photocatalytic activity of the $Pt(1\ 1\ 1)/TiO_2(h\ k\ l)$ interface depends on the type of reaction being studied. The reactivity of the interface is related to the presence of oxygen vacancies, which is a pivotal parameter towards improving catalytic or photocatalytic reactions [58, 59]. However, the catalytic or photocatalytic characteristic can be discussed in light of the d-band shape of the interface, as discussed previously with the d-band center (ϵ_d), and one can relate the ϵ_d shift with d-band width (w_d), also shown in Table 5. The isolated phases of TiO_2 and Pt presented $w_{(d-TiO_2)}$ and $w_{(d-Pt)}$ of 4.34 eV and 2.27 eV, respectively. For both $Pt(1\ 1\ 1)/TiO_2(h\ k\ l)$ interfaces, the w_d values decrease, whereas the $Pt(1\ 1\ 1)/TiO_2(0\ 0\ 1)$ interface, the w_d values of $w_{(d-Ti)}$ and $w_{(d-Pt)}$ were found to be 3.26 and 1.76, respectively. However, at the $Pt(1\ 1\ 1)/TiO_2(1\ 0\ 1)$ interface, the $w_{(d-TiO_2)}$ was smaller and $w_{(d-Pt)}$ slightly bigger, with values of 1.46 and 1.91, respectively. The $Pt(1\ 1\ 1)/TiO_2(1\ 0\ 1)$ interface d-band center (ϵ_d) is near the Fermi energy level than $Pt(1\ 1\ 1)/TiO_2(0\ 0\ 1)$ interface, which can be related to interfaces w_{d-Pt} with different values. Kolb *et al.* [60] presented, from the study about the strain in palladium materials, that an increase in the w_d causes the ϵ_d to shift towards the Fermi energy level, while a decrease in the w_d causes the ϵ_d to shift below the Fermi energy level. Therefore, the catalytic or photocatalytic behavior of the $Pt(1\ 1\ 1)/TiO_2(h\ k\ l)$ interface is influenced not only by the presence of oxygen vacancies but also by the intricate interplay of d-band characteristics. The $Pt(1\ 1\ 1)/TiO_2(1\ 0\ 1)$ interface tends to exhibit essential characteristics in reactions where states above the Fermi level are determining steps. However, the $Pt(1\ 1\ 1)/TiO_2(0\ 0\ 1)$ interface is better suited for reactions requiring stable bonding due to the possible presence of antibonding states below the Fermi level.

In order to understand the interfacial interactions between the $Pt(1\ 1\ 1)$ phase and $TiO_2(h\,k\,l)$ phase, the charge density difference (Δn_d), charge transfer (Δq), and the adsorption energy (E_{ads}) were calculated, as shown in Figure 18a-b.

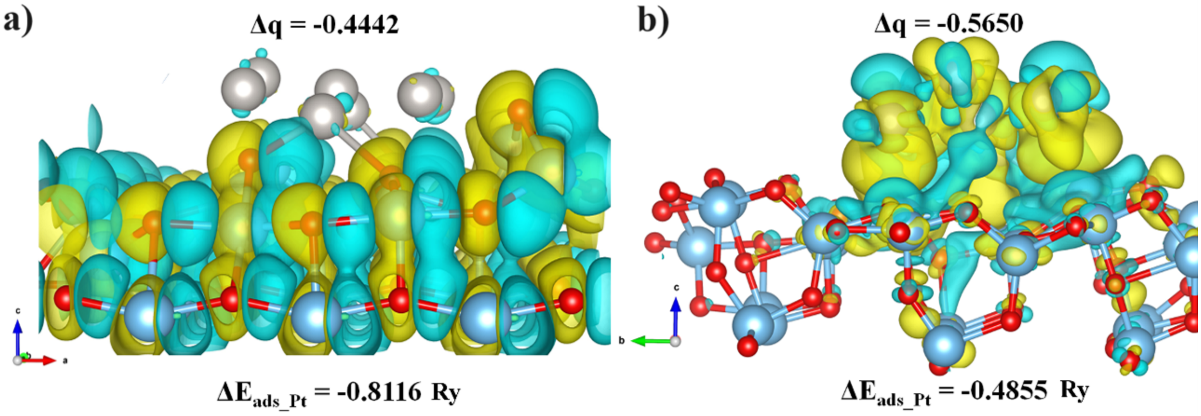

Figure 18 – Charge density difference (Δn_d) of (a) $Pt(1\,1\,1)/TiO_2(0\,0\,1)$ interface and (b) $Pt(1\,1\,1)/TiO_2(1\,0\,1)$. The yellow isosurface is the electron depletion region, and the cyan isosurface is the electron accumulation region, where the isosurface value is (a) 0.001 electron $Bohr^{-1}$ and (b) 0.003 electron $Bohr^{-1}$. $\Delta q/10^4$ represents charge transfer denoted in electrons, and ΔE_{ads} (Ry) represent the adsorption energy of the Pt phase.

Figure 18a indicates that the electron depletion and accumulation regions in the $Pt(1\,1\,1)/TiO_2(0\,0\,1)$ interface occur mainly in the TiO_2 phase. On the other hand, Figure 18b shows that in the same interface, the electron depletion region is localized to the $Pt(1\ 1\ 1)$ phase, whereas the electron accumulation region is localized to the $Pt(1\ 1\ 1)/TiO_2(1\ 0\ 1)$ interface region. Therefore, the electron (e^-) injection in the $Pt(1\,1\,1)/TiO_2(0\,0\,1)$ interface occur between Ti - O bond of the $TiO_2(0\,0\,1)$ with a charge transfer ($\Delta q/10^4$) of the 0.4442 e^-, and in the $Pt(1\,1\,1)/TiO_2(1\,0\,1)$ interface about 0.5650 e^- is transferred from $TiO_2(1\,0\,1)$ phase to $Pt(1\,1\,1)$phase. The adsorption energy (ΔE_{ads}) on the $Pt(1\,1\,1)/TiO_2(0\,0\,1)$ interface is predicted to be about 0.4 Ry smaller than $Pt(1\,1\,1)/TiO_2(1\,0\,1)$ interface, which showed that there are strong interfacial interactions in the $Pt(1\,1\,1)/TiO_2(0\,0\,1)$ interface than in the $Pt(1\,1\,1)/TiO_2(1\,0\,1)$ interface , which can be observed by the number of coordination bonds (Pt - Ti, Pt - O), previously shown in Figura 15. $Pt(1\,1\,1)/TiO_2(0\,0\,1)$ interface exhibited the highest number of metal/oxide bonds, resulting in lower adsorption energy, and the $Pt(1\ 1\ 1)/TiO_2(1\ 0\ 1)$ interface presented the lowest bond, corresponding to the highest adsorption energy. Previously, the Pt/TiO_2 interface interfacial behavior was described in the literature [50, 54, 61], showing that the Pt phase on the TiO_2(*h k l*) surfaces changes the electronic properties of the interface. However, the specific electronic interactions and charge transfers described strongly depend on the kind of interface studied, which leads to predicting the better Pt/TiO_2 interface that can be used in practical applications.

4.4 Conclusions

The use of Pt(*1 1 1*)/TiO_2(*h k l*) interface to improve catalytic or photocatalytic properties in comparison to the isolated phases, which can reduce costs, especially the high price of the platinum metal, is an adequate approach but requires better comprehension of the interaction metal/oxide. The influence of Pt(*1 1 1*) on the structural and electronic properties of TiO_2(*h k l*) was investigated through a combined experimental and theoretical investigation, such as Pechini method synthesis, XRD/Rietveld refinement, and density functional theory.

Based on the XDR and Rietveld refinement, it has been demonstrated that the Pt(*1 1 1*)/TiO_2(*h k l*) interface is formed through the Pechini method. The most significant symmetry planes between Pt and TiO_2 phases were observed to be Pt(*1 1 1*), TiO_2(*1 0 1*), and TiO_2(*0 0 1*). However, other planes were also detected, but with reflections of lower intensity. In the analysis of the structural properties, it was observed that the crystalline structure of the TiO_2 phase is more susceptible to deformation than the Pt phase. This is evident from the values of µstrain ($\mu strain_{TiO_2}$ > $\mu strain_{Pt}$) and bulk modulus ($B_{(0-TiO_2)}$<$B_{(0-Pt)}$). As a result, at the Pt(*1 1 1*)/TiO_2(*h k l*) interface, the TiO_2 phase undergoes stress induced by the Pt phase, in which the TiO_2 phase has a bigger volume change rate with t_{1-TiO_2} > t_{1-Pt} and produces more energy with the volume change (ΔH_{TiO_2} > ΔH_{Pt}).

The Pt(*1 1 1*)/TiO_2(*0 0 1*) and Pt(*1 1 1*)/TiO_2(*1 0 1*) interfaces were considered as the theoretical model from XDR/ Rietveld refinement results where the electronic and structural properties were obtained through DFT analysis. The Pt(*1 1 1*)/TiO_2(*0 0 1*) and Pt(*1 1 1*)/TiO_2(*1 0 1*) interfaces both presented $Pt - O$ and $Pt - Ti$ bonds. However, both interfaces presented more $Pt - Ti$ bonds than $Pt - O$ bonds. Therefore, the $Pt - Ti$ bonds influence the interaction of the metal/oxide interface. The electronic properties of the Pt(*1 1 1*)/TiO_2(*h k l*) interface were investigated in the light of the PDOS, charge density distribution (Δn), electron localization function (ELF), d-band center (ϵ_d) and d-band width (w_d). The PDOS behavior of the Pt(*1 1*

$1)/TiO_2(h\ k\ l)$ is different when compared with the isolate TiO_2 and Pt phases, where a new state between VB and CB is observed with the largest contribution of the $Pt-5d$ state. The Δn and ELF showed that they are located on the oxygen atoms in the TiO_2 phase and the Pt atoms in the Pt phase for both interfaces. At the $Pt(1\ 1\ 1)/TiO_2(h\ k\ l)$ interface, was observed $Pt-O$ and $Pt-Ti$ bonds. However, the interaction between $Pt(1\ 1\ 1)$ and $TiO_2(h\ k\ l)$ mainly occurs through the $Pt-Ti$ bonds. The behavior of the d-band demonstrated that the $Pt(1\ 1\ 1)/TiO_2(0\ 0\ 1)$ interface has antibonding states below the Fermi energy, while the $Pt(1\ 1\ 1)/TiO_2(1\ 0\ 1)$ interface has antibonding states above the Fermi energy. This has an impact on the catalytic or photocatalytic properties of the $Pt(1\ 1\ 1)/TiO_2(h\ k\ l)$ interface. Finally, at the $Pt(1\ 1\ 1)/TiO_2(0\ 0\ 1)$ interface, the charge is observed in the $Ti-O$ bond of the $TiO_2(0\ 0\ 1)$ phase, and at the $Pt(1\ 1\ 1)/TiO_2(1\ 0\ 1)$ interface the electrons is transferred from $Pt(1\ 1\ 1)$ phase to $TiO_2(1\ 0\ 1)$ phase.

Therefore, a structural and electronic comprehension of the $Pt(1\ 1\ 1)/TiO_2(h\ k\ l)$ interface can optimize the design and production of catalysts and photocatalysts based on the metal/oxide interface, which the $Pt(1\ 1\ 1)/TiO_2(0\ 0\ 1)$ and $Pt(1\ 1\ 1)/TiO_2(1\ 0\ 1)$ interfaces presented structural and electronic properties that can be achieve desired catalytic or photocatalytic behavior in practical applications.

4.5 Acknowledgments

The authors would like to thank the Brazilian research-funding institutions FAPEAM, and CNPq by financial resources. We also thank CENAPAD/SP, UFMT-STI/Server for providing computational time.

BIBLIOGRAPHY

1 KAKIHANA, M. Invited review "sol-gel" preparation of high temperature superconducting oxides. *Journal of sol-gel science and technology*, Springer, v. 6, p. 7–55, 1996. 88

2 RIETVELD, H. M. A profile refinement method for nuclear and magnetic structures. *Journal of applied Crystallography*, International Union of Crystallography, v. 2, n. 2, p. 65–71, 1969. 89

3 TOBY, B. H.; DREELE, R. B. V. GSAS-II: the genesis of a modern open-source all purpose crystallography software package. *Journal of Applied Crystallography*, International Union of Crystallography, v. 46, n. 2, p. 544–549, 2013. 89

4 THOMPSON, P.; COX, D. E.; HASTINGS, J. B. Rietveld refinement of Debye–Scherrer synchrotron X-ray data from Al_2O_3. *Journal of Applied Crystallography*, International Union of Crystallography, v. 20, n. 2, p. 79–83, 1987. 89

5 STEPHENS, P. W. Phenomenological model of anisotropic peak broadening in powder diffraction. *Journal of Applied Crystallography*, International Union of Crystallography, v. 32, n. 2, p. 281–289, 1999. 89, 92, 93

6 LARSON, A. C.; DREELE, R. B. V. Gsas. *Report lAUR*, p. 86–748, 1994. 89

7 CAGLIOTI, G.; PAOLETTI, A. t.; RICCI, F. Choice of collimators for a crystal spectrometer for neutron diffraction. *Nuclear Instruments*, Elsevier, v. 3, n. 4, p. 223–228, 1958. 89, 92

8 HOHENBERG, P.; KOHN, W. Inhomogeneous electron gas. *Physical review*, APS, v. 136, n. 3B, p. B864, 1964. 89

9 KOHN, W.; SHAM, L. J. Self-consistent equations including exchange and correlation effects. *Physical review*, APS, v. 140, n. 4A, p. A1133, 1965. 89

10 GIANNOZZI, P. et al. Quantum espresso: a modular and open-source software project for quantum simulations of materials. *Journal of physics: Condensed matter*, IOP Publishing, v. 21, n. 39, p. 395502, 2009. 89

11 PERDEW, J. P.; WANG, Y. Accurate and simple analytic representation of the electron-gas correlation energy. *Physical review B*, APS, v. 45, n. 23, p. 13244, 1992. 89

12 PERDEW, J. P.; BURKE, K.; ERNZERHOF, M. Generalized gradient approximation made simple. *Physical review letters*, APS, v. 77, n. 18, p. 3865, 1996. 89

13 VANDERBILT, D. Soft self-consistent pseudopotentials in a generalized eigenvalue formalism. *Physical review B*, APS, v. 41, n. 11, p. 7892, 1990. 89

14 WEN, B. et al. Site dependent reactivity of pt single atoms on anatase tio 2 (101) in an aqueous environment. *Physical Chemistry Chemical Physics*, Royal Society of Chemistry, v. 22, n. 19, p. 10455–10461, 2020. 90

15 MONKHORST, H. J.; PACK, J. D. Special points for brillouin-zone integrations. *Physical review B*, APS, v. 13, n. 12, p. 5188, 1976. 90

16 RIETVELD, H. Line profiles of neutron powder-diffraction peaks for structure refinement. *Acta Crystallographica*, International Union of Crystallography, v. 22, n. 1, p. 151–152, 1967. 91

17 KIBIS, L. S. et al. In situ probing of pt/tio 2 activity in low-temperature ammonia oxidation. *Catalysis science & technology*, Royal Society of Chemistry, v. 11, n. 1, p. 250–263, 2021. 93

18 GIANNAKAS, A. et al. Photocatalytic performance of pt-tio2, pt-n-tio2 and pt-n/f-tio2 towards simultaneous cr (vi) reduction/benzoic acid oxidation: Insights into photogenerated charge carrier dynamics and catalyst properties. *Journal of Photochemistry and Photobiology A: Chemistry*, Elsevier, v. 349, p. 25–35, 2017. 93

19 TASBIHI, M. et al. On the selectivity of co2 photoreduction towards ch4 using pt/tio2 catalysts supported on mesoporous silica. *Applied Catalysis B: Environmental*, Elsevier, v. 239, p. 68–76, 2018. 93

20 ISMAIL, A. A.; BAHNEMANN, D. W. One-step synthesis of mesoporous platinum/titania nanocomposites as photocatalyst with enhanced photocatalytic activity for methanol oxidation. *Green Chemistry*, Royal Society of Chemistry, v. 13, n. 2, p. 428–435, 2011. 93

21 PECHARSKY, V. K.; ZAVALIJ, P. Y. et al. Fundamentals of powder diffraction and structural characterization of materials [electronic resource]. Boston, MA: Springer US,. 93

22 MITTEMEIJER, E. J.; WELZEL, U. The "state of the art" of the diffraction analysis of crystallite size and lattice strain. *Zeitschrift für Kristallographie*, Oldenbourg Wissenschaftsverlag GmbH, v. 223, n. 9, p. 552–560, 2008. 93

23 MURUGESAN, S. et al. X-ray diffraction rietveld analysis and bond valence analysis of nano titania containing oxygen vacancies synthesized via sol-gel route. *Materials Chemistry and Physics*, Elsevier, v. 225, p. 320–330, 2019. 94, 95

24 IRSHAD, K. et al. Structural phase transition, equation of state and phase diagram of functional rare earth sesquioxide ceramics (eu1- x la x) 2o3. *Scientific Reports*, Nature Publishing Group UK London, v. 10, n. 1, p. 11829, 2020. 95

25 IRSHAD, K. A. et al. High pressure structural phase transitions in ho: Eu2o3. *Journal of Alloys and Compounds*, Elsevier, v. 725, p. 911–915, 2017. 95

26 KEANE, A. An investigation of finite strain in an isotropic material subjected to hydrostatic pressure and its seismological applications. *Australian Journal of Physics*, CSIRO Publishing, v. 7, n. 2, p. 322–333, 1954. 95

27 MURNAGHAN, F. Proceedings of the national academy of sciences of the united states. *America*, v. 30, n. 9, p. 244–247, 1944. 95

28 SCHETTINO, V.; BINI, R. *Materials under extreme conditions: molecular crystals at high pressure*. [S.l.]: World Scientific, 2013. 95

29 DONG, Z. et al. Pressure induced structural transformations of anatase tio 2 nanotubes probed by raman spectroscopy and synchrotron x-ray diffraction. *RSC advances*, Royal Society of Chemistry, v. 6, n. 80, p. 76142–76150, 2016. 96

30 PISCHEDDA, V. et al. Ultrastability and enhanced stiffness of 6 nm tio 2 nanoanatase and eventual pressure-induced disorder on the nanometer scale. *Physical review letters*, APS, v. 96, n. 3, p. 035509, 2006. 96

31 ÇAĞIN, T. et al. Thermal and mechanical properties of some fcc transition metals. *Physical review B*, APS, v. 59, n. 5, p. 3468, 1999. 96

32 KITTEL, C. *Introduction to solid state physics*. [S.l.]: John Wiley & sons, inc, 2005. 96

33 THAINES, E. H. et al. Structural and electrochemical analysis of ni/nio supercapacitor materials: A theoretical and experimental study. *Solid State Ionics*, Elsevier, v. 394, p. 116194, 2023. 96

34 RAHMAN, M. A.; RAHAMAN, M. Z.; RAHMAN, M. A. The structural, elastic, electronic and optical properties of mgcu under pressure: a first-principles study. *International Journal of Modern Physics B*, World Scientific, v. 30, n. 27, p. 1650199, 2016. 96

35 CHASE, M. W.; (US), N. I. S. O. *NIST-JANAF thermochemical tables*. [S.l.]: American Chemical Society Washington, DC, 1998. v. 9. 97

36 GOLDBERG, R. N.; HEPLER, L. G. Thermochemistry and oxidation potentials of the platinum group metals and their compounds. *Chemical Reviews*, ACS Publications, v. 68, n. 2, p. 229–252, 1968. 97

37 GRUSHOW, A.; ERVIN, K. M. Ligand and metal binding energies in platinum carbonyl cluster anions: Collision-induced dissociation of pt m- and pt m (co) n-. *The Journal of chemical physics*, American Institute of Physics, v. 106, n. 23, p. 9580–9593, 1997. 97

38 YU, Y.; ZHANG, W.; MEI, D. Artificial neural network potential for encapsulated platinum clusters in mof-808. *The Journal of Physical Chemistry C*, ACS Publications, v. 126, n. 2, p. 1204–1214, 2022. 98

39 HEREDIA, C. L.; FERRARESI-CUROTTO, V.; LÓPEZ, M. Characterization of ptn (n= 2–12) clusters through global reactivity descriptors and vibrational spectroscopy, a theoretical study. *Computational materials science*, Elsevier, v. 53, n. 1, p. 18–24, 2012. 98

40 MAHATA, A.; NAIR, A. S.; PATHAK, B. Recent advancements in pt-nanostructure-based electrocatalysts for the oxygen reduction reaction. *Catalysis Science & Technology*, Royal Society of Chemistry, v. 9, n. 18, p. 4835–4863, 2019. 98

41 KUMARI, S. et al. Electrocatalytic hydrogen evolution at full atomic utilization over ito-supported sub-nano-pt n clusters: High, size-dependent activity controlled by fluxional pt hydride species. *Journal of the American Chemical Society*, ACS Publications, v. 145, n. 10, p. 5834–5845, 2023. 98

42 CHEN, H. et al. Bonding and electron energy-level alignment at metal/tio2 interfaces: A density functional theory study. *The Journal of Physical Chemistry C*, ACS Publications, v. 120, n. 10, p. 5549–5556, 2016. 98, 101

43 FUJISHIMA, A.; HONDA, K. Electrochemical photolysis of water at a semiconductor electrode. *nature*, Nature Publishing Group UK London, v. 238, n. 5358, p. 37–38, 1972. 99

44 KAPILASHRAMI, M. et al. Probing the optical property and electronic structure of tio2 nanomaterials for renewable energy applications. *Chemical reviews*, ACS Publications, v. 114, n. 19, p. 9662–9707, 2014. 99

45 WANG, D.; LIU, Z.-P.; YANG, W.-M. Revealing the size effect of platinum cocatalyst for photocatalytic hydrogen evolution on tio2 support: a dft study. *ACS Catalysis*, ACS Publications, v. 8, n. 8, p. 7270–7278, 2018. 99

46 TAMURA, T. et al. First-principles study of the rectifying properties of pt/tio 2 interface. *Physical Review B*, APS, v. 80, n. 19, p. 195302, 2009. 99, 100

47 MO, L.-B. et al. Hydrogen impurity defects in rutile tio2. *Scientific Reports*, Nature Publishing Group UK London, v. 5, n. 1, p. 17634, 2015. 101

48 JR, E. J. L.; JONES, M. M. A complete table of electronegativities. *Journal of chemical education*, ACS Publications, v. 37, n. 5, p. 231, 1960. 101

49 ZHANG, D. et al. Experimental and density functional theory investigation of pt-loaded titanium dioxide/molybdenum disulfide nanohybrid for so 2 gas sensing. *New Journal of Chemistry*, Royal Society of Chemistry, v. 43, n. 12, p. 4900–4907, 2019. 101

50 WU, Z. et al. Microwave synthesis of pt clusters on black tio2 with abundant oxygen vacancies for efficient acidic electrocatalytic hydrogen evolution. *Angewandte Chemie*, Wiley Online Library, v. 135, n. 14, p. e202300406, 2023. 101, 105

51 CHEN, M.; GOODMAN, D. The structure of catalytically active gold on titania. *science*, American Association for the Advancement of Science, v. 306, n. 5694, p. 252–255, 2004. 102

52 ZHU, Y. et al. Inverse iron oxide/metal catalysts from galvanic replacement. *Nature Communications*, Nature Publishing Group UK London, v. 11, n. 1, p. 3269, 2020. 102

53 NAGABABU, P. et al. Synthesis of ni2p/cds and pt/tio2 nanocomposite for photoreduction of co2 into methanol. *Scientific Reports*, Nature Publishing Group UK London, v. 11, n. 1, p. 8084, 2021. 102

54 ZHOU, Y. et al. Interplay of pt and crystal facets of tio2: Co oxidation activity and operando xas/drifts studies. *ACS Catalysis*, ACS Publications, v. 6, n. 11, p. 7799–7809, 2016. 102, 105

55 ZHANG, Y. et al. Titania-morphology-dependent pt–tio2 interfacial catalysis in water-gas shift reaction. *ACS Catalysis*, ACS Publications, v. 13, n. 1, p. 392–399, 2022. 103

56 WU, X. et al. Origin of strong metal-support interactions between pt and anatase tio2 facets for hydrodeoxygenation of m-cresol on pt/tio2 catalysts. *Journal of Catalysis*, Elsevier, v. 418, p. 203–215, 2023. 103

57 CHEN, Y. et al. Facet-engineered tio2 drives photocatalytic activity and stability of supported noble metal clusters during h2 evolution. *Nature communications*, Nature Publishing Group UK London, v. 14, n. 1, p. 6165, 2023. 103

58 HUANG, Y. et al. Oxygen vacancy engineering in photocatalysis. *Solar RRL*, Wiley Online Library, v. 4, n. 8, p. 2000037, 2020. 103

59 PUIGDOLLERS, A. R. et al. Increasing oxide reducibility: the role of metal/oxide interfaces in the formation of oxygen vacancies. *Acs Catalysis*, ACS Publications, v. 7, n. 10, p. 6493–6513, 2017. 103

60 KIBLER, L. A. et al. Tuning reaction rates by lateral strain in a palladium monolayer. *Angewandte Chemie International Edition*, Wiley Online Library, v. 44, n. 14, p. 2080–2084, 2005. 103

61 WEI, Z.-W. et al. Reversed charge transfer and enhanced hydrogen spillover in platinum nanoclusters anchored on titanium oxide with rich oxygen vacancies boost hydrogen evolution reaction. *Angewandte Chemie*, Wiley Online Library, v. 133, n. 30, p. 16758–16763, 2021. 105

5

The Role of $Pt_3(1\ 1\ 1)$ *in Hydrogen and Water Splitting on the* $Pt_3(1\ 1\ 1)/TiO_2(h\ k\ l)$ *Interface: Theoretical Insights*

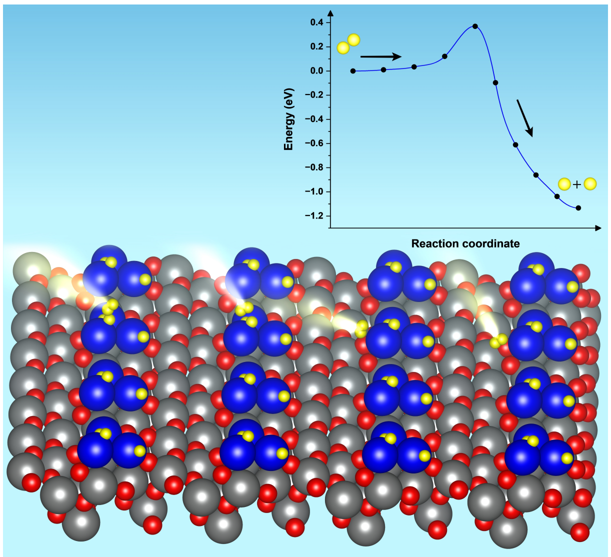

The Pt/TiO_2 interface presents potential as a photocatalyst for hydrogen evolution reactions (HER). However, the comprehension of hydrogen and water splitting on the $Pt(1\ 1\ 1)$ surface interface remains a considerable subject. We proposed the $Pt_3(1\ 1\ 1)/TiO_2(h\ k\ l)$ interface based on X-ray diffraction (XRD) with Rietveld refinement analysis, where reflections attributed to $Pt(1\ 1\ 1)$ and anatase $TiO_2(h\ k\ l)$ were observed. The theoretical modeling of the $Pt_3(1\ 1\ 1)/TiO_2(h\ k\ l)$ interface considering the fraction of approximately 60% of the TiO_2 phase and 40% of the Pt phase determined in the Rietveld refinement. The electronic properties were obtained using DFT/plane-wave calculation on a model with 39 atoms. The band structure and PDOS behavior of $Pt_3(1\ 1\ 1)/TiO_2(h\ k\ l)$ showed a new state between the valence and conduction bands, with contributions from the $Pt-5d$ state, giving the $Pt_3(1\ 1\ 1)/TiO_2(h\ k\ l)$ interface a metallic behavior. The initial steps of the hydrogen and water splitting and the transition state were determined by the nudged elastic band (NEB)

method, considering $H_2 \rightarrow H^*_{ads} + H^*_{ads}$ and $H_2O_ads \rightarrow OH^*_{ads} + H^*_{ads}$ on the Pt_3(*1 1 1*) surface of the Pt_3(*1 1 1*)$/TiO_2$(*h k l*) interface. The Pt_3(*1 1 1*)$/TiO_2$(*1 0 1*) interface presented the lowest activation energy for hydrogen molecule splitting of 0.19 eV with exothermic character. For water splitting, both Pt_3(*1 1 1*)$/TiO_2$(*h k l*) interfaces presented the same activation energy $\sim$ 1.4 eV with endothermic character. Therefore, when the hydrogen molecule splitting occurs on the Pt_3(*1 1 1*) surface is favorable, but for water splitting is not favorable, which may be an indication of the limitation in the hydrogen production rate (HGR) values compared with other catalysts.

Keywords: Pt_3(*1 1 1*)$/TiO_2$(*h k l*) interface, hydrogen splitting, water splitting, climbing nudged elastic band method, materials modeling.

5.1 Theoretical Details

The theoretical modeling of the Pt_3(*1 1 1*)$/TiO_2$(*h k l*) interface was based on the material obtained experimentally from a polymeric resin prepared by the Pechini method and characterized by X - ray diffraction with Rietveld refinement , see in Figure 37. The crystallographic parameters estimated by Rietveld refinement were used to calculate the electronic and structural properties and simulate the reactions on the Pt_3(*1 1 1*)$/TiO_2$(*h k l*) interface. The theoretical calculations were conducted using density functional theory [1, 2] plane-wave (DFT/plane-wave) implemented on the Quantum-ESPRESSO [3] package. The electronic and structural properties were calculated using the electronic exchange and correlation interactions described by the functional developed by Perdew-Burke-Ernzerhof [4] (PBE) and ultrasoft pseudopotentials proposed by Vanderbilt, with electrons from O (2s, 2p), Ti (3s, 3p, 4s, 3d), and Pt (4f, 5d, 6s) shells. We performed the optimization convergence test of the system, and the plane-wave basis set the energy cutoff for the smooth wave functions to be 55 Ry and the charge density cutoff to be 550 Ry. The electronic structure calculations were performed using a DFT/PBE+U approach with the Hubbard correction. We use the value of Ueff = 3.5 eV for $d - Ti$ and $p - O$, considering DFT/PBE+U_d+U_p. For the Brillouin zone, integrations were performed 4 x 4 x 2 k-points (Pt_3(*1 1 1*)$/TiO_2$(*h0 0 1*) interface), and 2 x 4 x 1 k-points (Pt_3(*1 1 1*)$/TiO_2$(*1 0 1*) interface) mesh sampling based on the Monkhorst-Pack scheme [5]. The Pt_3(*1 1 1*)$/TiO_2$(*h k l*) interface was simulated from a 2 x 2 slab constructed for the (*1 0 1*) and (*0 0 1*) planes with 36 atoms of the anatase TiO2 phase and 3 atoms of the platinum phase in the (*1 1 1*) – plane considering a maximum fraction of approximately 60% of the TiO_2 phase and 40% of the Pt phase determined in the Rietveld refinement.

The Pt_3(*1 1 1*)/TiO_2(*h k l*) interfaces were based on the orthorhombic system, and the electronic band structures (BS) were calculated using the k-points path reported by Curtarolo *et al.* [6]. The hydrogen and water splitting was simulated with climbing nudged elastic band method (CI-NEB), with the k-points grid was set a the Γ point. The d-band structure analysis was calculated from the Projected Density of States (PDOS) for Ti and Pt d-band center, where d-band center (ϵ_d) can be calculated from:

$$\epsilon_d = \frac{\int_{-\infty}^{E_F} E_{(n_d)}(E)dE}{\int_{-\infty}^{E_F} n_d(E)dE}, \tag{5.1}$$

where $n_d(E)$ is e density of states of Ti and Pt d-orbitals, obtained from PDOS.

The coordinates (*x y z*) determined by Rietveld refinement and used in the theoretical calculations are shown in annex C1 - supplementary information.

5.2 Results and discussion

5.2.1 Computational Modeling for Pt_3(*1 1 1*)/TiO_2(*h k l*) Interface

The modeling of the Pt_3(*1 1 1*)/TiO_2(*h k l*) interface was based on the X-ray diffraction (XDR) and Rietveld refinement, shown in Figure 37 and Table 14. Analyzing the XDR, it is possible to observe reflections related to the platinum (Pt) and dioxide titanium (TiO_2) phases, which reflections at 39.7178 (*1 1 1*) – *hkl* surface related to Pt crystalline phase (Pt - CIF ICSD 243678), and reflections at 25.2978 (101) – hkl surface and 37.6865 (*0 0 4*)-*hkl* surface to the anatase TiO_2 crystalline phase (TiO_2 – CIF ICSD 93098). The weight fraction of the TiO_2 phase constituted $\sim$ 60%, while the Pt phase contributed $\sim$ 40%. Thus, Density Functional Theory (DFT) analysis was conducted for modeling Pt_3(*1 1 1*)/TiO_2(*0 0 1*) and Pt_3(*1 1 1*)/TiO_2(*1 0 1*) interfaces with weight fractions approximately determined by Rietveld refinement, Figures 19a-b.

The bond lengths and type are factors that influence both the structural and electronic properties of the Pt_3(*1 1 1*)/TiO_2(*h k l*) interface. In Figure 19a-b, the $Pt-Pt$, $Pt-Ti$, and $Pt-O$ bonds at the interface can be observed, and the analysis of bond lengths between atoms is pivotal for understanding interface behavior. All the bond lengths of the optimized structures of

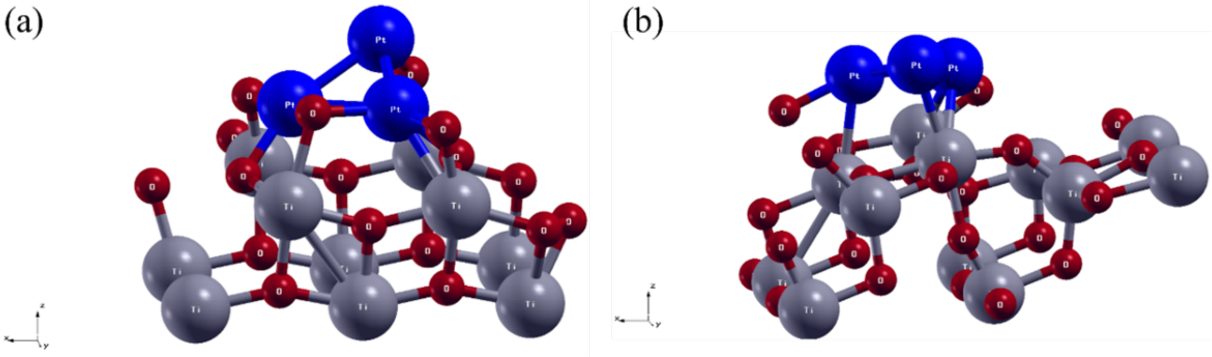

Figure 19 – The optimized structures of (a)$Pt_3(1\ 1\ 1)/TiO_2(0\ 0\ 1)$ interface and (b)$Pt_3(1\ 1\ 1)/TiO_2(1\ 0\ 1)$ interface. The red balls represent the oxygen atoms, the gray balls represent the titanium atoms, and the blue balls represent the platinum atoms.

the $Pt_3(1\ 1\ 1)/TiO_2(h\ k\ l)$ interface can be observed in Figure 38 and Table 15 . In the $Pt_3(1\ 1\ 1)/TiO_2(0\ 0\ 1)$ interface, Figure 19a, and $Pt_3(1\ 1\ 1)/TiO_2(1\ 0\ 1)$ interface, Figure 19b, the $Pt-Pt$ bond length on the Pt_3 ranging from 2.4817 Å up to 2.6397 Å. The $Pt-Pt$ bond length , whether in a cluster or supported on oxides, is reported to range from 2.50 Å to 2.80 Å [7–12]. The $Pt_3(1\ 1\ 1)/TiO_2(0\ 0\ 1)$ interface exhibits a single $Pt-Ti$ bond with a length of 2.6203 Å, involving a five-coordinated Ti atom (Ti-5C), and the $Pt_3(1\ 1\ 1)/TiO_2(1\ 0\ 1)$ interface displays four $Pt-Ti$ bonds ranging from 2.6372 Å to 2.8049 Å, involving both four-coordinated Ti atoms (Ti-4C) and five-coordinated Ti atoms (Ti-5C). The $Pt_3(1\ 1\ 1)/TiO_2(0\ 0\ 1)$ interface presented six $Pt-O$ bonds ranging from 1.8569 Å up to 2.0568 Å, and the $Pt_3(1\ 1\ 1)/TiO_2(1\ 0\ 1)$ interface two $Pt-O$ bonds with 2.0206 Å and 2.0643 Å. The observed bond lengths in the $Pt_3(1\ 1\ 1)/TiO_2(h\ k\ l)$ interfaces agree with the bond lengths reported in the literature [12–15].

5.2.2 Electronic Structure

The electronic structure was studied, analyzing the band's structures and projected density of states (PDOS) for the $Pt_3(1\ 1\ 1)/TiO_2(h\ k\ l)$ interface, shown in Figure 20a-b.

The electronic BS and PDOS calculated for $Pt_3(1\ 1\ 1)/TiO_2(h\ k\ l)$ interface indicate a metallic behavior in both interfaces, where the overlapping of the valence and conduction bands are observed. For the isolated phase, the anatase TiO_2 exhibits semiconductor behavior, with an indirect band gap ($M \to \Gamma/k$–path) calculated of 3.00 eV, while the experimentally determined band gap is 3.20 eV [16]. Additionally, the platinum phase exhibits metallic behavior, as shown in annex C1 - supplementary information Figure 38 . The PDOS behavior of the $Pt_3(1\ 1\ 1)/TiO_2(h$

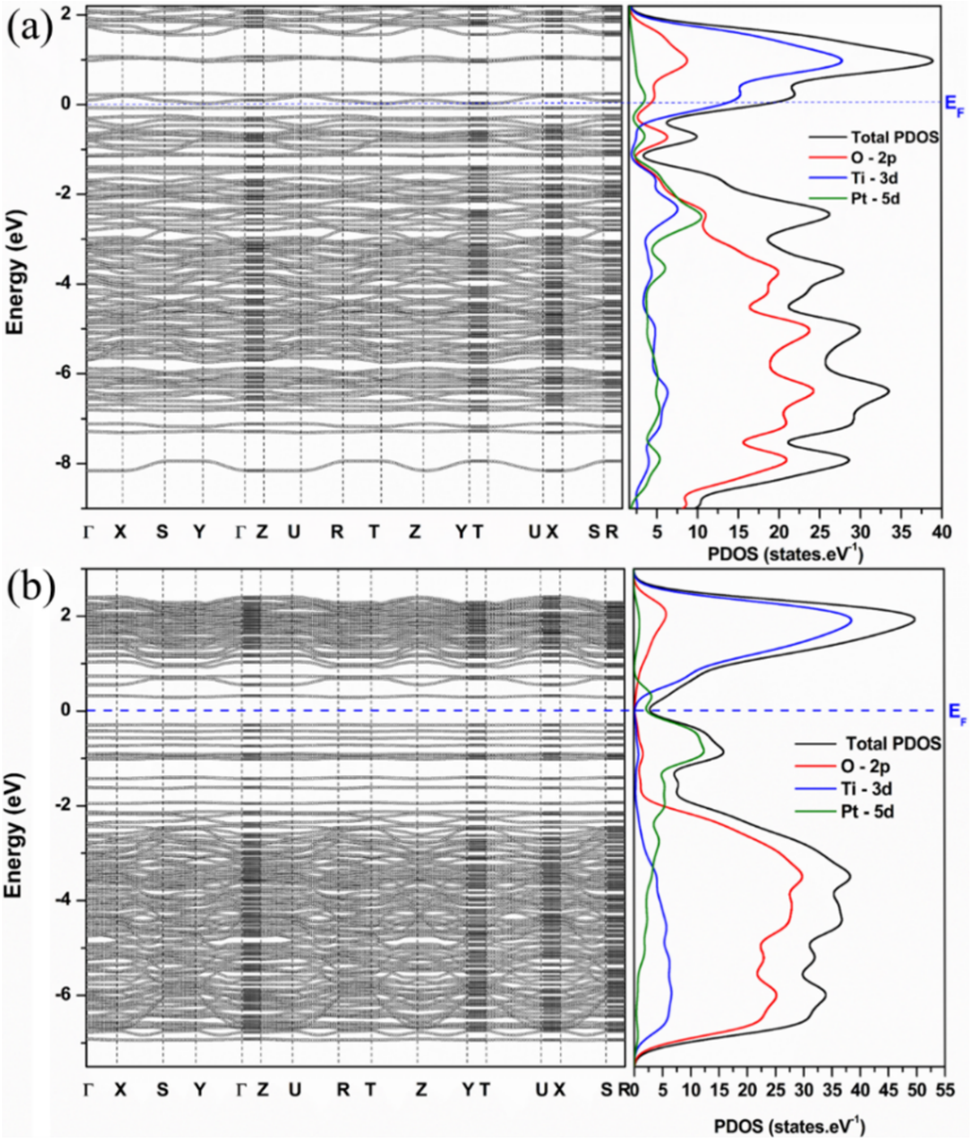

Figure 20 – Band Structures (BS) and Projected density of States (PDOS) for (a) $Pt_3(1\,1\,1)/TiO_2(0\,0\,1)$ interface and (b) $Pt_3(1\,1\,1)/TiO_2(1\,0\,1)$ interface.

$k\,l$) interfaces is similar to that of the anatase TiO_2 phase, as shown in Figure 20a-b. In both interfaces, it is possible to notice that the $O-2p$ states are localized in the valence band (VB) below the Fermi energy (E_F), while the Ti - $3d$ states are in the conduction band (CB) above E_F when compared to the PDOS of anatase TiO_2 (see Figure 39a). The metallic behavior observed in the $Pt_3(1\,1\,1)/TiO_2(h\,k\,l)$ interfaces is attributed to a new state between the VB and CB. In the $Pt_3(1\,1\,1)/TiO_2(0\,0\,1)$ interface, Figure 20a, the $O-2p$ states and $Pt-5d$ states are localized in this intermediate state between VB and CB, which can be associated with the $Pt-O$ bonds observed in the interface. However, in the $Pt_3(1\,1\,1)/TiO_2(1\,0\,1)$ interface, Figure 20b, the $Pt-5d$ states are localized in this intermediate state between VB and CB, as this interface exhibits $Ti-Pt$ bonds in the interface structure. Jin *et al.* [17] studied single metal/TiO_2 interfaces and their photocatalytic properties using DFT at the PBE exchange-correlation level. According to the authors [17], the electronic band structure of the Pt/$TiO_2(1\,0\,1)$ interface presented new bands between the VB and CB associated with the single platinum metal. Wang *et al.* [18] reported a study on the gas-sensing properties of the $Pt_3/TiO_2(1\,0\,1)$ interface. The authors [18] calculated the electronic structure of the $Pt_3/TiO_2(1\,0\,1)$ interface using DFT, also at the PBE level. The electronic band structure of the $Pt_3/TiO_2(1\,0\,1)$ interface revealed states between the VB and CB, exhibiting similar behavior as Jin *et al.* [17] observed.

The emergence of states between the VB and CB in the $Pt_3(1\,1\,1)/TiO_2(h\,k\,l)$ interfaces emphasizes the different bonding configurations, influencing the electronic structures, as observed in the BS and PDOS. Thus, the bonding within the optimized $Pt_3(1\,1\,1)/TiO_2(h\,k\,l))$ interfaces is also evident in the charge density distribution (Δn) and electron localization function ($ELF - \eta(r)$) of the $Pt_3(1\,1\,1)/TiO_2(h\,k\,l)$ interfaces, presented in Figure 21.

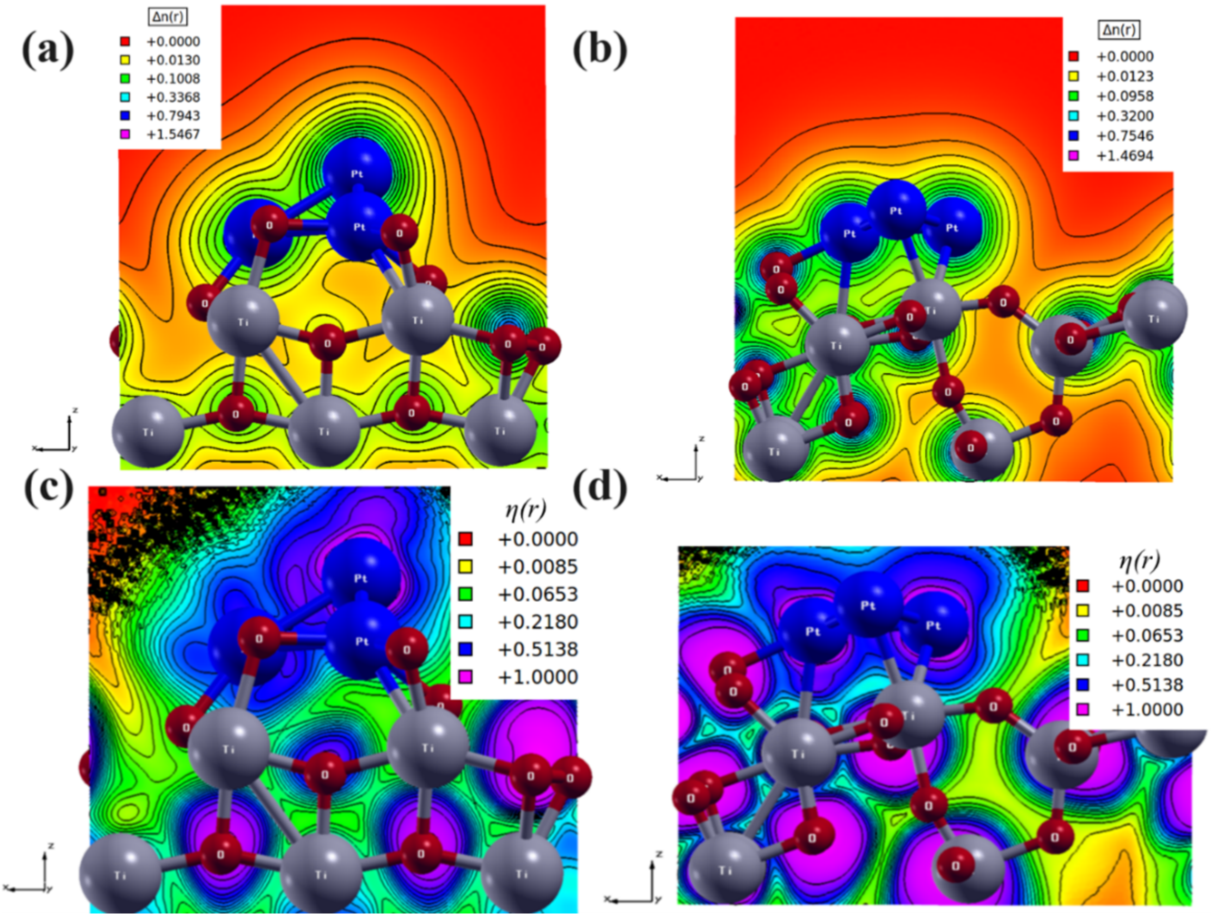

Figure 21 – 2D Charge density distribution (Δn) and 2D electron localization function ($ELF - \eta(r)$)of the (a) – (c) $Pt_3(1\,1\,1)/TiO_2(0\,0\,1)$ interface and (b) – (d) $Pt_3(1\,1\,1)/TiO_2(1\,0\,1))$ interface.

In Figure 21a-d, the 2D charge density distribution (Δn) and electron localization function ($ELF - \eta(r)$) are mainly localized on the oxygen atoms in the TiO_2 phase and the Pt atoms in the Pt phase for both interfaces. The Pt_3(*1 1 1*)/TiO_2(*0 0 1*) interface, Figure 21a, exhibited Δn maximum values (Δn_{max}) of approximately 1.54, while the Pt_3(*1 1 1*)/TiO_2(*1 0 1*) interface, Figure 21b, presented values around 1.47. The variation in Δn_{max} indicates that the electronic structure of the Pt_3(*1 1 1*)/TiO_2(*0 0 1*) interfaces depend on the TiO_2(*0 0 1*) and TiO_2(*1 0 1*) surfaces. Analyzing the 2D $ELF - \eta(r)$ maps, the Pt_3(*1 1 1*)/TiO_2(*0 0 1*) interface in Figure 21c exhibits $Ti - O$ bonds with ionic characteristics, displaying $\eta(r)$ values between $\sim$ 0.06 and $\sim$ 0.2, and the $Pt - O$ more covalent character than one $Pt - Ti$ bond, with the $\eta(r)$ values $\sim$ 0.5 and $\sim$ 0.2, respectively. In contrast, the Pt_3(*1 1 1*)/TiO_2(*1 0 1*) interface in Figure 21d demonstrates a more covalent character in the $Ti - O$ bonds compared to the Pt_3(*1 1 1*)/TiO_2(*0 0 1*) interface, with $\eta(r)$ values ranging between $\sim$ 0.2 and $\sim$ 0.5, and the $Pt - O$ bonds more covalent character than the $Pt - Ti$ bonds, with the $\eta(r)$ values $\sim$ 0.5 and $\sim$ 0.2, respectively. The overlapping isolines basins observed in both interfaces further evidenced all the bonds observed.

The anatase TiO_2 phase has been extensively discussed in the literature [19, 20], demonstrating that the Δn localizes on the oxygen atoms, which is attributed to the differing electronegativity values of oxygen and titanium atoms (*O* = 3.5, Ti = 1.32 on the Pauling scale [21]). However, the description of Δn for the Pt_3(*1 1 1*)/TiO_2(*h k l*) interface depends on factors such as the type of interface described, such as the use of clusters for the description of the Pt phase, crystalline type of the Pt phase, or the presence of only single Pt atom, along with variations in the TiO_2(*h k l*) planes. The Pt/TiO_2 interface can be described with a Pt single atom on the TiO_2(*1 0 1*), which was reported by Zhang *et al.* [22]. Density functional theory (DFT) and analysis of the Δn at the interface pointed to an accumulation in the oxygen atoms, and the overlapping Δn-basins in the $Ti - O$ bonds, indicating a covalent character in the structure. Additionally, the Pt single atom exhibited a gradual accumulation of charge, a behavior that can be associated with the adsorption of sulfur dioxide molecules on the TiO_2 surface. In contrast, Wu *et al.* [23] opted to use Pt clusters to investigate the Pt/TiO_2 interface, with application on electrocatalytic hydrogen evolution. The authors [23] built the Pt_4/TiO_2(*1 0 1*) and $Pt_4/TiO_2(101)V_OV$ interfaces using density functional theory (DFT) to analyze the electronic structure. The Pt_4 cluster presented a pyramid-like structure, exhibiting Δn at the Pt_4/TiO_2(*1 0 1*)V_OV interface, localized on the oxygen and platinum atoms near the TiO_2 surface. The platinum atom positioned farther from the TiO_2 surface displayed $\Delta n \sim 0$. Furthermore, the Δn localized at the interface indicated a covalent character, with $0 < \Delta n < 0.7$. Another type of Pt/TiO_2 interface was built using a unit cell model derived from the isolated phases, as reported by Chen *et al.* [13]. The $Pt(0\,0\,1)$ – fcc/$TiO_2(0\,0\,1)$ interface was constructed based on the unit cell of the isolated phase, producing two interface types: the first with $Pt - O$ bonds and the second with $Pt - Ti$ bonds. The Δn of the interface localized on the oxygen and platinum atoms near the TiO_2 surface for the first interface, while an increased localization of Δn was observed on the titanium and platinum atoms for the second interface. Therefore, a few types of Pt/TiO_2 interfaces can be studied or constructed, and these variations may have implications for the interface's diverse properties in various applications.

5.2.3 Reaction path of the hydrogen molecule splitting on the $Pt_3(1\;1\;1)/TiO_2(h\;k\;l)$ interfaces

Hydrogen molecule splitting was studied on the $Pt_3(1\,1\,1)/TiO_2(h\,k\,l)$ interfaces, considering their structural and electronic properties. The geometries of the interfaces, with species of the initial states (IS), transition state (TS), and final state (FS), are involved in the mechanism for hydrogen splitting for the $Pt_3(1\,1\,1)/TiO_2(0\,0\,1)$ interface and $Pt_3(1\,1\,1)/TiO_2(1\,0\,1)$ interface, as shown in Figure 22.

One hydrogen molecule was selected to aim for a molecular-scale understanding of the fundamental reaction pathway and to estimate the activation energy barrier for hydrogen molecule splitting, using CI-NEB calculations with ten images-steps, where IS and FS were proposed from a fundamental step of the physisorbed $H - H$ (H_2) to the dissociated state (H^*):

$$H - H_{phy} \rightarrow H^*_{ads} + H^*_{ads} \qquad \text{(reaction-2)}$$

where $2H^*$ are the species adsorbed on the $Pt_3(1\,1\,1)/TiO_2(h\,k\,l)$ interfaces. Hydrogen molecule splitting activation energy barrier (E_a) can be determined using the following equation:

$$E_a = E_{TS} - E_{IS}, \qquad (5.2)$$

where E_{TS} and E_{IS} are the energies of transition and initial states, respectively. The endothermic and exothermic of the reaction can be calculated by reaction energy (ΔE):

$$\Delta E = E_{FS} - E_{IS}, \qquad (5.3)$$

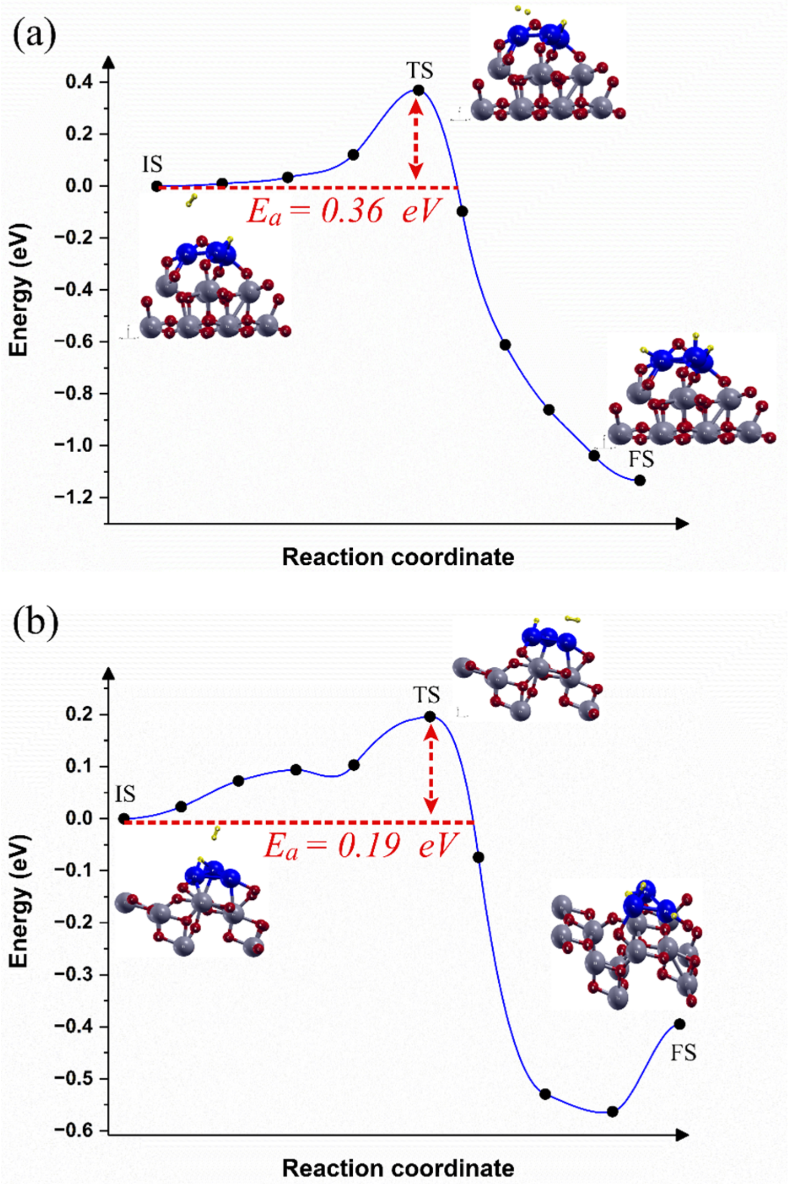

Figure 22 – Reaction pathway and reaction barrier of single hydrogen molecule splitting (a) $Pt_3(1\,1\,1)/TiO_2(0\,0\,1)$ interface and (b) $Pt_3(1\,1\,1)/TiO_2(1\,0\,1)$ interface. The yellow balls represent the hydrogen atoms.

where E_{FS} and E_{IS} are the energy of the final and initial states, respectively. All of the images of initial, transition, and final states of hydrogen splitting reactions can be seen in annex C1 - supplementary information, Figure 40.

The IS corresponds to the reagents in the reaction, where the H_2 molecule is physisorbed on the $Pt_3(1\,1\,1)/TiO_2(h\,k\,l)$ interface surfaces. The FS corresponds to the products, including dissociated hydrogen molecules, such as $2H^*_{ads}$ species adsorbed on the interface surface. The H_2 molecule dissociation on the $Pt(1\,1\,1)$ surface is related to a spontaneous process [24, 25]. Thus, the H_2 molecule was placed on the $Pt(1\,1\,1)$ surface direction, where the $Pt(1\,1\,1)$ surface has one adsorbed hydrogen, to simulate the initial spillover process [26, 27]. In both $Pt_3(1\,1\,1)/TiO_2(h$

k l) interfaces, the H_2 molecule is oriented towards Pt(*1 1 1*), with one of the hydrogen atoms positioned near the surface and the other farther away. This H_2 molecule geometry occurs when the H_2 molecule is produced by coupling the two H atoms desorbed from one metal/oxide surface [28]. For the reaction path, different TS values were determined for the Pt_3(*1 1 1*)/TiO_2(*0 0 1*) interface, Figure 22a, and Pt_3(*1 1 1*)/TiO_2(*1 0 1*) interface, Figure 22b. It is possible to notice that the H_2 molecule is dissociated on the Pt_3(*1 1 1*)/TiO_2(*0 0 1*) interface, with 0.8243 Å H - - H bond length and 2.0336/2.0889 H - - Pt bonds lengths. However, for the Pt_3(*1 1 1*)/TiO_2(*1 0 1*) interface, the TS consists of the H_2 molecule physisorbed on the surface yet with 0.7847 Å H – H bond length and 2.1537/2.1232 Å H - - Pt bonds lengths.

The ΔE calculation indicates that the hydrogen molecule splitting has an exothermic character for thePt_3(*1 1 1*)/TiO_2(*0 0 1*) interface (ΔE=-1.13 eV) andPt_3(*1 1 1*)/TiO_2(*0 0 1*) interface (ΔE=-0.39 eV). However, the E_a predicted for thePt_3(*1 1 1*)/TiO_2(*0 0 1*) interface andPt_3(*1 1 1*)/TiO_2(*1 0 1*) interface are 0.36 eV and 0.19 eV, respectively. Kwon *et al.* [29] studied the Pt/TiO_2 interface for H_2 sensing using an electrical measurement system. The authors [29] reported that the initial stage of H_2 sensing involves the H_2 molecules dissociation, with an activation energy of 36.4 kJ/mol (∼1.5 eV). However, with the spillover phenomenon, which occurs from the hydrogen-rich metal surface to sites where the surface is hydrogen-poor, the activation energy (E_a) is smaller. The initial mechanism involves the dissociation of H_2 molecules into $2H^*$ on the metal surface, as reported by Wang *et al.* [30], who studied semi-hydrogenation under hydrogen spillover on the Pt/zeolite interface. The author used the DFT/CI-NEB method to simulate the $H_2 \rightarrow 2H^*$ reaction on the Pt(*1 1 1*)/zeolite interface and determined E_a = 0.36 eV for the reaction. The Pt_3(*1 1 1*)/TiO_2(*h k l*) interfaces are little reported, and their application to hydrogen molecule splitting has not been studied yet. However, a similar structure, like Au_3(*1 1 1*)/TiO_2(*1 0 1*) interface, was related by Wan *et al.* [31], who investigated adsorption, dissociation, and spillover hydrogen on the Au_n(*1 1 1*)/TiO_2(*1 0 1*) interfaces. Through the DFT/CI-NEB method to simulate the H_2 dissociation on the Au_3(*1 1 1*)/TiO_2(*1 0 1*) interface presented E_a = 0.20 eV. Therefore, the determined E_a values aligned with the literature values, indicating that thePt_3(*1 1 1*)/TiO_2(*1 0 1*) interface is energetically more favorable for hydrogen molecule splitting than the Pt_3(*1 1 1*)/TiO_2(*0 0 1*) interface. On the other hand, thePt_3(*1 1 1*)/TiO_2(*0 0 1*) interface exhibits a more spontaneous process for hydrogen molecule splitting compared to the Pt_3(*1 1 1*)/TiO_2(*1 0 1*) interface, as it has a smaller ΔE.

The difference between E_a and ΔE of the Pt_3(*1 1 1*)/TiO_2(*h k l*) interfaces can be related to the electronic properties and the reaction mechanism, mainly to the transition state (TS). As shown previously, The Pt_3(*1 1 1*)$/TiO_2$(*0 0 1*) interface presented Δn_{max} value bigger than the Pt_3(*1 1 1*)$/TiO_2$(*1 0 1*) interface, which can be associated with the more spontaneous process. However, the smaller E_a presented by Pt_3(*1 1 1*)$/TiO_2$(*1 0 1*) interface can be linked to the differences in TS – step and the PDOS structure, as shown in Figure 23.

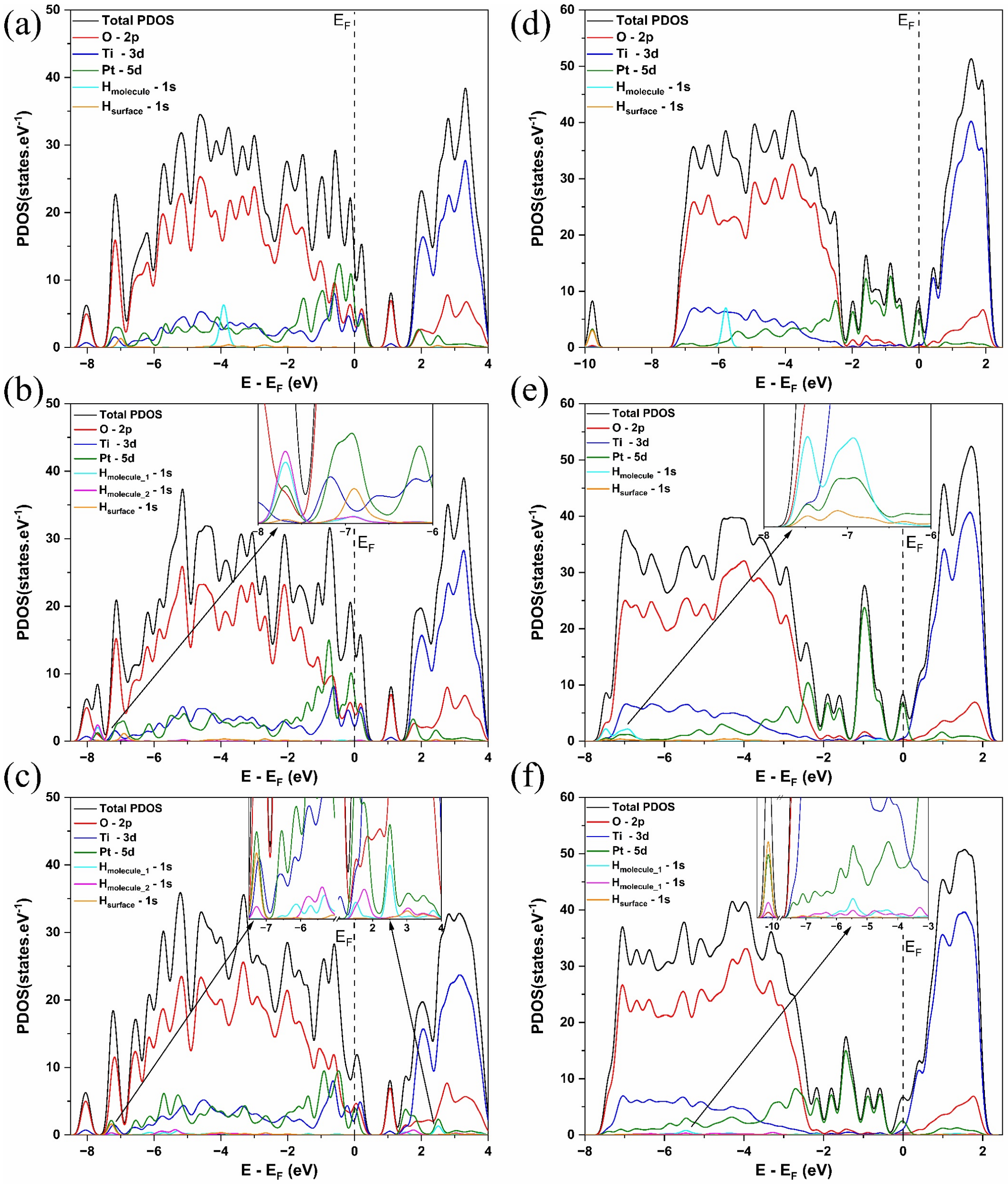

Figure 23 – Projected density of States (PDOS) for hydrogen splitting on the Pt_3(*1 1 1*)$/TiO_2$(*0 0 1*) interface (a) IS, (b) TS, (c) FS, and for Pt_3(*1 1 1*)$/TiO_2$(*1 0 1*) interface (d) IS, (e) TS, and (f) FS.

It is possible to observe in Figure 23a-f that the $Pt-5d$ states, green lines in PDOS, are localized near of the Fermi energy (E_F). In the initial state (*IS*) of the Pt_3(*1 1 1*)$/TiO_2$(*0 0 1*) interface, shown in Figure 23a, the $H-1s$ state of the H_2 molecule, cyan line in PDOS, is localized around -4.0 eV, and the $H-1s$ state of the H atom surface, orange line in PDOS, presented about -7.0 eV. For the IS of the Pt_3(1 1 1)$/TiO_2$(1 0 1) interface, shown in Figure 23d, the $H-1s$ state of the H_2 molecule is localized near -6.0 eV, and the $H-1s$ state of the H atom surface -10 eV. This indicates that the hydrogen interaction is more stable in the Pt_3(1 1 1)$/TiO_2$(1 0 1) interface for the IS.

In the transition state (TS) of the Pt_3(1 1 1)$/TiO_2$(0 0 1) interface, as shown in Figure 23b, the H_2 molecule is dissociated. The $H-1s$ state of the H atoms from the H_2 molecule is localized at a small energy level, approximately -7.7 eV (shown in the inset graph in Figure 23b), with the $Pt-5d$ state overlapping. The $H-1s$ state of the H atom on the surface does not change its localization, remaining around -7.0 eV. On the other hand, for the TS of the Pt_3(1 1 1)$/TiO_2$(1 0 1) interface, shown in Figure 23e, the H_2 molecule is not dissociated and is physisorbed on the surface. The $H-1s$ state of the H_2 molecule is localized above -7.5 eV (shown in the inset graph in Figure 23e), with the $Pt-5d$ state and $H-1s$ state of the H atom on the surface overlapping. Therefore, the transition state on the Pt_3(1 1 1)$/TiO_2$(0 0 1) interface exhibits states at lower energy levels than the Pt_3(1 1 1)$/TiO_2$(1 0 1) interface. This suggests that more energy is required for the hydrogen molecule splitting reaction to follow, resulting in a higher activation energy (E_a).

In the final state (FS) of the Pt_3(1 1 1)$/TiO_2$(0 0 1) interface, shown in Figure 23c, the $H-1s$ state of the H atoms from the H_2 molecule is localized in two regions: one at a lower energy level between -6.0 eV and -7.0 eV, and the other at a higher energy level between 2.0 eV and 3.0 eV above EF. The $H-1s$ state of the H atom on the surface is localized slightly below -7.0 eV (shown in the inset graph in Figure 23c). For the TS of the Pt_3(1 1 1)$/TiO_2$(0 0 1) interface, shown in Figure 23f, the $H-1s$ state of the H atoms from the H_2 molecule is localized -6.0 eV and -5.0 eV. The $H-1s$ state of the H atom on the surface is localized slightly below -10 eV, similar to the IS (shown in the inset graph in Figure 23f). Thus, states localized at a lower energy level in the Pt_3(1 1 1)$/TiO_2$(0 0 1) interface suggest a more spontaneous process, leading the atoms to a more stable state.

The PDOS structure of hydrogen molecule splitting on the Pt_3(1 1 1)$/TiO_2$($h\;k\;l$) interfaces contributes insights into the relationship between E_a and ΔE, presenting the energy level of states. Analyzing the behavior of the d-band can also play a fundamental role in understanding the reactivity of the Pt_3(1 1 1)$/TiO_2$($h\;k\;l$) interfaces. Table 6 shows the d-band center (ϵd), d-band width (w_d), and Fermi energy (E_F) levels of the isolated Pt_3(1 1 1)$/TiO_2$($h\;k\;l$) interfaces, initial state (IS), transition state (TS), and final state (FS) of hydrogen molecule splitting on the $Pt_3(1\ 1\ 1)/TiO_2(h\ k\ l)$ interfaces.

Table 6 – Electronic structure of the d-band projected: d-band center (ϵ_d), d-band width (w_d) and Fermi energy (E_F) of the TiO_2, Pt isolate phase and hydrogen splitting states on the $Pt_3(1\ 1\ 1)/TiO_2(h\ k\ l)$ interface.

d-band shape	$Pt_3(1\ 1\ 1)/TiO_2(0\ 0\ 1)$		$Pt_3(1\ 1\ 1)/TiO_2(1\ 0\ 1)$	
	Ti d-band	Pt d-band	Ti d-band	Pt d-band
ϵ_d	-3.37	-2.93	-4.84	-2.05
w_d	4.88	2.56	5.44	1.78
E_F	-1.74		-0.44	
	Initial state			
	Ti d-band	Pt d-band	Ti d-band	Pt d-band
ϵ_d	-4.40	-2.76	-6.62	-2.71
w_d	6.25	2.92	6.94	2.36
E_F	-1.96		-0.07	
	Transition state			
	Ti d-band	Pt d-band	Ti d-band	Pt d-band
ϵ_d	-4.42	-2.96	-6.69	-2.32
w_d	6.24	3.13	6.97	2.01
E_F	-1.75		-0.01	
	Final state			
	Ti d-band	Pt d-band	Ti d-band	Pt d-band
ϵ_d	-4.38	-3.32	-6.78	-2.97
w_d	6.22	3.18	6.98	2.37
E_F	-1.86		0.02	

Analyzing the isolated $Pt_3(1\ 1\ 1)/TiO_2(h\ k\ l)$ interfaces, it was observed that the $Pt_3(1\ 1\ 1)/TiO_2(0\ 0\ 1)$ interface the energy levels of ϵ_{d-Ti} and ϵ_{d-Pt} were found to be -3.37 eV and -2.76 eV, respectively. The Fermi energy is -1.96 eV, suggesting the presence of antibonding states above the Fermi energy, given that the ϵ_d values are near the Fermi level. In contrast, the $Pt_3(1\ 1\ 1)/TiO_2(1\ 0\ 1)$ interface exhibited ϵ_{d-Ti} and ϵ_{d-Pt} values of -4.84 eV and -2.05 eV, respectively. Both ϵ_d values are well below the Fermi energy level, indicating the presence of antibonding states below the Fermi energy. For the IS, overall ϵ_d and w_d values indicate a shift to lower energy. The ϵ_{d-Pt} of the $Pt_3(1\ 1\ 1)/TiO_2(0\ 0\ 1)$ interface varies by 0.17 eV, while the ϵ_{d-Pt} of the $Pt_3(1\ 1\ 1)/TiO_2(1\ 0\ 1)$ interface varies by 0.66 eV. This suggests that the $Pt_3(1\ 1\ 1)/TiO_2(1\ 0\ 1)$ interface is more influence on the interaction with hydrogen molecule. In the TS, the $Pt_3(1\ 1\ 1)/TiO_2(0\ 0\ 1)$ interface presented a w_{d-Pt} value of 3.13 eV, while the $Pt_3(1\ 1\ 1)/TiO_2(1\ 0\ 1)$ interface showed a w_{d-Pt} value of 2.01 eV, with the ϵ_{d-Pt} at a higher energy level. This indicates that the $Pt_3(1\ 1\ 1)/TiO_2(1\ 0\ 1$ interface has a smaller E_a compared to the $Pt_3(1\ 1\ 1)/TiO_2(0\ 0\ 1)$ interface. The smaller w_d values suggest a more selective reactivity during the hydrogen splitting process, contributing to E_a reduction. For FS, the ϵ_{d-Pt} value of -3.32 eV for the Pt_3(1 1 1)$/TiO_2$(0 0 1) interface indicates that the state is more stable than the FS for the Pt_3(1 1 1)$/TiO_2$(1 0 1) interface, which has ϵ_{d-Pt} values of -2.97 eV. Therefore, as shown in the PDOS structure (Figure 23c-f), the hydrogen molecule splitting on the Pt_3(1 1 1)$/TiO_2$(0 0 1) interface presents a more spontaneous process.

In summary, the reaction path of hydrogen molecule splitting on the Pt_3(1 1 1)$/TiO_2$(h k l) interfaces involved distinct reaction states. The initial state (IS) presented the physisorption of the H_2 molecule on the Pt_3(1 1 1)$/TiO_2$(h k l) interface, where the hydrogen molecule was oriented by thePt(1 1 1) surface. Different transition states (TS) were determined for the Pt_3(1 1 1)$/TiO_2$(0 0 1) and Pt_3(1 1 1)$/TiO_2$(1 0 1) interfaces, indicating distinct reaction pathways. The calculated ΔE values suggest an exothermic reaction of the hydrogen molecule splitting for both interfaces. However, The E_a value is smaller for the Pt_3(1 1 1)$/TiO_2$(1 0 1) interface. The PDOS analysis provided the interactions between hydrogen and Pt atoms in the IS, TS, and FS, highlighting the stability of the reaction state on the Pt_3(1 1 1)$/TiO_2$(0 0 1) interface . The d-band analysis showed the influence of the Pt_3(1 1 1)$/TiO_2$(1 0 1) interface on hydrogen molecule interaction, with implications for reactivity and E_a reduced.

5.2.4 Reaction path of the water splitting on the Pt_3(1 1 1)$/TiO_2$(h k l) interface

Water splitting was studied on the Pt_3(1 1 1)$/TiO_2$(h k l) interfaces, considering their structural and electronic properties. The geometries of the interfaces, with species of the initial states (IS), transition state (TS), and final state (FS), are involved in the mechanism for water splitting on thePt_3(1 1 1)$/TiO_2$(0 0 1) interface and Pt_3(1 1 1)$/TiO_2$(1 0 1) interface, as shown in Figure 24.

One water molecule was selected to aim for a molecular-scale understanding of the fundamental reaction pathway and to estimate the activation energy barrier for water splitting, using CI-NEB calculations with nine images-steps, where IS and FS were proposed from a fundamental step of the adsorbed $H – O – H$ (H_2O) to the dissociated states (OH^* + H^*):

$$H_2O_{ads} \rightarrow OH^*_{ads} + H^*_{ads} \qquad \text{(reaction-3)}$$

where OH^* and H^* are the species adsorbed on the Pt_3(1 1 1)$/TiO_2$(h k l) interfaces. The water

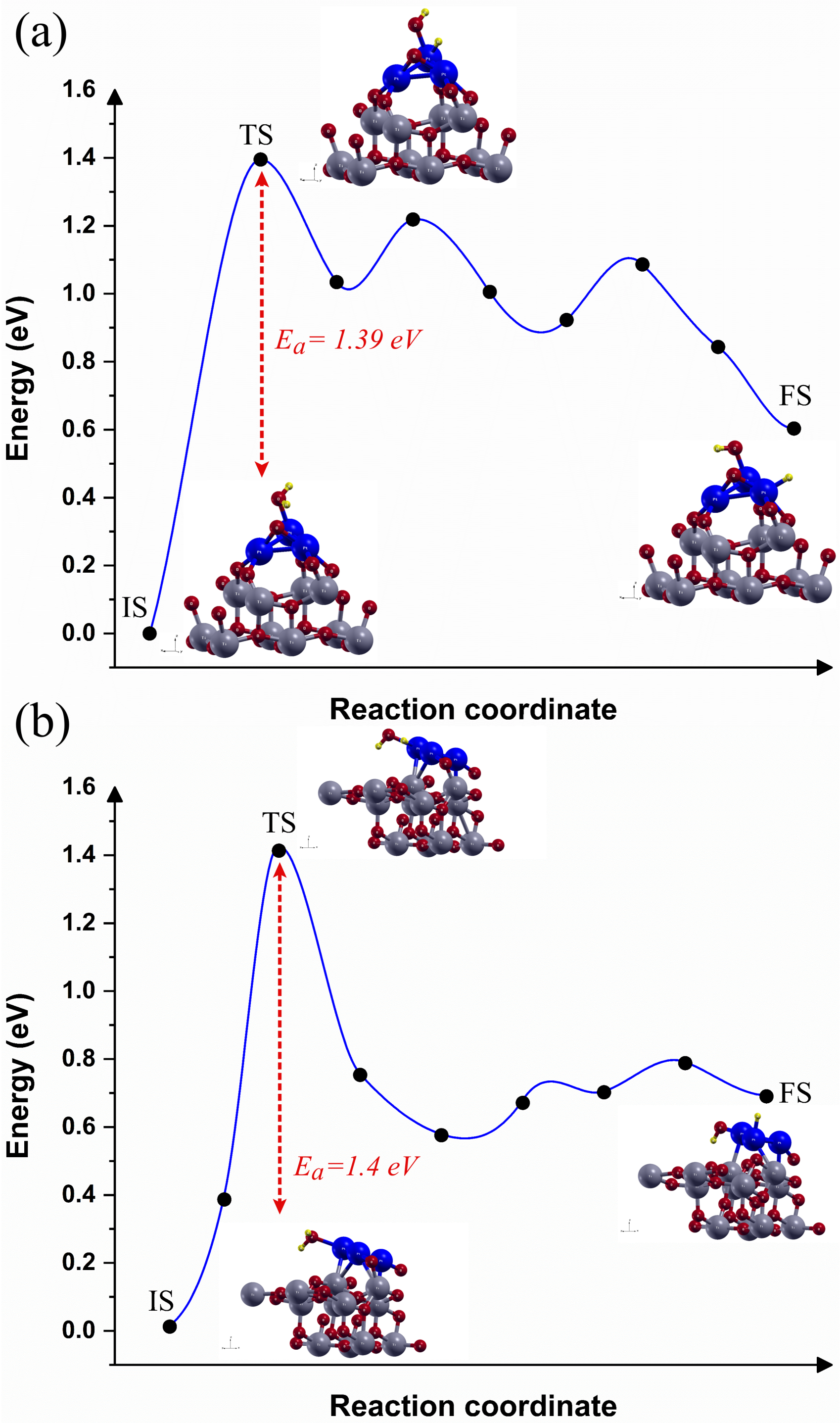

Figure 24 – Reaction pathway and reaction barrier of water splitting molecule splitting (a) $Pt_3(1\,1\,1)/TiO_2(0\,0\,1)$ interface and (b) $Pt_3(1\,1\,1)/TiO_2(1\,0\,1)$ interface. The yellow balls represent the hydrogen atoms.

splitting activation energy barrier (E_a) was determined by equation (5.2), and the endothermic and exothermic reaction was calculated by reaction energy (ΔE) – equation (5.3). All of the images of initial, transition, and final states of hydrogen splitting reactions can be seen in annex C1 - supplementary information, Figure 41.

The IS of splitting on the $Pt_3(1\ 1\ 1)/TiO_2(h\ k\ l)$ interfaces correspond to the water molecule adsorbed on the interface surfaces. The FS corresponds to the dissociated water molecule, such as OH^*, and H^*, species adsorbed on the interface surface. In both $Pt_3(1\ 1\ 1)/TiO_2(h\ k\ l)$ interfaces, one of the H atoms from the water molecule is oriented towards the $Pt_3(1\ 1\ 1)$ surface, with one of the H atoms positioned near the $TiO_2(1\ 0\ 1)$ surface in the $Pt_3(1\ 1\ 1)/TiO_2(1\ 0\ 1)$ interface. For the water splitting reaction path, similar TS were determined for the $Pt_3(1\ 1\ 1)/TiO_2(0\ 0\ 1)$ interface, Figure 24a, and $Pt_3(1\ 1\ 1)/TiO_2(1\ 0\ 1)$ interface, Figure 24b. It is possible to observe that the water molecule is dissociated on the $Pt_3(1\ 1\ 1)/TiO_2(0\ 0\ 1)$ interface, with 2.0543 Å $OH^* - Pt$ bond length and 1.6364 Å H – Pt bonds lengths. In the $Pt_3(1\ 1\ 1)/TiO_2(1\ 0\ 1)$ interface, the water molecule is dissociated with 2.0792 Å $OH^* - Pt$ bond length and 1.6244 Å $H - Pt$ bonds lengths. The ΔE calculation indicates that the water molecule splitting has an endothermic character for the $Pt_3(1\ 1\ 1)/TiO_2(0\ 0\ 1)$ interface (ΔE=0.60 eV) and $Pt_3(1\ 1\ 1)/TiO_2(0\ 0\ 1)$ interface (ΔE=0.69 eV). However, the E_a predicted for the $Pt_3(1\ 1\ 1)/TiO_2(0\ 0\ 1)$ interface and $Pt_3(1\ 1\ 1)/TiO_2(1\ 0\ 1)$ interface are 1.39 eV and 1.40 eV, respectively, it's practically the same E_a.

Water splitting on the $Pt_3(1\ 1\ 1)/TiO_2(h\ k\ l)$ interfaces has not been reported in the literature. However, other types of Pt/TiO_2 interfaces are discussed, as reported by Kong *et al.* [32], who studied the $Pt/TiO_2/Ni(OH)_2$ structure applied in water electrolysis. The authors [32] performed a theoretical study with DFT and reported a $Pt/TiO_2(1\ 0\ 1)$ interface, where the activation energy for water splitting was 0.22 eV. The chosen reaction mechanism involved adsorbing the water molecule on the $TiO_2(1\ 0\ 1)$ surface, with the OH^* specie adsorbed on the $TiO_2(1\ 0\ 1)$ surface, and the H^* specie adsorbed on the Pt surface. On the other hand, Dai *et al.* [33] studied the Pt/TiO_2–$P25$ interface for hydrogen evolution from water splitting. The authors [33] used Pt_9 and Pt_{13} clusters for the Pt/TiO_2–$P25$ interface, simulating water splitting by adsorbing the water molecule on the Pt phase at the interface limit with the TiO_2 phase's hydroxyl-rich surface. According to the authors [33], the activation energy was in the range of approximately 0.58 eV to 1.1 eV. Therefore, when the water splitting reaction occurs on the Pt surface, the trend is for the activation energy to be higher.

The similar behavior between E_a and ΔE of the$Pt_3(1\ 1\ 1)/TiO_2(h\ k\ l)$ interfaces can be related to the electronic properties and the reaction mechanism, mainly to the transition state (TS), which the H^* specie is adsorbed on the same Pt atom that the OH^* species, leaving the H^* specie there is a diffusion by spillover mechanism. However, the similar behavior presented by the $Pt_3(1\ 1\ 1)/TiO_2(1\ 0\ 1)$ interface can be analyzed by the PDOS structure, as shown in Figure 25.

It is possible to observe in Figure 25a-f that the $Pt-5d$ states, green lines in PDOS, are localized near the Fermi energy (E_F). In the IS of the $Pt_3(1\ 1\ 1)/TiO_2(0\ 0\ 1)$ interface, shown in Figure **??**a, the O_w-2p and H_w-1s states of the water molecule, cyan and purple lines in PDOS, respectively, are localized around -10 eV and range from -7 eV to -4 eV . In the IS of the $Pt_3(1\ 1\ 1)/TiO_2(1\ 0\ 1)$ interface, shown in Figure 25d, the O_w-2p and $H-1s$ states of the water molecule are localized around -9 eV and range from -7 eV to -4 eV, at very similar energy levels to the $Pt_3(1\ 1\ 1)/TiO_2(0\ 0\ 1)$ interface.

In the TS of the $Pt_3(1\ 1\ 1)/TiO_2(0\ 0\ 1)$ interface, as shown in Figure 7b, the water molecule is dissociated. The O_w- 2p and H_w-1s states of the water molecule are localized at a high energy level, approximately -8 eV, and a range from -3 eV to -1 eV, with the $Pt-5d$ state overlapping. In the TS of the $Pt_3(1\ 1\ 1)/TiO_2(1\ 0\ 1)$ interface, shown in Figure 25e, O_w-2p and H_w-1s states are localized above -8 eV and in a range from -4 eV to -2 eV, with the $Pt-5d$ state overlapping. Thus, the transition state on the $Pt_3(1\ 1\ 1)/TiO_2(0\ 0\ 1)$ interface exhibits states at similar energy levels to the $Pt_3(1\ 1\ 1)/TiO_2(1\ 0\ 1)$ interface. This indicates that a similar amount of energy is required for the water splitting reaction to follow, resulting in the same activation energy (E_a).

In the FS of the $Pt_3(1\ 1\ 1)/TiO_2(0\ 0\ 1)$ interface, shown in Figure 25c, the O_w-2p and H_w-1s from the water molecule are localized at a lower energy level around -7 eV and range from -4 eV to -2 eV. In the TS of the $Pt_3(1\ 1\ 1)/TiO_2(0\ 0\ 1)$ interface, shown in Figure 25f, the O_w-2p and H_w-1s from the water molecule are localized around -7 eV and range from -4 eV to -2 eV. The PDOS structure comparison of IS, TS, and FS for the $Pt_3(1\ 1\ 1)/TiO_2(0\ 0\ 1)$ and $Pt_3(1\ 1\ 1)/TiO_2(1\ 0\ 1)$ interfaces suggests that the water splitting reaction is energetically the same, as shown previously with the activation energy. In both interfaces, the water splitting is not favorable when considering the reaction on the $Pt_3(1\ 1\ 1)$ surface.

The PDOS structure of water splitting on the $Pt_3(1\ 1\ 1)/TiO_2(h\ k\ l)$ interfaces contributes insights into the energy level of states. The behavior of the d-band can also play a fundamental role in understanding the reactivity of the $Pt_3(1\ 1\ 1)/TiO_2(h\ k\ l)$ interfaces. Table 7 shows the d-band center (ϵ_d), d-band width (w_d), and Fermi energy (E_F) levels of the isolated $Pt_3(1\ 1\ 1)/TiO_2(h\ k\ l)$ interfaces, initial state (IS), transition state (TS), and final state (FS) of water splitting on the $Pt_3(1\ 1\ 1)/TiO_2(h\ k\ l)$ interfaces.

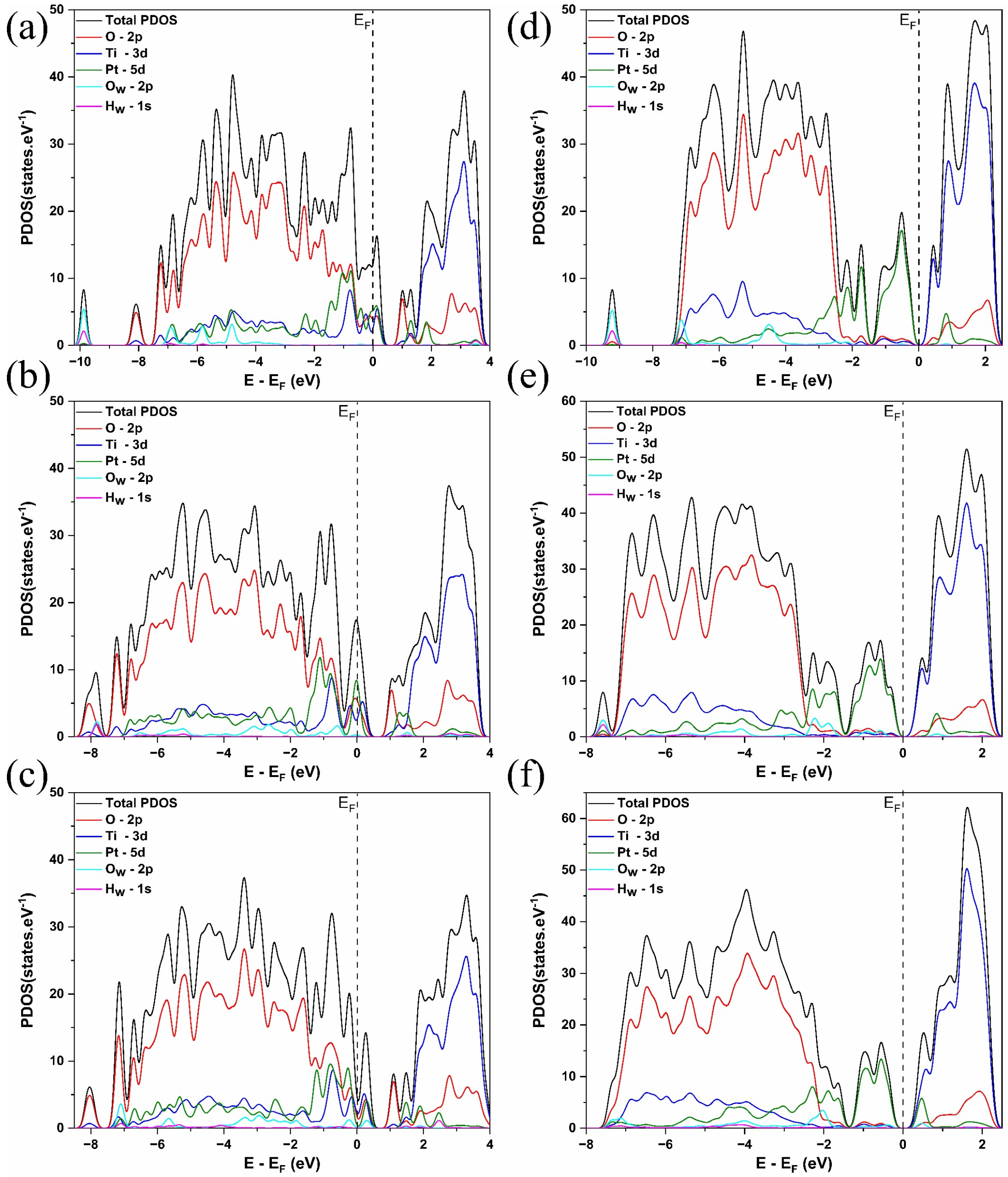

Figure 25 – Projected density of States (PDOS) for water splitting on the $Pt_3(1\ 1\ 1)/TiO_2(0\ 0\ 1)$ interface (a) IS, (b) TS, (c) FS, and for $Pt_3(1\ 1\ 1)/TiO_2(1\ 0\ 1)$ interface (d) IS, (e) TS, and (f) FS.

It is possible to notice in Table 7, that in the IS, all the ϵ_d values have shifted to lower energy levels, and for w_d values there is an increase. The ϵ_{d-Pt} of the $Pt_3(1\ 1\ 1)/TiO_2(0\ 0\ 1)$ interface varies by 0.17 eV ($\epsilon_{d-Pt(IS)} - \epsilon_{d-Pt(FS)}$) , while the ϵ_{d-Pt} of the $Pt_3(1\ 1\ 1)/TiO_2(1\ 0\ 1)$ interface varies by 0.07 eV $\epsilon_{d-Pt(IS)} - \epsilon_{d-Pt(FS)}$. This suggests that in both $Pt_3(1\ 1\ 1)/TiO_2(h\ k\ l)$ interfaces, there is a minimal influence on the interaction with the water molecule when oriented towards the $Pt_3(1\ 1\ 1)$ surface. In the TS, the $Pt_3(1\ 1\ 1)/TiO_2(0\ 0\ 1)$ interface presented a w_{d-Pt} value of 3.18 eV, while the $Pt_3(1\ 1\ 1)/TiO_2(1\ 0\ 1)$ interface showed a w_{d-Pt} value of 2.28

Table 7 – Electronic structure of the d-band projected: d-band center (ϵ_d), d-band width (w_d) and Fermi energy (E_F) of the TiO_2, Pt isolate phase and water splitting states on the $Pt_3(1\,1\,1)/TiO_2(h\;k\;l)$ interface.

d-band shape	$Pt_3(1\,1\,1)/TiO_2(0\,0\,1)$		$Pt_3(1\,1\,1)/TiO_2(1\,0\,1)$	
	Ti d-band	Pt d-band	Ti d-band	Pt d-band
ϵ_d	-3.37	-2.93	-4.84	-2.05
w_d	4.88	2.56	5.44	1.78
E_F	-1.74		-0.44	
	Initial state			
	Ti d-band	Pt d-band	Ti d-band	Pt d-band
ϵ_d	-4.54	-3.1	-6.49	-2.12
w_d	6.22	3.12	6.93	2.04
E_F	-1.4		-0.12	
	Transition state			
	Ti d-band	Pt d-band	Ti d-band	Pt d-band
ϵ_d	-4.53	-3.32	-6.57	-2.40
w_d	6.20	3.18	6.97	2.28
E_F	-1.65		-0.3	
	Final state			
	Ti d-band	Pt d-band	Ti d-band	Pt d-band
ϵ_d	-4.40	-3.17	-6.53	-2.49
w_d	6.22	3.17	7.01	2.23
E_F	-1.87		-0.47	

eV. This suggests that the $Pt_3(1\,1\,1)/TiO_2(1\,0\,1)$ interface could exhibit more selective reactivity during the water splitting reaction. However, ϵ_{d-Pt} of the $Pt_3(1\,1\,1)/TiO_2(0\,0\,1)$ interface varies by 0.22 eV, and the $Pt_3(1\,1\,1)/TiO_2(1\,0\,1)$ interface varies by 0.28 eV, contributing to similar E_a. For FS, the ϵ_{d-Pt} value of -3.17 eV for the $Pt_3(1\,1\,1)/TiO_2(0\,0\,1)$ interface indicates that the state is more stable than the FS for the $Pt_3(1\,1\,1)/TiO_2(1\,0\,1)$ interface, which has ϵ_{d-Pt} values of -2.49 eV. In contrast, the variation of the ϵ_{d-Pt} FS compared with ϵ_{d-Pt} TS, is 0.15 eV for $Pt_3(1\,1\,1)/TiO_2(0\,0\,1)$ interface and 0.09 eV for $Pt_3(1\,1\,1)/TiO_2(1\,0\,1)$ interface. Therefore, as shown in the reaction path (Figure 24), the PDOS structure (Figure 25a-f) and the analysis of d-band behavior (Table 7), the water splitting on the $Pt_3(1\,1\,1)$ surface of the $Pt_3(1\,1\,1)/TiO_2(h\;k\;l)$ interfaces will not be a spontaneous process.

The Pt/TiO_2 structure is used as a photocatalyst for hydrogen production from water splitting and has been reported in the literature to exhibit high hydrogen production rate (HGR) values, ranging from ∼325 to up to 1023 ($\mu mol.h^{-1}$) [34–37]. However, another structure has been reported with higher HGR values than the Pt/TiO_2 interface, such as $Fe_3O_4@C@TiO_2$ structure with an HGR value of 1593 ($\mu mol.h^{-1}$) [38], Cu/TiO_2 interface with an HGR value of 2061 ($\mu mol.h^{-1}$) [39], or $Cu/Ni@Ni/TiO_2$ structure with an HGR value of 13,450 ($\mu mol.h^{-1}$) [40].

Therefore, the Pt/TiO_2 interface, such as $Pt_3(1\,1\,1)/TiO_2(h\,k\,l)$ interfaces, has an HGR values limitation, as the water splitting reaction can occur on the$Pt(1\,1\,1)$ surface or $TiO_2(h\,k\,l)$ surface. When it occurs on the$Pt(1\,1\,1)$, as shown here, water splitting is not favorable. The reaction path of water splitting on the $Pt_3(1\,1\,1)/TiO_2(h\,k\,l)$ interfaces involves similar reaction states. The initial state (IS) presents the adsorption of the water molecule on the $Pt_3(1\,1\,1)/TiO_2(h\,k\,l)$ interface, where the hydrogen atoms are oriented by the$Pt(1\,1\,1)$ surface, with one of the H atoms positioned near the $TiO_2(1\,0\,1)$ surface in the $Pt_3(1\,1\,1)/TiO_2(1\,0\,1)$ interface. Similar transition states (TS) were determined for the $Pt_3(1\,1\,1)/TiO_2(0\,0\,1)$ and $Pt_3(1\,1\,1)/TiO_2(1\,0\,1)$ interfaces, indicating the same reaction pathways. The calculated ΔE values suggest an endothermic reaction of water splitting for both interfaces. The E_a value is similar for the $Pt_3(1\,1\,1)/TiO_2(h\,k\,l)$ interface. The PDOS analysis provided insights into the interactions between OH^* and H^* species from the water molecule and Pt atoms in the IS, TS, and FS, highlighting the energy levels of the reaction state on the $Pt_3(1\,1\,1)/TiO_2(0\,0\,1)$ interface. The d-band analysis showed the minimal influence of the $Pt_3(1\,1\,1)/TiO_2(1\,0\,1)$ interface on water molecule interaction, with implications for reactivity and E_a value.

5.3 Conclusions

The investigation into hydrogen and water splitting on the $Pt_3(1\,1\,1)/TiO_2(h\,k\,l)$ interface is adequate but requires a more comprehensive understanding of the reaction mechanism. The structural and electronic properties of the $Pt_3(1\,1\,1)/TiO_2(h\,k\,l)$ interface, as well as hydrogen and water splitting on the $Pt_3(1\,1\,1)$ surface, were investigated through DFT/plane-wave and DFT/CI-NEB.

The $Pt_3(1\,1\,1)/TiO_2(h\,k\,l)$ interface has been theoretically modeled based on X-ray diffraction with Rietveld refinement and synthesized using the Pechini method. The structural analysis showed that the $Pt_3(1\,1\,1)/TiO_2(h\,k\,l)$ interfaces exhibited $Pt-Pt$, $Pt-Ti$, and $Pt-O$ bonds. In the $Pt_3(1\,1\,1)/TiO_2(0\,0\,1)$ interface, more $Pt-O$ bonds are observed in the interface, while in the $Pt_3(1\,1\,1)/TiO_2(1\,0\,1)$ interface, more $Pt-Ti$ bonds in the interface. The electronic properties of the $Pt_3(1\,1\,1)/TiO_2(h\,k\,l)$ interface were investigated by analysis of the band structure, PDOS, charge density distribution (Δn), and electron localization function ($ELF-\eta(r)$). The BS and PDOS behavior for $Pt_3(1\,1\,1)/TiO_2(h\,k\,l)$ interface indicate the metallic behavior in both interfaces, where the overlapping of the valence and conduction bands.

The Pt_3(1 1 1)/TiO_2(0 0 1) interface, exhibited Δn_{max} ~1.54, while the Pt_3(1 1 1)/TiO_2(1 0 1) interface, presented Δn_{max}~1.47. The 2D $ELF - \eta(r)$ maps showed that the Pt_3(1 1 1)/TiO_2(0 0 1) interface exhibits $Ti - O$ bonds with ionic characteristics, and the $Pt - O$ more covalent character than one $Pt - Ti$ bond. The Pt_3(1 1 1)/TiO_2(1 0 1) interface demonstrates a more covalent character in the $Ti - O$ bonds compared to the Pt_3(1 1 1)/TiO_2(0 0 1) interface, and the $Pt - O$ bonds more covalent character than the $Pt - Ti$ bonds.

The mechanism reaction of the hydrogen molecule splitting leads to the H_2 molecule physisorbed in the reaction's initial state (IS). The transition states (TS) showed that the Pt_3(1 1 1)/TiO_2(0 0 1) interface presented the H_2 molecule dissociated and E_a=0.36 eV. For Pt_3(1 1 1)/TiO_2(1 0 1) interface, the TS presented the H_2 molecule physisorbed and E_a=0.19 eV. Thus, the Pt_3(1 1 1)/TiO_2(1 0 1) interface is energetically more favorable for hydrogen molecule splitting, and the Pt_3(1 1 1)/TiO_2(0 0 1) interface exhibits a more spontaneous process for hydrogen molecule with a smaller ΔE. The mechanism reaction of the water splitting leads to the water molecule absorbed on the Pt(1 1 1) surface of the Pt_3(1 1 1)/TiO_2(h k l) interface in the reaction's IS. Similar TS and E_a value were determined for the Pt_3(1 1 1)/TiO_2(0 0 1) and Pt_3(1 1 1)/TiO_2(1 0 1) interfaces, indicating the same reaction pathways. The ΔE values suggest an endothermic reaction of water splitting for both interfaces. Therefore, water splitting is not favorable on thePt_3(1 1 1)/TiO_2(h k l) interface, which may indicate the HGR values are limited compared to other structures for water splitting.

5.4 Acknowledgments

The authors would like to thank the Brazilian research-funding institutions FAPEAM and CNPq by financial resources. We also thank CENAPAD/SP and UFMT-STI/Server for providing computational time.

BIBLIOGRAPHY

1 HOHENBERG, P.; KOHN, W. Inhomogeneous electron gas. *Physical review*, APS, v. 136, n. 3B, p. B864, 1964. 114

2 KOHN, W.; SHAM, L. J. Self-consistent equations including exchange and correlation effects. *Physical review*, APS, v. 140, n. 4A, p. A1133, 1965. 114

3 GIANNOZZI, P. et al. Quantum espresso: a modular and open-source software project for quantum simulations of materials. *Journal of physics: Condensed matter*, IOP Publishing, v. 21, n. 39, p. 395502, 2009. 114

4 PERDEW, J. P.; BURKE, K.; ERNZERHOF, M. Generalized gradient approximation made simple. *Physical review letters*, APS, v. 77, n. 18, p. 3865, 1996. 114

5 MONKHORST, H. J.; PACK, J. D. Special points for brillouin-zone integrations. *Physical review B*, APS, v. 13, n. 12, p. 5188, 1976. 114

6 SETYAWAN, W.; CURTAROLO, S. High-throughput electronic band structure calculations: Challenges and tools. *Computational materials science*, Elsevier, v. 49, n. 2, p. 299–312, 2010. 115

7 YU, Y.; ZHANG, W.; MEI, D. Artificial neural network potential for encapsulated platinum clusters in mof-808. *The Journal of Physical Chemistry C*, ACS Publications, v. 126, n. 2, p. 1204–1214, 2022. 116

8 HEREDIA, C. L.; FERRARESI-CUROTTO, V.; LÓPEZ, M. Characterization of ptn (n= 2–12) clusters through global reactivity descriptors and vibrational spectroscopy, a theoretical study. *Computational materials science*, Elsevier, v. 53, n. 1, p. 18–24, 2012. 116

9 MAHATA, A.; NAIR, A. S.; PATHAK, B. Recent advancements in pt-nanostructure-based electrocatalysts for the oxygen reduction reaction. *Catalysis Science & Technology*, Royal Society of Chemistry, v. 9, n. 18, p. 4835–4863, 2019. 116

10 KUMARI, S. et al. Electrocatalytic hydrogen evolution at full atomic utilization over ito-supported sub-nano-pt n clusters: High, size-dependent activity controlled by fluxional pt hydride species. *Journal of the American Chemical Society*, ACS Publications, v. 145, n. 10, p. 5834–5845, 2023. 116

11 KANG, J. H. et al. Unusual non-bulk properties in nanoscale materials: thermal metal-metal bond contraction of γ-alumina-supported pt catalysts. *Journal of the american chemical society*, ACS Publications, v. 128, n. 37, p. 12068–12069, 2006. 116

12 CHEN, J. et al. Reverse oxygen spillover triggered by co adsorption on sn-doped pt/tio2 for low-temperature co oxidation. *Nature Communications*, Nature Publishing Group UK London, v. 14, n. 1, p. 3477, 2023. 116

13 CHEN, H. et al. Bonding and electron energy-level alignment at metal/tio2 interfaces: A density functional theory study. *The Journal of Physical Chemistry C*, ACS Publications, v. 120, n. 10, p. 5549–5556, 2016. 116, 120

14 PICCOLO, L. et al. Operando x-ray absorption spectroscopy investigation of photocatalytic hydrogen evolution over ultradispersed pt/tio2 catalysts. *ACS catalysis*, ACS Publications, v. 10, n. 21, p. 12696–12705, 2020. 116

15 CHEN, L. et al. Unlocking the catalytic potential of tio2-supported pt single atoms for the reverse water–gas shift reaction by altering their chemical environment. *JACS Au*, ACS Publications, v. 1, n. 7, p. 977–986, 2021. 116

16 KAPILASHRAMI, M. et al. Probing the optical property and electronic structure of tio2 nanomaterials for renewable energy applications. *Chemical reviews*, ACS Publications, v. 114, n. 19, p. 9662–9707, 2014. 116

17 JIN, C. et al. Effects of single metal atom (pt, pd, rh and ru) adsorption on the photocatalytic properties of anatase tio2. *Applied Surface Science*, Elsevier, v. 426, p. 639–646, 2017. 117, 118

18 WANG, Y. et al. Adsorption of sf6 decomposition components on pt3-tio2 (1 0 1) surface: A dft study. *Applied Surface Science*, Elsevier, v. 459, p. 242–248, 2018. 118

19 HU, Y. et al. Lattice distortion induced internal electric field in tio2 photoelectrode for efficient charge separation and transfer. *Nature Communications*, Nature Publishing Group UK London, v. 11, n. 1, p. 2129, 2020. 119

20 GAO, H.; DING, C.; DAI, D. Density functional characterization of c-doped anatase tio2 with different oxidation state. *Journal of Molecular Structure: THEOCHEM*, Elsevier, v. 944, n. 1-3, p. 156–162, 2010. 119

21 JR, E. J. L.; JONES, M. M. A complete table of electronegativities. *Journal of chemical education*, ACS Publications, v. 37, n. 5, p. 231, 1960. 119

22 ZHANG, D. et al. Experimental and density functional theory investigation of pt-loaded titanium dioxide/molybdenum disulfide nanohybrid for so 2 gas sensing. *New Journal of Chemistry*, Royal Society of Chemistry, v. 43, n. 12, p. 4900–4907, 2019. 119

23 WU, Z. et al. Microwave synthesis of pt clusters on black tio2 with abundant oxygen vacancies for efficient acidic electrocatalytic hydrogen evolution. *Angewandte Chemie*, Wiley Online Library, v. 135, n. 14, p. e202300406, 2023. 119

24 JR, N. B. A.; KASAI, H. Potential energy surfaces for h2 dissociative adsorption on pt (111) surface—effects of vacancies. *Surface and Interface Analysis: An International Journal devoted to the development and application of techniques for the analysis of surfaces, interfaces and thin films*, Wiley Online Library, v. 40, n. 6-7, p. 1103–1107, 2008. 121

25 CRUZ, A. et al. Theoretical study of the h 2 reaction with a pt 4 (111) cluster. *The Journal of chemical physics*, American Institute of Physics, v. 120, n. 13, p. 6222–6228, 2004. 121

26 KHOOBIAR, S. Particle to particle migration of hydrogen atoms on platinum—alumina catalysts from particle to neighboring particles. *The Journal of Physical Chemistry*, ACS Publications, v. 68, n. 2, p. 411–412, 1964. 121

27 LIU, Y. et al. Direct observation of accelerating hydrogen spillover via surface-lattice-confinement effect. *Nature Communications*, Nature Publishing Group UK London, v. 14, n. 1, p. 613, 2023. 121

28 GENG, Z. et al. Low-temperature hydrogen production via water conversion on pt/tio2. *The Journal of Physical Chemistry C*, ACS Publications, v. 122, n. 20, p. 10956–10962, 2018. 122

29 KWON, H. et al. Highly-sensitive h2 sensor operating at room temperature using pt/tio2 nanoscale schottky contacts. *Sensors and Actuators B: Chemical*, Elsevier, v. 241, p. 985–992, 2017. 122

30 WANG, S. et al. Insights into the active sites of dual-zone synergistic catalysts for semi-hydrogenation under hydrogen spillover. *AIChE Journal*, Wiley Online Library, v. 69, n. 3, p. e17886, 2023. 122

31 WAN, W. et al. Adsorption, dissociation, and spillover of hydrogen over au/tio2 catalysts: the effects of cluster size and metal–support interaction from dft. *The Journal of Physical Chemistry C*, ACS Publications, v. 122, n. 31, p. 17895–17916, 2018. 122

32 KONG, A. et al. Robust pt/tio2/ni (oh) 2 nanosheet arrays enable outstanding performance for high current density alkaline water electrolysis. *Applied Catalysis B: Environmental*, Elsevier, v. 316, p. 121654, 2022. 128

33 DAI, F. et al. Pt-surface oxygen vacancies coupling accelerated photo-charge extraction and activated hydrogen evolution. *Nano Research*, Springer, v. 16, n. 4, p. 4736–4741, 2023. 128

34 YU, J.; QI, L.; JARONIEC, M. Hydrogen production by photocatalytic water splitting over pt/tio2 nanosheets with exposed (001) facets. *The Journal of Physical Chemistry C*, ACS Publications, v. 114, n. 30, p. 13118–13125, 2010. 131

35 GAO, F.; XU, Z.; ZHAO, H. Flame spray pyrolysis made pt/tio2 photocatalysts with ultralow platinum loading and high hydrogen production activity. *Proceedings of the Combustion Institute*, Elsevier, v. 38, n. 4, p. 6503–6511, 2021. 131

36 ZHU, Z. et al. Efficient hydrogen production by photocatalytic water-splitting using pt-doped tio2 hollow spheres under visible light. *Ceramics International*, Elsevier, v. 42, n. 6, p. 6749–6754, 2016. 131

37 ABE, R. et al. A new type of water splitting system composed of two different tio2 photocatalysts (anatase, rutile) and a io3-/i- shuttle redox mediator. *Chemical physics letters*, Elsevier, v. 344, n. 3-4, p. 339–344, 2001. 131

38 SALEH, M. R. et al. Mil-53 (fe) for constructing hydrogenated fe3o4@ c@ tio2 double core-shell nanocrystals as superior bifunctional photocatalyst. *Journal of Photochemistry and Photobiology A: Chemistry*, Elsevier, v. 432, p. 114125, 2022. 131

39 YU, J.; HAI, Y.; JARONIEC, M. Photocatalytic hydrogen production over cuo-modified titania. *Journal of Colloid and Interface Science*, Elsevier, v. 357, n. 1, p. 223–228, 2011. 131

40 TIAN, H. et al. Fabrication of an efficient noble metal-free tio2-based photocatalytic system using cu–ni bimetallic deposit as an active center of h2 evolution from water. *Solar Energy Materials and Solar Cells*, Elsevier, v. 134, p. 309–317, 2015. 131

6

FINAL REMARKS

Our study presented the interaction between iron doping and TiO_2 photocatalytic properties, highlighting the potential for enhancing water splitting efficiency. Through the synthesis by the Pechini method and structural characterization, the Fe doping on anatase and rutile phases was elucidated. The results of the Fe-doped TiO_2's structural and electronic properties also offer insights into the improved photocatalytic activity. Through DFT calculation, the electronic structure modifications induced by Fe doping showed the efficiency of water splitting for sustainable energy applications.

Furthermore, our investigation into the $Pt(1\ 1\ 1)/TiO_2(h\ k\ l)$ interface showed the influence of the strains and facets on the structural and electronic properties. A Pt/tio2 theoretical model and structural and electronic properties were proposed through experimental and theoretical analysis. This analysis presented the metal/oxide interactions and characteristics of the $Pt(1\ 1\ 1)/TiO_2(h\ k\ l)$ interface, with percentages between metal and oxide.

Finally, our theoretical exploration of hydrogen and water splitting on the $Pt_3(1\ 1\ 1)/TiO_2(h\ k\ l)$ interface offers insights into reaction mechanisms and interface-driven catalysis. Through DFT/CI-NEB calculation, the structural and electronic properties influencing hydrogen and water splitting reactions were presented. Our results show the energetically favorable nature of hydrogen molecule splitting on specific interface orientations, highlighting the potential for efficient catalytic performance. However, challenges remain on the water splitting efficacy.

A

A1 - SUPPLEMENTARY INFORMATION

A.1 Supplementary Experimental Set-up

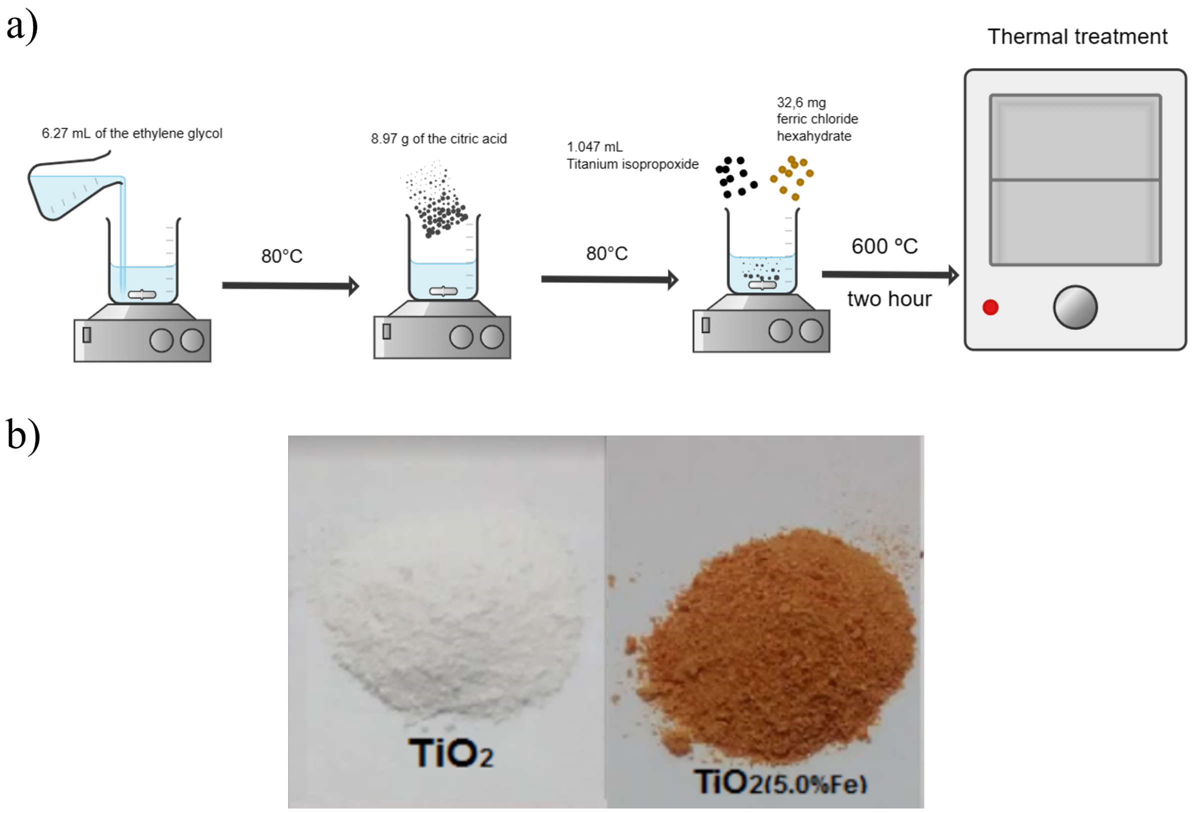

Figure 26 – a) Experimental Set-up and b) TiO_2 and Fe-doped TiO_2 in powder form.

A.2 Structural Description

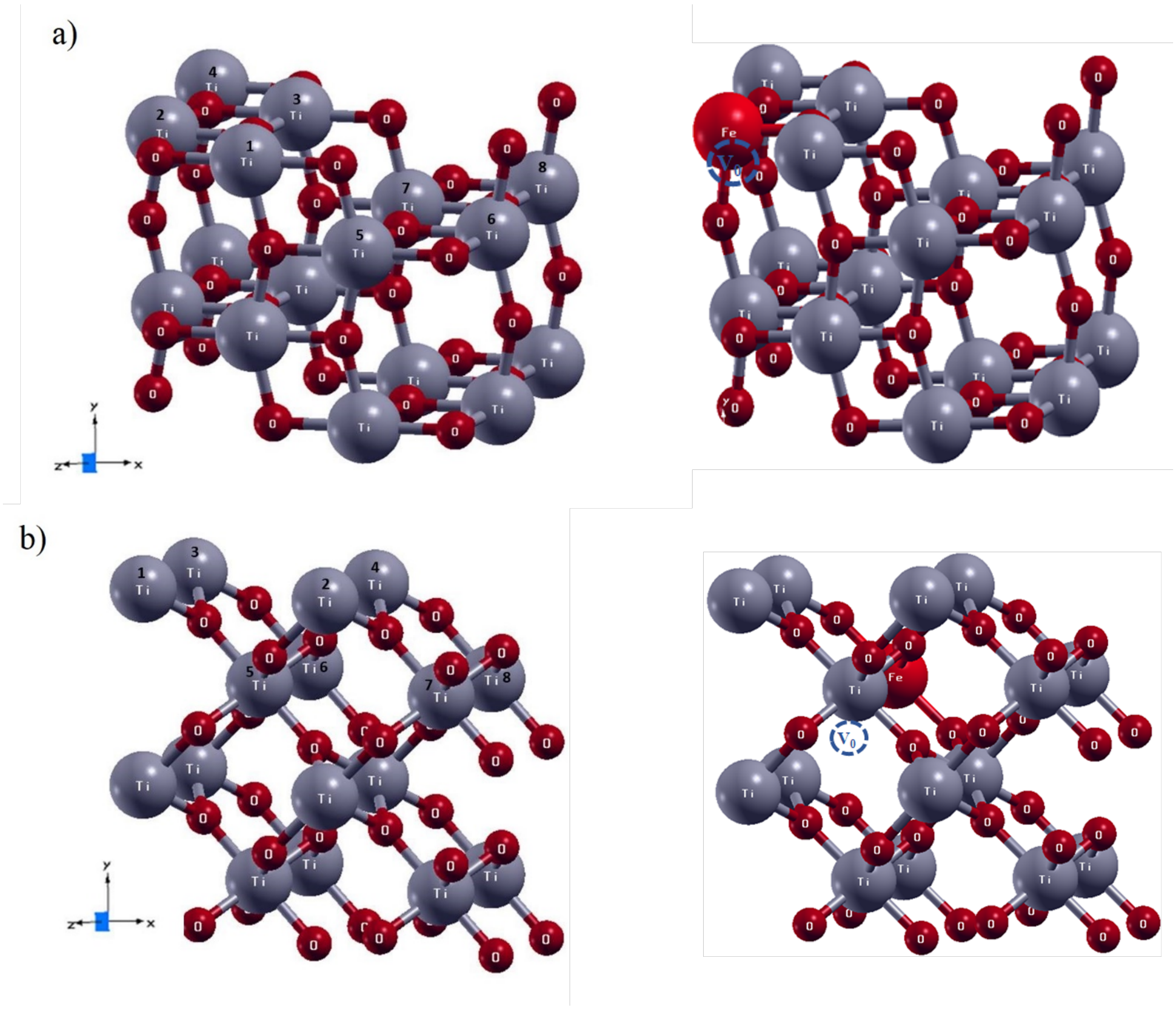

Figure 27 – Supercell TiO_2-anatase left and Fe-doped with vacancy right (a) and TiO_2-rutile and Fe-doped with vacancy right (b) in the plane (*0 1 0*) with possible doping sites (1-8).

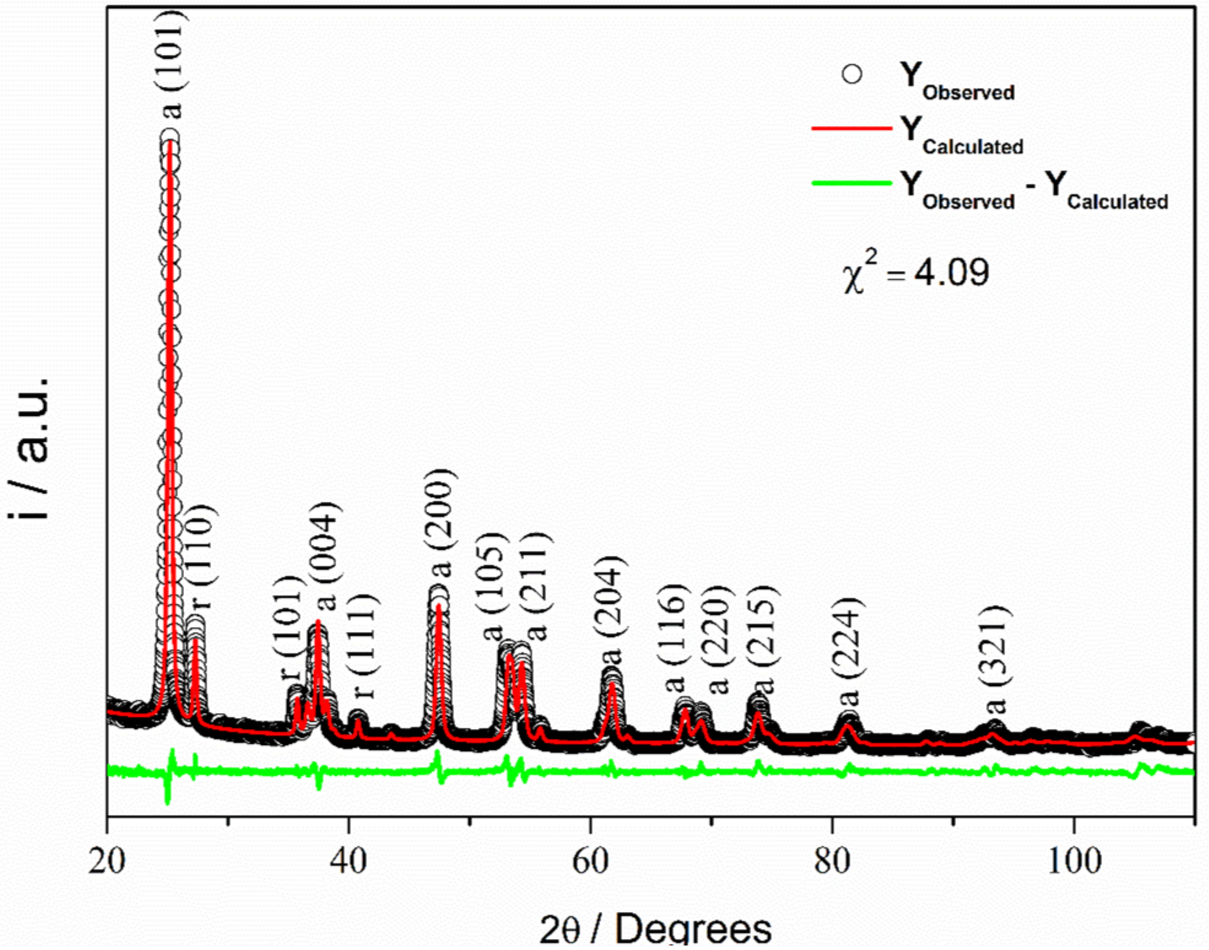

Figure 28 – Rietveld refinement pattern for TiO_2 P25-Degussa.

A.3 Electronic and Optical Properties

A.3.1 Band Structure

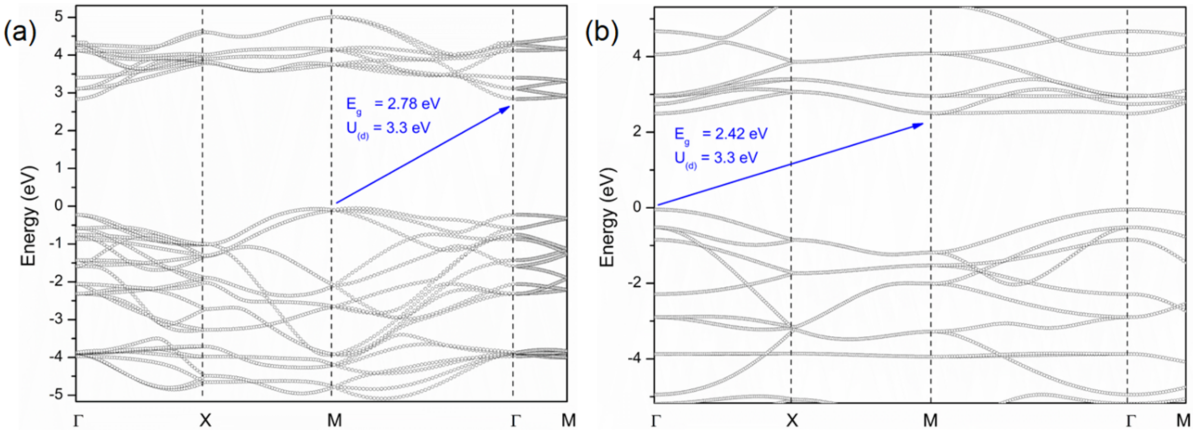

Figure 29 – Band structure for anatase TiO_2 (a) and rutile TiO_2 (b) from Rietveld refinement structure with U_d = 3.3 eV.

A.3.2 2 Experimental and Theoretical Solid State UV-Vis

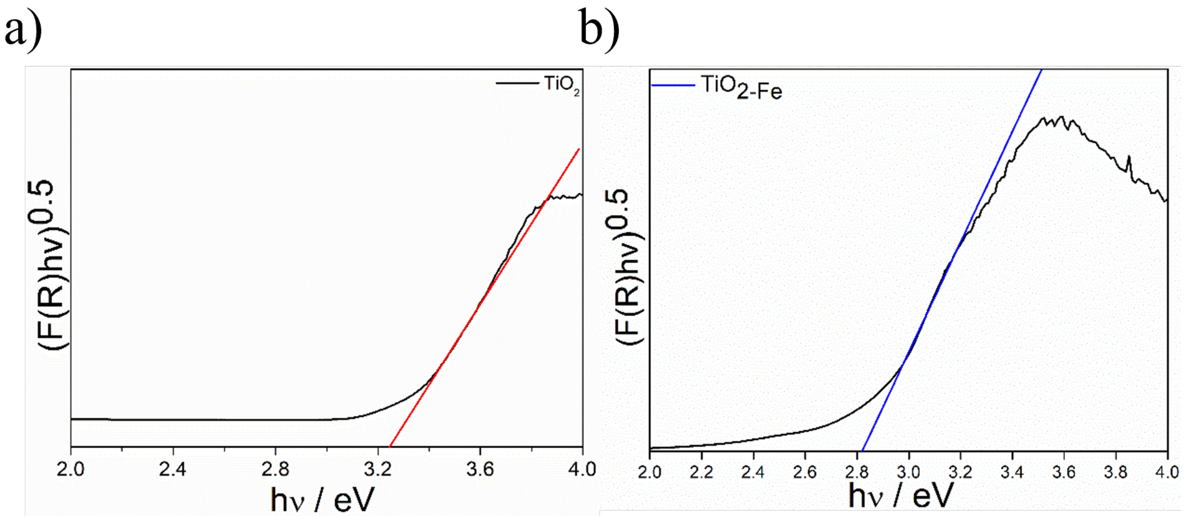

Figure 30 – UV-Vis diffuse reflectance spectroscopy with Wood-Tauc plots (a) pure TiO_2 and (b) Fe-doped TiO_2.

A.3.2.1 Frequency-Depend Optical Dielectric Constant

The optical dielectric function e was calculated in the range of 0 -10 eV. The optical dielectric constant within the framework of the random-phase approximation (RPA) [1] based on DFT ground-state calculations. The mentioned dielectric function consists of frequency-dependent real (ϵ^r) and imaginary part (ϵ^i), according to the equation:

$$\epsilon(\omega) = \epsilon^r(\omega) + i\epsilon^i(\omega), \tag{A.1}$$

The imaginary part, $\epsilon^i(\omega)$, can be calculated using the Kubo-Greenwood formalism [2]. Once we know the imaginary part, the real part can be obtained using the Kramers-Kroning relations [3]. Following Geldasa *et al.* [4], the refractive index(η), extinction coefficient (κ), absorption coefficient (α), reflectivity (R), and optical conductivity (σ) are calculated from the real and imaginary part of the dielectric function as follows:

$$\eta(E) = \left[\frac{\sqrt{\epsilon^r(E)^2 + \epsilon^i(E)^2} + \epsilon^r(E)}{2}\right]^{\frac{1}{2}}; \tag{A.2}$$

$$\kappa(E) = \left[\frac{\sqrt{\epsilon^r(E)^2 + \epsilon^i(E)^2} - \epsilon^r(E)}{2}\right]^{\frac{1}{2}}; \tag{A.3}$$

$$\alpha(E) = \frac{4\pi\kappa(E)}{\lambda}; \tag{A.4}$$

$$R(E) = \frac{(\eta(E)-1)^2+\kappa(E)^2}{(\eta(E)+1)^2+\kappa(E)^2}; \tag{A.5}$$

$$\sigma(E) = \frac{\omega\epsilon^i(\omega)}{4\pi}. \tag{A.6}$$

The calculations were performed using the same protocol but at the gamma point using the GIPAW pseudopotential [5].

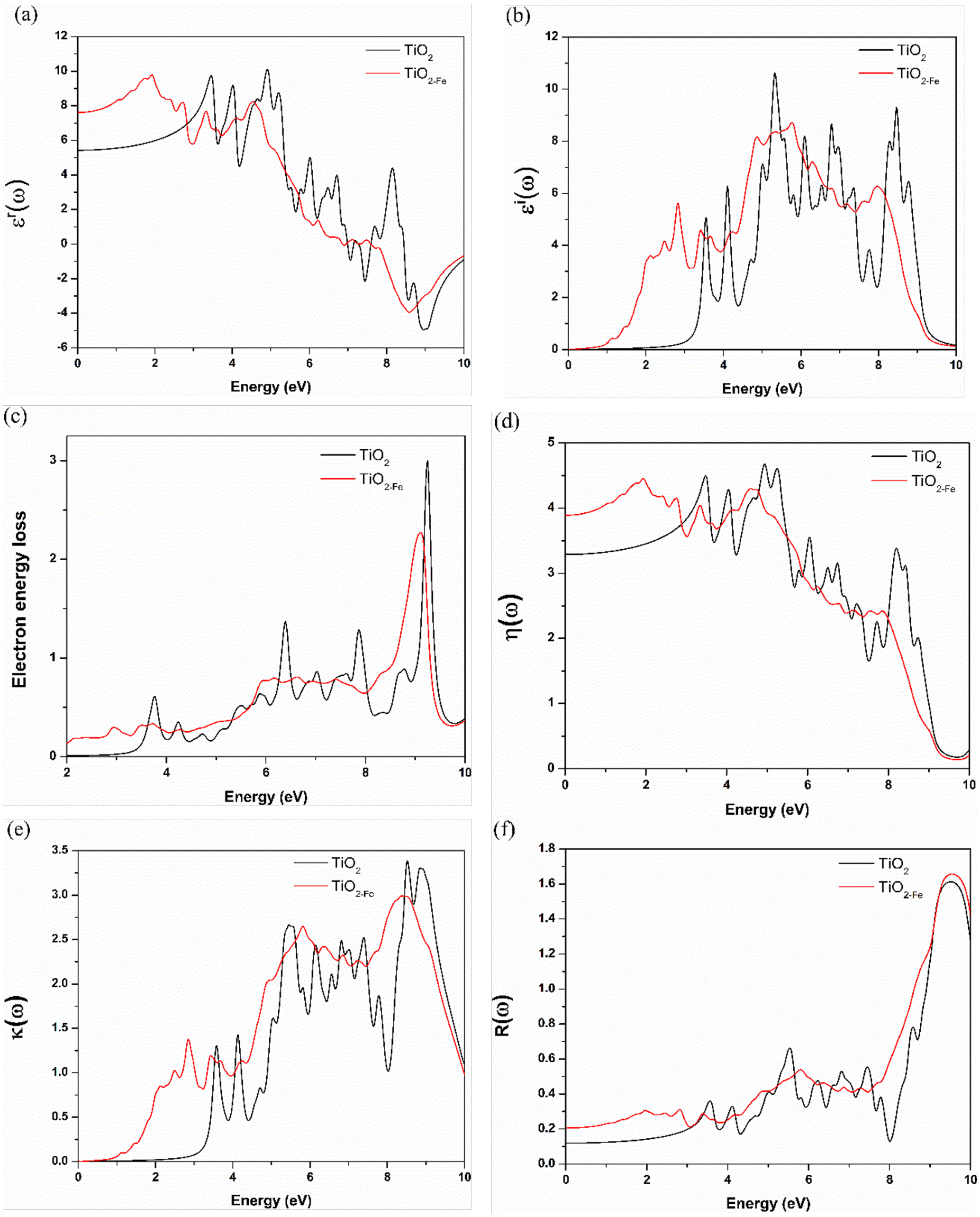

Figure 31 – (a) Real and (b) imaginary part of the dielectric function, (c) energy loss spectrum, (d) refractive index, (e)extinction coefficient, (f) reflectivity.

A.4 Electronic Charge Density

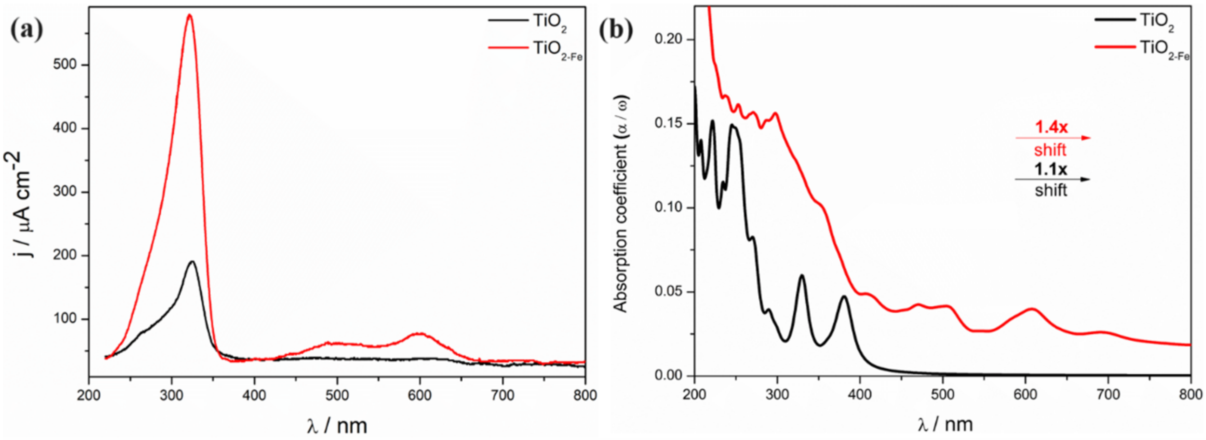

Figure 32 – (a) Experimental photocurrent as a function of wavelength spectra for Fe-doped TiO_2 and TiO_2 photoanodes and (b) Theoretical absorption coefficient as a function of wavelength spectra for Fe-doped TiO_2 and TiO_2.

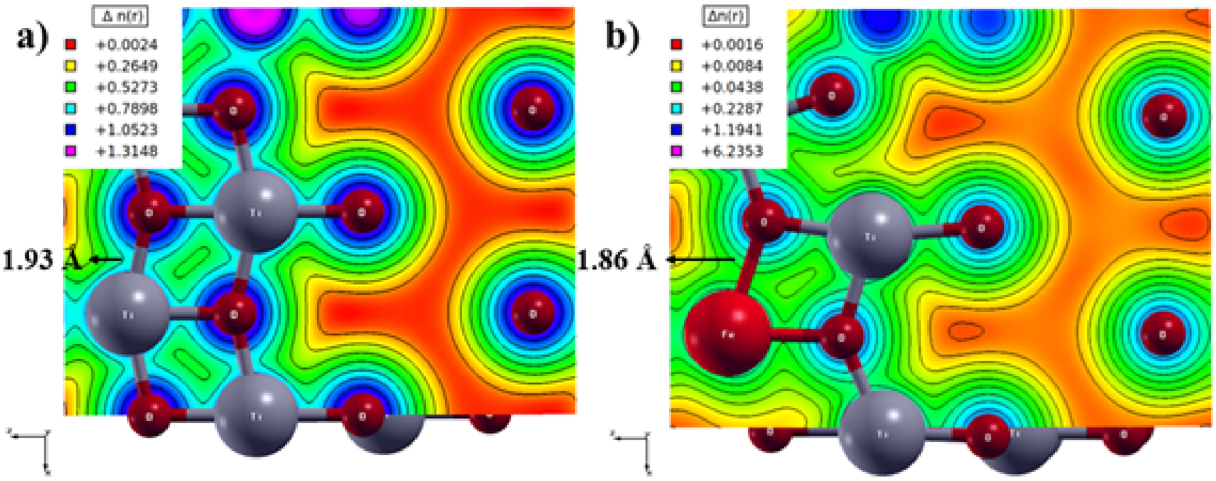

Figure 33 – Electronic charge density obtained for the system a) pure TiO_2 and b) Fe-doped TiO_2.

A.5 Photoelectrochemistry Study

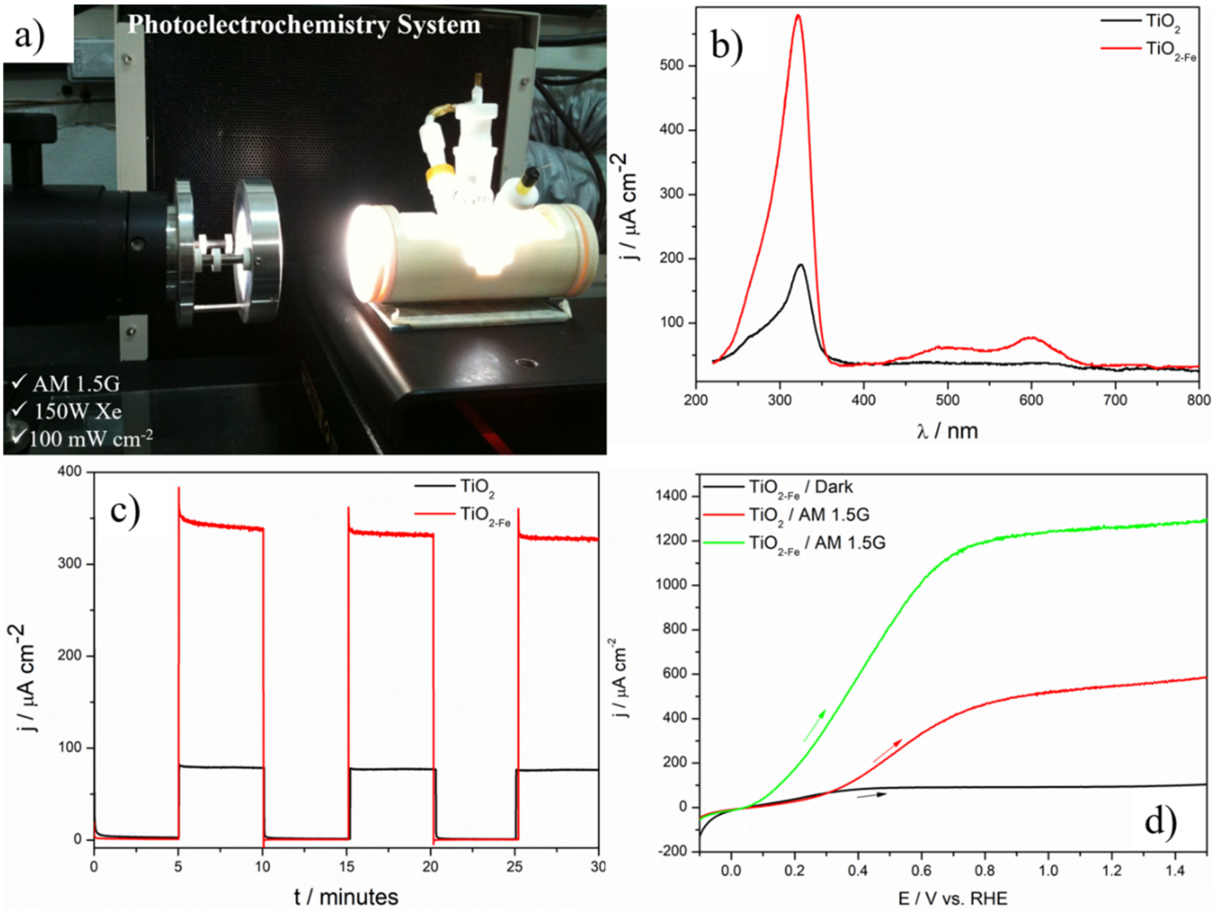

Figure 34 – a) Photoelectrochemical cell used in all water splitting studies b) Photocurrent spectra for Fe-doped TiO_2 and TiO_2 photoanodes, c) Photocurrent transients generated during photoirradiation (E = 0.5 V) for Fe-doped TiO_2 and TiO_2 photoanodes and d) Linear sweep voltammetry obtained for Fe-doped TiO_2 and TiO_2 photoanodes, v = 10 $mV\ s^{-1}$. All photoelectrochemical water splitting measurements were performed in a three-electrode configuration using a reversible hydrogen electrode (RHE) and a counter electrode of platinum wire. AM 1.5G (Newport Oriel Instrument model 66881 QTH).

A.6 Tables

A.7 Coordinates

Table 8 – Total energy Fe doped TiO_2-anatase and TiO_2-rutile.

Polymorph	Energy (Ry)	Fermi Energy (eV)
Anatase		
PURE	2896.600997	8.4178
Ti1-Fe	-3000.652840	8.8990
Ti2-Fe	-3000.899930	9.0297
Ti3-Fe	-3000.811130	8.7807
Ti4-Fe	-3000.868480	8.8943
Ti5-Fe	-3000.899859	9.0313
Ti6-Fe	-3000.899852	9.0300
Ti7-Fe	-3000.899770	9.0312
Ti8-Fe	-3000.870270	9.1059
Rutile		
PURE	-2896.105392	10.7816
Ti1-Fe	-2885.421740	10.1677
Ti2-Fe	-2847.495980	10.1051
Ti3-Fe	-2885.992590	10.2401
Ti4-Fe	-2846.539200	10.1164
Ti5-Fe	-2898.032690	10.2593
Ti6-Fe	-2898.454610	10.0787
Ti7-Fe	-2850.289570	10.0953
Ti8-Fe	-2849.085320	10.0977

Table 9 – Structural and statistical parameters using Rietveld refinement TiO_2(P25) and Fe doped TiO_2.

Parameters/phase	TiO_2		TiO_2 (P25)		TiO_2-Fe	
	a (ICSD - 202242)	r (ICSD - 7802)	a	r	a	r
a/Å	3.78479	4.5941	3.85743	4.68227	3.84426	4.66687
b/Å	3.78479	4.5941	3.85743	4.68227	3.84426	4.66687
c/Å	9.51237	2.9589	9.6837	3.0177	9.6562	3.00687
α/degrees	90	90	90	90	90	90
β/degrees	90	90	90	90	90	90
γ/degrees	90	90	90	90	90	90
V/Å3	136.3	62.4498	144.091	66.158	142.702	65.489
Wt. Fraction			0.87694	0.12306		
χ2			4.09		2.5	
R (F**2)			0.1057			
wRp			0.1084			
Rp			0.0780			

Coordinate (*x y z*) of the TiO2 anatase obtained from Rietveld refinement.

Ti	0.000000	0.946198	3.567139
Ti	0.000000	2.838593	5.945231
Ti	1.892395	2.838593	8.323324
Ti	1.892395	0.946198	1.189046
O	0.000000	0.946198	1.587234
O	0.000000	2.838593	7.925136
O	1.892395	2.838593	6.343419
O	1.892395	0.946198	3.168951
O	0.000000	2.838593	3.965327
O	0.000000	0.946198	5.547044
O	1.892395	0.946198	8.721512
O	1.892395	2.838593	0.790858

Coordinate (*x y z*) of the TiO_2 anatase$_{5\%-Fe}$ obtained from Rietveld refinement.

Ti	0.000000	0.960920	3.620925
Ti	0.000000	2.882760	6.034875
Ti	1.921840	2.882760	8.448825
Ti	1.921840	0.960920	1.206975
O	0.000000	0.960920	1.611167
O	0.000000	2.882760	8.044633
O	1.921840	2.882760	6.439066
O	1.921840	0.960920	3.216733
O	0.000000	2.882760	4.025116
O	0.000000	0.960920	5.630683
O	1.921840	0.960920	8.853017
O	1.921840	2.882760	0.802783

Coordinate (*x y z*) of the TiO_2 rutile obtained from Rietveld refinement.

Ti	0.000000	0.000000	0.000000
Ti	2.297050	2.297050	1.479450
O	1.404416	1.404416	0.000000
O	3.189684	3.189684	0.000000
O	0.892634	3.701466	1.479450
O	3.701466	0.892634	1.479450

Coordinate (*x y z*) of the TiO_2 rutile$_{5\%-Fe}$ obtained from Rietveld refinement.

Ti	0.000000	0.000000	0.000000
Ti	2.331000	2.331000	1.504100
O	1.425174	1.425174	0.000000
O	3.236827	3.236827	0.000000
O	0.905827	3.756174	1.504100
O	3.756174	0.905827	1.504100

Coordinate (*x y z*) of the supercell TiO_2 anatase (DFT).

Ti2	3.784832177	0.946004184	3.567119844
Ti1	3.784967548	2.839122858	5.944941128
Ti1	1.892089708	2.838853601	8.322127598
Ti2	1.891912238	0.946104415	1.190397089
O	3.784707694	0.946165411	1.582140590
O	3.784716393	2.838864944	7.929824461
O	1.892338832	2.838860138	6.337116688
O	1.892328844	0.946165989	3.175152240
O	3.784857431	2.838731466	3.959641571
O	3.784858625	0.946326642	5.552388566
O	1.892169074	0.946338365	8.713499162
O	1.892172981	2.838710405	0.798746235
Ti2	3.784761081	4.731189363	3.567157320
Ti1	3.784769485	6.623686312	5.944927985
Ti1	1.892236207	6.623882964	8.322108401
Ti2	1.892169180	4.731151418	1.190444003
O	3.784713857	4.731142391	1.582137655
O	3.784727106	6.623829836	7.929825849
O	1.892324959	6.623835216	6.337090627
O	1.892305802	4.731139997	3.175174794
O	3.784855996	6.623658808	3.959638788
O	3.784857607	4.731284542	5.552399753
O	1.892172119	4.731272171	8.713494674
O	1.892173953	6.623678945	0.798747584
Ti2	7.569928460	0.946127014	3.567046061
Ti1	7.569795267	2.838841365	5.944920090
Ti1	5.677160653	2.838775689	8.322128681
Ti2	5.677335272	0.946261114	1.190342057
O	7.569683617	0.946167715	1.582115721
O	7.569675780	2.838861929	7.929836738
O	5.677263551	2.838859499	6.337107083
O	5.677273422	0.946167400	3.175151040
O	7.569821399	2.838728509	3.959613281
O	7.569824686	0.946325561	5.552374522
O	5.677141125	0.946337914	8.713479154
O	5.677141932	2.838710460	0.798736304
Ti2	7.570002999	4.731062063	3.567104928
Ti1	7.569999429	6.623973942	5.944883127
Ti1	5.677012525	6.623965610	8.322088603
Ti2	5.677073146	4.730984877	1.190393474
O	7.569678805	4.731140763	1.582153489
O	7.569665120	6.623833534	7.929815150
O	5.677278112	6.623835391	6.337109571
O	5.677297699	4.731137963	3.175162213
O	7.569823813	6.623662194	3.959622298
O	7.569826010	4.731286782	5.552366996
O	5.677138352	4.731273247	8.713477919
O	5.677139928	6.623679084	0.798728894

Coordinate (*x y z*) of the supercell Fe-doped TiO_2 anatase (DFT).

Ti2	3.8840128845	0.9591895822	3.6608317588
Ti1	3.8719132455	2.8861832446	6.1353481083
Ti1	1.9251280712	2.8861851885	8.5573868816
Ti2	1.9400051390	0.9702895556	1.2405444446
O	3.8737910981	0.9365085565	1.6586922393
O	3.8581898451	2.8861802389	8.1404369979
O	1.9329296920	2.8861775990	6.5404191920
O	1.9456635750	0.9498367258	3.2399780268
O	3.8628161636	2.8861856422	4.1285404882
O	3.8660285907	0.9321821301	5.7154179494
O	1.8634676273	0.9503886260	9.0106626708
O	1.9883913475	2.8861826830	0.7831474031
Ti2	3.8840104261	4.8131800225	3.6608322447
Ti1	4.0994172575	6.7343375220	6.1513144223
Ti1	2.1147805689	6.7343432353	8.6259624556
Ti2	1.9400075010	4.8020831918	1.2405423301
O	3.8737889172	4.8358526611	1.6586893083
O	3.8236911391	6.7343484502	8.0677298042
O	1.5390398755	6.7343466897	6.8365291078
O	1.9456653412	4.8225296725	3.2399779389
O	3.9442906730	6.7343388830	4.1348841516
O	3.8660155971	4.8401833609	5.7154210890
O	1.8634704483	4.8219835724	9.0106586501
O	1.9366289651	6.7343403577	0.8305181981
Ti2	7.7248570101	1.0062012737	3.6184345480
Ti1	7.7325307692	2.8861800350	6.1114726001
Ti1	5.8151396861	2.8861768102	8.5693470454
Ti2	5.8054954029	0.9553491867	1.1770370328
O	7.7498977593	1.0193417519	1.6444164439
O	7.7465801541	2.8861852327	8.1027867140
O	5.7958027019	2.8861892695	6.5445378161
O	5.8055166294	0.9863145184	3.2394749214
O	7.7702574961	2.8861791880	4.0643079734
O	7.6932526303	0.9816475474	5.6297447120
O	5.8913063545	0.9622870004	9.0080672607
O	5.7551130585	2.8861793635	0.7822822973
Ti2	7.7248615104	4.7661514268	3.6184305975
Ti1	7.6618137384	6.7343340445	5.9402095795
Fe	5.8528699128	6.7343362221	8.7341568417
Ti2	5.8054933018	4.8169947635	1.1770383266
O	7.7499028595	4.7530142737	1.6444133891
O	5.9210260899	6.7343308292	6.6721524807
O	5.8055171761	4.7860402728	3.2394754794
O	7.7327184067	6.7343352573	4.0339401780
O	7.6932641010	4.7907100643	5.6297421270
O	5.8913003533	4.8100607064	9.0080739485
O	5.8782994940	6.7343380225	0.8635449615

Coordinate (*x y z*) of the supercell TiO_2 rutile (DFT).

Ti1	0.000351578	4.594017151	2.959372948
Ti2	2.296530386	2.296654089	1.479475173
O	1.397728400	1.397667258	2.958970999
O	3.195669449	3.195668504	2.958972063
O	0.899208134	3.694735040	1.479653287
O	3.694699862	0.899199698	1.479652625
Ti1	0.000277920	9.187780778	2.959362273
Ti2	2.296361409	6.891684674	1.479498342
O	1.397885017	5.992198900	2.958974053
O	3.195794992	7.790209428	2.958971287
O	0.899224688	8.288875923	1.479665824
O	3.694704686	5.493267422	1.479665228
Ti1	4.593938021	4.594024560	2.959370080
Ti2	6.891480125	2.296453422	1.479606214
O	5.992140642	1.397840927	2.958972729
O	7.790169418	3.195770716	2.958972593
O	5.493159295	3.694756526	1.479661873
O	8.288884115	0.899163791	1.479662641
Ti1	4.593938897	9.187844848	2.959440234
Ti2	6.891323676	6.891519789	1.479504821
O	5.992277574	5.992354986	2.958975746
O	7.790312616	7.790329672	2.958969395
O	5.493169425	8.288876684	1.479653846
O	8.288864082	5.493228954	1.479652179
Ti2	0.000298995	4.593951042	5.917408518
Ti2	2.296615612	2.296659926	4.437619984
O	1.397744902	1.397678908	5.917384794
O	3.195654851	3.195657919	5.917380240
O	0.899209082	3.694734682	4.438064535
O	3.694705579	0.899195879	4.438063666
Ti1	0.000273465	9.187774400	5.917324927
Ti2	2.296393475	6.891625155	4.437598098
O	1.397896550	5.992208617	5.917382102
O	3.195787845	7.790203168	5.917382378
O	0.899223027	8.288880023	4.438053178
O	3.694703651	5.493267714	4.438051770
Ti1	4.593851693	4.593982385	5.917421922
Ti2	6.891428935	2.296516052	4.437486415
O	5.992144165	1.397844839	5.917385508
O	7.790169758	3.195768294	5.917381816
O	5.493158859	3.694754420	4.438055632
O	8.288887716	0.899159919	4.438055225
Ti1	4.593846303	9.187701372	5.917327361
Ti2	6.891297679	6.891516254	4.437604304
O	5.992286191	5.992367583	5.917381277
O	7.790300790	7.790314969	5.917382657
O	5.493165383	8.288881862	4.438064596
O	8.288861084	5.493230877	4.438062645

Coordinate (x y z) of the supercell Fe – doped TiO2 rutile (DFT).

Ti1	-0.1119199180	4.5085398503	3.0181288128
Ti2	2.3991852668	2.3899585714	1.4940140236
O	1.4727757768	1.4993099078	3.0156013955
O	3.3008405699	3.2834387098	3.0107578643
O	0.9932155057	3.8422457743	1.5545837222
O	3.8182671507	1.0056503444	1.4859336844
Ti1	0.1023692079	9.3335637425	2.9986825906
Fe	2.5564349202	7.1740104722	1.3599871539
O	3.3076504305	7.9225183764	2.9533105627
O	0.9828262257	8.4320439346	1.5012552372
O	3.8129495834	5.5995713506	1.5021107555
Ti1	4.7128209463	4.7218009617	2.9994155690
Ti2	6.9938752878	2.3837723087	1.4524169297
O	6.1117006116	1.4994115409	3.0075350861
O	7.8814880343	3.2738836858	3.0114435013
O	5.6170351291	3.8156796263	1.4760079549
O	8.4287047944	1.0074960525	1.4762729395
Ti1	4.7120225709	9.3283299514	2.9930906333
Ti2	7.0508155780	7.0622064552	1.4848511956
O	6.1612931280	6.1365574656	3.0065400983
O	7.9455661447	7.9657456814	3.0011972727
O	5.6660355117	8.4793130510	1.4768666058
O	8.5019527926	5.6556288327	1.5432260751
Ti1	0.1656313580	4.7840928690	6.0800790184
Ti2	2.3959624348	2.3892513798	4.5326086735
O	1.4726301887	1.4940699222	6.0578612353
O	3.2776194560	3.2933572798	6.0601593303
O	1.0155731780	3.8756307526	4.4869898707
O	3.8021609408	0.9857520247	4.5292807162
Ti1	0.1019710497	9.3219261367	6.0612282221
Ti2	2.4897370609	7.1101778466	4.6163233498
O	1.4967304981	6.1114839932	6.1556248136
O	3.4225985210	8.0330727241	6.0648674299
O	0.9656470241	8.4195365859	4.5128805033
O	3.7982866702	5.5836036034	4.5126827667
Ti1	4.7009840460	4.7220630439	6.0605677315
Ti2	6.9919355265	2.3805111231	4.5626893559
O	6.1191915743	1.5081421961	6.0542199127
O	7.9277893123	3.3176596263	6.0553823194
O	5.6138387082	3.8144998622	4.5394902318
O	8.4276930806	1.0039467066	4.5395019225
Ti1	4.7666375690	9.3815951019	6.0464047401
Ti2	7.0510163434	7.0604303827	4.5234702773
O	6.1555010159	6.1363673563	6.0482282447
O	7.9559476606	7.9419044850	6.0510861861
O	5.6462882363	8.4632642208	4.5193937954
O	8.5367536467	5.6795635231	4.4789055075
O	8.288861084	5.493230877	4.438062645

BIBLIOGRAPHY

1 BRENER, N. Random-phase-approximation dielectric function for diamond, with local field effects included. *Physical Review B*, APS, v. 12, n. 4, p. 1487, 1975. 143

2 MORGAN, G.; GHASSIB, H. The kubo-greenwood formula and local field corrections. *Solid state communications*, Elsevier, v. 67, n. 11, p. 1035–1037, 1988. 143

3 ROESSLER, D. Kramers-kronig analysis of reflection data. *British Journal of Applied Physics*, IOP Publishing, v. 16, n. 8, p. 1119, 1965. 143

4 GELDASA, F. T. et al. Different metal dopants effects on the structural, electronic, and optical properties of β-pbo: a density functional theory study. *The European Physical Journal Plus*, Springer Berlin Heidelberg, v. 138, n. 2, p. 165, 2023. 143

5 PICKARD, C. J.; MAURI, F. All-electron magnetic response with pseudopotentials: Nmr chemical shifts. *Physical Review B*, APS, v. 63, n. 24, p. 245101, 2001. 144

B

B1 - SUPPLEMENTARY INFORMATION.

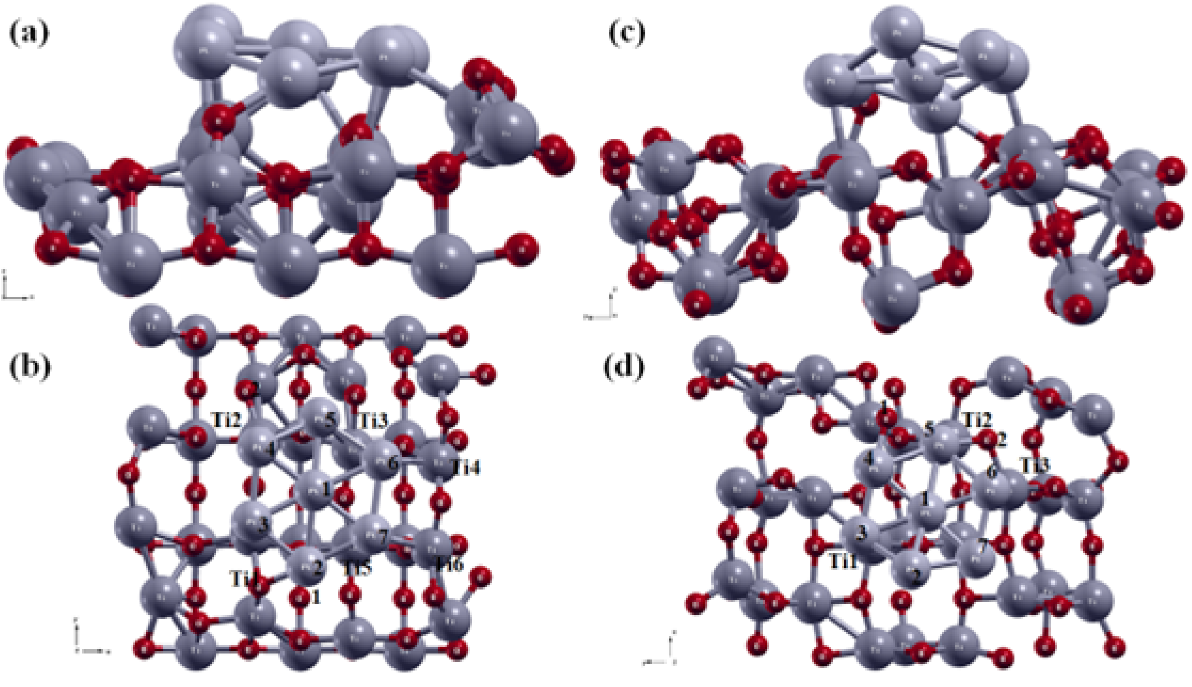

Figure 35 – The optimized structures of the (a) $Pt(1\ 1\ 1)/TiO_2(0\ 0\ 1)$ side view, (b) $Pt(1\ 1\ 1)/TiO_2(0\ 0\ 1)$ top, (c) $Pt(1\ 1\ 1)/TiO_2(1\ 0\ 1)$ side view, and (d) $Pt(1\ 1\ 1)/TiO_2(1\ 0\ 1)$ top view.

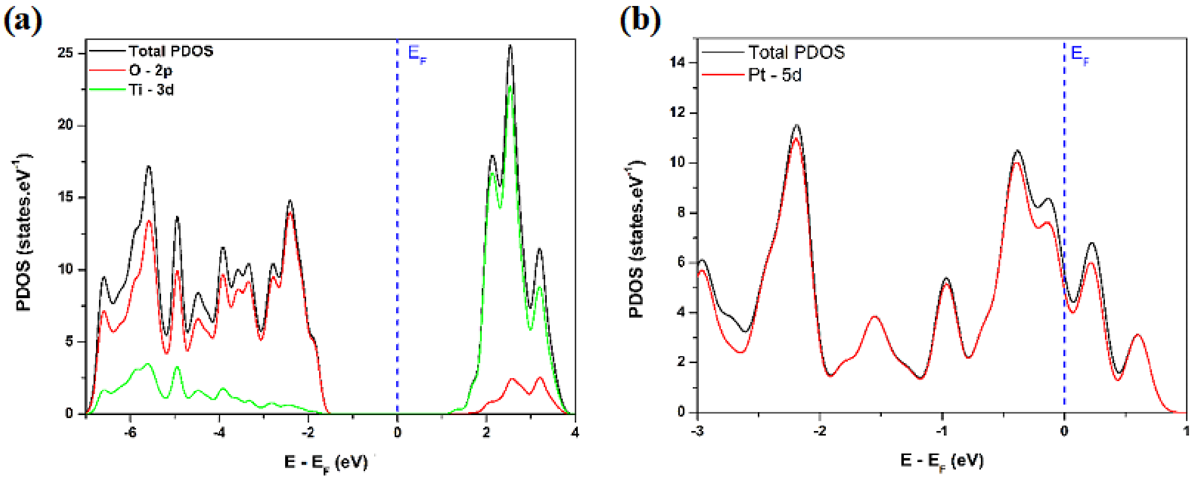

Figure 36 – Projected Density of States (PDOS) for (a) TiO_2 and (b) Pt.

Table 10 – **Coordinates (*x y z*) of the TiO_2 structure obtained from Rietveld refinement**

Ti	-0.00000	283.966	118.776
O	-0.00000	283.966	317.275
Ti	189.311	0.94655	593.881
Ti	189.311	283.966	356.329
Ti	-0.00000	0.94655	831.434
O	189.311	0.94655	792.380
O	189.311	283.966	554.828
O	-0.00000	0.94655	0.79723
O	189.311	283.966	157.830
O	-0.00000	0.94655	632.935
O	-0.00000	283.966	870.487
O	189.311	0.94655	395.382

Table 11 – **Coordinates (*x y z*) of the Pt structure obtained from Rietveld refinement**

Pt	0.00000	0.00000	0.00000
Pt	-0.00000	196.230	196.230
Pt	196.230	-0.00000	196.230
Pt	196.230	196.230	0.00000

Table 12 – Bond lengths of the optimized structures of the $Pt(1\ 1\ 1)/TiO_2(h\ k\ l)$

Distance (Å)	Pt**(1 1 1)/**TiO_2**(0 0 1)**	**Distance (Å)**	Pt**(1 1 1)/**TiO_2**(1 0 1)**
Pt1 – Pt2	2.8105	Pt1 – Pt2	2.5389
Pt1 – Pt3	2.5203	Pt1 – Pt3	2.6023
Pt1 – Pt4	2.6090	Pt1 – Pt4	2.5292
Pt1 – Pt5	2.6949	Pt1 – Pt5	2.6960
Pt1 – Pt6	2.6929	Pt1 – Pt6	2.5186
Pt1 – Pt7	2.6269	Pt1 – Pt7	2.5715
Pt2 – Pt3	2.6628	Pt2 – Pt3	2.6204
Pt3 – Pt4	2.7048	Pt3 – Pt4	2.5563
Pt4 – Pt5	2.6690	Pt4 – Pt5	2.6832
Pt5 – Pt6	2.7237	Pt5 – Pt6	2.7724
Pt6 – Pt7	2.7140	Pt6 – Pt7	2.6027
Pt7 – Pt2	2.6449	Pt7 – Pt2	2.5303
Pt2 – O1	2.0811	Pt3 – T1(6C)	2.7297
Pt3 – Ti1(6C)	2.6330	Pt4 – O1	2.0094
Pt4 – Ti2(5C)	2.3723	Pt5 – Ti2(6C)	2.7628
Pt5 – Ti2(6C)	2.6569	Pt5 – O2	2.1374
Pt5 – Ti3(6C)	2.6767	Pt6 – Ti3(6C)	2.4752
Pt6 – Ti3(6C)	2.6437	-	-
Pt6 – Ti4(4C)	2.7367	-	-
Pt7 – Ti5(6C)	2.7775	-	-
Pt7 – Ti6(6C)	2.6350	-	-

C

C1 - SUPPLEMENTARY INFORMATION.

C.1 X-ray diffraction (XRD) and Rietveld refinement

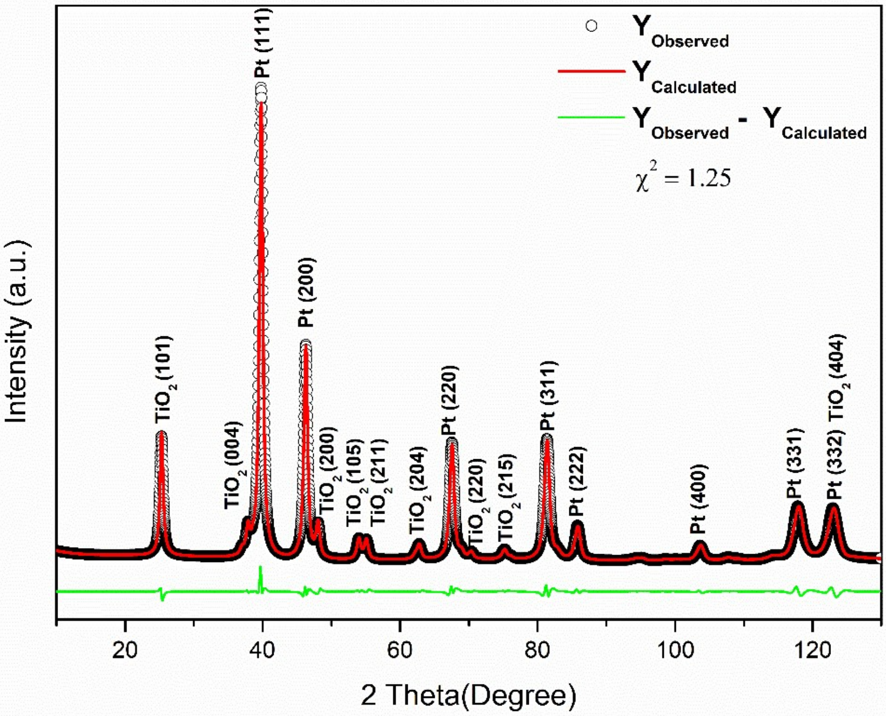

Figure 37 – XRD and Rietveld refinement pattern for Pt/TiO_2 crystalline material.

Table 13 – Structural and statistical parameters using Rietveld refinement for Pt/TiO_2 materials.

Parameters/phase	Tetragonal/Anatase - TiO_2	Cubic/Pt
a/Å	3.77891(11)	3.91492(3)
b/Å	3.77891 (0)	3.91492 (0)
c/Å	9.4799(5)	3.91492 (0)
α = β = γ /degrees	90.0	90.0
V/Å^3	135.374(9)	60.0026(15)
Particle size/nm	12.81	12.43
Wt. Fraction	0.59919	0.40081
χ^2	1.25	
R(F2)	0.0211	
wRp	0.0451	
GOF	1.16	

C.2 $Pt_3(1\ 1\ 1)/TiO_2(h\ k\ l)$ interfaces bonds.

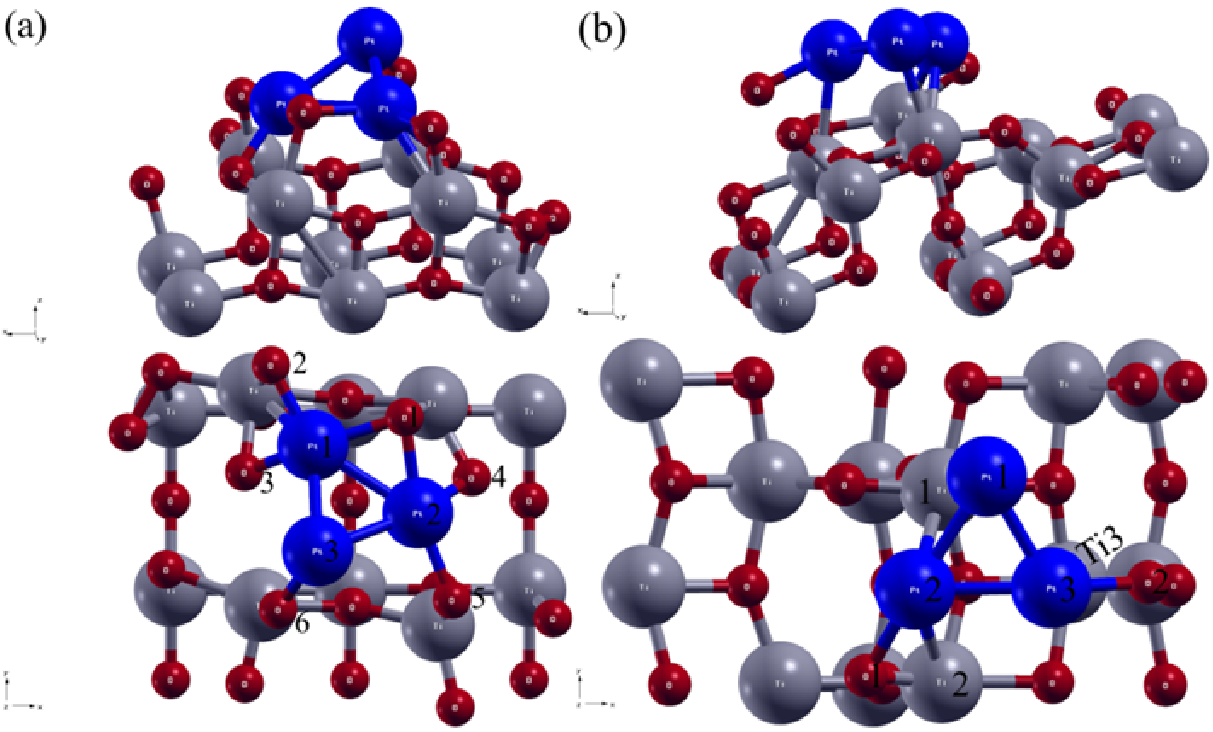

Figure 38 – The optimized structures of the (a) $Pt_3(1\ 1\ 1)/TiO_2(0\ 0\ 1)$ interface side and top view and (b) $Pt_3(1\ 1\ 1)/TiO_2(1\ 0\ 1)$ interface side and top view, respectively.

Table 14 – Bond lengths of the optimized structures of the $Pt_3(1\ 1\ 1)/TiO_2(h\ k\ l)$

Distance (Å)	$Pt_3(1\ 1\ 1)/TiO_2(0\ 0\ 1)$	Distance (Å)	$Pt_3(1\ 1\ 1)/TiO_2(1\ 0\ 1)$
Pt1 – Pt2	2.4817	Pt1 – Pt2	2.5438
Pt1 – Pt3	2.6397	Pt1 – Pt3	2.4860
Pt2 – Pt3	2.6042	Pt2 – Pt3	2.5546
Pt1 – Ti1$_{(5C)}$	2.6203	Pt1 – Ti1$_{(5C)}$	2.6372
Pt1 – O1	2.0238	Pt2 – Ti1$_{(5C)}$	2.7836
Pt1 – O2	1.9182	Pt2 – Ti2$_{(4C)}$	2.7145
Pt1 – O3	2.0035	Pt3 – Ti3$_{(5C)}$	2.8049
Pt2 – O1	2.0568	Pt2 – O1	2.0643
Pt2 – O4	1.9955	Pt3 – O2	2.0206
Pt2 – O5	1.9848	-	-
Pt3 – O6	1.8569	-	-

C.3 Band Structure and Projected Density of States (PDOS)

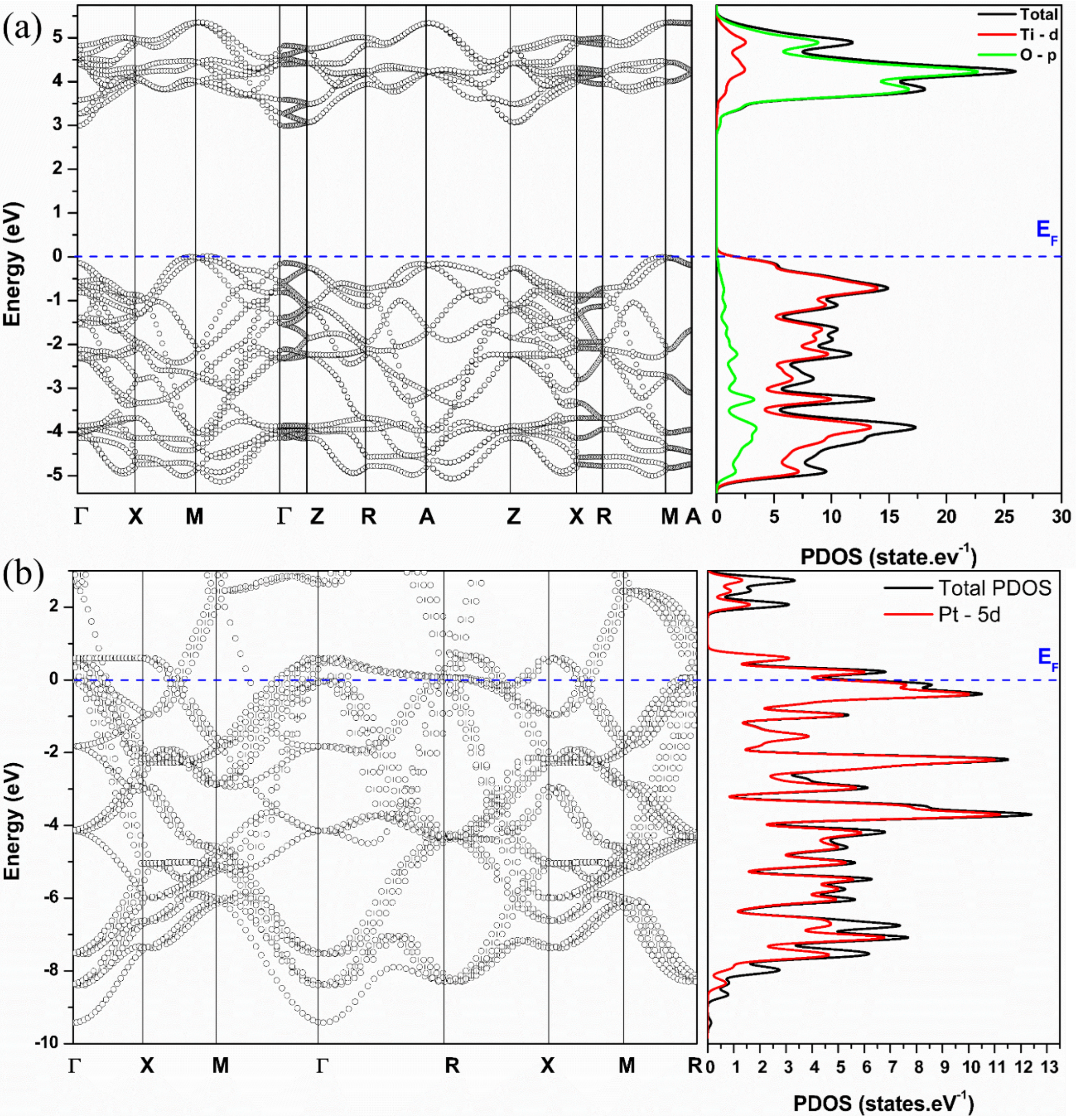

Figure 39 – Band Structure and Projected Density of States (PDOS) for (a) anatase TiO_2 and (b) Pt from Rietveld refinement structure.

C.4 Images of initial, transition, and final states of hydrogen and water splitting reactions.

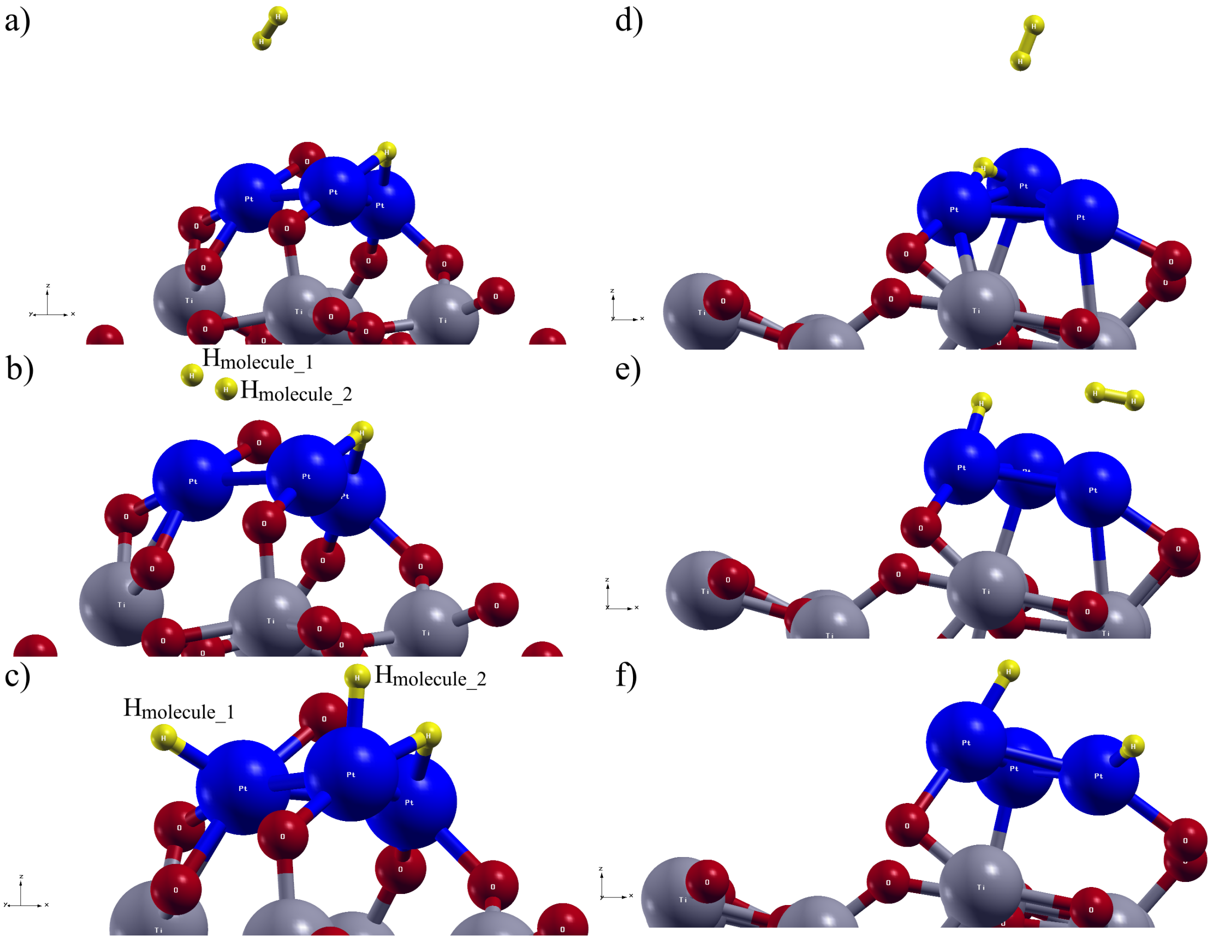

Figure 40 – Images of initial, transition, and final states of hydrogen splitting reactions (a), (b) and (c) $Pt_3(1\ 1\ 1)/TiO_2(0\ 0\ 1)$, (d), (e), and (f) $Pt_3(1\ 1\ 1)/TiO_2(1\ 0\ 1)$.

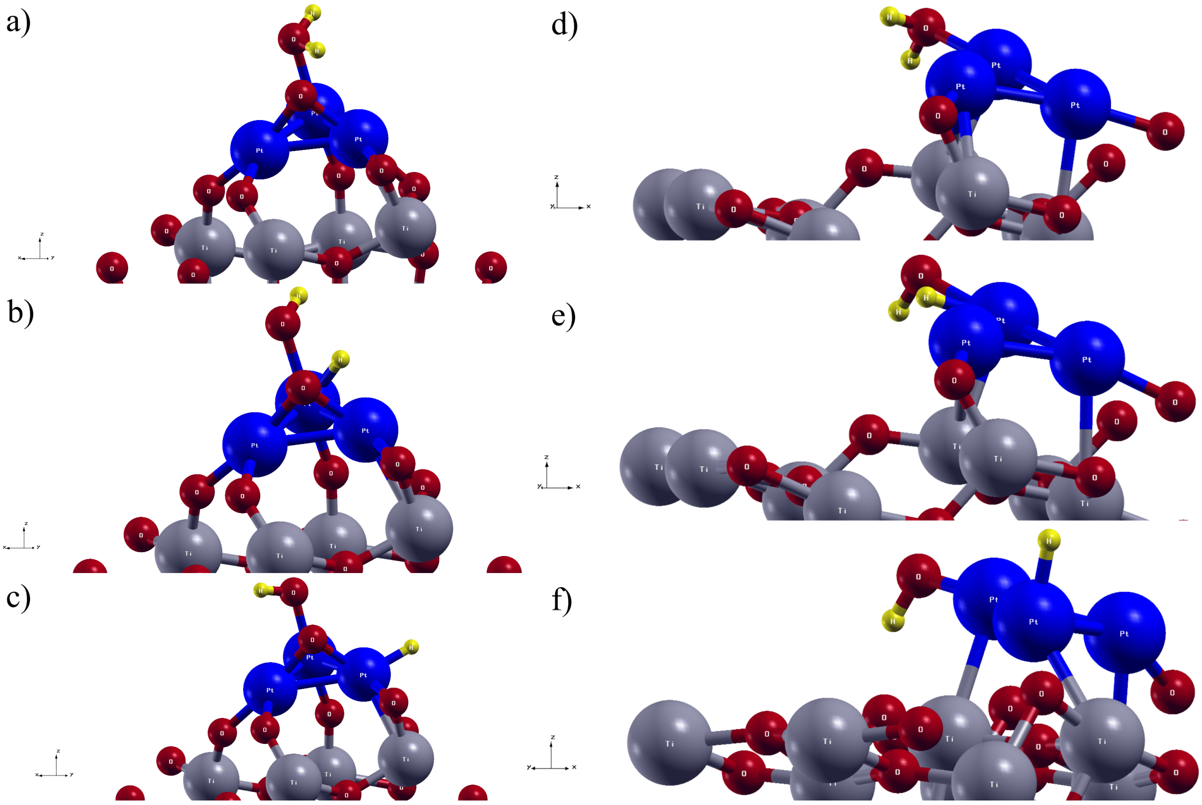

Figure 41 – Images of initial, transition, and final states of water splitting reactions (a), (b) and (c) $Pt_3(1\ 1\ 1)/TiO_2(0\ 0\ 1)$, (d), (e), and (f) $Pt_3(1\ 1\ 1)/TiO_2(1\ 0\ 1)$.

C.5 Coordinates (x y z)

Table 15 – Coordinates (x y z) of the TiO2 structure obtained from Rietveld refinement.

Ti	-0.00000	283.966	118.776
O	-0.00000	283.966	317.275
Ti	189.311	0.94655	593.881
Ti	189.311	283.966	356.329
Ti	-0.00000	0.94655	831.434
O	189.311	0.94655	792.380
O	189.311	283.966	554.828
O	-0.00000	0.94655	0.79723
O	189.311	283.966	157.830
O	-0.00000	0.94655	632.935
O	-0.00000	283.966	870.487
O	189.311	0.94655	395.382

Table 16 – Coordinates (x y z) of the Pt structure obtained from Rietveld refinement

Pt	0.00000	0.00000	0.00000
Pt	-0.00000	196.230	196.230
Pt	196.230	-0.00000	196.230
Pt	196.230	196.230	0.00000

C.6 Convergence test

The Figure 42 shows the parameterized cutoff energy for the Pt/TiO_2 interface on the (0 0 1) and (1 0 1) planes.

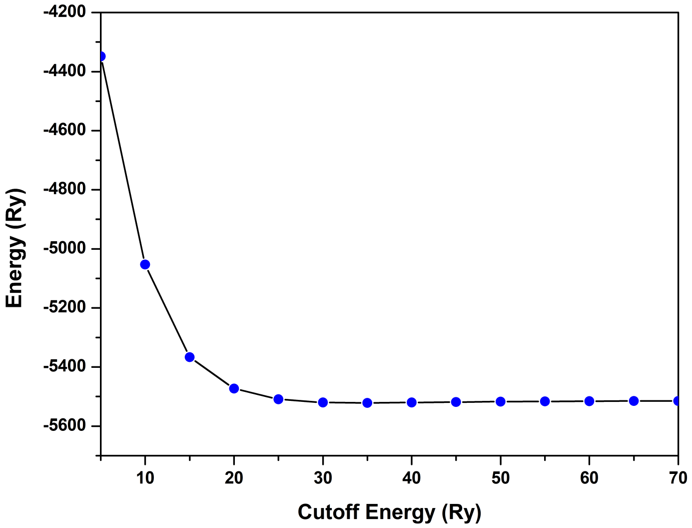

(a) Pt/TiO_2 on the (0 0 1) plane

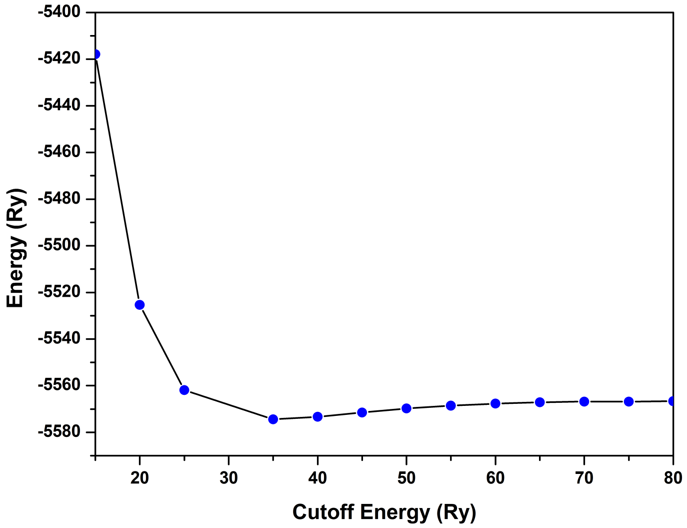

(b) Pt/TiO_2 on the (1 0 1) plane

Figure 42 – Convergence test of the cutoff energy for the $Pt/TiO_2/$ interface.

The minimum suggested cutoff energy in the pseudopotential file is 39 Ry for the platinum atom, 47 Ry for the oxygen atom, and 52 Ry for the titanium atom. Thus, an energy of 55 Ry was chosen for both systems. It can be observed in Figures 42a and 42b that from this energy onwards, the variation becomes constant

The parameterization for the *k*-points is shown in Table 17. The *k*-points used for the system with the plane (0 0 1) were 4 x 4 x 2. It is worth noting that the variation between the energy values is on the order of 10^{-4}. Other points were tested. However, *k*-points > 4 x 4 x 2 required a memory allocation exceeding 60 GB, making calculations for electronic properties unfeasible. For the system with the plane (1 0 1), the *k*-points used were 6 x 4 x 2, where the energy variation is on the order of 10^{-5}.

Table 17 – Test for the *k*-point mesh

	Energy (Ry)		Energy (Ry)
(0 0 1)		(1 0 1)	
2 X 2 X 1	-5516.15861	4 x 2 x 1	-5568.51449
4 X 4 X 2	-5516.15844	6 x 4 x 2	-5568.51448
		8 x 6 x 4	-5568.51448

C.7 Publications

- Real, C. G., Thaines, E. H. N. S., Pocrifka, L. A., Freitas, R. G., Singh, G., Zanin, H. Free-standing niobium pentoxide-decorated multiwalled carbon nanotube electrode: Charge storage mechanism in sodium-ion pseudocapacitor and battery. Journal of Energy Storage, v. 52, p. 104793, 2022.

- Nunes, W. G., Pires, B. M., Thaines, E. H. N. S., Pereira, G. M., da Silva, L. M., Freitas, R. G., Zanin, H.. Operando Raman spectroelectrochemical study of polyaniline degradation: A joint experimental and theoretical analysis. Journal of Energy Storage, v. 55, p. 105770, 2022.

- Freitas, B., Nunes, W. G., Real, C. G., Rodella, C. B., Doubek, G., da Silva, L. M., Thaines, E. H. N. S., Pocrifka, L. A., Freitas, R. G., Zanin, H.. Combining in situ electrochemistry, operando XRD & Raman spectroscopy, and density functional theory to investigate the fundamentals of Li 2 CO 3 formation in supercapacitors. Journal of Materials Chemistry A, v. 11, n. 38, p. 20636-20650, 2023.

- Thaines, E. H., Ferreira, C. S., Oliveira, A. C., Garcia, M. D., Freitas, R. G., Passos, R. R., Silva, E. C., Pocrifka, L. A. Structural and electrochemical analysis of Ni/NiO supercapacitor materials: A theoretical and experimental study. Solid State Ionics, v. 394, p. 116194, 2023.
- Thaines, E. H., Oliveira, A. C., Pocrifka, L. A., Duarte, H. A., Freitas, R. G. Influence of Fe-Doping on the Structural and Electronic Properties of the TiO2 Anatase: Rutile. The Journal of Physical Chemistry C, v. 127, n. 46, p. 22518-22529, 2023.